On the relationship between synthesis and stability in formamidinium lead triiodide perovskite



Benjamin M. Gallant

Corpus Christi College

Department of Physics

University of Oxford

A thesis submitted in fulfilment of the requirements for the degree of Doctor of Philosophy at the University of Oxford

July 2023

Declaration

This thesis is a result of my own work and includes nothing which is the result of collaboration except where explicitly stated in the text.

I declare that no part of this work has been submitted for a degree or any other qualification at this or any other university.

Benjamin M. Gallant, July 2023.

“God made the bulk; the surface was invented by the Devil”

Wolfgang Pauli, perhaps foreshadowing the invention of perovskite solar cells

On the relationship between synthesis and stability in formamidinium lead triiodide perovskite

Benjamin M. Gallant, Corpus Christi College, University of Oxford

A thesis submitted for the degree of Doctor of Philosophy. Hilary Term, 2023

Abstract

The work presented in this thesis principally investigates and develops the processing, properties and photovoltaic performance of formamidinium lead triiodide perovskite ($FAPbI_3$). Since its first use in perovskite solar cells (PSCs) by Eperon, et al., in 2014 this composition has often been overlooked by the perovskite research community in favour of alloying formamidinium (FA^+) with methylammonium (MA^+) or cesium (Cs^+), or iodide (I^-) with bromide (Br^-). This is principally due to the thermodynamic instability of the desirable photoactive α-phase under ambient conditions. α-$FAPbI_3$ has been shown to be kinetically metastable with respect to transformation to the photoinactive hexagonal δ-phase. However, typically this metastability is only on the order of days. By contrast, to be commercially relevant PSCs will need to remain stable under operation over at least several years. Often perovskite stability is attributed directly and solely to its composition. Here we explore mechanisms by which it is possible to substantially increase the stability of α-$FAPbI_3$, and critically use these to highlight that the process by which this perovskite is fabricated is integral to its resulting stability.

First, the motivation behind this work is presented (**Chapter 1**), followed by an overview of the relevant scientific theory underpinning our findings and inventions (**Chapter 2**). An in-depth description of the synthetic methods and the characterisation techniques employed in this work follows (**Chapter 3**).

In **Chapter 4** we present a novel process for the deposition of thin layers of α-$FAPbI_3$ that employs volatile, low-toxicity solvents compatible with large scale processing of perovskite materials. By first depositing a 2D perovskite material we are able to template the growth of highly crystalline α-$FAPbI_3$, which we show out-performs other state-of-the-art $FAPbI_3$-based materials.

Chapter 5 takes the α-$FAPbI_3$ material developed in the preceding chapter and spotlights the substantially improved ambient and thermal stability it displays in comparison to other state-of-the-art perovskites. We explore the mechanisms behind these enhancements and report preliminary work on the integration of our α-$FAPbI_3$ perovskite into highly stable PSCs. By comparison with a wide array of other perovskite materials we are able to directly link, and begin to explain, the process by which the perovskite is made with its resultant stability.

Finally, **Chapter 6** explores the role methylenediammonium dichloride ($MDACl_2$) plays in stabilising α-$FAPbI_3$. We show that previous reports claiming that the MDA^{2+} is incorporated into the perovskite lattice are erroneous, and that instead a complex array of chemical reactions in solution lead to the inclusion of tetrahyrdrotriazinium (THTZ-H^+) in the structure of $FAPbI_3$, resulting in a substantial increase in the ambient phase stability of this perovskite.

Having established that metal halide perovskites can function as highly effective photoabsorber materials in next-generation photovoltaics, research effort has now turned to developing perovskite materials that can deliver stable power output over a number of years. Pristine $FAPbI_3$ has, for the most part, been left out of this ongoing work. Perhaps it is time to reconsider?

Acknowledgements

None of this work would have happened if not for the support and guidance of Professor Henry J. Snaith. In 2018, Henry took a chance on a young student of chemistry, with no background in optoelectronics – even less perovskites – living on the other side of the planet. The opportunity to join Henry's group and study at the University of Oxford is one I will always be grateful for. Since then, the freedom Henry has afforded me to pursue my own scientific obsessions, and the faith placed in me, has allowed me to tread a path that still fascinates, frustrates and fulfils on a daily basis. I hope this thesis will demonstrate that this faith has not been misplaced.

Throughout my PhD I have had the support and guidance of an astounding number of fantastic scientists. In particular I will name just two; Philippe Holzhey who, despite our differences, taught me so much about the art of solar cell fabrication, and Dr Joel Smith whose unwavering support both as a scientific and personal mentor I fear I shall never repay. Thank you both, and to the many, many others who have imparted so much of their wisdom on me along the way.

I would not be where I am, nor who I am, today without the support of my parents. Thank you for encouraging me to always pursue my aspirations and to never cease exploring myself, and for stepping back at times to allow me the space to pursue both.

To all those who have loved, supported and let me into your lives these many years, you know who you are, and everything that you've done for me. This work is for all of you.

Publications

B.M. Gallant, P. Holzhey, S. Choudhary, K.A. Elmestekawy, J.A. Smith, J.M. Ball, M.G. Christoforo, P. Caprioglio, L.M. Herz, H.J. Snaith, "A green solvent system for templated sequential deposition of stable formamidinium lead triiodide for perovskite solar cells", *Under Review*

B.M. Gallant, E. A. Duijnstee, P. Holzhey, D. J. Kubicki, S. Collavini, B. Sturdza, H. C. Sansom, J.A. Smith, M.J. Gutmann, S. Saha, M. Gedda, M.I. Nugraha, M. Kober-Czerny, C. Xia, A.D. Wright, Y. Lin, A.J. Ramadan, E. Y.-H. Hung, S. Seo, S. Zhou, J. Lim, T.D. Anthopoulos, M.R. Filip, M.B. Johnston, R. Nicholas, J. Delgado, H.J. Snaith, "Understanding the degradation of methylenediammonium and its role in phase-stabilising formamidinium lead triiodide single crystals", J. Am. Chem. Soc. **2023**, 145 (18), 10275-10284, 10.1021/jacs.3c01531

X. Shen, **B.M. Gallant**, P. Holzhey, J.A. Smith, K.A. Elmestekawy, Z. Yuan, P.V.G.M. Rathnayake, S. Bernardi, A. Dasgupta, E. Kasparavicius, T. Malinauskas, P. Caprioglio, O. Shargaieva, Y. Lin, M.M. McCarthy, E. Unger, V. Getautis, A. Widmer-Cooper, L.M. Herz, H.J. Snaith, "Chloride-based additive engineering for efficient and stable wide-bandgap perovskite solar cells", Advanced Materials, **2023**, 10.1002/adma.202211742

K.A. Elmestekawy, **B.M. Gallant**, A.D. Wright, P. Holzhey, N.K. Noel, M.B. Johnston, H.J. Snaith, L.M. Herz, "Influence of intrinsic quantum confinement on photovoltaic performance in formamidinium lead triiodide thin films", ACS Energy Lett., **2023**, 8, 2543-2551, 10.1021/acsenergylett.3c00656

M. Taddei, J.A. Smith, **B.M. Gallant**, S. Zhou, R.J.E. Westbrook, Y. Shi, J. Wang, J.N. Drysdale, D.P. McCarthy, S. Barlow, S.R. Marder, H.J. Snaith, D.S. Ginger, “Ethylenediamine Addition Improves Performance and Suppresses Phase Instabilities in Mixed-Halide Perovskites”, ACS Energy Lett. **2022**, 7 (12), 4265–4273, 10.1021/acsenergylett.2c01998

J.A. Smith, O. Shargaieva, A. Shnier, R. Kilbride, N. Martsinovich, M. O’Kane, J. Pascual, B.M. Gallant, H. Sansom, M. Flatken, K-A. Zaininger, H. Näsström, J. Rawle, A. Dallman, N. Reeves-Mclaren, D. Wamwangi, D. Billing, E. Unger, A. Abate, O. Game, H. J. Snaith, D.G. Lidzey, “Understanding the role of methylamine in the crystallisation of halide perovskites using in-situ X-ray scattering”, *In Preparation*

S. Zhou, J. Zhang, Y. Shi, J.A. Smith, J. Drysdale, **B.M. Gallant**, R. Castañeda, P. Therdkatanyuphong, M. Taddei, D.P. McCarthy, S. Barlow, H. Sansom, R. Kilbride, A. Dasgupta, A. Marshall, J. Wang, D.S. Ginger, S.R. Marder, H.J. Snaith, “Effects of Applying Benzylamine as a Monoamine Additive Passivation in Wide-bandgap Perovskites”, *In Preparation*

Patents

B.M. Gallant, P.J. Holzhey, H.J. Snaith, “Perovskite Production Process”, **2021**, *Application number: GB2113494.5*

B.M. Gallant, P.J. Holzhey, E.A. Duijnstee, S. Collavini, J-L. Delago, H.J. Snaith, “Precursor compounds for perovskite materials”, **2022**, *Application number: GB2217726.5*

Key Presentations

Conference Talks

“From 2D to 3D: A green solvent system for templated sequential deposition of efficient and stable perovskite solar cells”, Spring MRS, Hawaii, 2022

“Green processing of high performance, highly stable formamidinium lead triiodide”, Supersolar, 2022

Poster Presentations

“Revealing the stabilising effect of $MDACl_2$ on α-$FAPbI_3$ as a new amidinium cation formed by in-situ degradation”, Fall MRS, Boston, 2022

Table of Contents

Chapter 1: Introduction

1.1 Unsustainable 18

1.2 Our Energy Crisis 19

1.3 Harnessing AM1.5G, economically 20

1.4 Metal Halide Perovskites 24

1.5 Structure of the Thesis 25

1.6 Bibliography 28

Chapter 2: Background Theory

2.1 Hybrid organic-inorganic metal halide perovskites

2.1.1 Composition and structure 29

2.1.2 Desirable properties 34

2.1.3 Solution processing 35

2.2 Perovskite solar cells

2.2.1 Semiconductors and Band Theory 39

2.2.2 The photovoltaic effect 42

2.2.3 Quantum efficiency, AM1.5 and the detailed balance limit 46

2.2.4 Solar cell operation 49

2.2.5 Perovskite solar cell architectures and performance 55

2.3 Bibliography 58

Chapter 3: Experimental Methods

3.1 Materials 62

3.2 Fabrication

3.2.1 Substrate Preparation 64

3.2.2 Electron Transport Materials 64
3.2.3 Hole Transport Materials 65
3.2.4 Perovskite Thin Film Materials 65
3.2.5 Perovskite Single Crystal Materials 70
3.2.6 Interlayer Materials 71
3.2.7 Electrode Materials 71
3.2.8 Encapsulation Methods 71
3.3 Characterisation
3.3.1 Optoelectronic Characterisation 75
3.3.2 Nuclear Resonance Spectroscopy 83
3.3.3 X-ray Diffraction 85
3.3.4 Microscopy 86
3.3.5 Compositional Analysis 86
3.3.6 Characterisation of Solar Cells 89
3.4 Bibliography 92

Chapter 4: A green solvent system for templated deposition of formamidinium lead trihalide perovskite solar cells

4.1 Introduction 94
4.2 A biorenewable, low toxicity solvent system 96
4.3 2D-templated growth of 3D perovskites 99
4.4 Investigating '2D-templated growth' 103
4.5 ^{t}2D-3D α-$FAPbI_3$: Optoelectronic and photovoltaic performance 109
4.6 Conclusion and outlook 114
Appendix A4.1 Solvents for scalable processing 116

Appendix A4.2 Relating $R_{BA\text{-}MA+}$ to <*n*> 118

4.7 Bibliography 122

Chapter 5: Enhancing formamidinium lead triiodide perovskite stability: process directs properties

5.1 Introduction 125

5.2 Enhanced ^{t}2D-3D $FAPbI_3$ phase stability 127

5.3 Enhanced ^{t}2D-3D $FAPbI_3$ thermal stability 133

5.4 ^{t}2D-3D $FAPbI_3$ perovskite solar cell stability 143

5.5 Conclusion and outlook 152

Appendix A5.1 TD-GCMS traces 155

5.6 Bibliography 161

Chapter 6: Understanding the degradation of methylenediammonium and its stabilisation of formamidinium lead triiodide single crystals

6.1 Introduction 163

6.2 Single crystal growth and optoelectronic performance 165

6.3 MDA^{2+} solution instability 169

6.4 $FAPbI_3$-$MDACl_2$ precursor solution chemistry 175

6.5 Solid-state compositional analysis of $FAPbI_3$ single crystals 181

6.6 Conclusion and outlook 191

Appendix A6.1 Single crystal X-ray diffraction (SCXRD) 193

Appendix A6.2 Mechanistic discussion 202

Appendix A6.3 Structural model of FAPbI3 with additive THTZ-H^{+} 207

6.7 Bibliography 212

Chapter 7: Conclusion

7.1 Key findings of the thesis 215

7.2 Outlook, and future investigation 217

List of Figures

Chapter 1: Introduction

1.1 Global Energy Consumption 19

1.2 Energy in the Earth system 20

1.3 Harnessing AM1.5 with perovskites 21

1.4 Levelized cost of electricity 23

Chapter 2: Theoretical Background

2.1 Perovskite ABX_3 crystal structure 30

2.2 Low-dimensionality perovskite-derived structures 33

2.3 Metal halide perovskite solution processing 36

2.4 Electronic band structure of $CsPbI_3$ 40

2.5 Band structure of conductors, semiconductors and insulators 41

2.6 The photovoltaic effect 43

2.7 Direct and indirect bandgap semiconductors 44

2.8 Detailed balance limit 48

2.9 $J-V$ characteristics of a solar cell 51

2.10 Circuit diagram of solar cell with parasitic losses 52

2.11 Impact of parasitic losses on $J-V$ characteristics 53

2.12 Perovskite solar cell device architectures 56

Chapter 3: Experimental Methods

3.1 Single crystal synthesis and device fabrication process 70

3.2 PSC encapsulation 74

Chapter 4: A green solvent system for templated deposition of formamidinium lead trihalide perovskite solar cells

4.1	Scalable processing compatibility	96
4.2	Mixed-phase 2D templates	101
4.3	Templated 2D to 3D (^{t}2D-3D) conversion	102
4.4	Optimising 2D template	104
4.5	Template-dependent lead (II) iodide content	105
4.6	Optimal 2D template	106
4.7	Unsuccessful $n = \infty$ ($MAPbI_3$) template	107
4.8	Optoelectronic performance	110
4.9	PSC operational performance	112
A4.1	Determining 2D template composition	120
A4.2	Controlling 2D template composition	121

Chapter 5: Enhancing formamidinium lead triiodide perovskite stability: process directs properties

5.1	Enhanced ambient stability: Absorbance	128
5.2	Enhanced ambient stability: XRD	129
5.3	Enhanced ambient stability: Visible light microscopy	130
5.4	Enhanced ambient stability: Scanning electron microscopy	131
5.5	Enhanced thermal stability	134
5.6	Investigating *sym*-triazine evolution	139
5.7	Operational material stability: Absorbance	143
5.8	Operational material stability: Visible light microscopy	144
5.9	Enhanced ambient PSC stability	145

5.10 p-i-n PSC champion performance 148

5.11 p-i-n PSC dark heat stability 149

5.12 p-i-n PSC photostability 150

5.13 p-i-n PSC damp-heat stability 150

5.14 p-i-n PSC heat-light stability 151

A5.1 Volatile products of perovskite thermal degradation 160

Chapter 6: Understanding the degradation of methylenediammonium and its stabilisation of formamidinium lead triiodide single crystals

6.1 Single crystal optoelectronics 166

6.2 Single crystal stability 167

6.3 Investigating α-$FAPbI_3$ single crystals with Raman spectroscopy 168

6.4 Degradation of MDA^{2+} 170

6.5 MDA^{2+} predicted NMR spectra 171

6.6 Demonstrating NH_4^+ as a degradation product 172

6.7 Degradation of MDA^{2+} 173

6.8 Mechanism of degradation of MDA^{2+} 174

6.9 Demonstrating HMTA-H^+ as a degradation product 175

6.10 $FAPbI_3$-M single crystal composition 177

6.11 THTZ-H^+ in $FAPbI_3$-M single crystals 178

6.12 THTZ-H^+ formation from $MDACl_2$ degradation in presence of FA^+ 179

6.13 THTZ-H^+ formation from MDA^{2+} or HMTA-H^+. 180

6.14 $FAPbI_3$-additive single crystal composition 182

6.15 ^{1}H solid-state NMR of $FAPbI_3$ single crystals 183

6.16 Quantitative ^{1}H MAS (50 kHz) NMR spectra 184

6.17 ^{13}C solid-state NMR of $FAPbI_3$ single crystals 185

6.18	Comparison of the ^{13}C signatures of FA^+ in δ- and α-phases	186
6.19	^{1}H-^{1}H spin diffusion spectroscopy	187
6.20	^{14}N solid-state NMR of $FAPbI_3$ single crystals	188
6.21	Quantifying chloride content	189
6.22	^{127}I NQR of $FAPbI_3$ single crystals	190
A6.1	Single crystal X-ray diffraction of $FAPbI_3$	195
A6.2	Diffraction patterns for $FAPbI_3$ crystals	196
A6.3	MDA^{2+} degradation mechanism	202
A6.4	Mechanistic justification for methaniminium from HMTA	204
A6.5	GBL washing experiments	209
A6.7	Non-FA^+ organics in $FAPbI_3$ single crystals	210

Chapter 1 – Introduction

1.1 – Unsustainable

Human exploitation of planet Earth is unsustainable. As a species, we are pleased to describe this planet as “ours”. However, for many this obsession with ownership is at the root of much that is dangerous in humanity’s dysfunctional relationship with Earth. Humans have drawn, and redrawn, the natural geography of this planet. Often with little or no regard for Earth’s current or future inhabitants. For example, recent research has found that worldwide between 2001 and 2015 more than 300 million hectares (1.27×10^{12} m^2) of forest was lost, with 25% of this land converted to commodity crops for human consumption[1]. Meanwhile, construction of urban centres and the increase in human population to fill them mean humans now comprise nine times more biomass than all wild mammals put together[2].

With burgeoning human population has come an ever-increasing demand for energy. Energy to heat our homes, to power our vehicles and to produce the goods we covet. Fuels are a convenient vessel for the storage and transport of energy. What’s more, humanity has conveniently discovered a fuel we can simply dig, drill or pump out of the ground; fossil fuels. Today these carbon rich fuel deposits also act as humanity’s primary energy source.

So, what’s the catch? There are two: (1) fossil fuels are a finite resource that will necessarily run out, and (2) exploitation of these fuels as a source of energy releases gases toxic to life into Earth’s atmosphere, while simultaneously transforming the planet into a greenhouse. Global warming, caused by the Greenhouse effect and driven by anthropogenic release of gases that are highly absorbent in the mid-infrared (IR), holds the potential to further resculpt Earth’s natural environment, irrevocably.

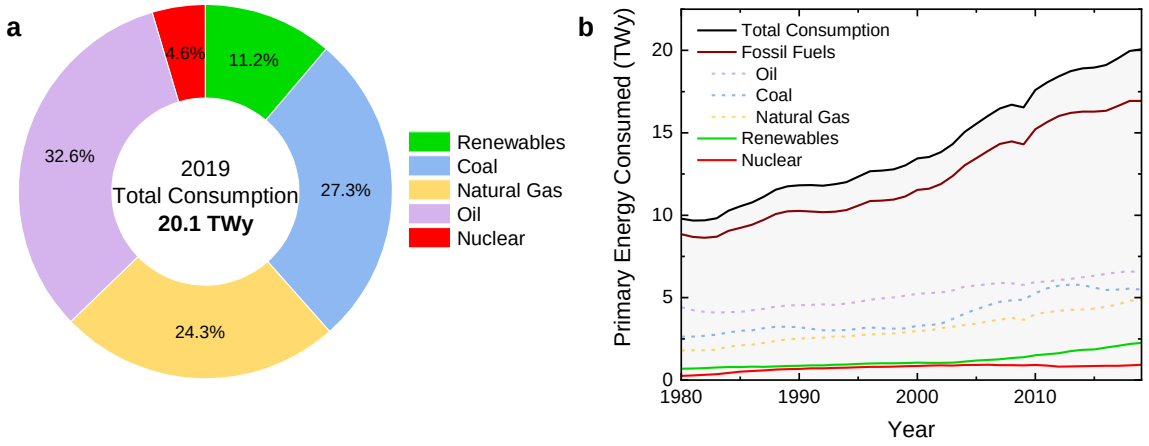


Figure 1.1 | Global energy consumption a) Total global primary energy consumption by source in 2019 [3]. **b)** Trend in global primary energy consumption since 1980 [3].

Despite these dangers, replacing fossil fuel use by modern society has proven exceptionally difficult. The challenge can be dissected to three main themes. First and second, the twin technical challenges of simultaneously replacing fossil fuels as a source of and a store of energy. Third, an apparent lack of political will to surmount either of these technical challenges, exacerbated by the need for decades-long research investment and set against the lucrative and immediate profits afforded by continued fossil fuel exploitation. This thesis puts forward novel research towards the first of these themes; harnessing alternative energy sources.

1.2 – Our Energy Crisis

Of the 20.1 TWy of primary energy consumed in 2019 just 11.2% was produced renewably, while fossil fuels provided 84.4% (**Figure 1.1a**)[3]. More alarmingly, if the average rate of increase in renewable and fossil fuel use recorded annually over the past decade (5.0% and 1.7%, respectively, **Figure 1.1b**)[3] continues, primary energy consumption from renewable sources will not even match fossil fuel use until 2083. Besides the catastrophic impact this trajectory will wreck on the planet, it is highly doubtful that the fossil fuel reserves required to allow such consumption exist on Earth

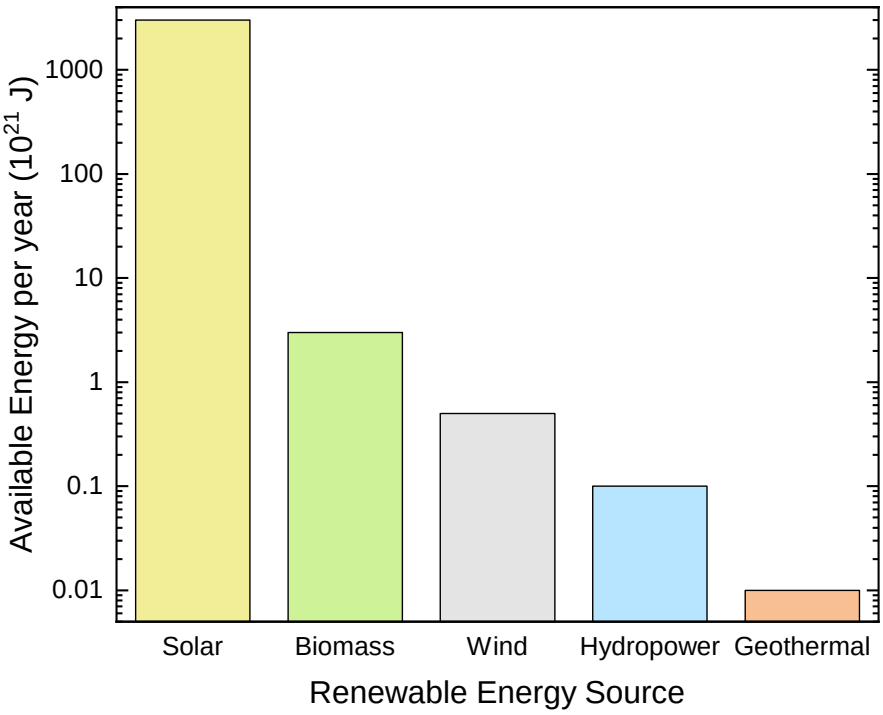


Figure 1.2 | Energy in the Earth system. Available energy per year in Earth system from renewable sources. Adapted from Environmental Chemistry, 9th Edition, S.E. Manahan (2005), CRC Press[4].

(50.4 TWy, annually, equivalent to 41.1 trillion litres of diesel). Remarkably, however, this quantity of energy arrives on earth every 2.5 minutes in the form of solar radiation. Harnessing this form of renewable energy – or others including wind, geothermal and hydropower – is not without technical challenges. In particular, for widespread replacement of hydrocarbon fuels in transportation novel fuels or batteries that can be used as short-term stores for energy collected renewably must be developed concurrently. However, the sheer scale of the renewable energy resources available in the Earth system cannot be overstated (**Figure 1.2**)[4]. Given these realities, asking *if* humanity will transition to renewable energy appears obsolete; the questions are now *how* and *when*.

1.3 – Harnessing AM1.5G, economically

As **Figure 1.2** shows, by far the most abundant source of energy available in the Earth system originates from our nearest star. As an approximate blackbody radiator, the

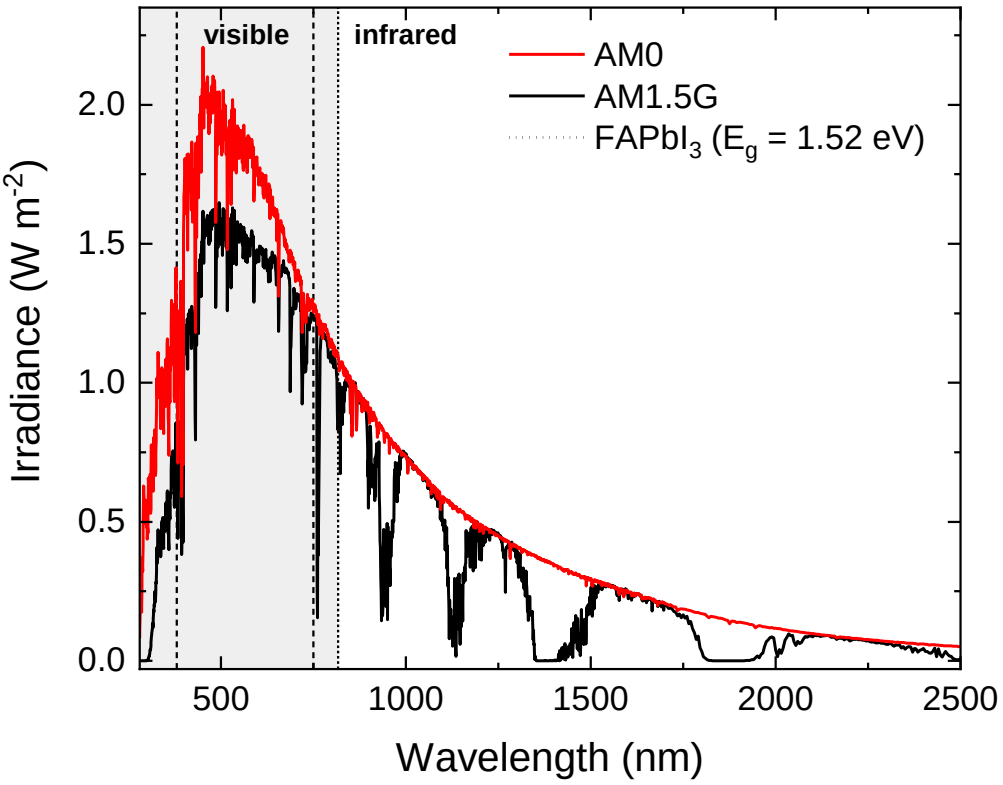


Figure 1.3 | Harnessing AM1.5 with perovskites. Solar spectrum, with (black, AM1.5G) and without (red, AM0) considering absorption and scattering by Earth's atmosphere.

Sun emits electromagnetic radiation in a continuous spectrum of wavelengths with radiance described by Planck's Law (**Figure 1.3**, AM0). The wavelength at which radiance peaks can be approximated using Wien's displacement law and the surface temperature of the Sun, giving a value of 500 nm. However, as discussed further in **Chapter 2**, spectrally non-uniform absorption and scattering of incident radiation by the Earth's atmosphere reduce irradiance at the surface. Accounting for atmospheric effects and standardising to a total irradiance of 100 mW cm^{-2} results in the air mass 1.5 global (AM1.5G) spectrum (**Figure 1.3**, AM1.5G), which is used around the world to test and report photovoltaic (PV) cell performance. As the so-called "detailed-balance limit" calculations show, the theoretical maximum power conversion efficiency (PCE) of a PV cell depends on the bandgap (E_g) of the semiconductor employed as its photoabsorber (see **Chapter 2.2.3**). The optimum E_g for a single-junction PV cell is

found to be 1.34 eV (925 nm), although small deviations in E_g (1.1-1.4 eV) lead to only minor losses in maximum theoretical PCE.

A number of semiconductor materials with $1.1 < E_g < 1.4$ eV have been developed and utilised in PV devices. Historically, silicon has dominated these technologies. However, with E_g ~1.1 eV silicon PV suffers from substantial voltage losses due carrier thermalisation of above-E_g photons. Moreover, a relatively low absorption coefficient means a thick layer of material (~180 µm) is required to access the highest photocurrents[5]. For high PCE, crystalline silicon (c-Si) is required, the production of which requires energy intensive Czochralski crystallisation at >1,700 K [6]. The need for thick, rigid crystalline layers also severely limits their use in flexible PV and therefore ultralight-weight Internet of Things (IoT) applications[7]. Principally to combat these limitations, a number of other semiconductor technologies have been developed, the majority of which are processable as thin film PV cells (nm to several µm thick). These include cadmium telluride (CdTe), copper indium gallium selenide (CIGS), gallium arsenide (GaAs), amorphous silicon (a-Si), metal halide perovskites and a wide range of organic materials[8].

The performance, fabrication costs and extent of commercialisation of these technologies varies widely. However, in many applications to be widely adopted all thin film PV cells must provide a competitive levelized cost of electricity (LCOE) that outperforms c-Si. LCOE is a measure considering the cost of installing and operating a generation facility against the amount of electricity produced across the lifetime of that facility, and expressed as a price per unit electrical energy generated. **Figure 1.4a** shows how the reported LCOE of newly-constructed power generation facilities varied between 2010 and 2021 for a range of energy sources[9]. By far the greatest rate of reduction in LCOE across these technologies has been in PV, which by 2021 has



Figure 4 | Levelized cost of electricity. a) Weighted average levelized cost of electricity (LCOE) from newly commissioned, utility-scale power generation technologies, 2010 to 2021. **b)** Weighted average levelized cost of electricity (LCOE) of utility-scale PV compared to fuel and CO_2 cost only for fossil gas in Europe, 2010-2022 (predicted costs in 2022). Reproduced from Renewable Power Generation Costs 2021, International Renewable Energy Agency (IRENA)[9].

collapsed to less than 12% of that achieved by new facilities commissioned in 2010. In the same period, the weighted average LCOE offered by new fossil fuel installations has only reduced to 86% of its 2010 value. Significantly, the LCOE offered by new PV installations is now lower on average than that achieved for fossil fuels (**Figure 1.4a and 1.4b)**[9].

1.4 – Metal Halide Perovskites

Among the latest generation of thin film PV materials, hybrid organic-inorganic metal halide perovskites have stood out. First reported in 1978 by Weber, et al.[10,11], it was not until 2006 that this class of materials was first employed in a PV device[12]. The 2009 report from Kojima, et al.[13], describing the use of a halide perovskite as a photosensitizer sounded the starters gun on a race to fabricate the highest possible performance perovskite solar cell (PSC) that, 13 years later, shows no sign of slowing down. In 2012 two further reports employing perovskite photosensitisers were released[14,15]. Crucially, Lee, et al., were able to show that the perovskite semi-conductor can itself provide exceptionally long charge carrier lifetime, effectively paving the way for planar PSCs based on a range of metal oxide electron transport layers (ETLs) and spiro-OMeTAD, a high-performance solid-state hole transport layer (HTL)[15]. The subsequent torrent of academic publications and commercial interest in this class of PVs has been remarkable, if not altogether undeserved. The blend of their unique optoelectronic and materials properties, and the tolerance of these properties to a wide variety of “low-tech” processing methods, render halide perovskites not only extremely facile to produce but also remarkably cheap[16]. Unlike c-Si, the performance of which is extremely sensitive to both material purity and the high-quality crystal growth, highly absorbing direct E_g perovskite materials with remarkably low trap densities, long charge carrier lifetimes and compositionally tuneable bandgaps can be fabricated by techniques as straightforward as spin or slot-die coating[17].

A number of outstanding technical challenges remain before halide perovskites could be expected to become commonplace in our everyday lives as sources of energy generation. Perhaps the two most critical of these are PSC stability[18] and the development of scalable processing techniques compatible with GW-scale production

of perovskite PV products[16]. This thesis will present recent advances in halide perovskite fabrication that address both these challenges.

1.5 – Structure of the Thesis

According to the detailed-balance limit, formamidinium lead triiodide ($FAPbI_3$) possesses the closest E_g (~1.5 eV) of any lead-based perovskite to that corresponding to the maximum theoretical solar cell PCE. $FAPbI_3$ also possesses greatly improved thermal stability when compared with the archetypal halide perovskite, methyammonium lead triiodide ($MAPbI_3$). However, the thermodynamically preferred phase of $FAPbI_3$ under ambient conditions is the hexagonal (*2H*) δ-phase, which is photoinactive. It is possible to fabricate $FAPbI_3$ in the desirable photoactive α-phase and, because of the kinetically complex transformation from α-to-δ, kinetically entrap α-$FAPbI_3$ as a metastable phase under ambient conditions. This work will present novel rationally-designed approaches to the scalable fabrication of highly stable α-$FAPbI_3$.

First, **Chapter 2** provides an overview of the theoretical background to the findings reported. This includes discussion of the structure and composition of metal halide perovskites, how these relate to their highly desirable optoelectronic properties and in particular methods for their facile solution processing. The function and characterisation of perovskite solar cells is then presented, including discussion of fundamental semiconductor physics as applied to perovskite materials.

Chapter 3 details the specific methods and characterisation techniques employed in the work presented here. This includes detailed discussion of the fundamentals of these characterisation techniques, with particular attention paid to how they may be best employed in the study of halide perovskite materials.

Chapter 4 introduces a novel low-toxicity, biorenewable solvent system from which a controllable range of 2D Ruddlesden-Popper perovskite compositions can be processed. It is shown that these 2D perovskites act as highly effective templates for subsequent transformation to α-$FAPbI_3$, which operate at over 20% efficiency when integrated into photovoltaic cells.

In **Chapter 5** we comprehensively investigate the stability enhancements imparted on α-$FAPbI_3$ as a result of the 2D-templated fabrication route presented in **Chapter 4**. We find that both the thermal and ambient phase stability of this important perovskite are substantially improved by fabrication via our process, in comparison to other state-of-the-art methods. Using a wide suite of characterisation methods, including thermal-desorption gas-chromatography mass-spectrometry, we shed light on the degradation processes occurring and discuss the possible origin of the observed enhancements. In particular we highlight the importance, not only of composition, but of fabrication process by which a perovskite material is made on its resulting stability. We report our ongoing work to integrate 2D-templated α-$FAPbI_3$ into p-i-n configuration PSCs in order to fully replicate the observed improvements in materials stability in PV devices.

Chapter 6 takes a different approach to stabilising α-$FAPbI_3$. Beginning with the widely reported high-performance α-$FAPbI_3$ additive methylenediammonium dichloride ($MDACl_2$) we demonstrate that – contrary to previous understanding – the MDA^{2+} dication is unstable in pH-neutral polar solutions, degrading rapidly to ammonium and hexamethylenetetramine (HMTA). We show that α-$FAPbI_3$ single crystals grown from a solution containing either $MDACl_2$ or HMTA show vastly improved stability with respect to transformation to the δ-phase. By performing a combination of liquid- and solid-state NMR measurements, along with X-ray diffraction (XRD) techniques, we find that previously unreported organic species are present in crystals. Remarkably,

however, these correspond to neither the MDA^{2+}, NH_4^+, HMTA nor any of the intermediates in the degradation pathway of $MDACl_2$. Instead we are able to show that interruption of the degradation pathway by reaction of these intermediates with excess FA^+ generates alternative organic species in-situ. It is these alternative products that are incorporated into the $FAPbI_3$ bulk material and lead to α-phase stabilisation.

Chapter 7 summarises all findings presented in the thesis and contextualises them in the current state-of-the-art.

1.6 – Bibliography

1. Curtis, P. G., Slay, C. M., Harris, N. L., Tyukavina, A. & Hansen, M. C. Classifying drivers of global forest loss. *Science (6407).* **361**, 1108–1111 (2018).

2. Bar-On, Y. M., Phillips, R. & Milo, R. The biomass distribution on Earth. *Proc. Natl. Acad. Sci. U. S. A.* **115**, 6506–6511 (2018).

3. US Environmental Information Administration. Estimation for Lagged Data in Selected International Energy Statistics. (2019).

4. Manahan, S. E. *Environmental Chemistry*. (CRC Press, 2005).

5. VDMA. *International Technology Roadmap for Photovoltaics*. (VDMA, 2020).

6. Czochralski, J. Ein Neues Verfahren Zur Messung Der Kristallisationsgeschwindigkeit Der Metalle. *Zeitschrift für Phys. Chemie* **92**, 219–221 (1918).

7. Um, H. D., Hwang, I., Choi, D. & Seo, K. Flexible Crystalline-Silicon Photovoltaics: Light Management with Surface Structures. *Accounts Mater. Res.* **2**, 701–713 (2021).

8. Massiot, I., Cattoni, A. & Collin, S. Progress and prospects for ultrathin solar cells. *Nat. Energy* **5**, 959–972 (2020).

9. Taylor, M., Ralon, P. & Al-Zoghoul, S. *Renewable Power Generation Costs in 2021*. (International Renewable Energy Agency, 2022).

10. Weber, D. $CH_3NH_3PbX_3$, a Pb(II)-System with Cubic Perovskite Structure. *Zeitschrift für Naturforsch. B* **33**, 1443–1445 (1978).

11. Weber, D. $CH_3NH_3SnBr_xI_{x-3}$ (x = 0-3), a Sn(II)-System with Cubic Perovskite Structure. *Z. Naturforsch* **33**, 862–865 (1978).

12. Kojima, A., Teshima, K., Shirai, Y. & Miyasaka, T. Novel Photoelectrochemical Cell with Mesoscopic Electrodes Sensitized by Lead-halide Compounds. *ECS Meet. Abstr.* **MA2008-02**, 27–27 (2006).

13. Kojima, A., Teshima, K., Shirai, Y. & Miyasaka, T. Organometal halide perovskites as visible-light sensitizers for photovoltaic cells. *J. Am. Chem. Soc.* **131**, 6050–6051 (2009).

14. Kim, H. S. *et al.* Lead iodide perovskite sensitized all-solid-state submicron thin film mesoscopic solar cell with efficiency exceeding 9%. *Sci. Rep.* (2012).

15. Lee, M. M., Teuscher, J., Miyasaka, T., Murakami, T. N. & Snaith, H. J. Efficient hybrid solar cells based on meso-superstructured organometal halide perovskites. *Science (6107).* **338**, 643–647 (2012).

16. Rong, Y. *et al.* Challenges for commercializing perovskite solar cells. *Science (6408).* **361**, (2018).

17. Nayak, P. K., Mahesh, S., Snaith, H. J. & Cahen, D. Photovoltaic solar cell technologies: analysing the state of the art. *Nat. Rev. Mater.* **4**, 269–285 (2019).

18. Snaith, H. J. & Hacke, P. Enabling reliability assessments of pre-commercial perovskite photovoltaics with lessons learned from industrial standards. *Nat. Energy* **3**, 459–465 (2018).

Chapter 2 – Theoretical Background

As their name suggests, hybrid organic-inorganic metal halide perovskite semiconductors are chemically, and structurally, complex. To fully appreciate their structure and fabrication from solution, and the critical role both of these play in the defining the properties of the resultant materials, a fundamental understanding of how matter exists and interacts in the solid and liquid states is necessary. Although a full treatment of the above would encompass a substantial part of all that is understood by the physical sciences, here a summary of the most critical considerations will be presented. Appropriate citations are provided throughout, however, much of the discussion presented on fundamental semiconductor physics and the photovoltaic effect draws from the more comprehensive treatments presented in Physics of Solar Cells (P. Würfel and U. Würfel, Wiley-VCH Verlag, 2016)[1] and The Physics of Solar Cells (J. Nelson, Imperial College Press, 2003)[2].

2.1 – Hybrid organic-inorganic metal halide perovskites

2.1.1 – Composition and structure

Perovskites are crystalline materials related by their common structure, which is the most abundant on Earth thanks to the abundance of silicate perovskites in the mantle[3]. The first report of the perovskite structure was in naturally occurring $CaTiO_3$ in 1839, typifying the general ABX_3 ionic formula, where A and B are cationic and X is anionic. As in all subsequent “3D” perovskite materials reported, this structure is based on a continuous network of corner-sharing BX_6 octahedral units, with A cations situated in the cuboctahedral interstices generated by the B-X scaffold (**Figure 2.1**)[4].

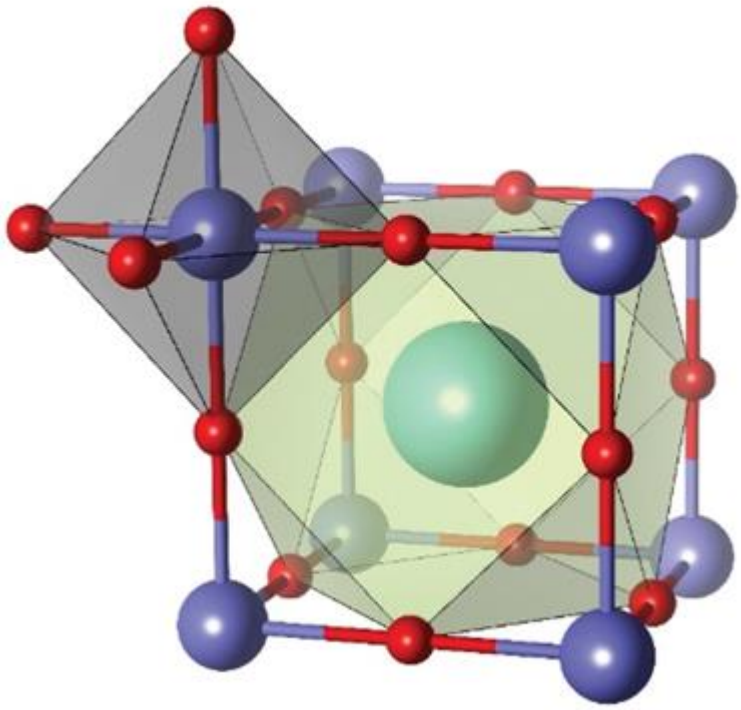


Figure 2.1 | Perovskite ABX_3 crystal structure. Generic primitive cubic unit cell common across ABX_3 perovskites. (A, blue; B, purple; X, red). A single corner-sharing BX_6 octahedron is shown. Note: radii shown are not representative; anion size reduced for clarity. Reproduced with permission from Seok, et al. (2020)[4].

The focus of this thesis will be lead (B^{2+} = Pb^{2+}) halide (X^- = I^-, Br^-, Cl^-) – in particular iodide – perovskites. Although a wide range of A-site cations have been proposed for lead halide perovskites, three in particular dominate; methylammonium (MA^+), formamidinium (FA^+) and cesium (Cs^+), or alloys thereof. A wide variety of bonding modes contribute to stabilising such structures, in part depending on composition. Although coulombic interactions certainly play a critical role, halogen bonding between halides and organic A-site cations is important in determining the dynamic disorder – or lack thereof – of that A-site cation, while the haloplumbate lattice itself shows substantial covalent character[5–7]. As will be discussed, recent research has shown that the covalency of this network is of critical importance to a number of the remarkable photovoltaic (PV) properties of halide perovskites.

Considering the complex bonding regime, a simple labelling of these materials as ionic is misleading. However, as set out first by Goldschmidt in 1926[8], for determination of structural stability alone, approximating constituents as hard spherical ions and considering only the geometry of their ionic radii results in a useful – if granular – metric to quantify the likelihood of forming a stable 3D perovskite. Goldschmidt defined a tolerance factor, τ, for the 3D ABX_3 structure as:

$$\tau = \frac{r_A + r_X}{\sqrt{2}(r_B + r_X)} \tag{2.1}$$

where r_A, r_B and r_X are the ionic radii of the A, B and X-site ions. It was proposed that a 3D perovskite structure would form if $0.8 < \tau \leq 1.0$, with τ = 1.0 being geometrically 'ideal'.

We note that the term "3D", as defined as comprising a corner-sharing network of BX_6 octahedra, is preferred herein over a crystal system description. This is due to the variety of de-symmetrising octahedral tilting effects observed in metal halide perovskites. The origin of octahedral tilting is strongly dependent on the composition, bonding and dynamics of a given perovskite. However, it is often observed that tilting leads to stabilisation of the ABX_3 structure, without substantially altering its desirable properties as a photoabsorber (for example bandgap or photoconductivity). The concurrent de-symmetrising effect also means the cubic space group – assigned in the idealised ABX_3 structure – is insufficient to describe the full range of 3D perovskite structures[9].

Unfortunately, it has been shown experimentally that Goldschmidt's tolerance factor inaccurately predicts 3D perovskite structure formation for many compositions[10]. As a result, a number of improvements have been reported recently to address challenges that are particular to metal halide perovskites. Examples include adapting the

commonly used Shannon ionic radii[11] for compatibility with metal halide perovskites by taking account of the substantial covalency of the M-X bond for heavier halides and introducing metrics to account for the globularity of organic A-site cations, rather than approximating them as hard spheres[12]. Realisation that, given the relative sizes of the contracted B^{2+} cation and charge-diffuse heavy halide anions, it is necessary to ensure separation of adjacent halides further led to the introduction of an octahedral factor[13,14], μ:

$$\mu = \frac{r_A}{r_X} \tag{2.2}$$

which must have $\mu \geq 0.41$, although octahedral tilting raises this lower bound. Combination of the Goldschmidt and octahedral factors with adapted Shannon radii and consideration of the oxidation state of the A-site cation, n_A, recently led Bartel, et al., to propose a new tolerance factor[10]:

$$\tau = \frac{1}{\mu} - n_A \left(n_A - \frac{r_A/r_B}{\ln(r_A/r_B)} \right) \tag{2.3}$$

where perovskite formation is predicted with 91% experimental accuracy if $\tau < 4.18$ across a wide range of oxide and halide perovskites.

In the search for new 3D perovskite compositions, the work of Goldschmidt and successors has been invaluable. However, of increasing attention has been a class of low-dimensional perovskites, which do not conform to the conventional ABX_3 formula. These materials are considered to be related to perovskites as they retain – to varying degrees – the extended corner-sharing BX_6 octahedral network. Layered 2D structures (Dion-Jacobson or Ruddlesden-Popper phases, most commonly), for example, comprise sheets of BX_6 octahedra that are continuous in two dimensions but of limited and well-defined thickness and interspaced by larger cations, which are

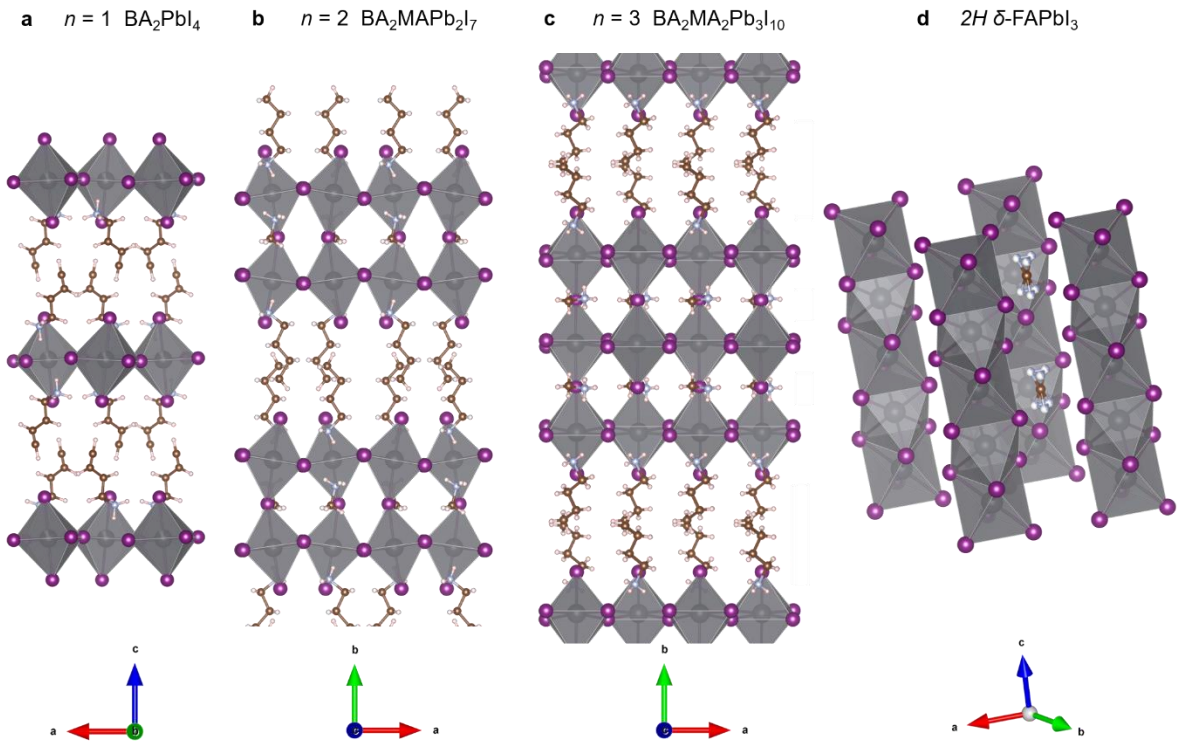


Figure 2.2 | Low dimensionality perovskite-derived structures. a-c, Structures of the three lowest dimensionality (n = 1,2,3) phases of the $BA_2MA_{n-1}Pb_nI_{3n+1}$ family of Ruddlesden-Popper 2D perovskites. **d**, Structure of *2H* δ-$FAPbI_3$, which consists of 1D chains of edge- and face-sharing BX_6 octahedra.

typically organic[15]. Such materials possess a range of exciting optoelectronic properties owing primarily to extremely poor charge carrier mobility across the organic spacer groups, which gives rise to a regular quantum-well structure in one dimension[16]. The width of each well is determined by the thickness of the organic-inorganic layers, which in turn are defined by the number of sheets of BX_6 octahedra, n, between adjacent organic spacers. n-dimensionality (n = 1,2,3,…) 2D perovskites (**Figure 2.2a-c**) are thus highly compositionally tailorable, depending on the organic-inorganic layer thickness as well as organic spacer length and rigidity[17]. Thus, so too are the excitonic properties arising from manipulation of the quantum confinement effects by simple compositional modification.

Of particular interest recently has been mixed-phase 2D-3D perovskite heterostructures[18–20]. This term has been used to describe a staggering array of

different semiconductor materials. However, in general it refers to a blending 3D and 2D perovskite structures, often but not necessarily in a crystallographically continuous fashion such as to form a single crystalline domain. Such materials have been shown to possess highly desirable optoelectronic properties, as well as imparting advantages to material stability with respect to the isolated 3D parent phase.

Beyond 2D layered perovskite structures, a wide array of 1D[21,22] and so-called 0D[23] perovskite-derived structures have been reported. One such is the commonly observed photoinactive *2H* hexagonal polytype of $FAPbI_3$, often referred to as the *δ*-phase[22] (**Figure 2.2d**), which is the thermodynamically preferred form of $FAPbI_3$ under ambient conditions.

2.1.2 – Desirable properties

The unique physics of metal halide perovskites have been widely explored. Here only an overview will be presented, with particular focus given to those properties that are most relevant to this work.

Lead iodide perovskites typically possess a direct bandgap, due to both their valence and conduction bands having significant contribution located on the Pb^{2+} cation. Overlap of Pb 6p and I 5s atomic orbitals leads *σ*-antibonding orbitals that contribute the highest density of states to the conduction band, while the valence band comprises *σ*-antibonding orbitals themselves arising from overlap between Pb 6s and I 5p orbitals[7,24]. With a direct bandgap comes favourable optical properties; remarkably high absorption coefficients, with steep absorption onset, and strong luminescence[25,26]. Moreover, strong orbital overlap across the octahedral framework between the Pb 6s and 6p, and I 5s and 5p orbitals, results in very small electron (0.15 m_e) and hole (0.12 m_e) effective masses, a fraction of the free electron mass[27,28]. Light

carrier masses allow for high-mobility band transport in halide perovskite materials, provided non-radiative recombination events are minimised. Such unfavourable recombination is typically associated with physical defects in the perovskite materials[26]. Perhaps one of the most remarkable properties of halide perovskites is the excellent “defect tolerance”. That is, that the optoelectronic performance of the material is relatively unaffected by even the presence of substantial defect densities (in comparison with other semiconductor materials). This is a key factor contributing to the facile solution processability of lead halide perovskites, which is critical to this thesis and will thus be explored in more detail in the next section. In part this tolerance to defects may also be attributed to the σ-antibonding character of the valence band maximum (VBM). Dangling bonds at defect sites possess energy close to their corresponding atomic orbitals, and thus possess energies between those of the bonding-antibonding orbital pair that made up the bond broken by the presence of a defect. As in metal halide perovskites bonding-antibonding orbital pairs tend to form within the valence band, rather than across the bandgap as is more typical for semiconductor materials (for example, the graphene $\pi - \pi^*$ bandgap), defects tend to have energies that are either within the valence band, or close to the band edge[29]. Thus, while the formation energy of some vacancy or interstitial defects is low, the density of deep trap states (those in the bandgap not close to the VBM or conduction band minimum, CBM) – from which release of entrapped charge carriers is energetically unlikely – is very low in the perovskite bulk[26,30]. Rapid exciton dissociation, due to the high dielectric constant of halide perovskites, also ensures a low rate of capture by charged defects and thus reduced trap-assisted recombination[26].

2.1.3 – Solution processing

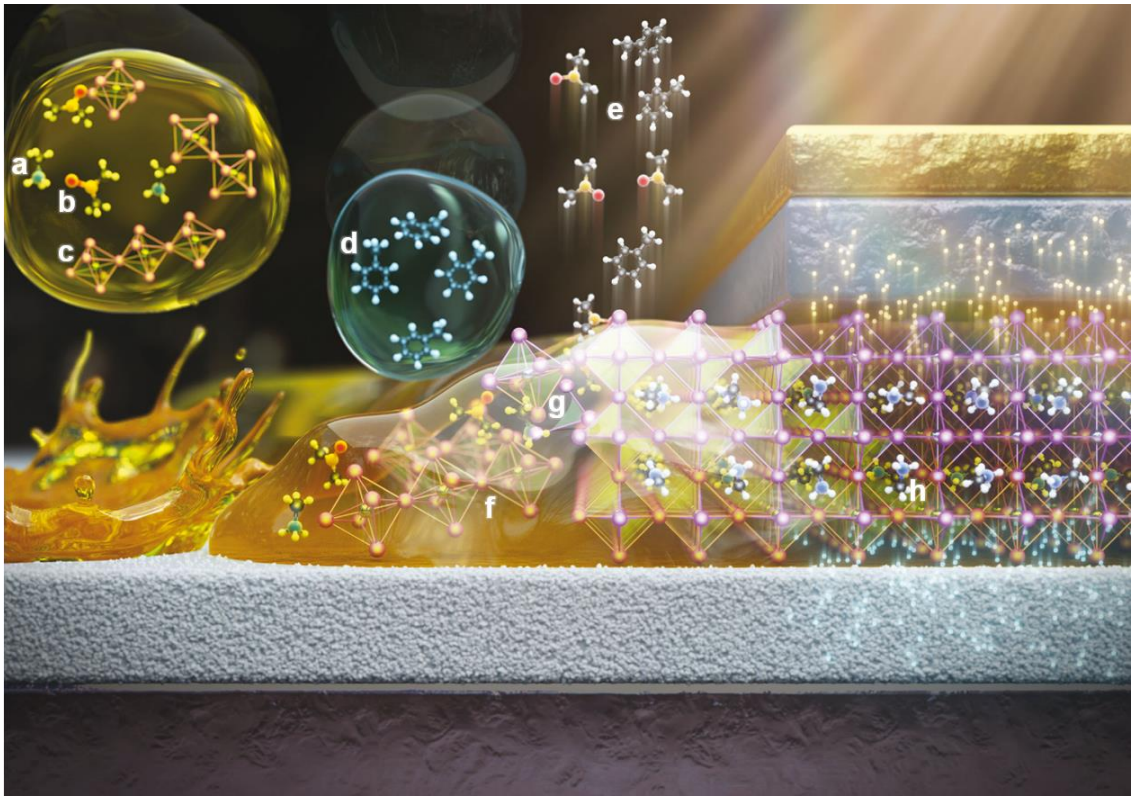


Figure 2.3 | Metal halide perovskite solution processing. a, Solvent-coordinated organic cations. **b**, Low-volatility, coordinating (polar) solvents. **c**, Haloplumbate complexes in solution. **d**, Non-coordinating (apolar) anti-solvent. **e**, Imiscibility-driven extraction of coordinating solvents. **f**, Crystallisation of perovskite *via* intermediate pathway under kinetic growth regime. **g**, Defect formation. **h**, (Vertical) phase segregation in growing perovskite material. Reproduced and adapted from M. Jung (2019), with permission[31].

Among the most attractive features of metal halide perovskites is their compatibility with solution processing methods. **Figure 2.3** summarises schematically the processes and components in action at the point of perovskite crystallisation during solution processing[31]. At research-scale typically spin coating techniques have dominated solution-processed perovskites. However, formulation of stable inks whose properties and composition can be readily manipulated opens the attractive possibility of scalable deposition techniques such as slot-die and spray coating, which are also compatible with roll-to-roll fabrication[32]. To take full advantage of such rapid and inexpensive deposition processes, it is necessary to develop an in-depth understanding of not only the chemical reactions and interactions between species dissolved in precursor solutions, but how these impact the crystallisation of the

perovskite material and direct its properties[31]. These issues are central to this thesis, which will principally explore them as applied to one particular perovskite composition; formamidinium lead triiodide ($FAPbI_3$). Thus, much of the subsequent theoretical background presented will focus on this particular material.

Like the archetypal halide perovskite, methylammonium lead triiodide ($MAPbI_3$)[33], the earliest reports (2014) of $FAPbI_3$ in a thin film perovskite solar cell (PSC)[34] employed a "one-step" deposition process using an ink solvated by *N*,*N*-dimethylformamide (DMF). In this process the ink is coated onto a spinning substrate and immediately heated, typically at between 100 °C and 150 °C, for between 10 and 45 minutes. As will be discussed further in **Chapters 5 and 6**, the photoactive cubic α-$FAPbI_3$ phase is thermodynamically unstable under ambient conditions with respect to the photoinactive hexagonal δ-phase, on account of the FA^+ cation's ionic radius being too large[35]. For this reason, crystallising compositionally- and phase-pure α-$FAPbI_3$ in a room temperature process has proven challenging to for the field. Thus, the majority of succeeding works have employed the general approach of alloying the A-site (and X-site) ions[36]. Today, both the highest efficiency[37–40] and the most stable[41,42] lead halide perovskites (typically $FA_{1-x}MA_xPb(I_{1-x}Br_x)_3$ with $0.01 \leq x \leq 0.1$ and $FA_{1-y}Cs_yPb(I_{1-y}Br_y)_3$ with $0.1 \leq y \leq 0.2$, respectively) employed in single-junction PSCs feature FA^+-rich materials fabricated *via* a one-step solution process.

However, approaches to perovskite fabrication beyond the one-step method have certainly been attempted. The so-called "two-step" or sequential deposition, first reported by Burschka, et al., in 2013 for $MAPbI_3$, introduces the precursor reagents (principally PbX_2 and AX salts) sequentially as two separate inks, based on orthogonal solvents[43]. Typically, PbX_2 is first introduced using polar solvents such as DMF or dimethyl sulfoxide (DMSO), before spin coating a solution of AX in an alcohol. As found

in the development of one-step depositions, reports of $FAPbI_3$ and FA^+-rich alloys fabricated *via* sequential depositions soon followed and now dominate recent reports utilising the sequential deposition[44,45].

Although both the one- and two-step deposition methods present fabrication advantages and disadvantages, one benefit of sequentially depositing is the ease with which the intermediate layer may be manipulated to direct subsequent growth. In particular, the deliberate retention of highly coordinating, non-volatile solvents (e.g. DMSO, DMF, γ-butyrolactone [GBL]) has become widespread. By this method, the intermediate is a layer formed of haloplumbate-solvent (Sol) complexes, which – unlike pure lead halide structures – already contain BX_6 and $BX_{6-n}[Sol]_n$ octahedra, which are more readily and effectively converted to the desired final 3D perovskite material[46–48]. The work presented herein (**Chapter 4**) builds upon these techniques to manipulate 3D perovskite growth *via* careful selection of an intermediate phase.

Similar lines of thinking by researchers favouring a one-step deposition process led to the – now nearly ubiquitous – method of antisolvent engineering[49]. Use of the same highly coordinating solvents (DMF, DMSO, GBL) in one-step precursor inks leads to formation of $(AX)_a(Sol)_b(PbX_2)_c$ intermediate solvent phases in the as-cast material[47,48]. Although it is possible to completely remove the retained solvent and to crystallise a 3D perovskite phase with thermal curing alone, often this leads to defective and poorly crystalline materials. As a result, it has become common place to apply an antisolvent (a liquid that is immiscible with the precursor solvent and in which perovskites are insoluble, such as toluene, chlorobenzene, anisole and diethyl ether) to the thin layer, usually dynamically during the spin coating process, aiming to rapidly remove the majority of the retained coordinating solvents and thus drive crystallisation of the final material[49,50].

2.2 – Perovskite solar cells

2.2.1 – Semiconductors and Band Theory

Among the categories by which materials may be classified, of particular interest in electronic applications is if, or under what conditions, materials conduct electrical charge. Most simply, we categorise materials as either insulators, conductors[1] or semiconductors. These may be distinguished by electronic band theory.

Band theory arises from a quantum mechanical consideration of the range of allowed energy levels that electrons may occupy in a given material. The combined effects of the bonding modes holding the atoms of the material together and the periodicity (or lack thereof) of the material act to constrain this range of allowed states, and to open up energy gaps between them. Where the allowed energetic states in a bulk material are so close in energy as to be considered continuous (in energy space), all such states are described together as a single electronic band. The energy spacings that arise between bands are irregular in both momentum and energy space. Drawing on a tight-binding model analysis, these spacings may be considering as arising from contributions of the various σ-, π- and δ-bonding and antibonding molecular orbitals holding the different atoms in the material's structure together. By way of example, **Figure 2.4** shows the contribution to electronic band structure of $CsPbI_3$ by each relevant Pb and I orbital[51], highlighting that it is principally the σ^* antibonding orbital, itself comprised of Pb 6s and I 5p atomic orbitals, that forms the valence band maximum, and the σ^* antibonding orbital comprised of Pb 6p and I 5s atomic orbitals that contributes to the conduction band minimum.

[1] Conductors can be further subdivided into metals and semimetals, where the difference is qualitatively the degree to which the valence and conduction bands overlap. They are not relevant for this thesis and will therefore not be discussed further.

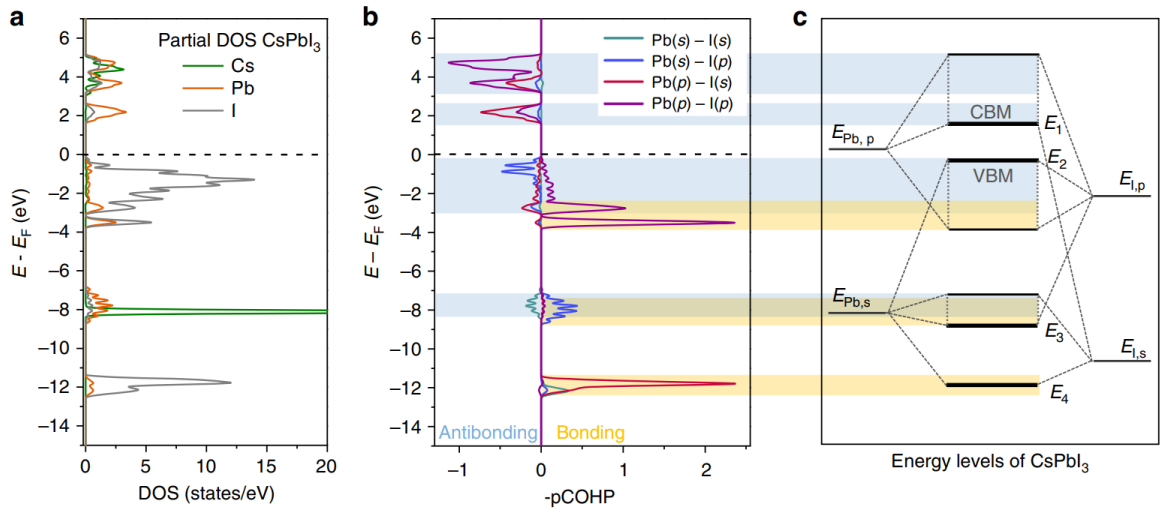


Figure 2.4 | Electronic band structure of cesium lead triiodide. Orbital contributions to the energy bands of $CsPbI_3$. (**a**) $CsPbI_3$ DOS projected on the Cs, Pb, and I atoms (partial DOS). (**b**) Orbital-resolved Crystal Orbital Hamiltonian Population (COHP); positive (negative) sign indicates bonding (anti-bonding) character. The line colours indicate which atomic orbitals are involved in the bonds (anti-bonds). (**c**) Schematic energy level diagram extracted from the COHP analysis; the energy levels E1 to E4 that are relevant for the tight-binding analysis are marked. Bonding interactions are shaded in yellow, and anti-bonding interactions in blue . Reproduced from S. Tao (2019), with permission[51].

To determine if a material is an insulator, conductor or semiconductor, consideration of all its electronic bands is not necessary. What is essential is their electronic occupation. The electronic occupancy of energetic states in a material is governed by the Pauli exclusion principle, which dictates that no two electrons may exist in the same quantum state (i.e. cannot have the same values for the four quantum numbers describing electrons). Given this condition, a maximum of two electrons (with opposing spin quantum numbers, $+\frac{1}{2}$ and $-\frac{1}{2}$) can occupy each allowed energy state, and so electrons in a material must be distributed in energy space across the allowed electronic bands.

The electronic occupancy of energetic states can be described by the Fermi function, such that probable occupancy is proportional to:

$$F(E,T) = \frac{1}{e^{\frac{E-E_F}{k_B T}} + 1} \tag{2.4}$$

where k_B is the Boltzmann constant, T is the temperature in Kelvin, E is the energy of a given state and E_F is the Fermi level (or energy). E_F defines the energy above which allowed states in a material have a <50% probability of being occupied by an electron at thermodynamic equilibrium. As the distribution in **Equation 2.4** describes, at non-zero temperatures, allowed energy states with $E > E_F$ have a non-zero probability of being occupied. Similarly, energy states with $E < E_F$ now have a non-zero probability of being unoccupied. Of course, for occupancy to be possible at all, there must be an allowed energy state corresponding with that energy, E. The electronic band with highest energy below the Fermi level is known as the valence band, while the band with lowest energy above the Fermi level is described as the conduction band.

In a conductor, the Fermi level is at energy such that it is within a continuum of allowed electronic states. As such, the valence band maximum (VBM) occurs in a continuum of allowed energy states and thus the next lowest allowed state (which is unoccupied at absolute zero, and is thus the conduction band minimum, CBM) is only of infinitesimally higher energy. Thus, at all real temperatures, a significant number of electrons exist in the conduction band and the material conducts electricity (**Figure 2.5a**). By contrast, an insulator is a material in which the Fermi level occurs in a wide

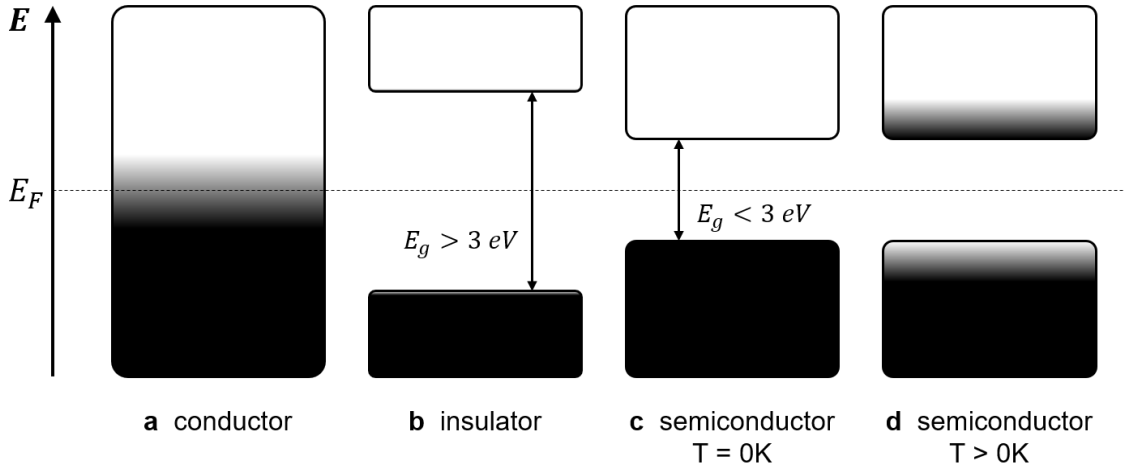


Figure 2.5 | Band structure of conductors, semiconductors and insulators. Band structure and density of occupied states (shading) for a conductor (**a**), an insulator (**b**), an intrinsic semiconductor at absolute zero (**c**) and an intrinsic semiconductor under thermal conditions (**d**).

(>3 eV) energy gap between bands, such that there are no allowed energy states close in energy to the Fermi level. Thus, even under thermal conditions, only an extremely small number of states in the conduction band are occupied (in line with **Equation 2.4**) and so electrons are immobilised in the valence band (**Figure 2.5b**). Like insulators, semiconductors possess a Fermi level that occurs in an energy gap between bands. Thus, like insulators, at absolute zero there is no population of electrons in the conduction band and thus the material does not conduct (**Figure 2.5c**). Unlike insulators, however, in a semiconductor the energy difference between the Fermi level and the VBM or CBM (or both) is small enough (≤3 eV) that under thermal conditions, or some other external energetic stimuli, there is a substantial population of electrons in the conduction band, and holes in the valence band, and so – under such conditions – the material conducts electrical charge (**Figure 2.5d**). The energy difference between the VBM and the CBM is described as the bandgap (E_g) of the material.

2.2.2 – The photovoltaic effect: absorption, extraction and recombination

Excitation of an electron from valence band to conduction band can be stimulated by a range of stimuli. However, for this thesis, transfer of energy by absorption of a photon of light with sufficient energy ($E \geq E_g$, to overcome the minimum energy gap between the two bands) is the most important (step 1, **Figure 2.6**). Photon energy, E, is described in quantum mechanics by the Planck-Einstein relation:

$$E = \frac{hc}{\lambda} = hv \tag{2.5}$$

where h is Planck's constant, c is the speed of light, which is equal to λv. Where the VBM and CBM are aligned in momentum space, the bandgap is described as direct (**Figure 2.7a**). As such, electrons transferring between VBM and CBM may do so without requiring a change in momentum. If, however, the VBM and CBM are offset

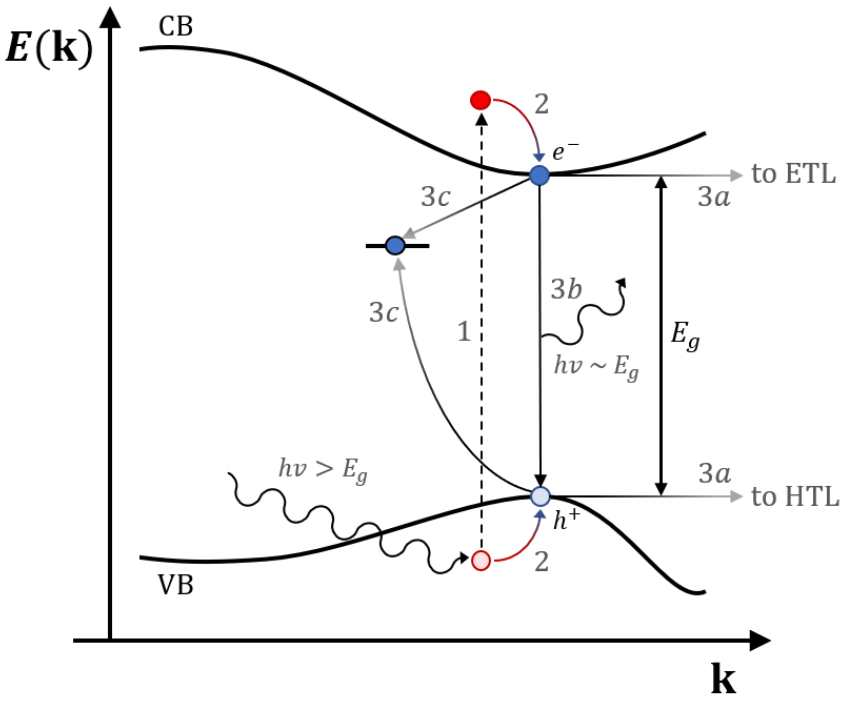


Figure 2.6 | The photovoltaic effect. Schematic showing the absorption of photons by a direct bandgap semiconductor (1), thermalisation of hot carriers (2), and either extraction of charges (3a) or recombination by radiative (3b) or trap-assisted non-radiative (3c) pathways.

by some momentum vector then not only must an appropriate amount of energy ($E \geq E_g$) be transferred, but a corresponding change in momentum must be supplied, typically as a phonon. Such a bandgap is described as indirect (**Figure 2.7b**). As a result, fewer photons of sufficient energy are absorbed by the same thickness of photoactive material. Thus, the absorption onset is much less sharp (as compared direct E_g materials) and much thicker layers of photoabsorbing material are necessary; ~200 µm for crystalline Si, compared to ~500 nm for halide perovskites, which possess a direct bandgap.

Absorption of photons with $E > E_g$ allow electrons from energy states in the valence band lower than the VBM to be promoted into the conduction band, and may enter states of higher energy than the CBM in the conduction band. In this case, however, rapid thermalisation by a range of pathways on the order of femtoseconds reduces the energy of the excited electrons to energies close to the CBM (step 2, **Figure 2.6**).

Promotion of an electron, e^-, to the conduction band leaves a hole, h^+, in the valence band. Coulombic attraction between these two charged particles binds them together in space, with the strength of this interaction (binding energy) depending strongly on the material in which they are generated. Such an $e^- - h^+$ pair is referred to as an exciton. In order to extract the photogenerated charges into an external circuit it is necessary to separate this pair. The magnitude of the exciton binding energy depends strongly on the dielectric constant of the material in which it is generated. As noted in **Section 2.1.2**, the dielectric constant of halide perovskites is typically very large, and so exciton dissociation occurs essentially spontaneously under thermal conditions, facilitating facile charge extraction (step 3a, **Figure 2.6**).

Rapid physical separation of e^- and h^+ due to low exciton binding energies has the additional benefit of reducing the likelihood of recombination. Recombination occurs when an e^- in the conduction band physically overlaps with a h^+ leading to its return

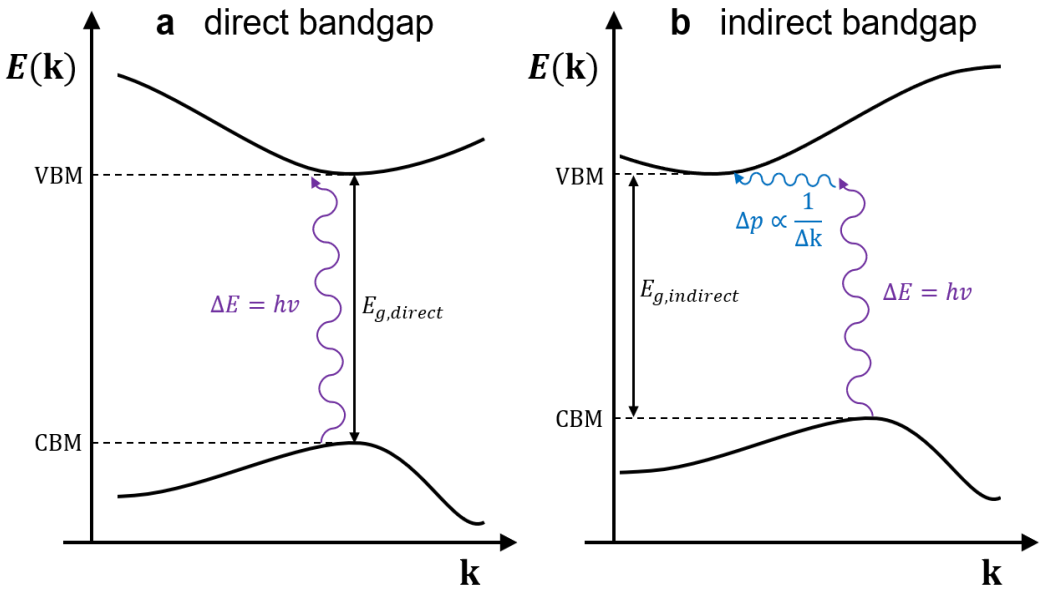


Figure 2.7 | Direct and indirect bandgap semiconductors. Excitation and separation of charges in direct (**a**) and indirect (**b**) bandgap semiconductors. Where the conduction band maximum (CBM) and valence band minimum (VBM) are not aligned in momentum space, an additional transfer of momentum is required simultaneous to photoexcitation for successful electron and hole formation. This transfer is typically provided by means of a lattice phonon.

to the valence band. Energy is released during this process, typically as either a photon (radiative recombination; step 3b, **Figure 2.6**) or by interaction with a phonon (vibrational energy; non-radiative recombination; step 3c, **Figure 2.6**). Overall, charge-carrier dynamics in perovskite semiconductors can be generally described using:

$$\frac{dn}{dt} = -k_1 n - k_2 n^2 - k_3 n^3 \quad (2.6)$$

where *n* is the photogenerated charge-carrier density, k_1 is the monomolecular recombination rate constant, associated with trap-mediated, typically non-radiative recombinations, k_2 is the bimolecular $e^- - h^+$ radiative recombination rate constant, and k_3 is the Auger recombination rate constant.

Charge-carrier densities in PSCs under operation are low enough that the rate of Auger recombination may be taken as negligible. Most trap-mediated recombination occurs when a charged defect (ion vacancy, interstitial ion, etc.) in the perovskite material leads to the local trapping of either an e^- or a h^+ [52,53]. Such defects cause local changes in the electronic band structure, in effect providing energetic states for charge carriers to occupy within the forbidden inter-band region. If such defect states are close in energy to the conduction (e^--trapping) or valence band (h^+-trapping) they are considered to be “shallow”, with the activation energy required to de-trap the entrapped carrier likely to be provided under thermal conditions. “Deep” traps, however, lead to long-lasting entrapment of carriers. Once a certain charge carrier is entrapped, the likelihood of a recombination occurring (by capture of a carrier of opposing charge) depends only linearly on the density of charge carriers, hence such recombination is monomolecular (**Equation 2.6**). Due to the trapping energy, the energy gap between the trapped and untrapped charge carriers is less than the bandgap of the semiconductor. Thus, while monomolecular recombination is typically

non-radiative, even when it is radiative the photons released have $E < E_g$ and so photon-recycling (absorption of re-emitted photons elsewhere in the photoactive layer) is not possible. As a result, minimising the density of deep-energy trap states by reducing the density of defects that give rise to them is an essential requirement for the synthesis of any semiconductor material. Charge-carrier recombination is discussed in more detail in **Chapter 3** in the context of time-correlated single photon counting and optical-pump terahertz-probe spectroscopy, and associated calculations.

2.2.3 – Quantum efficiency, AM1.5 and the detailed balance limit

Quantum efficiency in optoelectronics relates to the ratio of incident photons to photogenerated charge carriers. Two distinct forms of quantum efficiency are regularly used to quantify the performance of a photoabsorbing material (1) or a PV device (2):

1. Internal quantum efficiency (IQE) is the ratio of the number of incident photons absorbed by the photoactive layer in a PV device material to the number of charge carriers collected from that device.
2. External quantum efficiency (EQE) is the ratio of the number of photons incident on a PV device to the number of charge carriers collected from that device.

Both quantities are spectrally resolved, and IQE is necessarily always greater than EQE as in the latter measurement not all incident photons are absorbed by the photoactive layer due to reflection, incomplete absorption by the photoactive material or absorption of photons elsewhere in the device:

$$IQE(\lambda) = \frac{EQE(\lambda)}{1 - R(\lambda) - A(\lambda) - T(\lambda)} \tag{2.7}$$

where $R(\lambda)$ is the spectral reflectance of the device, $A(\lambda)$ is the spectral absorptance of non-photoactive layers in the device and $T(\lambda)$ is the spectral transmittance of the

device. $A(\lambda)$ may only be found by calculation and with knowledge of the spectrally-resolved absorption coefficients and thickness of all other photoinactive layers in the device. Typically, in PSCs $A(\lambda)$ is assumed to be negligible. Reflectance and transmittance can be measured readily.

While high quantum efficiency is essential for high PSC performance, the absolute number of charge carriers extracted as electrical current, and the energy each carries (voltage), are also critical for power output. The energy of the extracted carriers depends on the E_g of the photoabsorber, and on any losses that occur during extraction of charge from the PV device[53–56], as discussed further in **Section 2.2.4**. Extracted current depends on EQE, E_g of the photoabsorber and the spectrum of incident light.

Absorption and scattering of incident solar radiation by the Earth's atmosphere reduce irradiance at the surface, particularly in the near infrared (IR). The resulting spectrum, standardised to a total irradiance of 100 mW cm^{-2}, and at a realistic average zenith angle that simulates incident light passing through an effective atmospheric thickness 50% greater than Earth's atmosphere is known as the air mass 1.5 global (AM1.5G) spectrum, and is shown in **Figure 1.3**. This spectrum is used uniformly around the world to as a consistent illumination condition under which to test and report PV cell performance.

Given a known illumination spectrum and EQE, in order to maximise PV power output a compromise exists for the selection of the ideal photoabsorber E_g. This is because while high-E_g materials lead to higher energy per charge carrier, they are unable to absorb all energies in the AM1.5 spectrum. On the other hand, rapid thermalisation of carriers to the band edges (**Section 2.2.2**) necessarily reduces the energy per

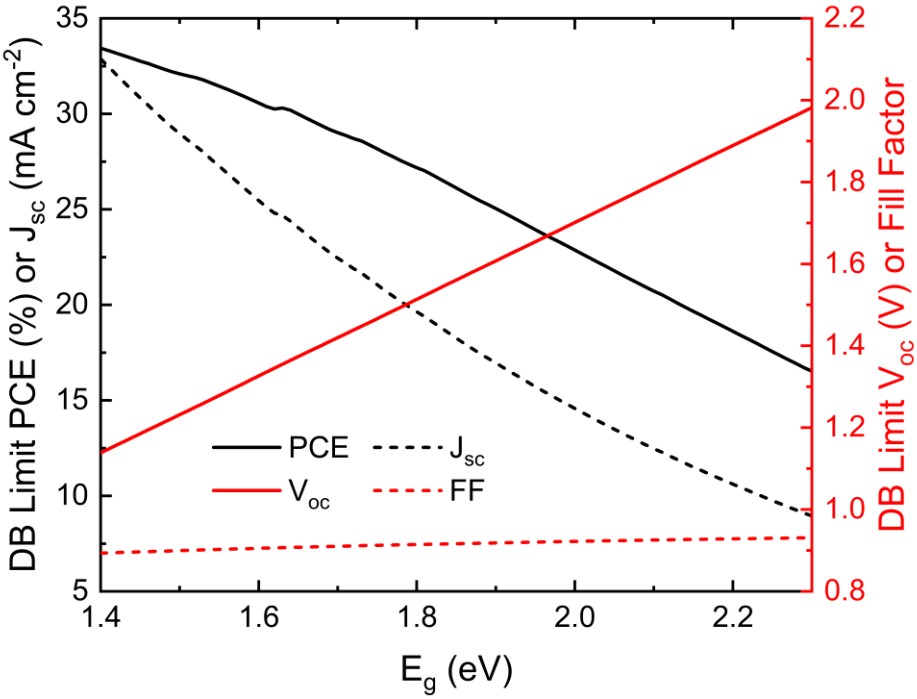


Figure 2.8 | Detailed balance limit. Dependence of maximum theoretical power conversion efficiency (PCE), short-circuit current density (J_{sc}), open-circuit voltage (J_{sc}) and fill factor (FF) on semiconductor bandgap (E_g) of a single-junction photovoltaic cell in the range of bandgaps relevant for lead halide perovskites.

extracted carrier to well below the E_g material, and so use of a low-E_g photoabsorber results in low power output despite absorption of many high energy photons.

The "detailed-balance limit" provides a theoretical framework from which to rationalise this compromise. The approach was first proposed in 1960[57] taking a thermodynamic balance between absorption and emission in the photoactive layer, and making several assumptions:

1. All photons of sufficient energies are absorbed and create an unbound e^- and h^+.
2. e^-'s and h^+'s thermalize to the band edges, and are in quasi-thermal equilibrium with the photoconductor temperature, resulting in quasi-Fermi level splitting.
3. Carrier mobility is infinite.

4. The only active recombination mechanisms are radiative.

Taking both the sun and the solar cell as blackbodies (at 6,000 K and 300 K, respectively) this model predicted a maximum 33.7% power conversion efficiency (η or PCE) could be achieved by a single-junction photovoltaic employing a photoabsorber of $E_g = 1.34$ eV. In 1984 Tiedje and Yablonovitch proposed an extended detailed-balance limit based on AM1.5 incident radiation and further accounting for both free carrier absorption[2] and Auger recombination, and modelling a realistic absorption coefficient function for c-Si[58]. Under this model the authors predict a maximum PCE of 29.8% for an absorber with $E_g = 1.12$ eV.

The lowest bandgap lead halide perovskite is α-$FAPbI_3$, with $E_g = 1.5$ eV, somewhat above the optimum for single junction PV. **Figure 2.8** shows how the maximum PCE and other PV cell metrics vary as a function of E_g under the original detailed-balance limit model.

2.2.4 – Solar cell operation

When under applied bias, in the absence of illumination, solar cells behave as diodes. Their current-voltage (J-V) behaviour in the dark can therefore be described using a modified ideal diode equation:

$$J_{dark}(V) = J_0\left(e^{\frac{qV}{nk_bT}} - 1\right) \tag{2.8}$$

where J_0 is the dark saturation current, q is the elemental charge, V is the applied voltage and n is the "ideality factor"[59]. n is related to the charge carrier recombination mechanism

[2] Free carrier absorption is when absorption of an incident photon leads to excitement of a charge carrier from a state inside one electronic band to another, unoccupied state in the same band.

Under operation (AM1.5 irradiation) the maximum possible current that can be extracted from the cell (which occurs under no applied bias at short circuit, J_{sc}) is given by:

$$J_{sc} = -q \int EQE(\lambda) \Phi^{AM1.5} d\lambda \tag{2.9}$$

where $\Phi^{AM1.5}$ is the spectrum flux under AM1.5 illumination. The net current generated in the photoactive layer of an ideal PV cell under illumination is therefore given by:

$$J(V) = J_{sc} - J_{dark}(V) = J_{sc} - J_0 \left(e^{\frac{qV}{nk_bT}} - 1 \right) \tag{2.10}$$

Figure 2.9 shows the J-V characteristics of a high-performance PV cell.

Equally important to the current output of a solar cell is its corresponding voltage output. The most commonly used metric is the open-circuit voltage (V_{oc}), which represents the maximum voltage available from a cell and occurs when there is no net current flow. V_{oc} is the forward bias across the solar cell due to photogenerated current in the solar cell junction (transport materials and photoactive layer). An expression for V_{oc} can be obtained by setting **Equation 2.10** to zero:

$$V_{oc} = \frac{nk_bT}{q} ln \left(\frac{J_{sc}}{J_0} + 1 \right) \tag{2.11}$$

The relationship between the E_g of a photoabsorber and the V_{oc} of a solar cell fabricated from that photoabsorber is complex. Recently, strides have been made to quantify V_{oc} losses by means of the quasi-Fermi level splitting[3] (QFLS) in devices of various architectures[53]. Comparison between the voltage predicted under the radiative

[3] QFLS is the energy difference between the absolute energy of photoexcited electrons in the conduction band (which is less than the CBM) and the energy of photoexcited holes in the valence band (which is less than the VBM).

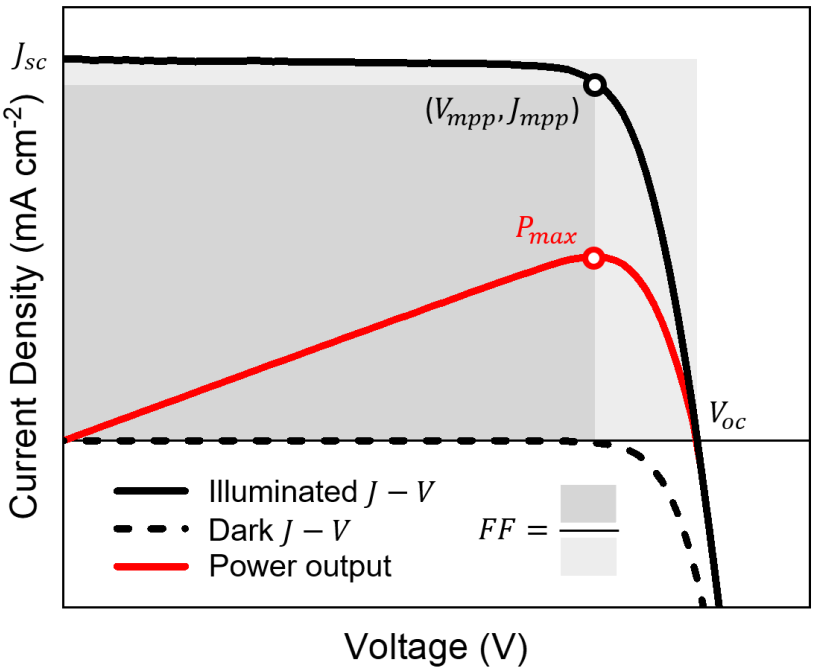


Figure 2.9 | $J-V$ characteristics of a solar cell.

limit, the QFLS and the experimental V_{oc} of PSCs have demonstrated that non-radiative recombination in the bulk perovskite and especially at interfaces within or between layers in the solar cell is principally responsible for voltage losses in PSCs. Factors such as energetic misalignment between semiconductor materials[54,55] in PSCs and ion segregation (in particular halide segregation)[56] have also been found to limit V_{oc}.

In a real cell, losses in current beyond the detailed-balance limit must be expected. In a poorly constructed cell such limitations could be due to inappropriate selection of charge carrier extraction materials (energetic misalignment) leading to a carrier blocking effect. Even in high-performance cells, however, losses are possible for instance due to the build up of mobile ions at the interface with a charge extraction material[60]. Generally, most such losses manifest themselves electrically in either a decrease in J_{sc}, a decrease in shunt resistance (R_{sh}) or an increase in series resistance (R_s).

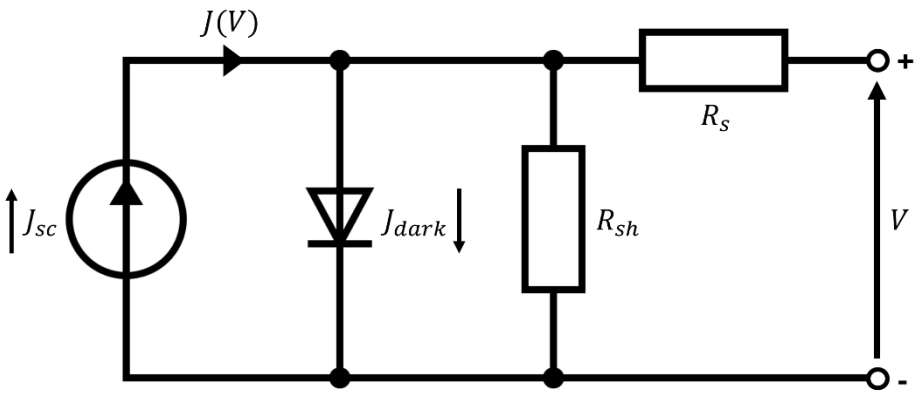


Figure 2.10 | Circuit diagram of solar cell with parasitic losses.

Low R_{sh} causes power losses in solar cells by providing an alternate current path for the photogenerated charge carriers, in parallel with that through the ideal cell (i.e. a cell where the diode is in parallel with an infinite resistance; $R_{sh} = \infty$). Such a diversion of charge reduces the amount of current flowing through the solar cell junction and thus also reduces the voltage from the solar cell. **Figure 2.10** shows the circuit diagram of a PV cell with significant "shunt pathways" (low R_{sh}). The effect on current loss of a shunt pathway depends on the potential difference across the cell, in line with Ohm's Law. We may modify **Equation 2.10** to account for current losses due to low R_{sh}:

$$J(V) = J_{sc} - J_{dark}(V) = J_{sc} - J_0\left(e^{\frac{qV}{nk_bT}} - 1\right) - \frac{V}{R_{sh}} \qquad (2.12)$$

Shunt pathways most often occur due to formation of pinholes[4], which are the filled by an overlying, higher conductivity material.

R_s is analogous to the internal resistance of an electrochemical cell. It should be minimised to reduce power losses by charge carriers doing work against R_s during extraction from the cell. R_s is increased by factors such as the use of thick layers of

[4] Pinholes are small (typically <100 nm) holes in thin layers of materials that occur by incomplete layer formation. Often, they are found at grain junctions where adjacently nucleated grains have failed to fuse entirely together. Pinholes may also develop in a material over time if that material is unstable with respect to material loss under degradation.

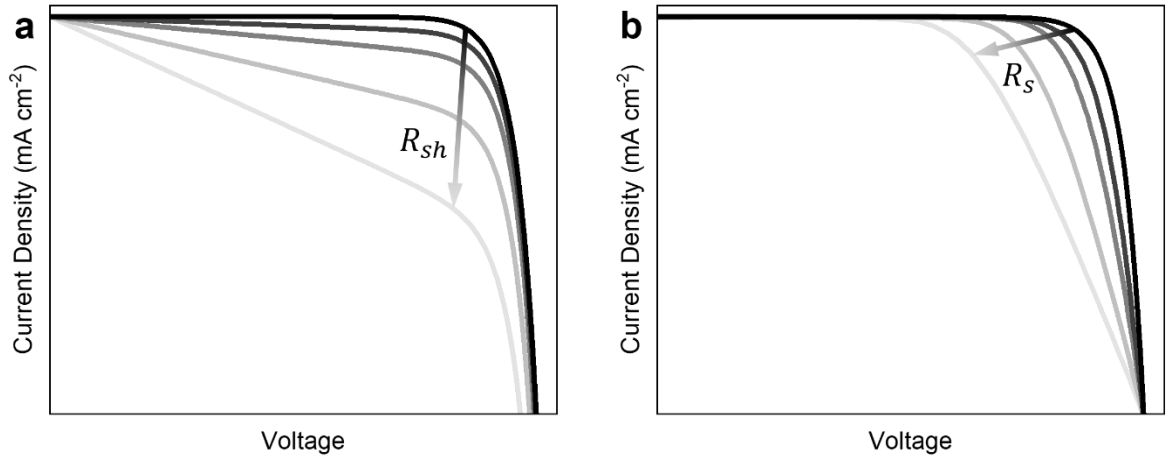


Figure 2.11 | Impact of parasitic losses on $J-V$ characteristics. Impact of increasing (**a**) shunt and (**b**) series resistance on $J-V$ characteristics of a solar cell.

low-conductivity materials or poor charge transport across an internal interface between layers in the cell. In effect a substantial R_s results in a reduction in the energy extracted per charge carrier, and thus in fact a reduction in the voltage of extracted carriers. This has a knock-on impact on current extraction itself. Current flow from a PV cell suffering from low R_{sh} and substantial R_s can be described by:

$$J(V) = J_{sc} - J_{dark}(V) = J_{sc} - J_0\left(e^{\frac{q(V+JR_s)}{nk_bT}} - 1\right) - \frac{(V+JR_s)}{R_{sh}} \qquad (2.13)$$

As parasitic losses due to both shunt and series resistance inadequacies mediate the relationship between the voltage and current extracted from a PV cell, both R_{sh} and R_s lead to a reduction in the fill factor of the PV cell. Fill factor is a parameter used to relate power extraction from a PV cell to J_{sc} and the open-circuit voltage (V_{oc}). J_{sc} and V_{oc} are the maximum current and voltage, respectively, that can be achieved from a PV cell. However, the power extracted from the cell under either of these conditions is zero. Power output is maximised at a specific current-voltage condition, denoted the maximum power point (MPP; J_{mpp}, V_{mpp}). Maximum power output (P_{output}) is then defined as:

$$P_{output} = J_{mpp} \cdot V_{mpp} \tag{2.14}$$

and the fill factor (FF) can be considered as parameterising the relationship between J_{mpp} and J_{sc}, and V_{mpp} and V_{oc}:

$$FF = \frac{J_{mpp}}{J_{sc}} \cdot \frac{V_{mpp}}{V_{oc}} \tag{2.15}$$

Graphically, **Equation 2.15** is a measure of the "squareness" of the $J-V$ curve (**Figure 2.9**). V_{mpp} is found by taking the first derivative of the power from the solar cell with respect to voltage:

$$V_{mpp} = V_{oc} - \frac{nk_bT}{q} ln\left(\frac{qV_{mpp}}{nk_bT} + 1\right) \tag{2.16}$$

with J_{mpp} then determined by substitution in **Equation 2.13**.

The modes by which R_s and R_{sh} reduce FF are different. An estimate for R_{sh} is found from the gradient of the $J-V$ curve around J_{sc}, where the term containing J_0 in **Equation 2.13** is negligible. **Figure 2.11a** thus shows the impact of increasing R_{sh} of FF. Contrastingly, R_s is estimated from the $J-V$ gradient around V_{oc} and impacts FF as shown in **Figure 2.11b**.

Typically, the most critically measure for a PV cell is the efficiency with which it converts incident electromagnetic power (P_{input}) to output electrical power:

$$\eta = \frac{J_{mpp} \cdot V_{mpp}}{P_{input}} \ (\mathbf{a}) \qquad \eta = \frac{FF \cdot J_{sc} \cdot V_{oc}}{P_{input}} \ (\mathbf{b}) \tag{2.17}$$

where η is the power conversion efficiency (PCE). There are a number of methods by which to measure the PCE of a PSC. The most common is to extract FF, J_{sc} and V_{oc} from a $J-V$ curve and use **Equation 2.17b**. Increasingly, however, it is appreciated that – especially for PSCs where $J-V$ hysteresis[61,62] and rapid ion migration under

illumination[60] can lead to misleading $J-V$ characteristics – use of a stabilised measurement protocol is necessary, whereby J_{mpp} and V_{mpp} are allowed to vary and stabilise over a short time period (~60 seconds). Once stabilised **Equation 2.17a** may be used to calculate a value for PCE, denoted herein as η_{mpp}.

2.2.5 – Perovskite solar cell architectures and performance

The highest performance single-junction PSC have now been certified with above 25% PCE[37–39]. The rapid increase in efficiency over the past decade of research owes itself to development in a wide range of areas. Neatly categorising these is challenging, but perhaps broadly they might be summarised as improvements in (1) perovskite bulk composition, (2) perovskite deposition techniques, (3) PSC architecture design and (4) passivation of the multitude of interfaces found in PSCs. All such enhancements in efficiency owe to minimising the performance losses discussed in **Section 2.2.4**.

However, PCE is not the only desirable quality in PSCs. As will be discussed in detail in **Chapters 5-6**, metal halide perovskites are themselves unstable with respect to compositional degradation[63,64]. Many of the other materials employed in PSCs as charge transport, charge blocking or electrode layers are also themselves unstable on relevant timescales. Further, physically contacting these materials together in PSCs, and passing current through them, can introduce yet more pathways for long-term power output degradation. As noted in **Chapter 1**, highly stable power output is critical for useful real-world PV applications.

Unfortunately, the majority of highly efficient PSCs reported to-date employ architectures that are especially unstable. In **Chapter 5** the various degradation routes common to the archetypal n-i-p (**Figure 2.12a**; electron transport layer, ETL-intrinsic photoactive semiconductor-hole transport layer, HTL) architecture are discussed in

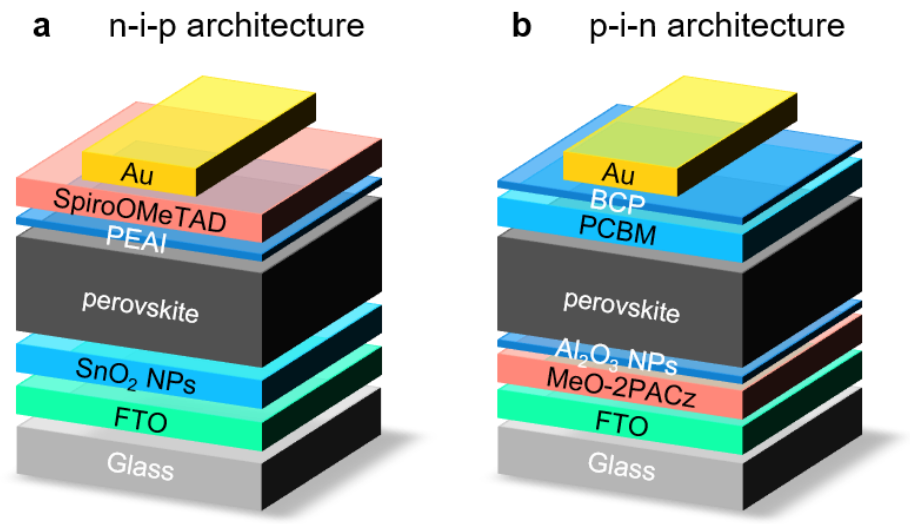


Figure 2.12 | PSC device architectures. Schematic diagrams of the n-i-p (**a**) and p-i-n (**b**) architectures used in solar cells reported in this thesis.

detail. For the most part these are based on either mesoporous TiO_2 [65] or planar SnO_2 [66] as ETLs. These materials require relatively high temperature processing, which may also be problematic for at-scale processing and for multi-junction PV devices. The ubiquitous HTL in n-i-p configuration remains Li-doped spiro-OMeTAD. This HTL is facile to deposit, forgiving of underlying morphology and can produce remarkably efficient PSCs. It is, however, typically the weakest link in such PSCs with respect to operational device stability[67–70].

As a result of the instabilities inherent to the n-i-p architecture, other PSC configurations have been explored, in particular the planar p-i-n (or "inverted") architecture (**Figure 2.12b**)[41,42]. Transport materials in p-i-n PSCs are typically organic semiconductors. Transparent HTLs such as PTAA[5] and poly-TPD[6] have been shown to be substantially more stable than doped spiro-OMeTAD[42]. However, their substantially lower conductivity necessitates much thinner layers of material, which renders their processing in a continuous layer on top of perovskites (as would be

[5] PTAA: poly(bis(4-phenyl)(2,4,6-trimethylphenyl)amine)
[6] polyTPD: poly[N,N′-bis(4-butylphenyl)-N,N′-bis(phen-yl)benzidine]

required in a n-i-p configuration) much more challenging. More recently a new class of carbazole-phosphonic acid self-assembled monolayers[71,72] (SAMs) have gained attention as high-performance HTLs, including one employed herein, MeO-2PACz[7]. However, the long-term stability of these materials when placed in contact with halide perovskites has not yet been clearly established. PCBM[8] and C_{60} are the most common ETLs employed in p-i-n cells, often in conjunction with a BCP[9] interlayer between the fullerene material and overlying metal cathode.

The PCE of p-i-n architecture PSCs has typically lagged behind that of those in n-i-p configuration, although in part this may be due to a smaller amount of research interest to-date. However, recently a highly impressive report from Jiang, et al., demonstrated p-i-n configuration PSCs with stabilised PCE of 25.4% and – perhaps more critically – when encapsulated retained >22% PCE for nearly 2,000 hours of continuous operation under 1-sun illumination at 55 °C[41].

2.3 – Conclusion and outlook on perovskite semiconductors

Metal halide perovskite semiconductors have emerged as a versatile and highly tuneable class of functional materials, having found application in devices as varied as X-ray detector arrays[73] and light-emitting diodes[74] (LEDs) over the past decade. As direct bandgap semiconductors, the extraordinarily high absorption coefficients of 3D halide perovskites have been put to great use in thin film photovoltaics. Today, the highest efficiency perovskite PVs achieve certified performance comparable to that of single crystal silicon PV (26.0% and 26.1%, respectively), while substantially

[7] [2-(3,6-dimethoxy-9H-carbazol-9-yl)ethyl]phosphonic acid
[8] PCBM: phenyl-C_{61}-butyric acid methyl ester
[9] BCP: bathocuproine

outperforming other thin film PV technologies including organic PV (19.2%), CdTe (22.3%) and CIGS (copper indium gallium selenide, 23.6%)[75].

However, as this thesis will explore further, crucial fundamental challenges remain for halide perovskite researchers if this material, and therefore any of its many applications, is to ever reach at-scale production in a useful product. Notably, material stability (in the bulk, or at its interfaces) and scalable processing techniques. Much of the future work in the field will doubtless focus on these key areas, although the true challenge – that of finding solutions to these limitations – will certainly also require substantial continued investigation of the fundamentals of perovskite properties and processing, in particular the link between controlled crystallisation at the point of fabrication and resulting material properties.

2.3 – Bibliography

1. Würfel, P. & Würfel, U. *Physics of Solar Cells*. (Wiley-VCH Verlag, 2016).
2. Nelson, J. *The Physics of Solar Cells*. (Imperial College Press, 2003).
3. Stixrude, L. & Lithgow-Bertelloni, C. Geophysics of chemical heterogeneity in the mantle. *Annu. Rev. Earth Planet. Sci.* **40**, 569–595 (2012).
4. Seok, S. Il & Guo, T. F. Halide perovskite materials and devices. *MRS Bull.* **45**, 427–430 (2020).
5. Goesten, M. G. & Hoffmann, R. Mirrors of Bonding in Metal Halide Perovskites. *J. Am. Chem. Soc.* **140**, 12996–13010 (2018).
6. Wuttig, M. *et al.* Halide Perovskites: Advanced Photovoltaic Materials Empowered by a Unique Bonding Mechanism. *Adv. Funct. Mater.* **32**, (2022).
7. Fabini, D. H., Seshadri, R. & Kanatzidis, M. G. The underappreciated lone pair in halide perovskites underpins their unusual properties. *MRS Bull.* **45**, 467–477 (2020).
8. Goldschmidt, V. M. Die Gesetze der Krystallochemie. *Naturwissenschaften* **14**, 477–485 (1926).
9. Glazer, A. M. The classification of tilted octahedra in perovskites. *Acta Crystallogr. Sect. B Struct. Crystallogr. Cryst. Chem.* **28**, 3384–3392 (1972).
10. Bartel, C. J. *et al.* New tolerance factor to predict the stability of perovskite oxides and halides. *Sci. Adv.* **5**, 1–10 (2019).
11. R. D. S. Revised Effective Ionic Radii and Systematic Studies of Interatomie Distances in Halides and Chaleogenides. *Acta Cryst.* **32**, 751–767 (1976).
12. Travis, W., Glover, E. N. K., Bronstein, H., Scanlon, D. O. & Palgrave, R. G. On the application of the tolerance factor to inorganic and hybrid halide perovskites: A revised system. *Chem. Sci.* (2016).

13. Li, C., Soh, K. C. K. & Wu, P. Formability of ABO3 perovskites. *J. Alloys Compd.* **372**, 40–48 (2004).

14. Li, C. *et al.* Formability of ABX_3 (X = F, Cl, Br, I) halide perovskites. *Acta Crystallogr. Sect. B Struct. Sci.* **64**, 702–707 (2008).

15. Grancini, G. & Nazeeruddin, M. K. Dimensional tailoring of hybrid perovskites for photovoltaics. *Nat. Rev. Mater.* **4**, 4–22 (2019).

16. Zhang, F. *et al.* Advances in two-dimensional organic-inorganic hybrid perovskites. *Energy and Environmental Science* **13**, 1154–1186 (2020).

17. Li, X., Hoffman, J. M. & Kanatzidis, M. G. The 2D halide perovskite rulebook: How the spacer influences everything from the structure to optoelectronic device efficiency. *Chem. Rev.* **121**, 2230–2291 (2021).

18. Jeong, S. *et al.* Cyclohexylammonium-Based 2D/3D Perovskite Heterojunction with Funnel-Like Energy Band Alignment for Efficient Solar Cells (23.91%). *Adv. Energy Mater.* **11**, 1–12 (2021).

19. Jang, Y. W. *et al.* Intact 2D/3D halide junction perovskite solar cells via solid-phase in-plane growth. *Nat. Energy* **6**, 63–71 (2021).

20. Niu, T. *et al.* High performance ambient-air-stable $FAPbI_3$ perovskite solar cells with molecule-passivated Ruddlesden-Popper/3D heterostructured film. *Energy Environ. Sci.* **11**, 3358–3366 (2018).

21. Yuan, Z. *et al.* One-dimensional organic lead halide perovskites with efficient bluish white-light emission. *Nat. Commun.* **8**, (2017).

22. Gratia, P. *et al.* The Many Faces of Mixed Ion Perovskites: Unraveling and Understanding the Crystallization Process. *ACS Energy Lett.* **2**, 2686–2693 (2017).

23. Sun, S. *et al.* 0D Perovskites: Unique Properties, Synthesis, and Their Applications. *Adv. Sci.* **8**, 1–23 (2021).

24. Frost, J. M. *et al.* Atomistic origins of high-performance in hybrid halide perovskite solar cells. *Nano Lett.* **14**, 2584–2590 (2014).

25. De Wolf, S. *et al.* Organometallic halide perovskites: Sharp optical absorption edge and its relation to photovoltaic performance. *J. Phys. Chem. Lett.* **5**, 1035–1039 (2014).

26. Ball, J. M. & Petrozza, A. Defects in perovskite-halides and their effects in solar cells. *Nat. Energy* **1**, (2016).

27. Walsh, A. Principles of chemical bonding and band gap engineering in hybrid organic-inorganic halide perovskites. *J. Phys. Chem. C* **119**, 5755–5760 (2015).

28. Brivio, F., Butler, K. T., Walsh, A. & Van Schilfgaarde, M. Relativistic quasiparticle self-consistent electronic structure of hybrid halide perovskite photovoltaic absorbers. *Phys. Rev. B - Condens. Matter Mater. Phys.* **89**, 1–6 (2014).

29. Huang, Y. T., Kavanagh, S. R., Scanlon, D. O., Walsh, A. & Hoye, R. L. Z. Perovskite-inspired materials for photovoltaics and beyond-from design to devices. *Nanotechnology* **32**, (2021).

30. Brandt, R. E., Stevanović, V., Ginley, D. S. & Buonassisi, T. Identifying defect-tolerant semiconductors with high minority-carrier lifetimes: Beyond hybrid lead halide perovskites. *MRS Commun.* **5**, 265–275 (2015).

31. Jung, M., Ji, S. G., Kim, G. & Seok, S. Il. Perovskite precursor solution chemistry: From fundamentals to photovoltaic applications. *Chem. Soc. Rev.* **48**, 2011–2038 (2019).

32. Li, Z. *et al.* Scalable fabrication of perovskite solar cells. *Nature Reviews Materials* **3**, (2018).

33. Akihiro Kojima, Kenjiro Teshima, Yasuo Shirai, and T. M. Organometal Halide Perovskites as Visible- Light Sensitizers for Photovoltaic Cells. *J Am Chem Soc* **131**, 6050–6051 (2009).

34. Eperon, G. E. *et al.* Formamidinium lead trihalide: A broadly tunable perovskite for efficient

planar heterojunction solar cells. *Energy Environ. Sci.* **7**, 982–988 (2014).

35. An, Y. *et al.* Structural Stability of Formamidinium- and Cesium-Based Halide Perovskites. *ACS Energy Lett.* **6**, 1942–1969 (2021).

36. McMeekin, D. P. *et al.* A mixed-cation lead mixed-halide perovskite absorber for tandem solar cells. *Science (6269).* (2016). doi:10.1126/science.aad5845

37. Min, H. *et al.* Perovskite solar cells with atomically coherent interlayers on SnO_2 electrodes. *Nature* **598**, 444–450 (2021).

38. Jeong, J. *et al.* Pseudo-halide anion engineering for α-$FAPbI_3$ perovskite solar cells. *Nature* **592**, (2021).

39. Yoo, J. J. *et al.* Efficient perovskite solar cells via improved carrier management. *Nature* **590**, 587–593 (2021).

40. Jeon, N. J. *et al.* Compositional engineering of perovskite materials for high-performance solar cells. *Nature* **517**, 476–480 (2015).

41. Jiang, Q. *et al.* Surface reaction for efficient and stable inverted perovskite solar cells. *Nature* **611**, 278–283 (2022).

42. Lin, Y. H. *et al.* A piperidinium salt stabilizes efficient metal-halide perovskite solar cells. *Science (6499).* **369**, 96–102 (2020).

43. Burschka, J. *et al.* Sequential deposition as a route to high-performance perovskite-sensitized solar cells. *Nature* **499**, 316–319 (2013).

44. Bu, T. *et al.* Lead halide-templated crystallization of methylamine-free perovskite for efficient photovoltaic modules. *Science (6548).* **372**, 1327–1332 (2021).

45. Jiang, Q. *et al.* Surface passivation of perovskite film for efficient solar cells. *Nat. Photonics* **13**, 460–466 (2019).

46. Yang, W. S. *et al.* High-performance photovoltaic perovskite layers fabricated through intramolecular exchange. *Science (6240).* **348**, 1234–1237 (2015).

47. Cao, J. *et al.* Identifying the Molecular Structures of Intermediates for Optimizing the Fabrication of High-Quality Perovskite Films. *J. Am. Chem. Soc.* **138**, 9919–9926 (2016).

48. Tanaka, H. & Nakamura, E. Chemical Pathways Connecting Lead(II) Iodide and Perovskite via Polymeric Plumbate(II) Fiber. (2015). doi:10.1021/jacs.5b10599

49. Jeon, N. J. *et al.* Solvent engineering for high-performance inorganic-organic hybrid perovskite solar cells. *Nat. Mater.* **13**, 897–903 (2014).

50. Taylor, A. D. *et al.* A general approach to high-efficiency perovskite solar cells by any antisolvent. *Nat. Commun.* **12**, 1–11 (2021).

51. Tao, S., I. Schmidt, G. Brocks, J. Jiang, I. Trance, K. Meerholz, S. Olthof, Absolute energy level positions in tinand lead-based halide perovskites. *Nat. Commun.* **10,** 2560 (2019).

52. Wolff, C. M., Caprioglio, P., Stolterfoht, M. & Neher, D. Nonradiative Recombination in Perovskite Solar Cells: The Role of Interfaces. *Adv. Mater.* **31**, (2019).

53. Caprioglio, P. *et al.* On the Relation between the Open-Circuit Voltage and Quasi-Fermi Level Splitting in Efficient Perovskite Solar Cells. *Adv. Energy Mater.* **9**, (2019).

54. Stolterfoht, M. *et al.* The impact of energy alignment and interfacial recombination on the internal and external open-circuit voltage of perovskite solar cells. *Energy Environ. Sci.* **12**, 2778–2788 (2019).

55. Le Corre, V. M. *et al.* Charge Transport Layers Limiting the Efficiency of Perovskite Solar Cells: How to Optimize Conductivity, Doping, and Thickness. *ACS Appl. Energy Mater.* **2**, 6280–6287 (2019).

56. Mahesh, S. *et al.* Revealing the origin of voltage loss in mixed-halide perovskite solar cells. *Energy Environ. Sci.* **13**, 258–267 (2020).

57. Shockley, W. & Queisser, H. Detailed balance limit of efficiency of p-n junction solar cells. *Renew. Energy Four Vol. Set* **32**, 510–519 (1960).

58. Tiedje, T., Yablonovitch, E., Cody, G. D. & Brooks, B. G. Limiting Efficiency of Silicon Solar Cells. *IEEE Trans. Electron Devices* **31**, 711–716 (1984).

59. Caprioglio, P. *et al.* On the Origin of the Ideality Factor in Perovskite Solar Cells. *Adv. Energy Mater.* **10**, 1–9 (2020).

60. Thiesbrummel, J. *et al.* Universal Current Losses in Perovskite Solar Cells Due to Mobile Ions. *Adv. Energy Mater.* **11**, (2021).

61. Tress, W. *et al.* Understanding the rate-dependent J-V hysteresis, slow time component, and aging in $CH_3NH_3PbI_3$ perovskite solar cells: The role of a compensated electric field. *Energy Environ. Sci.* **8**, 995–1004 (2015).

62. Chen, B., Yang, M., Priya, S. & Zhu, K. Origin of J-V Hysteresis in Perovskite Solar Cells. *J. Phys. Chem. Lett.* **7**, 905–917 (2016).

63. Schwenzer, J. A. *et al.* Thermal Stability and Cation Composition of Hybrid Organic-Inorganic Perovskites. *ACS Appl. Mater. Interfaces* **13**, 15292–15304 (2021).

64. Turren-Cruz, S. H., Hagfeldt, A. & Saliba, M. Methylammonium-free, high-performance, and stable perovskite solar cells on a planar architecture. *Science (6413).* **362**, 449–453 (2018).

65. Roose, B. *et al.* Mesoporous SnO_2 electron selective contact enables UV-stable perovskite solar cells. *Nano Energy* **30**, 517–522 (2016).

66. Uddin, A. & Yi, H. Progress and Challenges of SnO_2 Electron Transport Layer for Perovskite Solar Cells: A Critical Review. *Sol. RRL* **6**, (2022).

67. Li, Z. *et al.* Extrinsic ion migration in perovskite solar cells. *Energy Environ. Sci.* **10**, 1234–1242 (2017).

68. Zhao, X., Kim, H. S., Seo, J. Y. & Park, N. G. Effect of Selective Contacts on the Thermal Stability of Perovskite Solar Cells. *ACS Appl. Mater. Interfaces* **9**, 7148–7153 (2017).

69. Ren, G. *et al.* Strategies of modifying spiro-OMeTAD materials for perovskite solar cells: a review. *J. Mater. Chem. A* **9**, 4589–4625 (2021).

70. Kasparavicius, E. *et al.* Oxidized Spiro-OMeTAD: Investigation of Stability in Contact with Various Perovskite Compositions. *ACS Appl. Energy Mater.* **4**, 13696–13705 (2021).

71. Al-Ashouri, A. *et al.* Monolithic perovskite/silicon tandem solar cell with >29% efficiency by enhanced hole extraction. *Science (6522).* **370**, 1300–1309 (2020).

72. Al-Ashouri, A. *et al.* Conformal monolayer contacts with lossless interfaces for perovskite single junction and monolithic tandem solar cells. *Energy Environ. Sci.* **12**, 3356–3369 (2019).

73. Deumel, S. *et al.* High-sensitivity high-resolution X-ray imaging with soft-sintered metal halide perovskites. *Nat. Electron.* **4**, 681-688 (2021).

74. Sun, Y. *et al.* Bright and stable perovskite light-emitting diodes in the near-infrared range. *Nature,* **615**, 830-835 (2023).

75. National Renewable Energy Laboratory. NREL Efficiency Chart. Available at: https://www.nrel.gov/pv/assets/pdfs/best-research-cell-efficiencies.pdf (Accessed: 02 July 2023)

Chapter 3 – Experimental Methods

3.1 – Materials

Fluorine-doped tin oxide-coated glass substrates (8 or 15 Ω cm^{-2}, AMG), HelioSeal™ PVS 101 (ADCO products), SOLAR ASCE™ TR04BA Olefin copolymer, 3M™ Charge-Collection Solar Tape 3007, tin (IV) oxide (15 wt.% in H_2O colloidal dispersion, Alfa Aesar), lead(II) iodide (99.99%, trace metal basis, Tokyo Chemical Industries), lead(II) bromide (99.999%, trace metal basis, Sigma Aldrich), methylammonium iodide (>99.99%, Greatcell Solar Materials), methylammonium bromide (>99.99%, Greatcell Solar Materials), methylammonium chloride (>99.99%, Greatcell Solar Materials), formamidinium iodide (>99.99%, Greatcell Solar Materials), formamidinium bromide (>99.99%, Greatcell Solar Materials), phenethylammonium iodide (>99%, Greatcell Solar Materials), cesium iodide (99.999% trace metal basis, Alfa Aesar), methylenediammonium dichloride (>98%, Sigma Aldrich), hexamethylenetetramine (>99.0%, Sigma Aldrich), ammonium chloride (>99.5%, Sigma Aldrich), spiro-OMeTAD (2,2',7,7'-Tetrakis(N,N-di-p-methoxyphenylamino)-9,9'-spirobifluoren, >99.5%, Luminescence Technology Corp.), FK209 Co(III) TFSI salt (tris(2-(1H-pyrazol-1-yl)-4-tert-butylpyridine)cobalt(III) tri[bis(trifluoromethane)sulfonimide], 98%, Sigma Aldrich), bis(trifluoromethylsulfonyl)amine lithium salt (99.95%, Sigma Aldrich), MeO-2PACz ([2-(3,6-dimethoxy-9H-carbazol-9-yl)ethyl]phosphonic acid, Tokyo Chemical Industries), phenyl-C_{61}-butyric acid methyl ester ($PC_{61}BM$, Solenne), bathocuproine (98%, Alfa Aesar), gold pellets (99.999%, Kurt J. Lesker Company). *n*-butylamine (99.5%, Sigma Aldrich), 2-methyltetrahydrofuran (Biorenewable, anhydrous, >99.0%, contains 250 ppm BHT as inhibitor, Sigma Aldrich), tetrahydrofuran (anhydrous, >99.9%, contains 250 ppm BHT as inhibitor, Sigma

Aldrich), *n*-butanol (anhydrous, 99.8%, Sigma Aldrich), 2-propanol (anhydrous, 99.5%, Sigma Aldrich), ethanol (anhydrous, 99.5%, Sigma Aldrich), chlorobenzene (anhydrous, 99.8%, Sigma Aldrich), acetonitrile (anhydrous, 99.8%, Sigma Aldrich), dimethyl sulfoxide (anhydrous, 99.8%, Sigma Aldrich), *N,N*-dimethylformamide (anhydrous, 99.8%, Sigma Aldrich), 4-*tert*-butylpyridine (98%, Sigma Aldrich), γ-butyrolactone (99+%, Alfa Aesar), dimethyl sulfoxide-d^6 (99.9 atomic% ^{2}H, Sigma Aldrich). All chemicals were used as received and without any further purification besides hexamethylenetetramine and ammonium chloride, which were both dried in a vacuum oven at 60 °C for 48 hours before use.

3.2 – Fabrication

3.2.1 – Substrate preparation

Prior to use, all FTO-coated substrates were scrubbed with an aqueous 2 vol% Decon 90 solution, rinsed with deionised water, sonicated in acetone and subsequently sonicated in 2-propanol.

All other non-aqueous chemicals were stored in a N_2-filled glovebox before use and protected from exposure to light.

3.2.2 – Electron transport materials

3.2.2.1 SnO_2 nanoparticle layer

A colloidal suspension of tin oxide nanoparticles (400 µL) was diluted with ultrapure water (2,600 µL). In an atmosphere containing minimum moisture (<5% relative humidity), 200 µL of this solution was placed statically on a UV-ozone treated (15 minutes) substrate coated with a fluorine-doped tin oxide layer (15 Ω cm^{-2}), then spun at 4,000 rpm (1,000 rpm s^{-1}) for 30 seconds before being immediately annealed at 150 °C for 30 minutes in the same environment. The substrates were allowed to cool, then immediately subjected to a further 15 minutes of UV-ozone treatment before being immediately used in the following processing step.

3.2.2.2 Phenyl-C_{61}-butyric acid methyl ester ($PC_{61}BM$) layer

A solution of $PC_{61}BM$ (20 mg ml^{-1}) in a 3:1 chlorobenzene:dichlorobenzene mixture was prepared in a N_2 atmosphere, stirred overnight at room temperature, and then filtered with 0.45 µm PTFE filter before use. 50 µL of this solution was spin-coated dynamically (2,000 rpm) and dried at 100 °C for 5 minutes. This process was carried out in a N_2 atmosphere.

3.2.3 – Hole transport materials

3.2.3.1 Spiro-OMeTAD layer

A solution of spiro-OMeTAD (0.070 mmol, 85.8 mg) dissolved in chlorobenzene (1,000 µL) and doped with 8.4 µL of a 0.250 M solution of tris(2-(1*H*-pyrazol-1-yl)-4-*tert*-butylpyridine)cobalt(III) tri[bis(trifluoromethane)sulfonimide] in acetonitrile, 19.4 µL of a 1.8 M solution of bis(trifluoromethylsulfonyl)amine lithium salt in acetonitrile, and *tert*-butyl pyridine (0.231 mmol, 38.0 µL). This solution was spin-coated dynamically at 2,500 rpm for 30 seconds, in a N_2-containing glovebox.

3.2.3.2 MeO-2PACz layer

MeO-2PACz was dissolved in anhydrous ethanol at a concentration of 0.33 mg mL^{-1} and placed in an ultrasonic bath for 15 min (30-40 °C) before use. The solution was prepared and deposited in a N_2 atmosphere, but briefly opened to air before use. 80 µl of this solution was dropped in the centre of the substrate and allowed to spread for ~5 s. The substrate was then spun at 3,000 rpm for 30 s.

3.2.4 – Perovskite thin film materials

In this work a wide range of state-of-the-art perovskite materials are investigated and reported upon, notably during thermal stability testing *via* XRD and TG-GC-MS analysis. This is done to offer the reader the widest possible context in which to understand the advantages for material stability offered by the ^{t}2D-3D α-$FAPbI_3$ material, and the templated sequential approach more broadly. The overwhelming majority of materials employed, other than that novel to this work, have been developed in our laboratory on the basis of prior publications; both from within our

group, and from other leading investigators in our field around the world. Here we present a comprehensive list of all materials utilised herein, an overview of our processing of them, and an exhaustive list of prior work from which we have developed these.

3.2.4.1 ^{t}2D-3D α-$FAPbI_3$

2-methyltetrahydrofuran (1,500 µL) and *n*-butylamine (1.90 mmol, 187.6 µL) were added to lead iodide (1.266 mmol, 583.5 mg) and methylammonium iodide (1.139 mmol, 181.1 mg) and agitated until all solids were fully dissolved. 50 µL of this solution was spin-coated dynamically at 2,500 rpm for 45 seconds in an environment at between 20-22% relative humidity and <22 °C. The substrates were immediately annealed at 70 °C for 10 minutes in the same environment. After cooling, the substrates were coated with 350 µL of a 0.1 M solution of formamidinium iodide (0.500 mmol, 86.0 mg) dissolved in *n*-butanol (5,000 µL). After 45 seconds of static soaking, the substrates were spun at 4,000 rpm (1,000 rpm s^{-1}) for 45 seconds, then immediately annealed for 10 minutes at 70 °C, followed by 30 minutes at 180 °C.

3.2.4.2 α-$FAPbI_3$ without MACl additive (DMF:DMSO)

Stoichiometric FAI and PbI_2 were dissolved in a 4:1 mixture of DMF:DMSO at 1.2 M concentration. 150 µL of this solution was dispensed statically on a FTO substrate under an atmosphere of air controlled to 18-24% relative humidity. The substrate was spun at 6,000 rpm (12,000 rpm s^{-1}) for 35 seconds. At 10 seconds into this procedure, 800 µL of diethyl ether antisolvent was dispensed slowly onto the spinning substrate. The substrate was then heated in ambient air at either 150 °C for 10 minutes (Fig. 5.4c) or 180 °C for 50 minutes (Fig. 5.4d). This protocol is adapted from that of Kim, et al.[1]

3.2.4.3 α-$FAPbI_3$ with excess (40 mol%) MACl additive (DMF:DMSO)

Stoichiometric FAI and PbI_2 were dissolved in a 4:1 mixture of DMF:DMSO at 1.8 M concentration, along with a 40 mol% excess of MACl. 150 µL of this solution was dispensed statically on a FTO substrate under an atmosphere of air controlled to 18-24% relative humidity. The substrate was spun at 6,000 rpm (12,000 rpm s^{-1}) for 35 seconds. At 10 seconds into this procedure, 800 µL of diethyl ether or anisole antisolvent was dispensed slowly onto the spinning substrate. The substrate was then heated in ambient air at 150 °C for 10 minutes. This protocol is adapted from that of Kim, et al.[1]

3.2.4.4 α-$FAPbI_3$ *via* sequential deposition (DMF:DMSO)

A 1.5 M solution of PbI_2 in DMF:DMSO (9:1) was prepared. 150 µL of this solution was dispensed statically on a FTO substrate under in an inert atmosphere (N_2). The substrate was spun at 1,500 rpm (300 rpm s^{-1}) for 30 seconds. The substrate was then annealed for 60 seconds at 70 °C. A further 150 uL of a solution containing FAI, MAI and MACl in a 1:0.075:0.25 stoichiometry dissolved in IPA was dispensed on the substrate before immediately spinning the substrate at 2,500 rpm (1,00 rpm s^{-1}) for 30 seconds. The substrate was then immediately removed to an atmosphere of air with relative humidity controlled to between 25-30% and thermally cured at 150 °C for 15 minutes[2].

3.2.4.5 $FA_{0.83}Cs_{0.17}Pb(I_{0.9}Br_{0.1})_3$ (DMF:DMSO)

FAI (207.0 mg), PbI_2 (568.0 mg), $PbBr_2$ (80.0 mg) and CsI (64.0 mg) were dissolved in 1 mL of a 4:1 mixture of DMF:DMSO (1.23 M). 100 µL of this solution was dispensed statically on a FTO substrate under in an inert atmosphere (N_2). The substrate was spun at 2,000 rpm (1,000 rpm s^{-1}) for 10

seconds, followed by an increase to 6,000 rpm (2,000 rpm s^{-1}) for a further 35 seconds. 10 seconds before the end of this procedure, 170 µL of anisole or diethyl etherantisolvent was dispensed onto the spinning substrate. The substrate was then heated in the same environment at either 100 °C for 15 minutes, 150 °C for 10 minutes or 180 °C for 50 minutes. This protocol is adapted from one in common use within our group, for example as described by McMeekin, et al[3].

3.2.4.6 $(FAPbI_3)_{0.95}(MAPbBr_3)_{0.05}$ with excess (35 mol%) MACl additive (DMF:DMSO)

Stoichiometric FAI and PbI_2 were dissolved in a 19:1 ratio with stoichiometric MABr and $PbBr_2$, in a 8:1 mixture of DMF:DMSO at 1.8 M concentration, along with a 35 mol% excess of MACl. 150 µL of this solution was dispensed statically on a FTO substrate under an atmosphere of air controlled to 18-24% relative humidity. The substrate was spun at 6,000 rpm (12,000 rpm s^{-1}) for 35 seconds. At 10 seconds into this procedure, 800 µL of diethyl ether antisolvent was dispensed slowly onto the spinning substrate. The substrate was then heated in ambient air at 150 °C for 10 minutes. This protocol is adapted from that of Min, et al.[4]

3.2.4.7 $(MAPbCl_3)_{0.03}(FA_{0.78}Cs_{0.22}Pb(I_{0.85}Br_{0.15})_3)_{0.97}$ ("triple halide perovskite") (DMF:DMSO)

FAI, CsI, PbI_2 and $PbBr_2$ were mixed in stoichiometric ratio 0.78 : 0.22 : 0.85 : 0.15. To these, $PbCl_2$ and MACl (1:1 by mol) powders were added such that they comprise 3 mol% of the total precursor solids. These precursors were dissolved in a 3:1 mixture of DMF:DMSO. 100 µL of this solution was spread statically on a FTO substrate under in an inert atmosphere (N_2). The substrate

was spun at 5,000 rpm (2,500 rpm s^{-1}) for 50 seconds. Between 25-30 seconds from the beginning of this procedure, 200 µL of methyl acetate antisolvent was dispensed onto the spinning substrate. The substrate was then heated in the same environment at 100 °C for 30 minutes. This protocol is adapted from that of Xu, et al.[5]

3.2.4.8 $FA_{0.79}MA_{0.16}Cs_{0.05}Pb(I_{0.83}Br_{0.17})_3$ ("triple cation perovskite") (DMF:DMSO)

A precursor solution containing FAI, PbI_2, MABr and $PbBr_2$ in a 1:1.1:0.2:0.2 stoichiometry at 1.1 M (with respect to Pb^{2+}) concentration was prepared using a DMF:DMSO (4:1) solvent mixture. A 1.5 M solution of CsI in DMSO was prepared separately and added to the precursor solution such that the desired composition was achieved. 100 µL of the precursor solution was then dispensed statically on a FTO substrate under in an inert atmosphere (N_2). The substrate was spun at 1,000 rpm (1,000 rpm s^{-1}) for 10 seconds, followed by an increase to 6,000 rpm (2,000 rpm s^{-1}) for a further 20 seconds. 5 seconds before the end of this procedure, 100 µL of chlorobenzene antisolvent was dispensed onto the spinning substrate. The substrate was then heated in the same environment at 100 °C for 60 minutes.[6]

3.2.4.9 $MAPbI_3$ (DMF:DMSO)

A 1.3 M solution of PbI_2 and MAI in 1:1 stoichiometry was prepared using a 4:1 v/v DMF:DMSO solvent mixture. 100 µL of the precursor solution was then dispensed statically on a FTO substrate under in an inert atmosphere (N_2). The substrate was spun at 1,000 rpm (1,000 rpm s^{-1}) for 10 seconds, followed by an increase to 6,000 rpm (2,000 rpm s^{-1}) for a further 30 seconds. 20 seconds before the end of this procedure, 150 µL of chlorobenzene antisolvent was

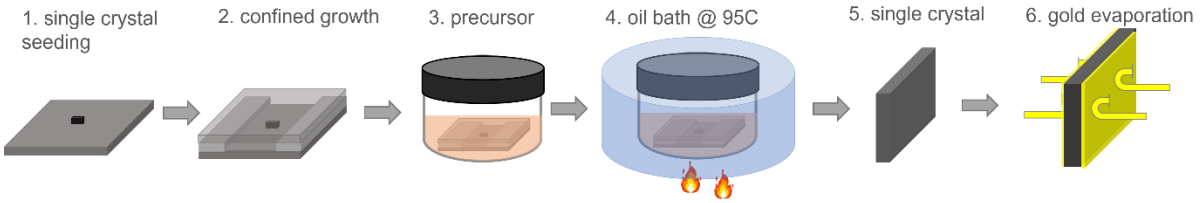


Figure 3.1 | Schematic illustration of the single crystal synthesis and device fabrication process. 1. Single crystal seeding; 2. Seed crystal in confined growth template; 3. Addition of precursor solution; 4. Crystal growth in oil bath at 95 °C; 5. Free-standing single crystal; 6. Gold evaporation and gold wire attachment for electrical characterization measurements.

dispensed onto the spinning substrate. The substrate was then heated in the same environment at 100 °C for 45 minutes.[7]

3.2.4.10 $MAPbI_3$ (ACN)

MAI and PbI_2 were mixed in a 1:1.06 stoichiometry and ACN added such that the concentration was 0.5 M with respect to Pb (II). A black suspension is formed within a few seconds of mixing. Methylamine gas (40 wt.% in ethanol) is bubbled through this solution by means of a carrier gas (N_2) until the solution was fully dissolved. 100 µL of this solution was dispensed dynamically on a FTO substrate (2,000 rpm) under an atmosphere of dry air (<5% relative humidity). The substrate was then heated in the same environment at 100 °C for 45 minutes.

This protocol is adapted from that of Noel, et al.[8]

3.2.5 – Perovskite single crystal materials

All single crystals were fabricated from a seed crystal by following a previously published experimental protocol[9,10]. The control $FAPbI_3$ single crystals are prepared by dissolving equimolar FAI and PbI_2 in γ-butyrolactone (GBL). The solution is then stirred at 60 °C for one hour. Then the solution is filtered with a 25 mm diameter 0.45 µm GMF filter. 4 ml of the filtrate is then placed in a vial that contains a seed $FAPbI_3$

crystal, and the vial is kept in an oil bath undisturbed at 95 °C for 12 hours. The crystals were then dried in a vacuum oven at 180 °C. For the $FAPbI_3$-M and $FAPbI_3$-H single crystals, an equimolar amount of FAI and PbI_2 is dissolved in GBL by stirring at 60 °C for one hour. Then 3.8 mol% of $MDACl_2$ or 0.56 mol% HMTA was added to the $FAPbI_3$ perovskite precursor solution and stirred 60 °C for 4 hours. Then the same procedure as for the control crystals was followed.

3.2.7 – Interlayer materials

3.2.7.1 Phenethylammonium iodide

A 20 mM solution of phenethylammonium iodide (0.200 mmol, 49.8 mg) in 2-propanol (10,000 µL) was spin-coated dynamically on top of the perovskite material at 5,000 rpm for 45 seconds, in a N_2-containing glovebox.

3.2.7.2 Bathocuproine

A bathocuproine solution (0.5 mg ml^{-1}) in *n*-propanol was prepared in a N_2 atmosphere and stirred overnight (heated at 70 °C if required to achieve full dissolution) and filtered (0.45 µm PTFE filter) before use. 80 µL of this solution was spin-coated dynamically (2,000 rpm) and dried at 100 °C for 5 minutes. This process was carried out in a N_2 atmosphere.

3.2.8 – Electrode materials

3.2.8.1 Gold

75 nm of gold was thermally evaporated at an initial rate of 0.1 As^{-1} at a pressure < 2 x 10^{-6} torr.

3.2.9 – Encapsulation methods

In order to withstand the harsh, humid conditions of the “damp-heat” accelerated aging test (**Chapter 5**) we developed new encapsulation methods based on an industry

standard poly(isobutene) edge sealant tape (HelioSeal™ PVS 101). Below we describe how we use perform this encapsulation in the case of both thin films and solar cell devices. Images of the encapsulated products are shown in **Chapter 5, Figure 5.12a**.

3.2.9.1 Thin films

30 mm x 30 mm FTO-coated glass substrates were used. A perovskite layer was deposited on top of this, and a PMMA layer (2.5 mg mL^{-1} in toluene) was spin-coated on top. A razor blade was used to remove the perovskite and PMMA from all but the central 10 mm x 10 mm region of the substrate. Two layers of four 20 mm x 10 mm strips of edge sealant tape were placed in an interlocking array on top of the substrate in the areas from which the perovskite was removed, ensuring that only small (< 1 mm) gaps were left between the strips. A second FTO-coated glass substrate was placed on top of the interlocking array of tape such that the FTO was in contact with the tape. This assembly was placed in an oven at 110 °C for 10 minutes with a weight of several kg's placed on top to ensure sufficient pressure was exerted to expand and compress the edge sealant tape as it is heated.

3.2.9.2 Solar cell devices

This full-device encapsulation was developed with the assistance of Dr Joel Smith. The text and figures below were prepared by Benjamin M. Gallant and Dr Joel Smith.

Encapsulation process (**Figure 3.3**):

1. Prepare PSCs as described above.

2. Attach solar ribbon wires 93M™ Charge-Collection Solar Tape 3007) to appropriate electrodes (see **Figure 3.3**).
3. Place polyolefin foil (SOLAR ASCE™ TR04BA Olefin copolymer, 30 mm x 30 mm in recess of recessed glass substrate (70 mm x 70 mm with 32 mm x 32 mm recess).
4. Place interlocking strips of butyl rubber (50 mm x 10 mm) around each edge of bottom glass plate, ensuring < 1 mm gaps left between strips.
5. Place device with ribbons in recess, with ribbons overlaid on edge sealant tape, cleaning any glue from ribbon in regions where crossing edge sealant tape.
6. Add second layer of edge sealant strips on top of ribbon.
7. Place polyolefin foil (35 mm x 35 mm) on top of device.
8. Place non-recessed top glass plate on top.
9. Vacuum seal and heat at up to 150 C under static vacuum.

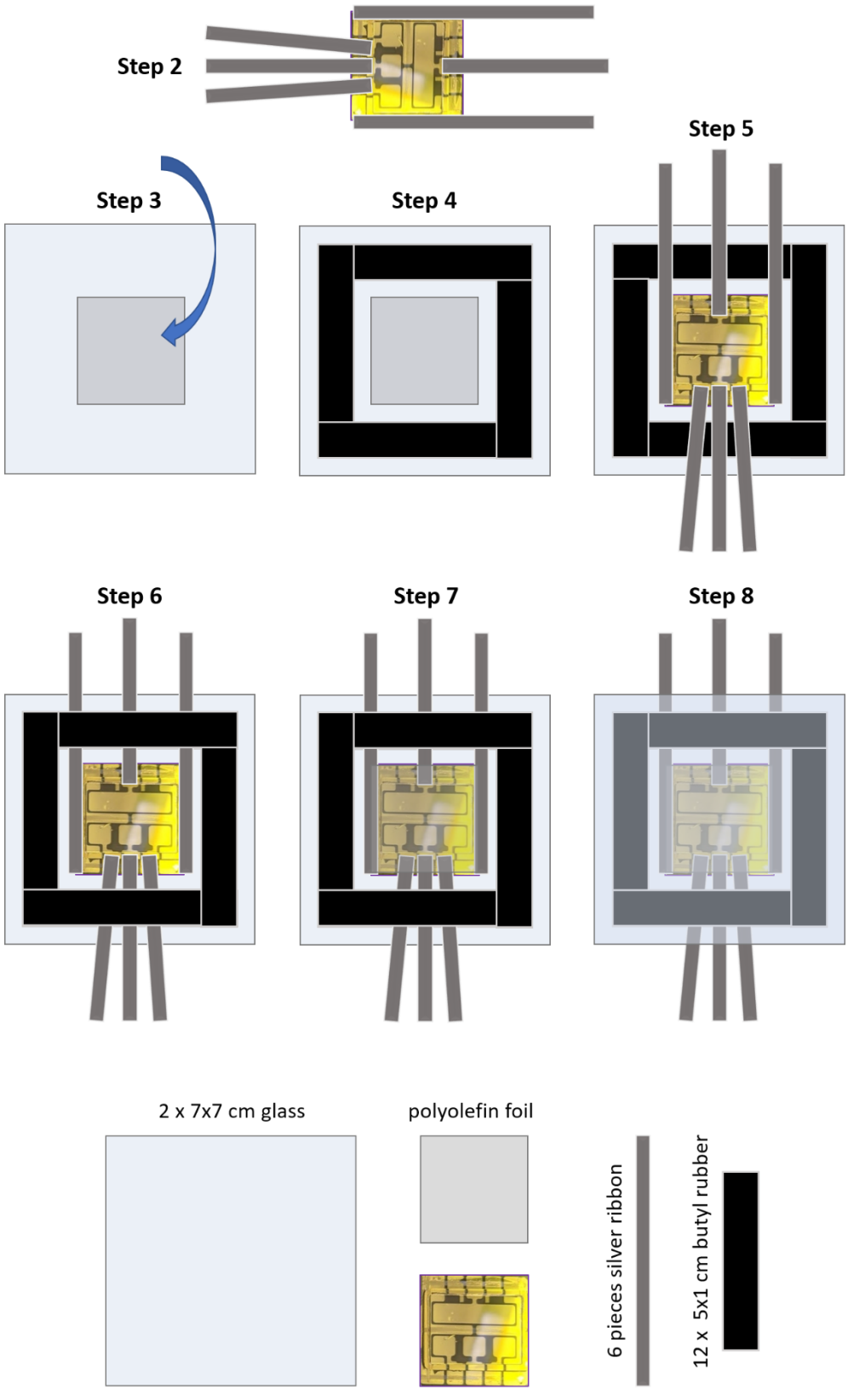


Figure 3.2 | PSC encapsulation. Schematic representation of encapsulation process for PSC encapsulation. Steps correspond to those set out in **Section 3.2.9.2.**

3.3 – Characterisation

3.3.1 – Optoelectronic characterisation

3.3.1.1 Raman Spectroscopy

All measurements carried out by Bernd Sturdza. The following text is written by Bernd Sturdza.

Raman spectra were acquired with a Jobin Yvon T64000 triple spectrometer and an Andor DU420A-OE CCD. The spectrometer was calibrated with the 520.7 cm^{-1} line of a Silicon wafer before each measurement. Samples were excited with a Ventus solo Nd:YAG laser (λ = 532 nm) and the incident laser irradiation of the samples was strictly kept at intensities below 5 W/cm^2 to prevent laser induced degradation. This has been a major source of confusion for $FAPbI_3$ Raman mode assignment in the literature and we thus opted for longer exposure times at extremely low laser intensities.

Raman spectroscopy has been used extensively to distinguish the δ- and α-phases in $FAPbI_3$, as the different symmetries of the two phases allow identification via their Raman signatures. Han et al. were the first to report Raman signatures for both phases, assigning peaks at 111 cm^{-1} and 135 cm^{-1} to the δ- and α-phase, respectively[11]. This assignment has been used in numerous studies[12–14] since, even though the cubic Pm-3m symmetry of the α-phase is predicted to be Raman inactive by group theory. Two recent reports by Driscoll *et al.* and Ibaceta-Jana *et al.* dissent previous assignments and provide experimental evidence that the α-phase is Raman inactive[15,16]. These reports match our observations.

Comment on selection of peak at 108 cm^{-1}:

There are four modes of the inorganic framework in the δ-phase: 35, 55, 83 and 108 cm^{-1}. Raman modes become harder to detect the closer they appear to the laser line (0 cm^{-1}) due to its linewidth. This has two consequences:

1. Most Raman spectrometers can only detect the line at 108 cm^{-1}, as they use optical filters to cut out the laser line.
2. For modes closer to the laser line, there will be more of a background issue from the tail of the laser line. This could be subtracted, but for a quantitative analysis it's easier to take a line slightly further away.

For compounds containing organic entities in an inorganic framework, like $FAPbI_3$, we can separate the Raman modes of the framework from the modes of the organic part. Modes of FA are all substantially above 200 cm^{-1}; modes of the haloplumbate framework in the range <200 cm^{-1}. By looking at the 108 cm^{-1} peak, we are probing the PbI bond. However, we prefer to think about this in terms of the symmetry of the PbI cage instead of individual bonds, as the symmetry defines whether something is Raman active or not.

3.3.1.2 Time-integrated Photoluminescence

All measurements carried out by Dr Chelsea Xia and Dr Adam Wright. The following text is written by Dr Chelsea Xia and Dr Adam Wright.

PL spectra of single crystal samples were acquired using a time-correlated single photon counting (TCSPC) setup (FluoTime 300, PicoQuant GmbH). Samples were photoexcited using a 507 nm laser (LDH-P-C-510, Pico Quant GmbH) pulsed at a frequency of 40 MHz. The PL was dispersed using a monochromator, detected with hybrid photomultiplier detector assembly (PMA Hybrid 40, PicoQuant GmbH) and integrated over time.

3.3.1.3 Transient photo-conductivity (TPC)

All measurements carried out by Manuel Kober-Czerny. The following text was first drafted by Manuel Kober-Czerny.

An Nd:YAG laser (Ekspla NT342A, 10 Hz with 3.74 ns FWHM) is coupled into an optical parametric oscillator to obtain various wavelengths in a home-built setup. The laser is attenuated by an optical density filter to reach several fluences for each wavelength (typically between 1.5 and 0.01 μJ cm^{-2}). The spot size of the pulsed light is 0.5 cm^2, which is 10x larger than the single crystals used, ensuring that they are uniformly excited. A small DC bias (< 5 mV/μm) is applied across two in-plane (lateral) gold electrodes that have been evaporated directly onto the single crystal. We monitor the voltage drop across the variable series resistor through a parallel oscilloscope (1MΩ input impedance) to determine the potential dropped across the two in-plane Au electrodes on the sample. We then extract the photoconductivity directly from the data and estimate the sum-mobility (Σμ) taking recombination and the free carrier fraction into account. The estimation error is greatly influenced by the sample thickness. For more detail see our recent work[19,20].

3.3.1.4 Ultraviolet-Visible Absorption Spectroscopy

Reflectance (R) and transmittance (T) spectra were recorded on a Varian Cary 1050 UV Vis spectrophotometer equipped with an integrating sphere. From these measurements, and in combination with the photoactive layer thickness (d), spectrally resolved absorption coefficients (α) were calculated via $\alpha = -\frac{1}{d}\ln(\frac{T}{1-R})$. Assuming a direct bandgap semi-conductor, bandgaps were calculated via a Tauc analysis, wherein the x-intercept of the linear region of the bandedge was found on a plot of $(\alpha hv)^{0.5}$ against photon energy, hv.

Separately, absorbance spectra were measured with a Varian Cary 300 Bio UV-visible spectrophotometer with a 50x50 mm reflective neutral density filters with an optical density of 3.0 (made out of UV fused silica).

3.3.1.5 Time-Correlated Single Photon Counting (TCSPC)

All measurements on thin films were carried out by Karim A. Elmestekawy, and on single crystals by Dr Chelsea Xia and Dr Adam Wright. The following text was first drafted by Karim A. Elmestekawy.

Time-resolved PL of thin films samples on quartz substrates was measured using TCSPC following excitation by a 398 nm picosecond pulsed diode laser at a repetition rate of 2.5 MHz (PicoHarp, LDH-D-C-405M). The resultant PL was collected and coupled into a grating spectrometer (Princeton Instruments, SP-2558), which directed the spectrally dispersed PL onto a photon-counting detector (PDM series from MPD), whose timing was controlled with a PicoHarp300 TCSPC event timer. The PL transients were measured at 810 nm, corresponding to the peak PL intensity in the steady-state PL spectrum of this composition.

We fitted a stretched exponential function $I = I_0 e^{(\frac{t}{\tau_{\text{char}}})^{\beta}}$ to the PL intensity to account for the local distribution of monoexponential decay rates, whose effective lifetime is given by $\tau_{\text{eff}} = \frac{\tau_{\text{char}}}{\beta}\Gamma(\frac{1}{\beta})$. τ_{char} is the characteristic lifetime corresponding to the time taken for the PL intensity to drop to I_0/e, and β is the distribution coefficient that encompasses the case for monoexponential decays for the case $\beta = 1$, and the cases for a range of decay times (or potentially higher-order effects) as it decreases[21,22]. To account for the PL originating from electron-hole recombination we further double the effective fitted lifetime in order to extract the monomolecular charge-carrier recombination rate k_1, such

that $k_1 = 1/2\tau_{\text{eff}}$, assuming $I \propto k_2 n^2$ at our excitation fluence of 81 nJ cm^{-2} [23,24]. The samples were all mounted in a vacuum cell under low pressure ($\sim 10^{-2}$ mbar).

This spectroscopic technique initially generated charge-carriers closer to the surface of the film through which excitation occurs, owing to most of the 398 nm excitation being absorbed in the first 100 nm. This also accounts for the fast decay at very early times; most of the photogenerated charge-carriers will be initially generated closer to the surface where the density of trap states is higher than in the bulk, resulting in a rapid drop in PL intensity at very early times before the charge-carriers diffuse away further from the surface. The diffusion along the thickness of the film towards the bulk and perpendicular diffusion away from the excitation spot results in the local distribution of mono-exponential recombination rates assumed for our use of the stretch exponential fits.

3.3.1.6 Optical-Pump Terahertz-Probe (OPTP) Spectroscopy

All measurements carried out by Karim A. Elmestekawy. The following text was first drafted by Karim A. Elmestekawy.

An amplified laser system (Spectra Physics, MaiTai – Ascend – Spitfire), with a 5 kHz repetition rate, centre wavelength of 800 nm and pulse duration of 35 fs is used to generate the THz radiation using a spintronic emitter. The THz probe is then focused onto the sample, overlaid with a 400 nm excitation pump that is generated using a Beta Barium Borate (BBO) crystal. The THz radiation transmitted through the sample is then detected via free-space electro-optical sampling in a ZnTe (110) crystal of thickness 200 μm[25].

OPTP spectroscopy allows us to non-invasively probe the dielectric response of a medium and examine the charge carriers that modify the material's conductivity at THz frequencies after a well-defined time delay after optical excitation. This approach allows us to investigate the local charge-carrier dynamics and quantify the effective mobilities and bimolecular recombination rates of the photogenerated charge carriers.

Charge-carrier sum mobility

Time-resolved variations in the THz transmission ($\Delta T/T$) through the sample can be measured by varying the time delay between the pump and probe beams, and this change in electric-field transmission at the peak of the THz pulse (t_{gate}) can be in turn related to the change in the photoconductivity (ΔS) of the thin film (films whose thickness *d* is much smaller than the THz wavelengths λ_{THz}), using:

$$\Delta S = -\epsilon_0 c(n_a + n_b)\frac{\Delta T(t_{\mathrm{gate}} = 0)}{T} \tag{3.1}$$

where $\epsilon_0 c$ is the invert of the vacuum impedence, and n_a and n_b are the refractive indices of the mediums surrounding the sample (vacuum and the substrate).

The charge-carrier mobility (μ) and change in photoconductivity (ΔS) have a linear relationship that holds for low fluences in which monomolecular

$$\mu = \frac{\Delta S A_{\mathrm{eff}}}{Ne} \tag{3.2}$$

recombination dominates (< 50 μJ cm^{-2}, linear region of decay, see **Figure 4.8d-f**), described using:

where A_{eff} is the effective area of overlap between the optical pump and the THz probe, and *N* is the number of photoexcited charge carriers.

The number of photoexcited charge carriers can be calculated using:

$$N = \Phi \frac{E\lambda}{hc}(1 - R_{\text{pump}} - T_{\text{pump}}) \tag{3.3}$$

where Φ is the branching ratio of free charge-carriers to photons absorbed, $(1 - R_{\text{pump}} - T_{\text{pump}})$ is the fraction of the 400 nm pump beam absorbed by the sample, λ and *E* are the wavelength and pulse energy of the excitation pulse, and $\frac{E\lambda}{hc} = N_{\text{ph}}$ is the number of photons in a pump pulse.

We can then combine **Equation 3.1**, **Equation 3.2**, and **Equation 3.3** to calculate the effective charge-carrier mobility as:

This effective mobility is the effective sum mobility of photogenerated electrons

$$\Phi\mu = -\epsilon_0 c(n_a + n_b)\frac{A_{\text{eff}}hc}{Ee\lambda(1 - R_{\text{pump}} - T_{\text{pump}})}\left(\frac{\Delta T\left(t_{\text{gate}}, t_{\text{pump-probe}} = 0\right)}{T}\right) \tag{3.4}$$

and holes, and it reflects the true sum mobility when the photons absorbed are fully converted to free charge carriers ($\Phi = 1$)

Transient decay fitting

The ΔS transients can be globally fitted to extract k_2, with k_1 *and* k_3 either ignored (set to 0) or set to a reasonable value, as the excitation fluences used for the experiments conducted here lead the fluence-dependent decays over the first nanosecond after excitation to be primarily affected by bimolecular electron-hole recombination captured by the rate constant k_2.

Charge-carrier dynamics in perovskite semiconductors can be generally described using:

$$\frac{dn}{dt} = -k_1 n - k_2 n^2 - k_3 n^3 \tag{3.5}$$

where *n* is the photogenerated charge-carrier density, k_1 represents the monomolecular recombination rate constant, associated with trap-mediated recombinations, k_2 represents the bimolecular electron-hole recombination, and k_3 represents Auger recombination. Here, trap-mediated recombination rates are too low to have any influence over the first nanosecond (hence k_1 may be ignored), while charge-carrier densities were kept below the limit for which Auger recombination begins to dominate (k_3 may be ignored).

This leads to the analytical expression for *n*:

$$n(t) = \frac{1}{(\frac{1}{n_0} + k_2 t)} \tag{3.6}$$

where n_0 is the initial number density of free charge carriers at $t = 0$.

Using **Equation 3.2** and **Equation 3.4**, the photogenerated charge-carrier density is proportional to the change in the photoconductivity (ΔS):

$$n = \Phi \, \mathrm{C} \, \Delta S(t) \tag{3.7}$$

where C = $\tilde{n}/\Delta S_0$ is the proportionality constant between the initial change in photoconductivity (ΔS_0) and absorbed photon density ($\tilde{n}$), given by:

$$\tilde{n} = \frac{E\lambda}{hcdA_{\mathrm{eff}}}(1 - R_{\mathrm{pump}} - T_{\mathrm{pump}}) \tag{3.8}$$

Substituting **Equation 3.8** into **Equation 3.5** gives:

$$\frac{d(\Delta S)}{dt} = -\Phi k_2 C \, (\Delta S)^2 \tag{3.9}$$

The global fits across all fluences to this ODE are used to extract the effective bimolecular recombination rate constant $\Phi \mathrm{k}_2$. Similar to the calculated mobilities, the values presented for k_2 are underestimates for the true intrinsic values.

To account for the spatially-varying charge-carrier density across the thickness of the film, the fitting algorithm considers an exponentially decaying charge-carrier density; done by dividing the film into 30 equally-thick slabs and individually computing the decay function for each slab.

Finally, the diffusion length L_{D} can then be calculated by using the diffusion coefficient *D* (calculated from the mobility) and recombination rate R_{n} (calculated from the recombination rates k_1, k_2, and k_3):

$$L_{\mathrm{D}} = \sqrt{\frac{D}{R_{\mathrm{n}}}} = \sqrt{\frac{k_{\mathrm{B}} T \mu}{e(k_1 + k_2 n + k_3 n^2)}} \tag{3.10}$$

where *T* is the temperature, and k_{B} is the Boltzmann constant, and *n* is the charge-carrier density photogenerated under normal operating conditions (1 sun) equalling roughly to $1\mathrm{x}10^{15}\ \mathrm{cm}^{-3}$, for which k_2 and k_3 make only small contributions.

3.3.2 – Nuclear Magnetic Resonance (NMR) and Nuclear Quadrupole Resonance (NQR) Spectroscopy

3.3.2.1 Liquid-state Nuclear Magnetic Resonance Spectroscopy.

For experiments represented in **Chapter 6**, **Figures 6.4, 6.6, 6.7, 6.9, 6.14**:

^{1}H-NMR spectra (in DMSO-d^6) were taken on a Bruker NMR spectrometer (300 MHz) at room temperature. Chemical shifts (δ) are reported in ppm. The signal from residual non-deuterated DMSO solvent is used for reference.

For experiments represented in **Chapter 6**, **Figures 6.11, 6.12**:

A two-channel Bruker Avance III HD Nanobay 400 MHz instrument running TOPSPIN 3 equipped with a 5 mm z-gradient broadband/fluorine observation

probe is used. The signal from residual non-deuterated DMSO solvent is used for reference.

For experiments represented in **Chapter 6**, **Figure 6.10**:

Spectra were acquired with a Bruker AVIIIHD 600 equipped with a BBO prodigy probe. Directionless enhancement of polarisation transfer (DEPT) experiments were carried out as described by Doddrell, et al.[26]

3.3.2.2 Solid-state Nuclear Magnetic and Quadrupole Resonance Spectroscopy

All measurements carried out by Dr Dominik Kubicki and Benjamin M. Gallant.

The single crystal samples were packed into a 1.3 mm (1 GHz, ^{1}H measurements), 3.2 mm (500 MHz, ^{14}N measurements) or 4 mm (600 MHz, ^{13}C measurements and ^{127}I NQR) zirconia rotors. The samples were compacted to enable stable spinning which necessarily led to the crystals being crushed. We note that the α-phase stability of all crystals is reduced by the crushing process. It is unclear if this is due to the application of pressure itself, or due to increased exposure to airborne moisture as a result of the increased surface area of the crushed material. We find that instantaneous phase degradation is suppressed by crushing in a N_2 glovebox, suggesting that moisture and/or oxygen play at least some role.

Solid-state MAS NMR spectra of ^{1}H (1000.4 MHz) were recorded on a Bruker Avance Neo 23.5 T spectrometer equipped with a 1.3 mm MAS probe using 100 kHz RF field amplitude. ^{1}H chemical shifts were referenced to TMS using the residual GBL signal as an internal reference (4.35 ppm for -CH_2-O-). Quantitative ^{1}H spectra were recorded using a recycle delay of 300 s (The

longest T_1 time of 40-50 s corresponded to the FA moieties). ^{1}H-^{1}H spin-diffusion spectra were recorded with a recycle delay of 2-3 s, mixing time of 2-3 s, and 600 slices in the indirect dimension. ^{13}C MAS spectra were recorded on a Bruker Avance III 11.7 T (150.7 MHz) spectrometer equipped with a 4 mm CPMAS probe using 71 kHz RF field amplitude, a recycle delay of 10 s, and referenced to solid adamantane (38.48 ppm for -CH_2-). 74 kHz ^{1}H decoupling was used. ^{14}N MAS spectra were recorded on a Bruker Avance III 11.7 T (43.3 MHz) spectrometer equipped with a 3.2 mm CPMAS probe using 25 kHz RF field amplitude, a recycle delay of 0.1 s, and referenced to solid adamantane using the ratio of gyromagnetic ratios in accordance with the IUPAC recommendation. The rotors were spun using dry nitrogen. ^{127}I NQR spectra were recorded on a Bruker Avance III spectrometer equipped with a 4 mm CPMAS probe using 42 kHz RF field amplitude, a recycle delay of 0.05 s with the probe placed outside the stray field of the magnet. For NQR measurements, the sample was static.

3.3.3 – X-ray Diffraction (XRD)

3.3.3.1 1D XRD

The 1D-XRD patterns were obtained with a Panalytical X'Pert Pro X-Ray diffractometer with $CuK_{\alpha 1}$ (1.54060 Å) source.

3.3.3.2 2D XRD

The 2D-XRD patterns using a Rigaku SmartLab X-ray diffractometer with $CuK_{\alpha 1}$ (1.54060 Å) source and a HyPix-3000 2D hybrid pixel array detector. A heating stage was employed in conjunction with the Rigaku SmartLab diffractometer for relevant measurements.

3.3.3.3 Single crystal X-ray diffraction (SCXRD)

All measurements carried out by Dr Matthias Gutmann. The following text was first drafted by Dr Matthias Gutmann and Dr Harry Sansom.

Single crystal X-ray diffraction (SCXRD) was collected on a Rigaku Oxford Diffraction XTaLAB Synergy diffractometer with Mo Kα (λ = 0.71073) wavelength, located in the laboratories at the ISIS Neutron and Muon Source, Oxfordshire, U.K. Crystal data was indexed and reduced using CrysalisPro and the structures solved using ShelXL implemented through Olex2. Before measuring the crystals, they were heated to 453 K (180 °C) in an N_2 stream for 2.5 minutes to convert any δ-$FAPbI_3$ decomposition products that may have formed during storage back in to the black 3D perovskite α-phase. They were then cooled back down to 290 K for data collection.

3.3.4 – Microscopy

3.3.4.1 Scanning Electron Microscopy (SEM)

A FEI Quanta 600 FEG Environmental Scanning Electron Microscope (ESEM) was employed to investigate perovskite layer morphology. Accelerating voltages between 4-15 kV were employed for various analyses.

3.3.4.2 Visible Light Microscopy (VLM)

Optical microscope images were taken on a Nikon Eclipse LV100ND microscope in transmission mode with Nikon TU Plan Fluor lenses (10x/0.30 A, 20x/0.45 A, 50x/0.60 B, 100x/0.90 A). The images are taken with an attached Nikon Digital Camera D6.10.

3.3.5 – Compositional Analysis

3.3.5.1 Thermal Desorption-Gas Chromatography-Mass Spectrometry (TD-GCMS)

Thin layers (<1 μm) of perovskite material on fluorine-doped tin oxide-coated glass substrates were loaded into a thermal extractor unit (Micro-Chamber/Thermal Extractor M-CTE250, Markes International) and heated at 165 °C for 60 minutes under a flow of N_2 gas (50 mL min^{-1}). Volatile components released during extraction were collected onto sorbent-packed collection tubes. The sorbent tubes are then loaded into a thermal desorption unit and heated rapidly to desorb the volatiles concentrated in the tube, which are then passed *via* N_2 carrier gas into the gas chromatography-mass spectrometry instrument (Agilent 5977B GC/MSD). Identification of the volatile components was done by comparison to the NIST 17 Mass Spectral Library. All reported species showed a >85% match with the database compound. MS results the received a <85% identification score against the NIST 17 library are considered to be unknown/unidentifiable, and the corresponding to peaks in the GC trace are unlabelled.

Prior to use, a chamber blank was taken, on each of the four thermal extraction (TE) chambers used. When taking the blank an uncoated FTO/glass substrate was loaded into the TE chamber and heated at 165 °C for 60 minutes under a flow of N_2 gas (50 mL min^{-1}). Any volatile components desorbed from the substrate/chamber were collected by the collection tubes, which were subsequently subjected to TD-GCMS analysis (as described above) and the resulting GC traces from the four chambers taken as a background for all subsequent measurements of samples collected from each of the chambers. The sorbent material itself within the tubes is made up of a range of highly porous adsorbent materials such as silica gel, activated charcoal, MOF structures, and a range of organic polymers and plastics. These materials are

susceptible to trace decomposition themselves, in particular the organic materials. This leads to the presence of common plastic decomposition products (e.g. acrylates, phthalates) in the GC trace of the blank. These materials may not always be produced in identical quantity during the subsequent measurement of samples, and so, when the blank GC trace is subtracted from the sample GC trace, negative peaks may appear in the final, corrected trace. Similarly, such decomposition products may be produced in greater quantities during some sample measurements and thus not be corrected for by the reference GC trace and appear as substantial contaminants. Where the mass spectra of these achieve >85% identification score against NIST 17, they are identified in in **Figure A5.3**.

The chambers were heated to 300 °C and purged with N_2 gas between TE of different samples to eliminate cross contamination between samples.

3.3.5.2 Electron Probe Microanalysis (EPMA)

All measurements carried out by Dr Andrew Matzen and Benjamin M. Gallant.

Electron probe micro-analyses were performed on a Cameca SX-5 FEG in the Department of Earth Sciences at the University of Oxford. Samples were mounted in epoxy resin, ground flat and polished under oil, using a combination of silicon carbide and diamond laps. Samples were coated with ~20 nm of carbon to minimise any charge build-up during the analysis. A 15 kV accelerating voltage was employed, with beam currents between 20 and 24 nA and a nominal spot size of 10 μm. Cl, I, and Pb were quantified using NaCl, Tl(Br,I), and galena (PbS) standards respectively. On-peak counting times for Cl (Kα) and Pb (Mα) were 60 s and 45 s for I (Lα), with half of on-peak counting

times at each of the high and low background positions. Using these conditions the observed intensity of I X-rays is time-dependent, decreasing somewhat throughout the analysis. Thus, we applied a time dependent intensity (TDI) correction (e.g., Nielsen et al.[27]) to the I X-ray intensity whereby the on-peak intensity was sub-divided into 22 equal time segments and the count-rate extrapolated back to the intensity at the start of the analysis (T=0). An overlap correction of Pb (Mα) on Cl (Kα) was corrected using nominally Cl-free galena. The concentration of hydrogen, carbon, and nitrogen were added as knowns (based on an approximately pure FA^+ organic composition) to the f(rz) matrix-correction routine employed.

3.3.6 – Characterisation of Solar Cells

3.3.6.1 Current-voltage (J–V) and maximum power point (MPP) measurements

Current-voltage (J–V) and maximum power point (MPP) measurements were measured (2400 series source meter, Keithley Instruments) in ambient air under both light (simulated AM 1.5 irradiance generated by a Wavelabs SINUS-220 simulator) and in the dark. The active area of the solar cell was masked with a black-anodised metal aperture to either 0.25 or 1.00 cm^2, within a light-tight holder. The ‘forward’ J–V scans were measured from short-circuit to forward bias and the ‘backward’ scans were from forward bias to short-circuit, both at a scan rate of 245 mVs^{-1}. Active MPP tracking measurements using a gradient descent algorithm were performed for at least 30 s to obtain the steady-state power conversion efficiency. Some cells exhibited improvement over multiple measurements, in which case the peak performance was reported. This typically took two to five J–V scan plus MPP tracking iterations

for the highest efficiency cells, in a measurement time of around 2–5 minutes. The intensity of the solar simulator was set periodically such that the short-circuit current density from a KG3-filtered Si reference photodiode (Fraunhofer ISE) matched its 1-sun certified value. A local measurement of the intensity before each batch of solar cell measurements were performed, was made by integrating the spectrum obtained from the solar simulator's internal spectrometer. By taking the ratio of this internal intensity measurement to one obtained at the time of calibration we determined the equivalent irradiance at the time of measurement. For the data presented in this publication, this gave values ranging from 0.985-1.005 suns equivalent, which have been applied to the calculation of power conversion efficiencies for each individual measurement. The spectral mismatch factor was estimated to be 1.022 according to a previously reported method[28]. This has also been applied to calculate power conversion efficiencies. We estimate the systematic error of this setup to be on the order of ± 5% (relative).

3.3.6.2 External Quantum Efficiency (EQE)

External quantum efficiency (EQE) measurements were performed using a custom setup. The solar cells were illuminated with a 250 W quartz-tungsten halogen lamp that was first passed through a monochromator (Princeton Instruments SP2150) with a filter wheel (Princeton Instruments FA2448), then chopped with an optical chopper (Thorlabs MC2000B) at 280Hz, and finally focussed onto the sample with a smaller spot size than the solar cell area (as defined by the metallic top contact). The amplitude of the resulting AC current signal was measured with a lock-in amplifier (Stanford Research Systems SR830) as the voltage drop across a 50 Ohm resistor in series with the solar

cell. A reference measurement of a calibrated Si photodiode of known EQE (Thorlabs FDS100-CAL) was used to correct the measured signal from the solar cell to absolute units. White light bias was applied using LEDs.

3.4 – Bibliography

1. Kim, M. *et al.* Methylammonium Chloride Induces Intermediate Phase Stabilization for Efficient Perovskite Solar Cells. *Joule* 1–14 (2019).
2. Gutierrez-partida, E. *et al.* Large-grain double cation perovskites with 18 μs lifetime and high luminescence yield for efficient inverted perovskite solar cells. *ACS Energy Lett. (3)* **6**, 1045-1054 (2021).
3. McMeekin, D. P. *et al.* A mixed-cation lead mixed-halide perovskite absorber for tandem solar cells. *Science (6269).* (2016).
4. Min, H. *et al.* Efficient, stable solar cells by using inherent bandgap of a-phase formamidinium lead iodide. *Science (6466).* **366**, 749–753 (2019).
5. Xu, J. *et al.* Triple-halide wide-band gap perovskites with suppressed phase segregation for efficient tandems. *Science (6482).* **367**, 1097–1104 (2020).
6. Saliba, M. *et al.* Cesium-containing triple cation perovskite solar cells: Improved stability, reproducibility and high efficiency. *Energy Environ. Sci.* **9**, 1989–1997 (2016).
7. Holzhey, P. *et al.* A chain is as strong as its weakest link – Stability study of $MAPbI_3$ under light and temperature. *Mater. Today* **29**, 10–19 (2019).
8. Noel, N. K. *et al.* A low viscosity, low boiling point, clean solvent system for the rapid crystallisation of highly specular perovskite films. *Energy Environ. Sci.* **10**, 145–152 (2017).
9. Nayak, P. K. *et al.* Mechanism for rapid growth of organic-inorganic halide perovskite crystals. *Nat. Commun.* **7**, 1–8 (2016).
10. Wenger, B. *et al.* Consolidation of the optoelectronic properties of $CH_3NH_3PbBr_3$ perovskite single crystals. *Nat. Commun.* **8**, 590 (2017).
11. Han, Q. *et al.* Single Crystal Formamidinium Lead Iodide (FAPbI3): Insight into the Structural, Optical, and Electrical Properties. *Adv. Mater.* **28**, 2253–2258 (2016).
12. Steele, J. A. *et al.* Direct Laser Writing of δ- To α-Phase Transformation in Formamidinium Lead Iodide. *ACS Nano* **11**, 8072–8083 (2017).
13. Kontos, A. G. *et al.* Halogen-NH2+ Interaction, Temperature-Induced Phase Transition, and Ordering in $(NH_2CHNH_2)PbX_3$ (X = Cl, Br, I) Hybrid Perovskites. *J. Phys. Chem. C* **124**, 8479–8487 (2020).
14. Erkılıç, U., Ji, H. G., Nishibori, E. & Ago, H. One-step vapour phase growth of two-dimensional formamidinium-based perovskite and its hot carrier dynamics. *Phys. Chem. Chem. Phys.* **22**, 21512–21519 (2020).
15. Driscoll, E. H., Orera, A., Anderson, P. A., Sanjuán, M. L. & Slater, P. R. Raman spectroscopy insights into the α- And δ-phases of formamidinium lead iodide ($FAPbI_3$). *Dalt. Trans.* **50**, 3315–3323 (2021).
16. Ibaceta-Jaña, J. *et al.* Hidden polymorphism of $FAPbI_3$ discovered by Raman spectroscopy. *Phys. Chem. Chem. Phys.* **23**, 9476–9482 (2021).
17. Wright, A. D. *et al.* Ultrafast Excited-State Localization in $Cs_2AgBiBr_6$ Double Perovskite. *J. Phys. Chem. Lett.* **12**, 3352–3360 (2021).
18. Lindsey, C. P. . & Patterson, G. D. Detailed comparison of the Williams–Watts and Cole–Davidson functions. *J. Chem. Phys.* **73**, 3348–3357 (1980).
19. Lim, J. *et al.* Long-range charge carrier mobility in metal halide perovskite thin-films and single crystals via transient photo-conductivity. *Nat. Commun.* **13**, 1–9 (2022).
20. Lim, J. *et al.* Elucidating the long-range charge carrier mobility in metal halide perovskite thin films. *Energy Environ. Sci.* **12**, 169–176 (2019).

21. Longo, G. *et al.* Understanding the Performance-Limiting Factors of Cs2AgBiBr6Double-Perovskite Solar Cells. *ACS Energy Lett.* **5**, 2200–2207 (2020).

22. Savill, K. J. *et al.* Impact of Tin Fluoride Additive on the Properties of Mixed Tin-Lead Iodide Perovskite Semiconductors. *Adv. Funct. Mater.* **30**, 1–13 (2020).

23. Yamada, Y., Nakamura, T., Endo, M., Wakamiya, A. & Kanemitsu, Y. Photocarrier recombination dynamics in perovskite $CH_3NH_3PbI_3$ for solar cell applications. *J. Am. Chem. Soc.* **136**, 11610–11613 (2014).

24. Yamada, Y., Endo, M., Wakamiya, A. & Kanemitsu, Y. Spontaneous defect annihilation in CH3NH3PbI3 thin films at room temperature revealed by time-resolved photoluminescence spectroscopy. *J. Phys. Chem. Lett.* **6**, 482–486 (2015).

25. Joyce, H. J., Boland, J. L., Davies, C. L., Baig, S. A. & Johnston, M. B. A review of the electrical properties of semiconductor nanowires: Insights gained from terahertz conductivity spectroscopy. *Semiconductor Science and Technology* **31**, (2016).

26. Doddrell, D. M., Pegg, D. T. & Bendall, M. R. Distortionless enhancement of NMR signals by polarization transfer. *J. Magn. Reson.* **48**, 323–327 (1982).

27. Nielsen, C. H. & Sigurdsson, H. Quantitative methods for electron microprobe analysis of sodium in natural and synthetic glasses. *Am. Mineral.* **66**, 547–552 (1981).

28. Snaith, H. J. How should you measure your excitonic solar cells? *Energy Environ. Sci.* **5**, 6513–6520 (2012).

Chapter 4 – A green solvent system for templated deposition of formamidinium lead trihalide perovskite solar cells

The work in this chapter is adapted from: “A green solvent system for templated sequential deposition of stable formamidinium lead triiodide for perovskite solar cells”, Benjamin M. Gallant, Philippe Holzhey, Saqlain Choudhary, Karim A. Elmestekawy, Joel A. Smith, James M. Ball, M. Greyson Christoforo, Pietro Caprioglio, Laura M. Herz, Henry J. Snaith (*Under review*).

4.1 – Introduction

N,N-dimethylformamide (DMF) is highly toxic[1], yet remains the primary solvent employed in the overwhelming majority of solution-processed perovskite solar cells (PSCs) reported to-date achieving >21% steady-state power conversion efficiency[2,3]. However, as solution processing at industrial scale dictates that the majority of solvents employed must be volatilised into the atmosphere[1], the hazard of employing toxic solvents becomes ever more problematic as PSCs are industrialised. In light of this, several DMF-free solvent systems have been established for perovskite solution processing, notably based on *N*-methylpyrrolidone (NMP)[4], γ-butyrolactone (GBL)[5], 2-methoxyethanol (2ME)[6] and acetonitrile (ACN) in combination with methylamine gas[7]. However, as **Figure 4.1a** shows, NMP, 2ME and ACN do not provide the desired reduction in toxicity, while GBL is an illegal narcotic on account of its metabolite, γ-hydroxybutyrate (GHB)[8,9]. Furthermore, the use of MA gas as a co-solvent poses further problems of volatility, where escape of the MA gas can render

the solution unstable and pose a toxicology risk itself. Moreover, while dimethyl sulfoxide (DMSO) – the typical companion to DMF in perovskite solution processing – is non-toxic as a neat liquid, in the context of lead salt solvation DMSO's proficiency as a percutaneous absorption (skin-penetration) enhancer[10,11] is of acute concern for at-scale processing (**Figure 4.1b**).

Solvent selection is also critical in directing and controlling perovskite crystallisation. A range of perovskite solvate intermediates have been reported, including PbI_2•$(Sol)_n$ (Sol = DMSO[12], DMF[12], NMP[13]; n = 1, 2), $MA_2Pb_3I_8$•2DMSO[14], $FA_2Pb_3I_8$•4DMF[13,15] and $(Sol)_nFAPbI_3$ (Sol = DMF, NMP; n = 1, 2)[16]. Control of the growth of these intermediates can be achieved by a range of means including manipulating precursor solvent mixture, substrate or solution temperature, or concentration. Meanwhile, conversion of such intermediates to the desired perovskite phase by subsequent application of heat[17], antisolvent[5], solutions containing A-site halides[18] (such as formamidinium iodide, FAI), or combinations thereof, is then controlled in order to induce optimal material properties. Perhaps the most limiting of these properties is the inherent instability of metal halide perovskites, particularly under external stimuli including heat, light and moisture. Here we develop a novel approach to perovskite processing in which conventional solvate intermediate phases are replaced by a solid-state 2D perovskite material, which we show serves as a templating layer directing the subsequent growth of α-$FAPbI_3$ perovskite. We not only find that α-$FAPbI_3$ fabricated *via* this process performs effectively in PSCs (**Chapter 4**), but that 2D-templated growth imbues α-$FAPbI_3$ with substantially improved ambient, thermal and photostability in comparison to ubiquitous DMF:DMSO solvated, anti-solvent engineered processing routes (**Chapter 5**). Our development of a processing route that shares very little in common with conventional perovskite fabrication further

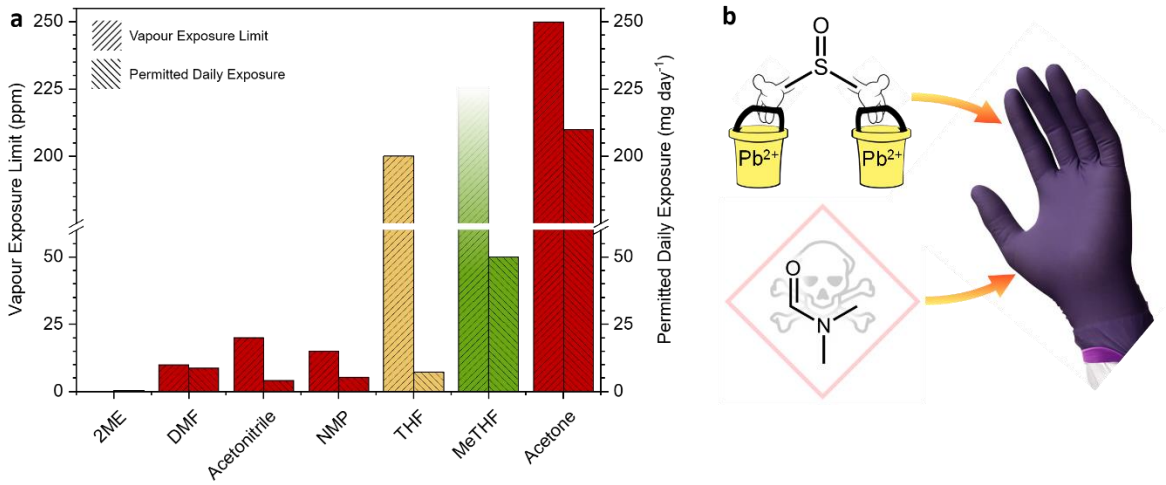


Figure 4.1 | Scalable processing compatibility. a, Preferential properties of THF and MeTHF as solvents in industrial processes where vapour phase exposure is unavoidable. Solvents shown in green are produced industrially from biorenewable sources, in yellow may be produced biorenewably but typically are not, and in red cannot be produced from renewable sources. No vapour exposure limit (VEL) has yet been legislated for MeTHF, however the significantly higher permitted daily exposure (PDE) limit and similar vapour phase properties of MeTHF compared with THF validate our assumption that MeTHF's VEL will be at least comparable to that of THF[8,9]. **b**, Schematic demonstrating toxicity dangers concerning lead salt-containing DMF (carcinogen) and DMSO (skin-penetration enhancer) solvents.

enables us to disentangle many variables of processing that impact perovskite stability and begin to demonstrate why conventional processing methods are fundamentally part of the perovskite stability problem.

4.2 – A biorenewable, low toxicity solvent system

The integral role of precursor solution chemistry in controlling the outcome of perovskite solution deposition has often been overlooked. Research has repeatedly shown that coordination complexes formed dynamically in such solutions directly influence the nucleation and growth of the perovskite layer, and thus on its crystallinity, morphology and optoelectronics[19–21]. Direct crystallisation of precursor solutions has demonstrated that metal-solvent coordination interactions are sufficiently robust to be retained into the solid-state and are therefore presumed to likewise play an important role controlling haloplumbate intermediates in parent solutions and during crystallisation[19]. A range of approaches to pseudo-quantify solvent coordinating ability

have been reported, including dielectric constant, Hansen solubility parameters, Mayer bond order and the Gutmann donor number (D_N) (**Table 4.1**). Although no single metric is expected to perfectly characterise the complex range of precursor-solvent interactions, perovskite solvent systems reported to-date appear to be best represented by D_N[22,23]. D_N is defined as negative of the enthalpy value (kcal mol^{-1}) for 1:1 adduct formation between the Lewis base in question and the standard Lewis acid $SbCl_5$ solvated by noncoordinating 1,2-dichloroethane. That the donor number shows the strongest correlation with successful perovskite solvation suggests that the Lewis acid-base interaction between metal and solvent is the most significant for precursor dissolution and control of subsequent solution-state interactions. Moreover, out of the drive towards DMF-free processing, new and general models for perovskite solvation are beginning to crystallise. In reporting their DMSO/ACN/2-methoxyethanol (2-ME) ternary solvent mixture, Deng, et al., identified the role of two solvent classes; DMSO as a non-volatile coordinating solvent and both ACN and 2-ME as volatile non-

Solvent	D_N / kcal mol^{-1}	MBO	ε	δ_P / $MPa^{1/2}$
BA	42.0	-	4.92	-
DMPU	33	-	36.1	-
DMSO	29.8	1.50	46.7	16.4
NMP	27.3	1.90	32.2	12.3
DMF	26.6	1.88	36.7	13.7
THF	20.0	-	7.6	-
GBL	18.0	1.99	40.2	16.6
ACN	14.1	3.03	37.5	18.0
MeTHF	12.0	-	7.0	-
NME	2.7	-	35.9	-

Table 4.1 | Perovskite solvents. Table summarising solvents reported to date commonly used in dissolution of lead (II) salts during lead halide perovskite solution processing. D_N = Gutmann donor number, MBO = Mayer bond order, ε = dielectric constant, δ_P = Hansen solubility parameter for dipolar intermolecular interactions, BA = *n*-butylamine, DMPU = *N*,*N′*-dimethylpropyleneurea, DMSO = dimethylsulfoxide, NMP = *N*-methylpyrrolidone, DMF = dimethylformamide, THF = tetrahydrofuran, GBL = γ-butyrolactone, ACN = acetonitrile, MeTHF = 2-methyltetrahydrofuran, NME = nitromethane.

coordinating solvents[6]. The key differentiator between solvents of these two classes is D_N (**Table 4.1**).

Although Deng, et al.'s claim that ACN and 2-ME are non-coordinating should be contested (as these solvents are at least capable of dissolution-reprecipitation type processes and thus catalyse the conversion of perovskite precursors, $AX + BX_2$, into ABX_3 powders) we recognise in this analysis the potential for a general family of co-solvent systems. Here we present novel binary solvent systems consisting of biorenewable cyclic ethers and alkylamine liquids, in which the latter serves both as a coordinating co-solvent and as an additive within the perovskite lattice. These systems can be considered part of this family of solvent mixtures all comprising poorly Pb^{2+}-coordinating solvents as the majority component alongside strongly Pb^{2+}-coordinating solvents[6]. Here cyclic ethers take on the role of the poorly coordinating solvent while butylamine (BA), which is liquid at room temperature, acts as the strongly coordinating solvent. We find that both tetrahydrofuran (THF) and 2-methyltetrahydrofuran (MeTHF) are suitable poorly-coordinating solvents, however we focus especially on the latter on account of its biorenewable production, significantly lower toxicity and favourable vapour pressure for scalable solution processing. Vidal, et al.[1], recently highlighted that THF's high vapour pressure renders its lifetime environmental impact relatively large compared with less volatile perovskite solvents due to additional greenhouse gas emissions resulting from energy-intensive solvent recapture. However, a lifecycle analysis of MeTHF conducted by Slater, et al.[24], demonstrated a 97% reduction in lifetime emissions associated with the use of MeTHF as compared to THF, due mostly to its biorenewable production and significantly lower vapour pressure. Moreover, MeTHF has recently been recommended by both the European Medicines Agency (EMA) and the Food and Drug Administration (FDA) as a Class 3

solvent (“solvents with low toxic potential”) with a permitted daily exposure (PDE) limit of 50 mg day^{-1} [8]. This exposure limit is much higher than that of THF (7.2 mg day^{-1}), which Vidal, et al.[1], demonstrate already possesses significant toxicological advantages over other common perovskite solvents (**Figure 4.1a**). *n*-Butanol, which we employ as a solvent in the second step of the perovskite deposition is also a Class 3 solvent, with PDE > 50 mg day^{-1} [8]. Furthermore, as solution processing demands that the majority of solvents employed are volatilised, the other safety-critical parameters for at-scale processing are the vapour exposure limit and the lower flammability limit. To our knowledge, no vapour exposure limit has yet been legislated upon for MeTHF. However, the seven-fold improvement in permitted daily exposure and similar vapour phase properties of MeTHF compared with THF validate our presumption that MeTHF’s vapour exposure limit will be at least comparable to that of THF (200 ppm) if not significantly higher; a substantial improvement on DMF (10 ppm). The lower flammability limit of all solvents commonly used for perovskite processing are comparable. Extended discussion of these parameters is offered in **Appendix A4.1** (p116). Besides these, the critical advantage of both THF and MeTHF over the previously reported ACN systems is that use of highly volatile MA gas is precluded. We have experienced persistent challenges of ambient MA volatilisation from solutions co-solvated by this amine.

4.3 – 2D-templated growth of 3D perovskites

Notwithstanding the volatility of MA, amines hold their own critical advantage against other Lewis basic Pb^{2+}-coordinating solvents; they also behave as Brønsted-Lowry bases in precursor solutions. In our newly developed system, the inclusion of BA alongside methylammonium iodide (MAI) leads to a Brønsted-Lowry H^+ exchange in solution – on account of the higher pK_{aH} of BA compared to MA – and the in-situ

production of *n*-butylammonium (BA^+). We dissolve MAI and lead (II) iodide in our MeTHF:BA solvent system and cast a thin layer by spin-coating and drying at 70 °C for ten minutes. Incorporation of both BA^+ and methylammonium (MA^+) within the perovskite lattice leads to highly crystalline 2D Ruddlesden-Popper phase perovskites (RPPs) based on the $(BA^+)_2(MA^+)_{n-1}Pb_nI_{3n+1}$ family, where BA^+ serves as the large A-site cation (A') and MA^+ as the small A-site cation (A)[25] (**Figure 2.2**). The *n* described by this empirical formula is often used to differentiate RPP phases by the number (n) of lead-halide octahedral planes interspersed with layers of the large A' cations. In steady-state photoluminescence (PL), X-ray diffraction (XRD) and absorbance measurements, which we show in **Figure 4.2**, we observe multiple peaks consistent with the presence of multiple RPP phases. By varying BA:MA^+ precursor stoichiometry ($R_{BA\text{-}MA+}$ = [BA]/[MA^+]) we are able to control the average RPP phase composition, denoted <*n*> (**Appendix A4.2**, p118).

Although 2D RPPs – and in particular 2D-3D RPP phase mixtures – have been utilised as photo-absorbers in efficient PSCs, these typically display non-ideal bandgaps for use in single-junction photovoltaics[26]. Instead we propose an alternative application of 2D mixed-phase RPPs; as solid-state intermediates in a solution-processed sequential deposition of 3D perovskites. Among the advantages of the sequential processing approach, the ease with which haloplumbate intermediates might be controllably and rationally designed is pivotal. Intermediates featuring coordinating solvents such as DMSO and NMP have proven popular, however relatively little is yet understood regarding how such species arise or are transformed into 3D perovskites[4,27,28].

To convert the RPP materials into 3D α-$FAPbI_3$ layers, we dispensed a solution of formamidinium iodide (FAI) in *n*-butanol on top of the substrate and allowed

conversion *via* cation exchange to occur over a controlled time before spin-coating. In **Figure 4.3a** we present the PL spectra of precursor RPP films as a function of conversion time. **Figure 4.3b** tracks the corresponding evolution of absorbance during conversion. As FA^+ cations intercalate into the 2D material, we observe a gradual

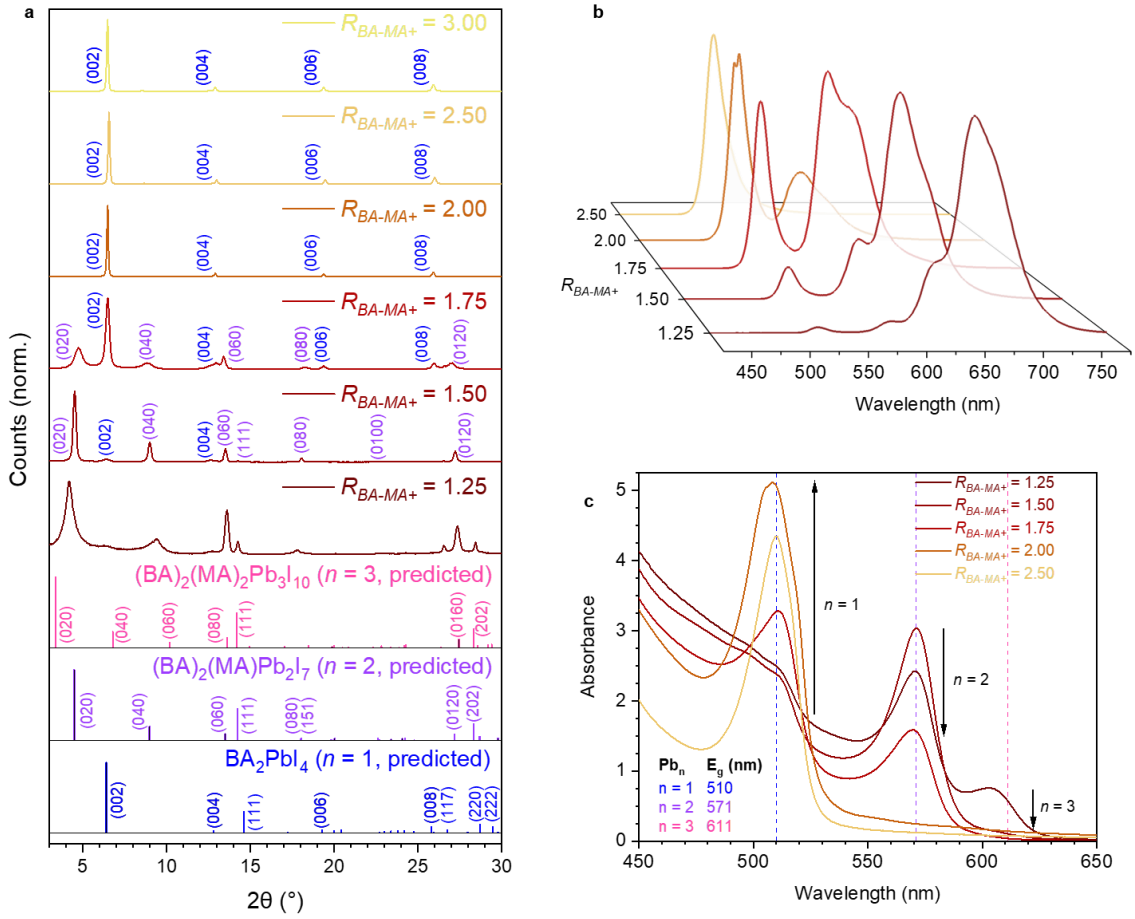


Figure 4.2 | Mixed-phase 2D templates. X-ray diffraction (XRD) patterns (**a**), steady-state photoluminescence (SSPL) emission spectra (normalised) (**b**) and absorbance spectra (**c**) corresponding to phase-mixed 2D RPP ($BA_2MA_{n-1}Pb_nI_{3n+1}$) layers processed from MeTHF. R_{BA-MA+} = [BA]/[MA^+]. Reflections have been assigned with the (hkl) set of planes that gives rise to them, from a given pure *n* 2D RPP phase, based on powder diffraction patterns of the *n* = 1-3 phases simulated using VESTA software and crystal structures reported by Stoumpos, et al.[41] Assignments are not presented in the case of the R_{BA-MA+} = 1.25 template as they are uncertain in some cases. Apparent shifts in the (0k0) planes of the *n* = 2 phase are unaccounted for but may indicate either the introduction of anisotropic strain into the material, or the nanoscale intermixing of higher *n* phases. The latter explanation is consistent with the substantially increased FWHM of XRD peaks observed for this template, and with the appearance of absorbance features below the bandgap of the *n* = 2 phase. Bandgaps (E_g) overlayed on the absorbance spectra shown are also taken from Stoumpos, et al.[52] The inconsistency in apparent phase composition between SSPL and XRD measurements is likely due to a combination of photon-recycling effects and charge carrier thermalisation, leading to lower bandgap phases being overrepresented in emission spectra.

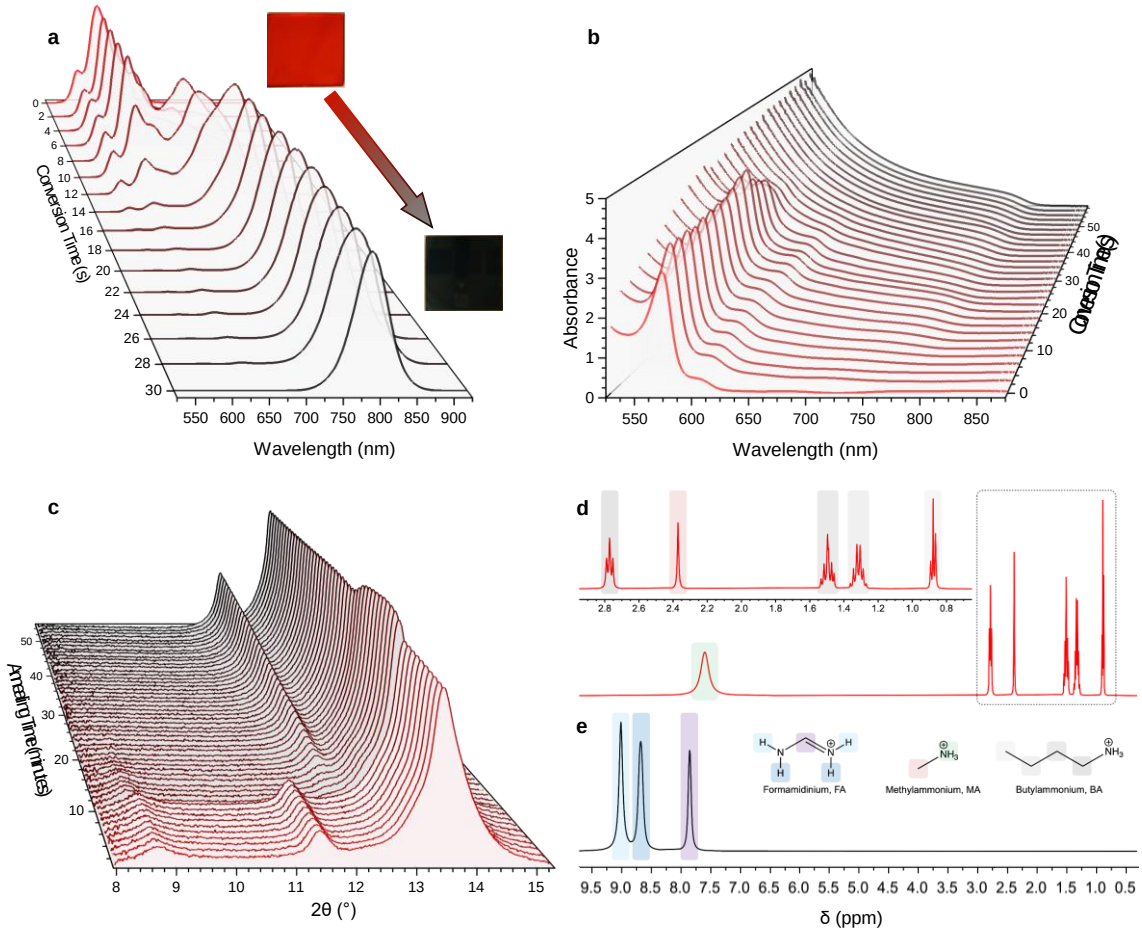


Figure 4.3 | Templated 2D to 3D (^{t}2D-3D) conversion. Tracking photoluminescence (normalised) (**a**) and absorbance (**b**) of optimised 2D template ($R_{BA\text{-}MA+}$ = 1.5) converting to 3D α-$FAPbI_3$ during soaking in conversion solution. Unconverted 2D intermediate shown at t = 0 s. Insets: images of thin layers of 2D template (red) and 3D (black) perovskites. (**c**) In-situ X-ray diffraction (XRD) patterns tracking removal of remnant 2D material and subsequent ripening of ^{t}2D-3D ($R_{BA\text{-}MA+}$ = 1.5) α-$FAPbI_3$ under thermal annealing at 70 °C for 10 minutes, followed by 180 °C. Intensity is plotted vertically as a log scale. ^{1}H solution Nuclear Magnetic Resonance (NMR) spectra of (**d**) 2D template ($R_{BA\text{-}MA+}$ = 1.5) (inset shows expanded region of spectrum corresponding to methyl and methylene signals, highlighted in dashed box) and (**e**) ^{t}2D-3D α-$FAPbI_3$.

reduction in the PL intensity at the original emission wavelengths and the emergence of longer wavelength emission features. We interpret this to be due to FA^+ exchanging with MA^+ and BA^+ and at first increasing the <*n*>-value in the now "triple cation" RPP perovskite, before the resultant film becomes close to entirely α-$FAPbI_3$. After spin-coating to remove the majority of the excess conversion solution, subsequent thermal annealing completes conversion to the 3D perovskite, driving out remnant BA^+ and MA^+. **Figure 4.3c** shows in-situ XRD analysis during the thermal annealing. ^{1}H solution

NMR spectroscopy measurements of the α-$FAPbI_3$ layers dissolved in DMSO-d^6 (**Figure 4.3d-e**) confirm the absence of residual MA^+. We have therefore demonstrated the BA/MA RPP perovskite as a 'template' for the growth of the 3D α-$FAPbI_3$ material. We refer to this from hereon as templated 2D to 3D (^{t}2D-3D) conversion.

4.4 – Investigating '2D-templated' growth

Scanning electron microscopy (SEM) images of α-$FAPbI_3$ processed *via* a range of 2D templates of varying <*n*> reveal a wide variety of microstructures. Use of high ratio of BA to MA ($R_{BA\text{-}MA+}$) (low <*n*>) 2D templates resulted in a mesoporous structure in the 3D perovskite layer (**Figure 4.4a-b**), and even macroscopic cracking of the thin-films (**Figure 4.4a**, inset). XRD analysis of α-$FAPbI_3$ processed from intermediate $R_{BA\text{-}MA+}$ ratios reveals how gradual reduction of $R_{BA\text{-}MA+}$ (toward higher <*n*>) leads to a pronounced increase in lead (II) iodide (PbI_2) content in the as annealed films (**Figure 4.5c**). We observe a consistent trend with the appearance of hexagonal PbI_2 platelets, which appear brighter in the SEM images (**Figure 4.4c-g**)[29]. Similar to the effect observed for low-*n* templates, conversion from high-*n* 2D perovskites also leads to mesoscopic porosity visible *via* SEM (**Figure 4.4h**). However, in contrast to low-*n* template use, XRD analysis of low-*n*-converted 3D materials demonstrates significant PbI_2 content. In **Figure 4.5c** we show the ratio of peak areas between the peak corresponding to the (001) of PbI_2 and the (100) of α-$FAPbI_3$, which we take as a metric for comparing the relative quantities of these two phases in final converted material, as the 2D template is varied. We rationalise these observations by considering the careful balance of factors that control optimum <*n*> for ^{t}2D-3D conversion.

Ideally BA^+ content in the RPP layer should be minimised to both diminish the need for subsequent BA^+ extraction, and minimize the volume change upon conversion. The low lead halide density of 2D templates rich in the *n* = 1 phase demands significant

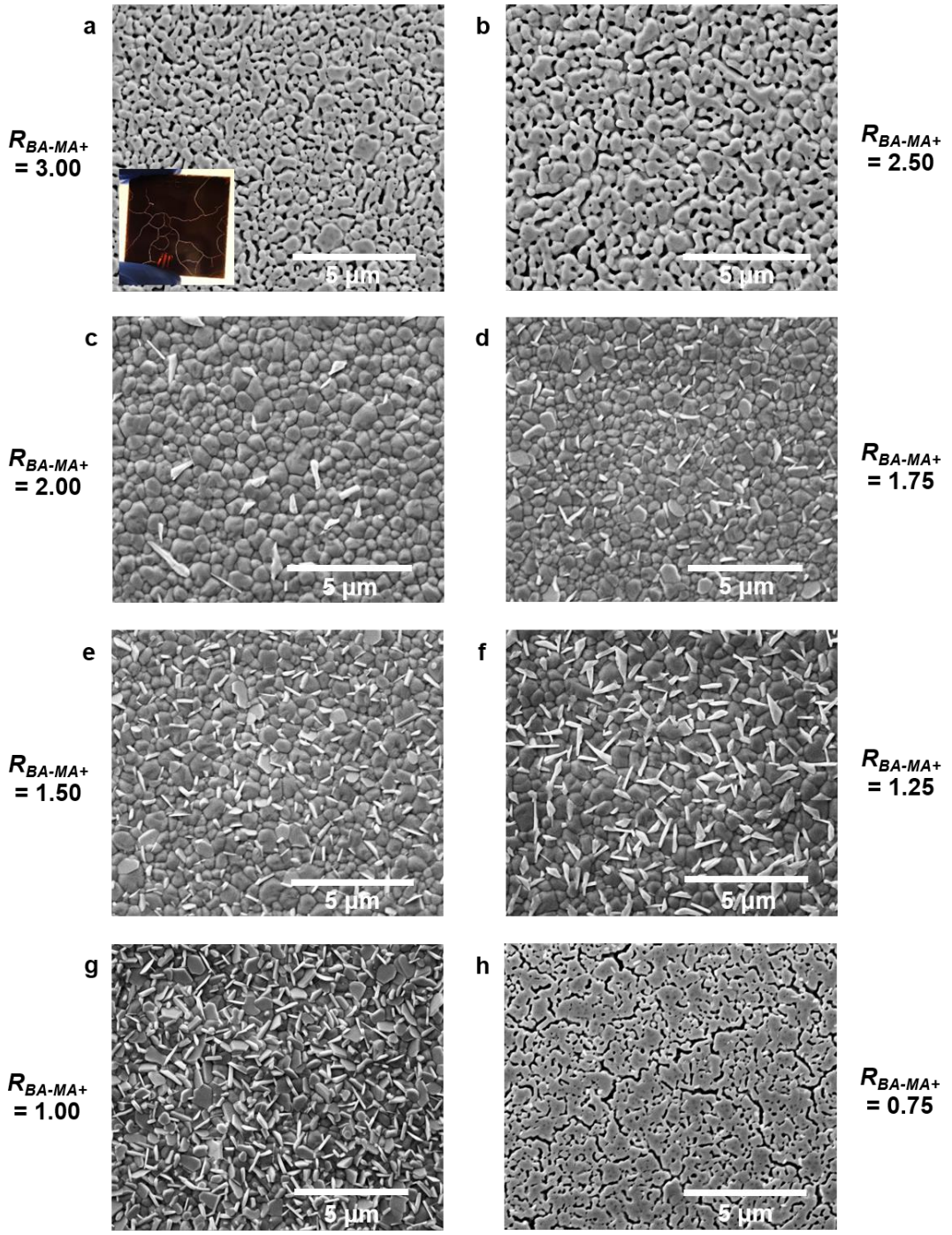


Figure 4.4 | Optimising 2D template. Scanning Electron Microscopy (SEM) images showing the microstructure of ^{t}2D-3D α-$FAPbI_3$ layers when a series of 2D templates processed from THF with varying $R_{BA\text{-}MA+}$ are converted sequentially. $R_{BA\text{-}MA+}$ = (**a**) 3.00 (inset: photograph showing macroscopic cracking of 3D perovskite layers converted from $R_{BA\text{-}MA+}$ = 3.00 intermediates due to extreme volume contraction), (**b**) 2.50, (**c**) 2.00, (**d**) 1.75, (**e**) 1.50, (**f**) 1.25, (**g**) 1.00, (**h**) 0.75.

volume contraction in order to form a continuous lattice of 3D corner-sharing lead-halide octahedra. Where the strain required for uninterrupted fusion of adjacent 2D lead-halide layers into a 3D lattice is too large, this may be relieved by pores and

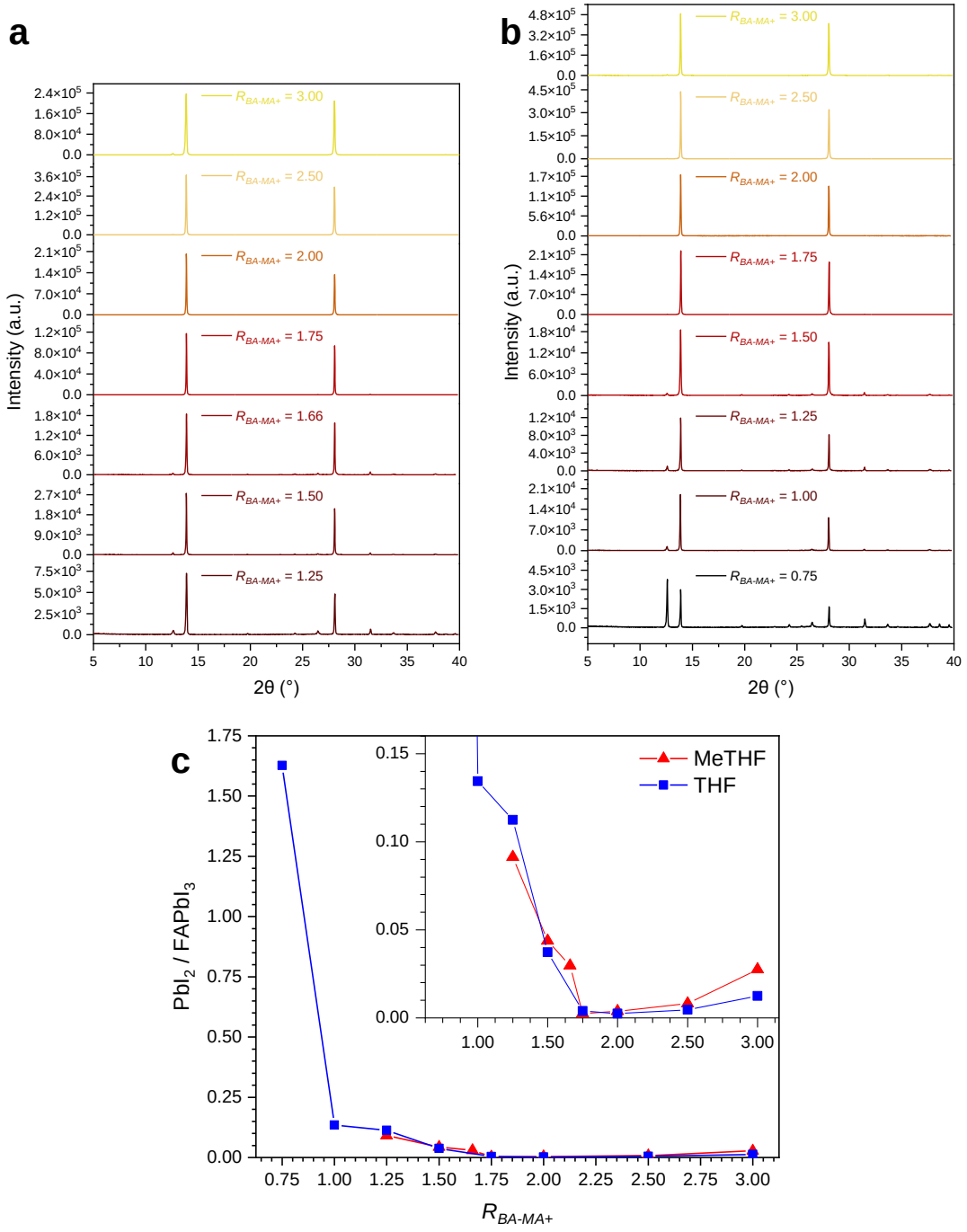


Figure 4.5 | Template-dependent lead (II) iodide content. X-ray diffraction (XRD) patterns of ^{t}2D-3D α-$FAPbI_3$ layers produced when a series of 2D templates processed from MeTHF (**a**) and THF (**b**) with varying $R_{BA\text{-}MA+}$ are converted sequentially. (**c**) Plot showing lead iodide (PbI_2) content as a phase fraction in comparison to ^{t}2D-3D α-$FAPbI_3$ extracted from XRD diffraction patterns (**a**, **b**) *via* peak integration of PbI_2 (001) and α-$FAPbI_3$ (100) scattering peaks. Inset shows expanded view for low-PbI_2 region.

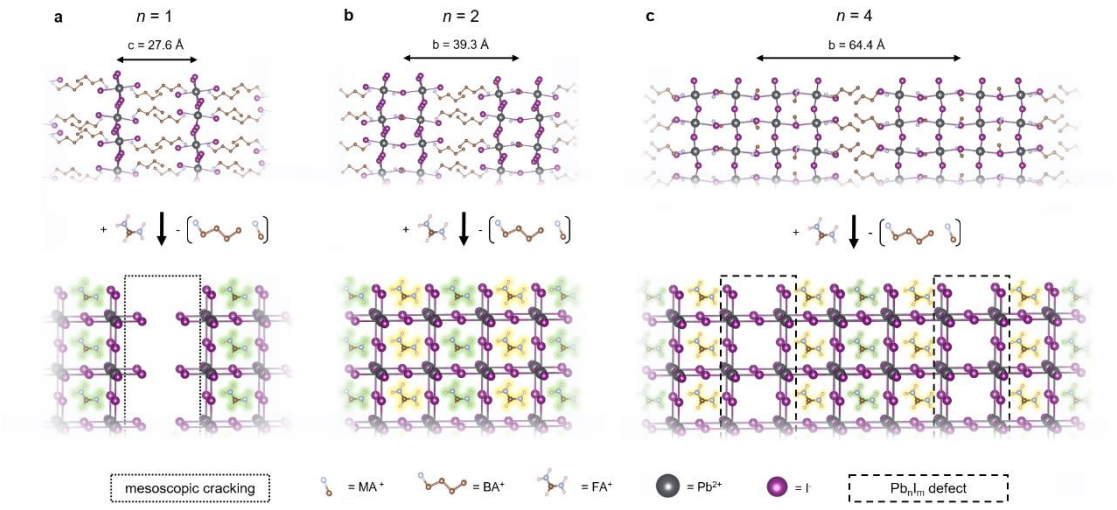


Figure 4.6 | Optimal 2D template. Schematic diagrams depicting the conversion of (**a**) BA_2PbI_4 (*n* = 1) (**b**) $BA_2MAPb_2I_7$ (*n* = 2), and (**c**) $BA_2MA_3Pb_4I_{13}$ (*n* = 4) into 3D α-$FAPbI_3$. FA^+ highlighted in green has replaced BA^+ in the organic channels of the 2D template, while FA^+ highlighted in yellow has replaced MA^+ in the inorganic layers. Double-headed arrows display layer thickness. We highlight that this is a schematic representation only, not based on calculations, and constructed using VESTA software using .cif files taken from the publication of Stoumpos, et al.[52]

cracks opening within the perovskite film, at the expense of increased surface area and hence surface free energy. **Figure 4.6a** presents schematically how such features may occur. Observation of mesoscopic cracking in **Figure 4.4a-b** thus underscores the importance of minimising volume contraction by employed 2D templates containing *n* > 1 phases.

Mechanistic rationalisation of the microstructures observed in 3D-converted high *n* (low $R_{BA\text{-}MA+}$) templates is more involved. However, we propose that two controlling criteria are critical; organic channel density and the thickness of the corner-sharing haloplumbate layers in the 2D template. To demonstrate the integral role organic channels play in effecting conversion, we attempt the conversion of pure $MAPbI_3$ (representing $(BA^+)_2(MA^+)_{n-1}Pb_nI_{3n+1}$ with $n = \infty$) with our 0.1 M FAI solution in *n*-butanol. **Figure 4.7a** shows the absorption spectra of this '$MAPbI_3$ template' and material resulting from its attempted conversion. The presence of an absorption feature corresponding to PbI_2 in the converted layer, and the blue-shifted absorption

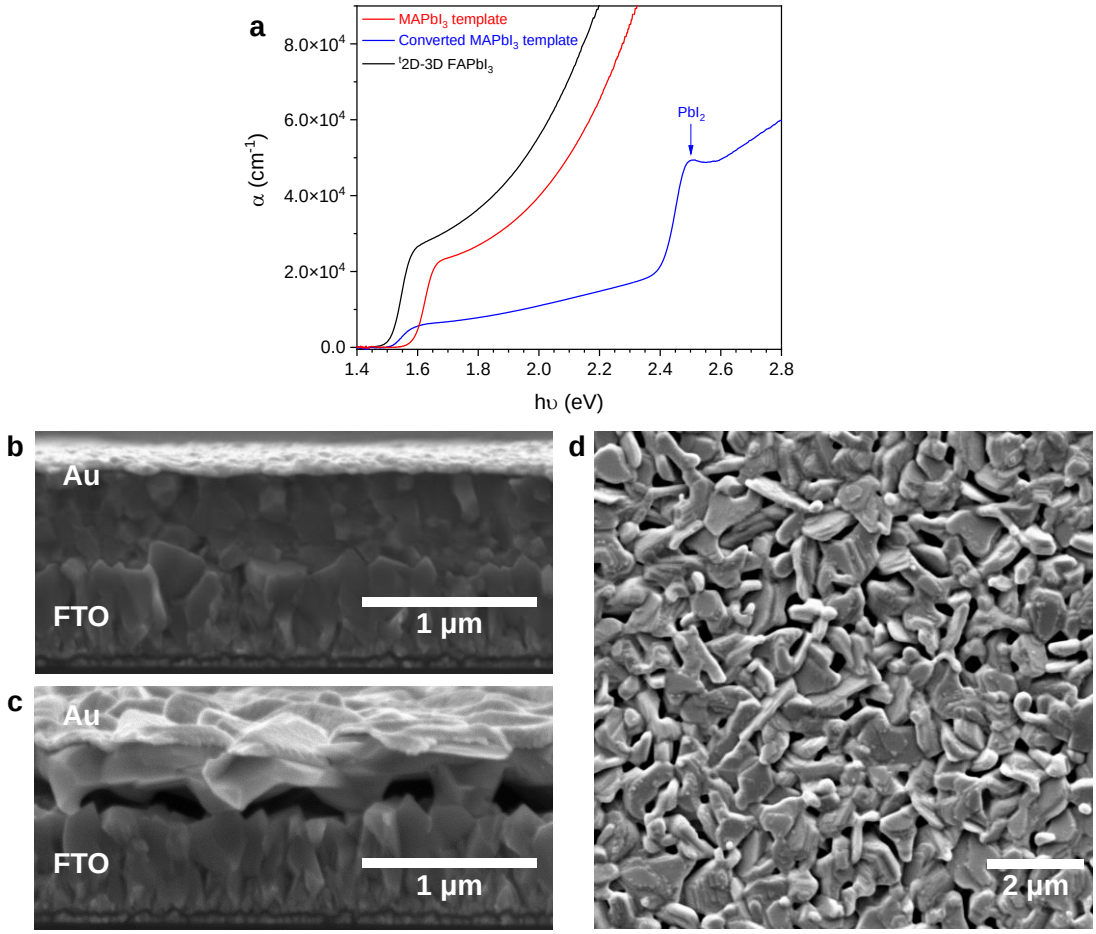


Figure 4.7 | Unsuccessful *n* = ∞ ($MAPbI_3$) template. **a**, Absorption coefficient spectra corresponding to a $MAPbI_3$ layer (500 nm thickness, processed *via* acetonitrile/methylamine gas) (red) serving as the *n* = ∞ member of the $BA_2MA_{n-1}Pb_nI_{3n+1}$ family of templates and undergoing an attempted conversion to α-$FAPbI_3$ (blue) (cured at 180 °C for 30 minutes). ^{t}2D-3D α-$FAPbI_3$ is shown for comparison (black). The band-edge of converted $MAPbI_3$ template indicates that complete conversion to lower-bandgap $FAPbI_3$ has not been achieved. Moreover, the appearance of an absorption feature corresponding to PbI_2 indicates incomplete conversion has been achieved. Cross-sectional scanning electron microscopy (SEM) images of $MAPbI_3$ template (**b**) and converted $MAPbI_3$ template (**c**). **d**, Top view SEM image of converted $MAPbI_3$ template.

onset as compared to α-$FAPbI_3$, indicate that complete conversion of the $MAPbI_3$ template has not been achieved. This is as expected; *n*-butanol does not significantly disrupt inorganic haloplumbate structures, thus cation intercalation and extraction is expected to be facilitated by – and occur most rapidly *via* – the organic channels found only in our 2D perovskite templates. Thus, reduction of organic channel density by reducing BA^+ content in a template (towards low $R_{BA\text{-}MA+}$) limits cation exchange, ultimately leading to severely limited conversion in the $MAPbI_3$ template. In **Figure 4.7b-c** we show cross-sectional SEM images of the $MAPbI_3$ template, and the

converted template, revealing the formation of significant voids at the bottom of the perovskite layer during conversion.

In addition to the effect of reduced organic channel density, thicker inorganic layers found in higher *n* RPPs render cation exchange within the 2D templates' lead-halide scaffold more challenging. For $n > 2$ phases, complete extraction of MA^+ from and intercalation of FA^+ cations into the intact inorganic scaffold requires migration across multiple perovskite A-sites, penetrating through layers of Pb^{2+} cations that act as an energetic barrier to this ion movement on account of their charge. Any MA^+ not extracted from the converted template could be expected to volatilise during subsequent thermal curing at 180 °C, *via* mechanisms discussed in **Section 5.3.** As **Figure 4.7c** describes schematically, such a process would yield Pb^{2+} and I^--rich regions in the forming 3D perovskite, and ultimately regions of crystalline PbI_2 upon grain ripening during thermal curing. This proposed mechanism is not only consistent with the gradual increase in PbI_2 content observed in converted $1.00 \leq R_{BA\text{-}MA+} \leq 1.75$ templates, but also justifies the extreme increase in PbI_2 observed for $R_{BA\text{-}MA+} < 1$. XRD of the same series of 2D perovskites (**Figure 4.5b**) revealed that the $R_{BA\text{-}MA+}$ = 0.75 template as the only one to contain majority $n \geq 4$ RPP phases. Furthermore, in an effect similar to that observed for low-*n* templates, volume contraction anticipated by this mechanism upon conversion from high-*n* 2D perovskites to PbI_2-rich material may also lead to mesoscopic cracking on account of the significantly smaller unit cell volume of lead (II) iodide compared with mixed-phase $(BA^+)_2(MA^+)_{n-1}Pb_nI_{3n+1}$ perovskites[26,30]. Thus, our proposed mechanism is consistent with the microstructure observed for $R_{BA\text{-}MA+}$ = 0.75 (**Figure 4.4h**). PbI_2 formation and associated lattice contraction is likely also responsible for the voids observed at bottom of our converted '$MAPbI_3$ template', and microstructure observed in top view SEM (**Figure 4.4f-g**).

The mechanics of ^{t}2D-3D growth require significant further investigation. However, overall it is clear that, unlike intermediates featuring coordinating solvents or other lower-dimensionality materials reported to-date[31–33], the $\langle n \rangle > 1$ RPPs reported here hold two critical advantages as sequential deposition intermediates for 3D perovskites: an extended corner-sharing haloplumbate lattice already present in the intermediate ready to serve as a scaffold for 3D perovskite growth; and built-in organic channels within the lead-halide scaffold that can facilitate intercalation of a conversion solution containing A-type cations. As we show, the presence of the pre-existing corner-sharing lead-halide scaffold is imperative for effective conversion, minimising lattice rearrangement and volume contraction during formation of the 3D cubic perovskite. In effect the 2D RPPs act not simply as intermediates – such as those in conventional sequential processing, whose primary role is to supply solvent-coordinated lead (II) halide complexes – but as templates for the subsequent growth of the 3D perovskite.

4.5 – ^{t}2D-3D α-$FAPbI_3$: Optoelectronic and photovoltaic performance

To investigate if our ^{t}2D-3D α-$FAPbI_3$ films have useful optoelectronic properties, we compare them with α-$FAPbI_3$ perovskites fabricated *via* two conventional solution processing approaches utilising DMF:DMSO solvent mixtures; with and without methylammonium chloride (MACl) additive[34]. MACl has been shown to improve perovskite material quality, stability and optoelectronic performance[34–36]. Time-resolved PL measurements reveal an order of magnitude improvement in PL lifetime for ^{t}2D-3D α-$FAPbI_3$ compared with MACl-free $FAPbI_3$, and a factor of three enhancement compared to MACl-additive $FAPbI_3$ (**Figure 4.8a-c, g**). By fitting fluence-dependence of PL decays from films of the three materials (**Figure 4.8a-c**), we determine a reduction in the monomolecular trap-assisted recombination rate constant, implying suppression of non-radiative recombination centres. Notably, for

the conventional MACl-free $FAPbI_3$, much higher excitation fluences and charge-carrier densities are required for recombination dynamics to transition from a "trap-mediated" monomolecular decay regime to intrinsic bimolecular radiative recombination[37–39]. To probe the charge carrier mobility of these materials, we performed optical-pump-terahertz-probe (OPTP) photoconductivity spectroscopy (**Figure 4.8d-f**) measurements. We determine that the effective sum of mobilities

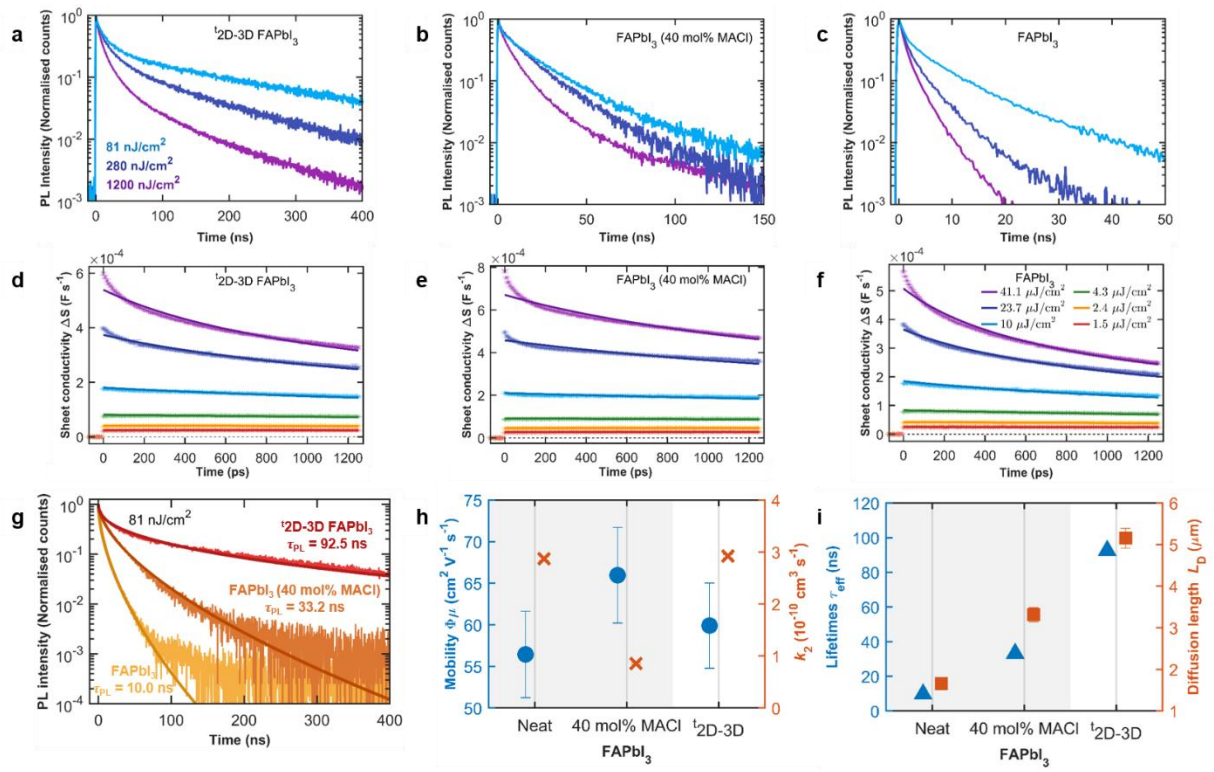


Figure 4.8 | Optoelectronic performance. *All samples prepared by B. Gallant. All measurements and analysis carried out by K. Elmestekawy.* Fluence dependence of the time-resolved photoluminescence (PL) transients after 398-nm excitation (2.5 MHz repetition rate) for thin films of t2D-3D $FAPbI_3$ (**a**), $FAPbI_3$ (40 mol% MACl additive) (**b**), and additive-free $FAPbI_3$ (**c**). PL was detected at 810 nm. The time scale is changed for composition for best visual clarity of the fluence-dependence transients. The legend in **a** also applies to **b**, and **c**. Optical-pump THz-probe photoconductivity (OPTP) transients for t2D-3D $FAPbI_3$ (**d**) $FAPbI_3$ (40 mol% MACl additive) (**e**), and additive-free $FAPbI_3$ (**f**). Solid lines are the global fits to solutions of the rate equation expressed in **Chapter 3, Eq. 3.5**. The legend in **f** also applies to **d** and **e**. **g**, Summary of time-resolved PL transients of $FAPbI_3$ materials made using different fabrication methods. PL lifetimes, τ_{PL}, determined by stretched exponential fits are shown on the figure labelling. Solid lines are stretched-exponential fits to the measured data. Charge-carrier recombination and mobility parameters extracted from OPTP (**h**), and TRPL (**i**) spectroscopy. Effective mobilities $\Phi\mu$ and the bimolecular recombination rate k_2 are extracted from the measured onset value of the photoconductivity, and from global fits to the photoconductivity transients, respectively. PL lifetimes τ_{eff} are extracted from the TRPL fits (at an excitation fluence of 81 nJ cm^{-2}) and diffusion lengths L_D are derived under normal solar operating conditions of charge-carrier densities of n ~ 10^{15} cm^{-3}.

(electron and hole) and the bimolecular recombination rate k_2 of charge carriers, are largely unaffected by differences in film fabrication (**Figure 4.8h**). All the $FAPbI_3$ films that we study here have a very high mobility of approximately 60 $cm^2\ V^{-1}\ s^{-1}$, which are some of the highest such values reported for thin layer $FAPbI_3$ and attest to the generally high quality of the fabricated layers[40]. However, as a result of the highly effective suppression of trap-mediated charge-carrier recombination, $FAPbI_3$ fabricated *via* the ^{t}2D-3D approach achieves a significantly improved charge-carrier diffusion length under solar illumination conditions of 5.3 ± 0.2 μm, significantly higher than that for either $FAPbI_3$ material processed from DMF:DMSO (1.7 ± 0.2 μm and 3.3 ± 0.2 μm for neat and MACl-containing $FAPbI_3$) (**Figure 4.8i**). We describe all spectroscopic measurements and calculations in detail in **Chapter 3.3.1**.

In order to determine if the improved optoelectronic properties of the ^{t}2D-3D α-$FAPbI_3$ films translate into improved PSCs we fabricated n-i-p structured devices composed of FTO / SnO_2 / ^{t}2D-3D α-$FAPbI_3$ / PEAI passivation / spiro-OMeTAD / Au, which we show a cross-sectional SEM image of in **Figure 4.9f**. In **Figure 4.9a-d** we show the current-voltage curves and maximum power point tracked efficiency (η_{mpp}) for champion devices of both 0.25 cm^2 and 1 cm^2 respectively, and determine a η_{mpp} of 20.1% and 18.4% respectively. In **Figure 4.9e** we present the distribution of optimised 0.25 cm^2 and 1.00 cm^2 PSCs fabricated from ^{t}2D-3D α-$FAPbI_3$. As the crystallisation of the perovskite layer, its microstructure, and therefore also the interfaces it forms with adjacent charge transport layers are all determined by the solvent system employed, development of an entirely new solvent mixture and approach to 3D perovskite growth is expected to require substantial optimisation to achieve high performance PSCs. Therefore, the most appropriate point for comparison of the performance of these cells is against other PSCs fabricated via low toxicity or DMF-

and DMSO-free processes. To the best of our knowledge, there has been just one report employing MeTHF as a solvent for perovskite materials. In 2021 A. Doolin, et

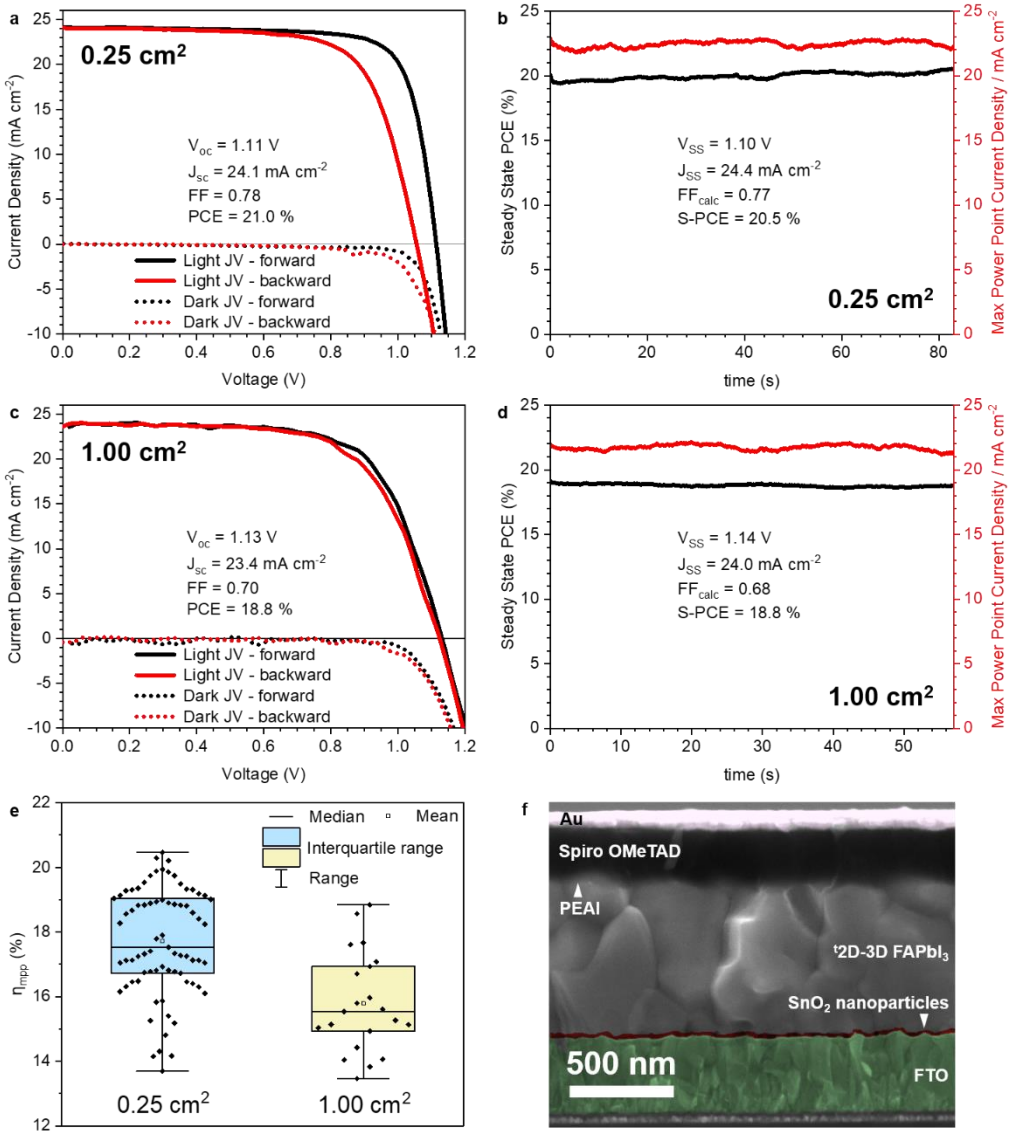


Figure 4.9 | PSC operational performance. J-V characteristics and corresponding maximum power point tracked efficiency (η_{mpp}) and current density (J_{mpp}) measured at maximum power point for champion devices fabricated from ^{t}2D-3D α-$FAPbI_3$ with illuminated area 0.25 cm^2 (**a-b**) and 1.00 cm^2 (**c-d**). Light J-V and η_{mpp} measurements were performed under simulated AM1.5 100.7 $mWcm^{-2}$ irradiance, accounting for the spectral mismatch factor. J_{sc} = short-circuit current density, V_{oc} = open-circuit voltage, FF = fill factor, V_{mpp} = maximum power point voltage. **e**, Distribution of highest performing ^{t}2D-3D α-$FAPbI_3$ 0.25 cm^2 (75 cells) and 1.00 cm^2 (21 cells) solar devices fabricated *via* our optimised recipe across three representative batches during this work, containing a total of 87 small area (0.25 cm^2; 14% excluded) and 29 large area (1.00 cm^2; 28% excluded) cells. Devices with maximum power point tracked efficiency (η_{mpp}) below 13% are considered not representative as they fall below 67% of the champion performance (interpreted as the maximum performance achievable by a fully optimised solar cell fabricated by our method), and thus are excluded. **f**, Cross-sectional scanning electron microscopy image of PSC fabricated utilising ^{t}2D-3D α-$FAPbI_3$.

al. reported a quaternary solvent blend including MeTHF (40% DMSO, 30% DMPU[10], 20% MeTHF, 10% EtOH) to solubilise $MAPbI_3$ and fabricated solar cells achieving champion efficiency (reverse scan) of 16.1%[41]. Other attempts to use ether solvents have included THF/2-ME[11] and THF/EtOH solvent blends, both allowing one-step depositions of $MAPbI_3$ and achieving 17.1% (stabilised)[42] and 19.5% (stabilised)[43] PCE, respectively. A similar approach reported by Y. Deng, et al blending ACN and 2-ME with a small volume% of DMSO boosted the efficiency of DMF-free coated $MAPbI_3$ to an impressive 21.3% (reverse scan)[6]. However, as with the ACN/MA solvent route originally developed in our group[7], upon which this work is based, all these approaches are limited to the archetypal $MAPbI_3$ perovskite. As has been shown, employing A-site cations besides MA^+, such as FA^+ and Cs^+, offer significant advantage in particular for thermal stability[44] and bandgap engineering[45]. As such, besides in absolute performance, our MeTHF/BA sequential deposition route to $FAPbI_3$ represents a substantive improvement in this regard. Ionic liquids have recently been developed as promising perovskite solvents beyond $MAPbI_3$. In particular, methylammonium formate has recently been used to solvate a one-step deposition of $(FA_xMA_{1-x})PbI_3$ that has achieved a remarkable 23.7% (stabilised) efficiency. It is not yet clear what the toxicological implications of at-scale processing from ionic liquid solvents might be, however these impressive initial results certainly warrant further study. However, perhaps the most impressive performance achieved by a PSC fabricated via DMF- and DMSO-free solvent systems reported to-date is from a recent work by the group of Seok and co-workers. By mixing EtOH with DMA (*N*,*N*-dimethylacetamide) in a 2:1 ratio and employing a range of alkyammonium chlorides the authors were able to

[10] DMPU = dimethylpropyleneurea
[11] 2-ME = 2-methoxyethanol

deposit $FAPbI_3$ by a one-step method and achieve efficiencies up to 25.1% (reverse scan). Such impressive results demonstrate that, with a well-optimised solar cell architecture, use of non-conventional perovskite solvent systems can be used to produce perovskite materials of comparable quality to those fabricated from DMF:DMSO. It is, however, notable that in this case DMA is a direct analogue of DMF with a PDE of 10.9 mg day^{-1}, very similar to that of DMF (8.8 mg day^{-1}), and thus is likely not suitable for at-scale processing. In this context, the new low toxicity solvent system presented here allowing access to $FAPbI_3$-based perovskites, and the n-i-p PSC performance achieved, are a promising contribution to the ongoing work in the field toward scalable solution processing of perovskite solar cells.

4.6 – Conclusion and outlook

We have presented a novel solvent system based on a volatile, biorenewable solvent, and a sequential deposition route offering a number of crucial advantages for scalable PSC fabrication. In particular, the substitution of DMF (permitted daily exposure limit = 8.8 mg day^{-1}) with biorenewably produced MeTHF (permitted daily exposure limit = 50 mg day^{-1}) represents a substantial improvement in the scalability of perovskite solution processing. However, although MeTHF is extremely promising as a poorly Pb^{2+}-coordinating solvent for perovskite precursors, the requirement to blend the liquid with a second, highly coordinating solvent to achieve full solvation is both a limitation and an opportunity for further improvement. Here we have relied upon butylamine as the co-solvating agent, introducing limitations on toxicity and necessitating a 2D RPP intermediate material. As we show, by retaining the pre-existing extended haloplumbate lattice present in 2D RPP perovskites upon subsequent conversion, we are able to employ such materials as highly effective templates for 3D perovskites.

However, future investigation in pursuit of non-toxic, high volatility coordinating solvents could produce a truly green solvent system compatible with at-scale processing in air. Nonetheless, here we show impressive optoelectronic properties and competitive PSC device efficiencies via the ^{t}2D-3D approach from MeTHF/BA, particularly considering demonstrated absence of MA^{+} in the final 3D perovskite material.

Appendix A4.1: Solvents for scalable processing

A critical factor that has often been missed in assessing the suitability of a solvent for solution-processing applications is that the majority solvents necessarily must go through the vapour phase during extraction from the deposited layers. The more efficient the deposition technique is in minimising volume of wasted precursor ink, the higher the relative volume of solvent that must be vaporised (i.e. not lost as liquid phase precursor solution). The important implication of this observation is that most available solvent selection guides – which are typically based on pharmaceutical applications, where solvents are expected to remain in the liquid phase – are inappropriate aides in the selection of scalable solvent systems for solution processing.

Two commonly cited solvent selection guides are presented by Prat, et al.[46,47], and have been relied upon in a number of perovskite green solution processing reports[1,41,48]. However, Prat, et al., introduce a 'Safety' rating for common pharmaceutical solvents, which is principally based on the solvents' flash points; the lowest temperature at which its vapours ignite in the presence of an ignition source. Critically, the flash point is strongly dependent on the vapour pressure of the solvent. The higher the vapour pressure, the higher the proportion of a given volume of the (liquid) solvent that is expected to exist as vapours at the surface of the liquid, at a given temperature. As a result, solvents with high vapour pressures (THF, MeTHF, ACN) score poorly on such safety ratings. However, as the majority of liquid solvents – regardless of vapour pressure – must pass into the vapour phase during the solution processing of a thin film by scalable deposition techniques, flash point is clearly an inappropriate measure of relative solvent safety.

There is certainly an inflammation hazard associated with vaporised solvents. However, the most relevant vapour pressure-independent measure is the lower flammability limit (LFL), measured as the lowest v/v% of the flammable solvent in air that's capable of igniting. To our knowledge, no LFL has yet been determined for MeTHF, but for vast majority of common solvents (DMSO, DMF and THF included) the LFL is between 1 and 4% (**Table A4.1**).

Moreover, besides LFL the other key flammability concern for solution processing is the autoignition temperature (T_a) of solvent (mixtures) employed. As **Table A4.1** shows, the T_a for DMSO is relatively close to its boiling point. Wang, et al., have also reported that the onset temperature for exothermic decomposition events in solutions of DMSO is reduced by other chemicals including halides and a number of acids and bases[11]. Along with the skin-penetrating enhancement of DMSO, these findings show how – despite its widely positive reception – there are significant concerns regarding the use of this solvent in at-scale solution processing.

Table A4.1 | Scalable perovskite solution processing. Parameters of significance for scalable solution processing for a range of solvents relevant to this work. LFL = lower flammability limit, T_a = autoignition temperature, PDE = permitted daily exposure. Note: a high value of 'Safety Score' corresponds to nominally 'less safe' solvent (see discussion above).

Solvent	Prat, et al., Safety Score [47]	Boiling Point / °C [47]	Vapour Pressure / hPa at 20 °C [48]	Flash Point / °C [47]	LFL / % by volume of air [50]	T_a / °C [50]	PDE / mg day^{-1} [8,9]
THF	6	66	200	-14	2	321	7.2
MeTHF	6	80.2	136	-11	unknown	270	50
DMSO	1	189	3.5	95	2.6	215	>50
DMF	3	153	0.6	58	2.2	445	8.8
***n*-butanol**	3	118	5.8	35	1	343	>50

Appendix A4.2: Relating $R_{BA\text{-}MA+}$ to <*n*>

<*n*> is determined by considering the molar ratio of BA^+ to MA^+ in the deposited RPP material. As such, although correlated, the precise relationship between $R_{BA\text{-}MA+}$ and the value of <*n*> for a given phase mixture is not straightforward. The inequivalent pK_{aH}'s of BA and MA and the apparent preferential formation of the thermodynamically favoured *n* = 1 phase in the RPP layers[51] result in significantly greater BA^+ inclusion than suggested by the precursor stoichiometry ($R_{BA\text{-}MA+}$). By dissolving RPP layers processed with varying $R_{BA\text{-}MA+}$ in deuterated DMSO we conduct ^1H solution Nuclear Magnetic Resonance (NMR) spectroscopy measurements (**Figure A4.1**). From integration of signals corresponding to BA and MA we determine the BA^+:MA^+ stoichiometry in the deposited RPP layers and thus calculate true <*n*> values. A full description of the relationship between <*n*> and BA^+:MA^+ stoichiometry is provided below. For the convenience of the reader, however, in this work we describe the mixed-phase RPPs in terms of $R_{BA\text{-}MA+}$.

For a 2D phase mixture containing phases $n = 1, 2, 3 \ldots \mathrm{p}$, with each phase present in corresponding mole fraction $a, b, c \ldots q$ such that:

$$a + b + c + \cdots + q = 1 \tag{4.1}$$

where a is the mole fraction of $n = 1$ phase present, b is the mole fraction of $n = 2$ phase present, etc., then overall the phase mixture may be represented as:

$$< n > = a + 2b + 3c + \cdots + pq \tag{4.2}$$

From our ^1H NMR experiments we are able to determine, by integration of the signals corresponding to the MA^+ and BA^+ methyl groups (δ = 2.38 (s), 0.89 (t) ppm,

respectively), the molar proportion of BA^+ to MA^+ present in each 2D RPP template, which we denote R_{exp}. Thus, for the 2D RPP family $BA_2MA_{n-1}Pb_nI_{3n+1}$, this quantity may be calculated as:

$$R_{exp} = \frac{[BA^+]}{[MA^+]} = \frac{2a + 2b + 2c + \cdots + 2q}{b + 2c + \cdots + [p-1]q} \tag{4.3}$$

Combining **Eq. 4.1** and **Eq. 4.3**:

$$R_{exp} = \frac{2}{b + 2c + \cdots + [p-1]q} \tag{4.4}$$

Thus, by expressing **Eq. 4.2** in the form:

$$< n > = (a + b + c + \cdots + q) + (b + 2c + \cdots + [p-1]q) \tag{4.5}$$

and combining **Eq. 4.1**, **Eq. 4.4** and **Eq. 4.5**, it is clear that:

$$< n > = 1 + 2{R_{exp}}^{-1} = 1 + \frac{2[MA^+]}{[BA^+]} \tag{4.6}$$

for any mixture of RPP phases.

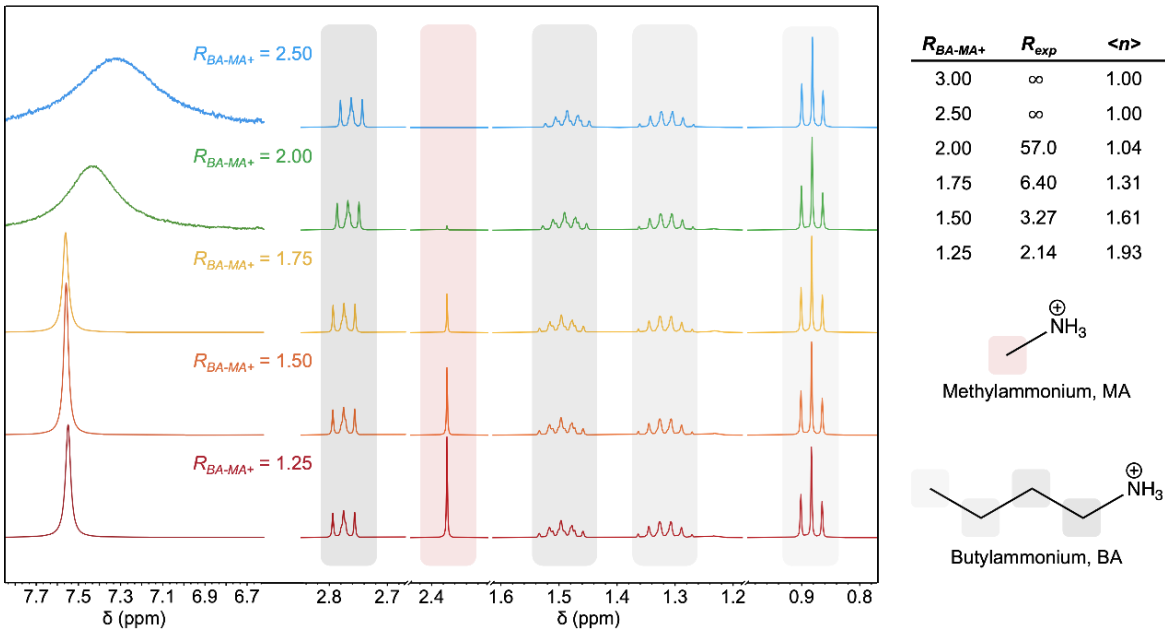


Figure A4.1 | Determining 2D template composition. ^{1}H solution Nuclear Magnetic Resonance (NMR) spectra of mixed-phase $BA_2MA_{n-1}Pb_nI_{3n+1}$ RPP layers dissolved in d^6-DMSO. Integration of the signals corresponding to MA's and BA's methyl groups (δ = 2.38 (s), 0.89 (t) ppm, respectively) confirm the reduction in BA:MA ratio in the deposited thin films as $R_{BA\text{-}MA+}$ is reduced, and are used to calculate the true molar ratio of BA^+ to MA^+ in the deposited RPP material (R_{exp}). From this analysis we calculate the true <*n*> value of the mixed-phase layers.

Figure A4.2 maps the true values for <*n*> calculated by applying **Eq. 4.6** to the experimental data provided in **Figure A4.1**. In the region $R_{BA\text{-}MA+} \leq 2$ the incorporation of MA^+ – despite the thermodynamic preference for the *n* = 1 phase (containing no MA^+), and despite a film growth environment in which more than sufficient BA^+ is available to crystallise the thermodynamically favoured *n* = 1 phase (note: the *absolute* molar quantities of all precursors in the 50 uL of precursor solution used in spin-coating the 2D RPP layers is much greater than those found in the subsequently deposited layer, suggesting none is ever limiting during crystallisation other than in a kinetic regime) – suggests that crystallisation is kinetically controlled and thus that composition is a function of the relative likelihood of the immediate coordination environment of Pb^{2+} ions in the precursor solution containing BA^+ or MA^+ cations. As pK_{aH} (BA) < pK_{aH} (MA) we expect for $R_{BA\text{-}MA+} > 2$ the Pb^{2+} coordination environment to contain on average at least 2 BA^+ cations and so formation of the thermodynamically

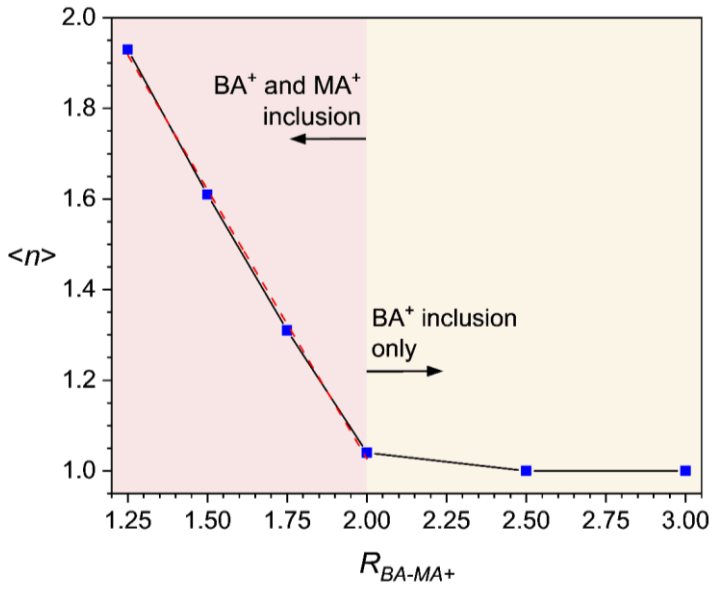


Figure A4.2 | Controlling 2D template composition. Relationship between BA:MA^+ precursor stoichiometry, $R_{BA\text{-}MA+}$, and average *n* phase of 2D RPP materials, <*n*>.

preferred *n* = 1 phase is not kinetically prohibited. Thus, the experimentally determined values for <*n*> in this region all reflect near phase-pure *n* = 1 RPPs.

For $R_{BA\text{-}MA+} \leq 2$, we expect the Pb^{2+} coordination environment to contain on average < 2 BA^+ cations and so crystallisation under kinetic control results in the incorporation of a proportion of MA^+, despite this being thermodynamically disfavoured. Fitting of the region where $R_{BA\text{-}MA+} \leq 2$ shows a strong linear relationship with slope = -1.19. A slope of -1 would imply equal preference for MA^+ and BA^+ in this BA^+-limited regime. Instead the slope suggests that for Pb^{2+} centres at which crystallisation of the preferred *n* = 1 phase is not possible, MA^+ is preferentially incorporated into the *n* > 1 phases leading to their being over-represented at $R_{BA\text{-}MA+} \leq 2$. We speculate that this is likely a kinetic effect. The globularity of MA^+ renders its inclusion in the growing perovskite structure significantly more likely than BA^+, as the latter cation is far less likely to be appropriately oriented at the instant of crystallisation.

4.7 – Bibliography

1. Vidal, R. *et al.* Assessing health and environmental impacts of solvents for producing perovskite solar cells. *Nat. Sustain.* **4**, 277–285 (2021).

2. Jeong, J. *et al.* Pseudo-halide anion engineering for α-$FAPbI_3$ perovskite solar cells. *Nature* **592**, (2021).

3. Yoo, J. J. *et al.* Efficient perovskite solar cells via improved carrier management. *Nature* **590**, 587–593 (2021).

4. Zhou, Y. *et al.* Room-temperature crystallization of hybrid-perovskite thin films via solvent-solvent extraction for high-performance solar cells. *J. Mater. Chem. A* **3**, 8178–8184 (2015).

5. Jeon, N. J. *et al.* Solvent engineering for high-performance inorganic-organic hybrid perovskite solar cells. *Nat. Mater.* **13**, 897–903 (2014).

6. Deng, Y. *et al.* Tailoring solvent coordination for high-speed, room-temperature blading of perovskite photovoltaic films. *Sci. Adv.* **5**, (2019).

7. Noel, N. K. *et al.* A low viscosity, low boiling point, clean solvent system for the rapid crystallisation of highly specular perovskite films. *Energy Environ. Sci.* **10**, 145–152 (2017).

8. International council for harmonisation of technical requirements for pharmaceuticals for human use. *Guideline for Residual Solvents: Q3C(R8)*. (ICH, 2021).

9. International council for harmonisation of technical requirements for pharmaceuticals for human use. *Guideline for Residual Solvents: Q3C(R8) - PDE for 2-methyltetrahydrofuran, cyclopentyl methyl ether, and tertiary-butyl alcohol.* (ICH**,** 2020).

10. Williams, A. C. & Barry, B. W. Penetration enhancers. *Adv. Drug Deliv. Rev.* **56**, 603–618 (2004).

11. Wang, Z., Richter, S. M., Gates, B. D. & Grieme, T. A. Safety concerns in a pharmaceutical manufacturing process using dimethyl sulfoxide (DMSO) as a solvent. *Org. Process Res. Dev.* **16**, 1994–2000 (2012).

12. Cao, J. *et al.* Identifying the Molecular Structures of Intermediates for Optimizing the Fabrication of High-Quality Perovskite Films. *J. Am. Chem. Soc.* **138** (31), 9919-9926 (2016).

13. Bu, T. *et al.* Lead halide–templated crystallization ofmethylamine-free perovskite for efficientphotovoltaic modules. *Science.* **372** (6548), 1327-1332 (2021).

14. Guo, Y. *et al.* Chemical Pathways Connecting Lead(II) Iodide and Perovskite via Polymeric Plumbate(II) Fiber. *J. Am. Chem. Soc.* **137** (50), 15907-15914 (2015).

15. Guo, Y. *et al.* Formamidinium Haloplumbate Intermediates: The Missing Link in a Chain of Hybrid Perovskites Crystallization. *Chem. Mater.*, **32** (18), 7739–7745 (2020)

16. Huang, X. *et al.* Solvent Gaming Chemistry to Control the Quality of Halide Perovskite Thin Films for Photovoltaics. *ACS Cent. Sci.* 2022, **8** (7), 1008–1016 (2022)

17. Eperon, G. E. et al. Formamidinium lead trihalide: A broadly tunable perovskite for efficient planar heterojunction solar cells. *Energy Environ. Sci.* **7**, 982–988 (2014)

18. Burschka, J. et al. Sequential deposition as a route to high-performance perovskite-sensitized solar cells. *Nature*, **499**, 316–319 (2013).

19. Guo, Y. *et al.* Chemical Pathways Connecting Lead(II) Iodide and Perovskite via Polymeric Plumbate(II) Fiber. *J. Am. Chem. Soc.* **137**, 15907–15914 (2015).

20. Yan, K. *et al.* Hybrid Halide Perovskite Solar Cell Precursors: Colloidal Chemistry and Coordination Engineering behind Device Processing for High Efficiency. *J. Am. Chem. Soc.* **137**, 4460–4468 (2015).

21. Hu, Q. *et al.* In situ dynamic observations of perovskite crystallisation and microstructure evolution intermediated from $[PbI_6]^{4-}$ cage nanoparticles. *Nat. Commun.* **8**, 1–9 (2017).

22. Chao, L. *et al.* Solvent Engineering of the Precursor Solution toward Large-Area Production of Perovskite Solar Cells. *Adv. Mater.* **2005410**, 1–23 (2021).

23. Hamill, J. C., Schwartz, J. & Loo, Y. L. Influence of Solvent Coordination on Hybrid Organic-Inorganic Perovskite Formation. *ACS Energy Lett.* **3**, 92–97 (2018).

24. Slater, C. S., Savelski, M. J., Hitchcock, D. & Cavanagh, E. J. Environmental analysis of the life cycle emissions of 2-methyl tetrahydrofuran solvent manufactured from renewable resources. *J. Environ. Sci. Heal. - Part A Toxic/Hazardous Subst. Environ. Eng.* **51**, 487–494 (2016).

25. Zhang, F. *et al.* Advances in two-dimensional organic-inorganic hybrid perovskites. *Energy and Environmental Science* **13**, 1154–1186 (2020).

26. Zheng, X. *et al.* Managing grains and interfaces via ligand anchoring enables 22.3%-efficiency inverted perovskite solar cells. *Nat. Energy* **5**, (2020).

27. Yang, W. S. *et al.* High-performance photovoltaic perovskite layers fabricated through intramolecular exchange. *Science (6240).* **348**, 1234–1237 (2015).

28. Cao, J. *et al.* Identifying the Molecular Structures of Intermediates for Optimizing the Fabrication of High-Quality Perovskite Films. *J. Am. Chem. Soc.* **138**, 9919–9926 (2016).

29. Luo, D. *et al.* Enhanced photovoltage for inverted planar heterojunction perovskite solar cells. *Science (6396).* **360**, 1442–1446 (2018).

30. Palosz, B. The structure of PbI_2 polytypes *2H* and *4H*: A study of the *2H-4H* transition. *J. Phys. Condens. Matter* **2**, 5285–5295 (1990).

31. Zhang, Y. *et al.* From 2D to 3D: A facile and effective procedure for fabrication of planar $CH_3NH_3PbI_3$ perovskite solar cells. *J. Mater. Chem. A* **6**, 17867–17873 (2018).

32. Miao, Y. *et al.* From 1D to 3D: Fabrication of $CH_3NH_3PbI_3$ Perovskite Solar Cell Thin Films from (Pyrrolidinium)PbI_3 via Organic Cation Exchange Approach. *Energy Technol.* **2000148**, 1–5 (2020).

33. Adjokatse, S., Fang, H. H., Duim, H. & Loi, M. A. Scalable fabrication of high-quality crystalline and stable $FAPbI_3$ thin films by combining doctor-blade coating and the cation exchange reaction. *Nanoscale* **11**, 5989–5997 (2019).

34. Kim, M. *et al.* Methylammonium Chloride Induces Intermediate Phase Stabilization for Efficient Perovskite Solar Cells. *Joule*, **3** (9), 1–14 (2019).

35. Ye, F. *et al.* Roles of MACl in Sequentially Deposited Bromine-Free Perovskite Absorbers for Efficient Solar Cells. *Adv. Mater.* **2007126**, 1–8 (2020).

36. Xie, F. *et al.* Vertical recrystallization for highly efficient and stable formamidinium-based inverted-structure perovskite solar cells. *Energy Environ. Sci.* **10**, 1942–1949 (2017).

37. Stranks, S. D. *et al.* Recombination Kinetics in Organic-Inorganic Perovskites: Excitons, Free Charge, and Subgap States. *Phys. Rev. Appl.* **034007**, (2014).

38. Yamada, Y., Endo, M., Wakamiya, A. & Kanemitsu, Y. Spontaneous defect annihilation in CH3NH3PbI3 thin films at room temperature revealed by time-resolved photoluminescence

spectroscopy. *J. Phys. Chem. Lett.* **6**, 482–486 (2015).

39. Yamada, Y., Nakamura, T., Endo, M., Wakamiya, A. & Kanemitsu, Y. Photocarrier recombination dynamics in perovskite $CH_3NH_3PbI_3$ for solar cell applications. *J. Am. Chem. Soc.* **136**, 11610–11613 (2014).

40. Herz, L. M. Charge-Carrier Mobilities in Metal Halide Perovskites: Fundamental Mechanisms and Limits. *ACS Energy Lett.* **2**, 1539–1548 (2017).

41. Doolin, A. J. Sustainable solvent selection for the manufacture of methylammonium lead triiodide ($MAPbI_3$) perovskite solar cells. *Green Chem.* **23**, 2471-2486 (2021).

42. Cassella, E. J. Binary Solvent System Used to Fabricate Fully Annealing-Free Perovskite Solar Cells. *Adv. Energy Mater.* **13**, 20223468 (2023).

43. Liu, Q. A mixed solvent for rapid fabrication of large-area methylammonium lead iodide layers by one-step coating at room temperature. *J. Mater. Chem. A,* **7**, 18275-18284 (2019).

44. Turren-Cruz, S. H., Hagfeldt, A. & Saliba, M. Methylammonium-free, high-performance, and stable perovskite solar cells on a planar architecture. *Science (6413).* **362**, 449–453 (2018).

45. McMeekin, D. P. et al. A mixed-cation lead mixed-halide perovskite absorber for tandem solar cells. *Science* (6269), **351**, 151-159 (2016).

46. Prat, D. *et al.* CHEM21 selection guide of classical- and less classical-solvents. *Green Chem.* **18**, 288–296 (2015).

47. Prat, D., Hayler, J. & Wells, A. A survey of solvent selection guides. *Green Chem.* **16**, 4546–4551 (2014).

48. Zhang, M. *et al.* Green Anti-Solvent Processed Planar Perovskite Solar Cells with Efficiency Beyond 19%. *Sol. RRL*, 2, 1700213 (2018).

49. Reichardt, C. *Solvents and Solvent Effects in Organic Chemistry*. (Wiley-VCH, 2002). doi:10.1002/3527601791

50. Yaws, C. *Matheson gas data book*. (McGraw-Hill, 2001). doi:1001/cat/bib/4480977

51. Mao, L., Stoumpos, C. C. & Kanatzidis, M. G. Two-Dimensional Hybrid Halide Perovskites: Principles and Promises. *J. Am. Chem. Soc.* **141** (3), 1171–1190 (2019).

52. Stoumpos, C. C. *et al.* Ruddlesden-Popper Hybrid Lead Iodide Perovskite 2D Homologous Semiconductors. *Chem. Mater.* (2016).

Chapter 5 – Enhancing formamidinium lead triiodide perovskite stability: process directs properties

The work in this chapter is adapted from: “A green solvent system for templated sequential deposition of stable formamidinium lead triiodide for perovskite solar cells”, Benjamin M. Gallant, Philippe Holzhey, Saqlain Choudhary, Karim A. Elmestekawy, Joel A. Smith, James M. Ball, M. Greyson Christoforo, Pietro Caprioglio, Laura M. Herz, Henry J. Snaith (*Under review*).

5.1 – Introduction

As discussed in **Chapter 1**, in order to compete with established PV technologies perovskite solar cells must be capable of producing consistent power output over the lifetime of their application, anticipated to be on the order of years. From the perspective of the research community there are two halves to the challenge of improving perovskite solar cell (PSC) stability. First, identifying sources of instability and developing solutions that minimise or avoid these. Second, establishing consistent and appropriate accelerated aging tests in order to avoid undesirable multi-year field tests, and to fairly and usefully compare the performance of PSCs fabricated in different ways by different groups of researchers.

To address the latter of these challenges, efforts have been made recently to gain consensus amongst PSC researchers on standardising accelerated aging tests. Most notable is a statement published in 2020 by 59 leading investigators in the field putting forward a raft of test conditions based on the International Summit on Organic

Photovoltaic Stability (ISOS) protocols along with a range of additional tests to account for properties specific to PSCs[1]. Having such a wide range of test conditions, and understanding that an effective PV cell must withstand all of these, is especially critical to perovskite PV in which it has been well established that the degradation behaviour of PSCs is particularly sensitive to the operational conditions they are subjected to[2].

Not only are degradation pathways specific to the applied aging test conditions, often they are specific to a PSC's architecture and components. Broadly we may separate instabilities in PSCs into three categories. (1) Those associated with changes in the bulk perovskite. (2) Those associated with changes in other materials in the PSC, for example transport layers. (3) Those introduced at the interface between, or as a result of physically and electronically contacting any two layers in a PSC. By way of examples, the thermal decomposition of $MAPbI_3$ (MA^+, methylammonium) perovskite into PbI_2, the de-doping of Li^+ ions from spiro-OMeTAD and the migration of Au through a PSC, correspond to each of these categories, respectively.

Here we build on the work presented in **Chapter 4** by first investigating the effect of processing $FAPbI_3$ via the 2D-templated sequential route (^{t}2D-3D $FAPbI_3$) on the stability of the bulk perovskite, in isolation. We find that ^{t}2D-3D $FAPbI_3$ shows a remarkable improvement in α-phase and thermal stability. By a combination of characterisation techniques and in comparison with a range of other state-of-the-art perovskite materials fabricated via a range of different processes we are able to tease out many of the influences of ink chemistry, deposition conditions and perovskite composition on the resulting perovskite materials' stability. Overall, we are able to demonstrate that the process by which a perovskite material is fabricated is critical to its ultimate composition and structure, and thus to its operational stability, even when nominally the same perovskite is being employed.

Having established that ^{t}2D-3D $FAPbI_3$ shows promising material stability under various conditions, we attempt to translate this stability enhancement into PSCs employing ^{t}2D-3D $FAPbI_3$ as the photoabsorbing layer. In **Chapter 4** we reported PSCs based on the n-i-p architecture. As will be explored, this architecture is often unsuitable in the pursuit of PV devices that display both high power conversion efficiency (PCE) and long-term stable power output. As such, we endeavour to fabricate PSCs with a p-i-n architecture known to be more stable. Having achieved this, and also developed robust encapsulation approaches for our devices, we demonstrate promising PSC stability under 85 °C, 85% relative humidity ("damp heat", ISOS-D-3) and 85 °C, 1 sun illumination (ISOS-L-2) accelerated aging conditions.

5.2 – Enhanced ^{t}2D-3D $FAPbI_3$ phase stability

Despite the favourable bandgap of α-$FAPbI_3$ for single-junction PSCs, the well-known phase instability of this material is an inherent drawback in its selection as our target composition. At room temperature the hexagonal photoinactive delta (δ, *2H*) phase of $FAPbI_3$ is thermodynamically preferred. Although kinetic entrapment of the α-phase is possible, phase transformation is known to be accelerated by a range of external influences, including ambient moisture[3], and materials properties, such as iodide-defects[4]. To assess the ambient phase stability of our ^{t}2D-3D α-$FAPbI_3$ material compared to $FAPbI_3$ fabricated by other state-of-the-art methods we perform a series of characterisation experiments on the same three materials presented in **Chapter 4** (^{t}2D-3D α-$FAPbI_3$, $FAPbI_3$ coated from DMF:DMSO with 40 mol% excess MACl added and neat $FAPbI_3$ coated from DMF:DMSO) as they evolve for 500 hours under ambient conditions (18-22 °C, 20-55% relative humidity).

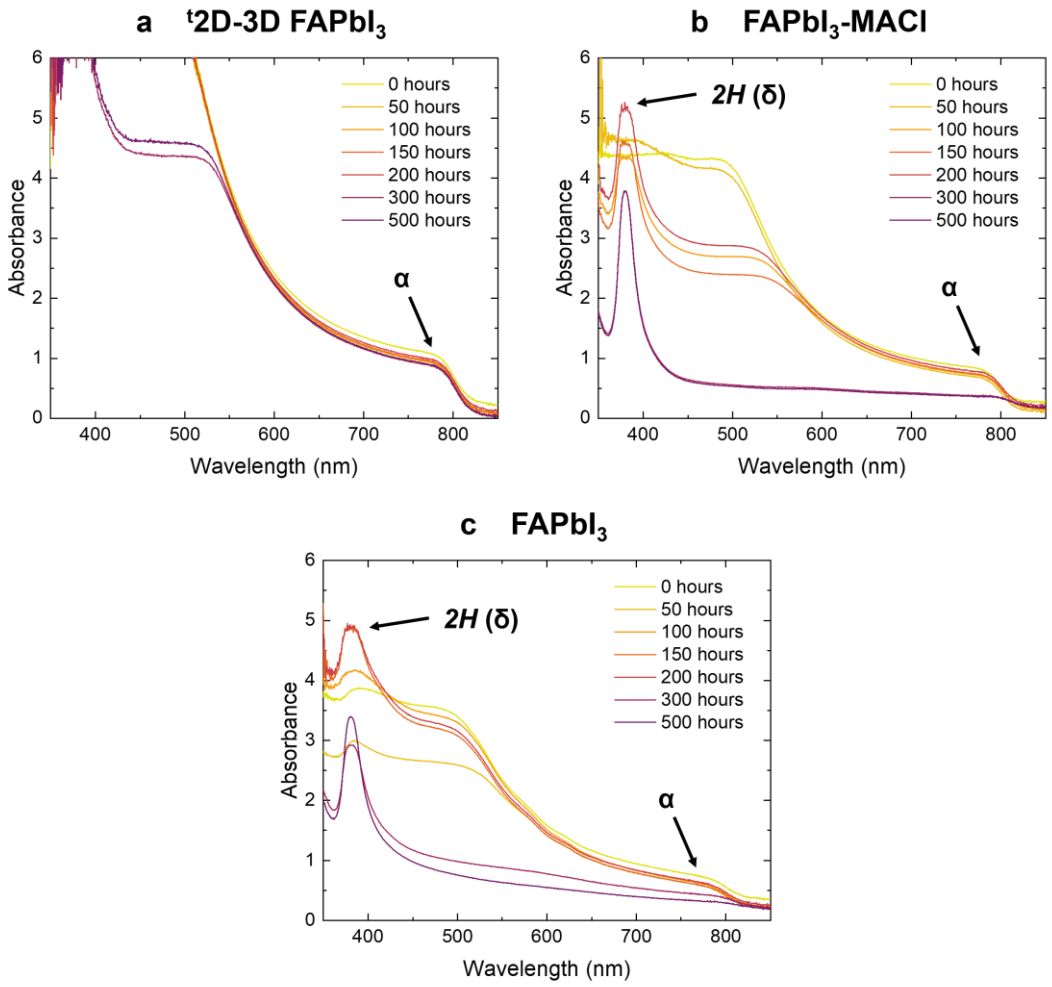


Figure 5.1 | Enhanced ambient stability: Absorbance. Evolution of absorbance spectra of ^{t}2D-3D $FAPbI_3$ (**a**), $FAPbI_3$-MACl (**b**) and $FAPbI_3$ (**c**) over 500 hours under ambient conditions (18-22 °C, 20-55% relative humidity).

In **Figure 5.1** we show the evolution in absorbance spectra of the three materials, where there is a stark contrast. The absorbance of ^{t}2D-3D α-$FAPbI_3$ remains broadly unchanged, in particular in the region near the α-phase band-edge suggesting that most of the α-$FAPbI_3$ material remains intact and does not transform to the *2H* or any other polytype phase over this time period. By contrast, both $FAPbI_3$-MACl and $FAPbI_3$ show substantial reduction in absorbance at the band-edge, in favour of a growing absorption feature at 380 nm. On the basis of our corresponding XRD measurements (**Figure 5.2**), for example $FAPbI_3$ after 500 hours of aging, we assign the development of this feature to the formation of the *2H* phase. As all three $FAPbI_3$ materials degrade, an absorbance feature with an onset around 550 nm appears. It is challenging to

assign this feature unambiguously, however it may correspond to formation of lower-bandgap polytypes (e.g. *4H*, *6H*), amorphous PbI_2 (we eliminate crystalline PbI_2) on

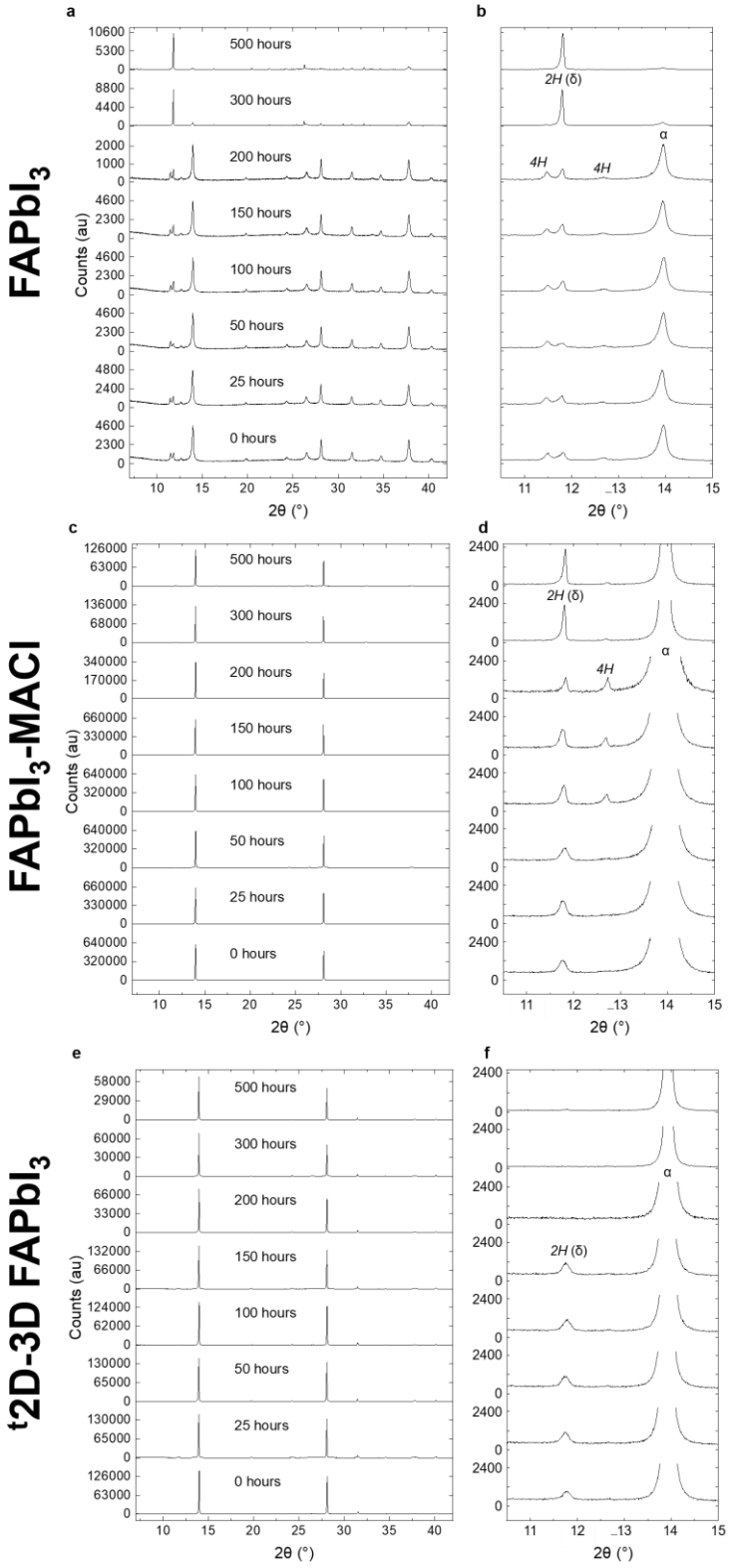


Figure 5.2 | Figure 5.2 | Enhanced ambient stability: XRD. a, Evolution of $FAPbI_3$ (**a**), $FAPbI_3$-MACl (**b**) and ^{t}2D-3D $FAPbI_3$ (**c**) under ambient conditions (18-22 °C, 20-55% relative humidity). **b**, **d**, **f**, Expansions of **a**, **c** and **e**, respectively, to highlight evolution of minority phases

the basis of our complimentary XRD measurements, **Figure 5.2**), or simply a reduction in the total optical density of the black α-$FAPbI_3$ phase in this region as pinhole formation occurs. In particular, both DMF:DMSO-cast materials also show substantial

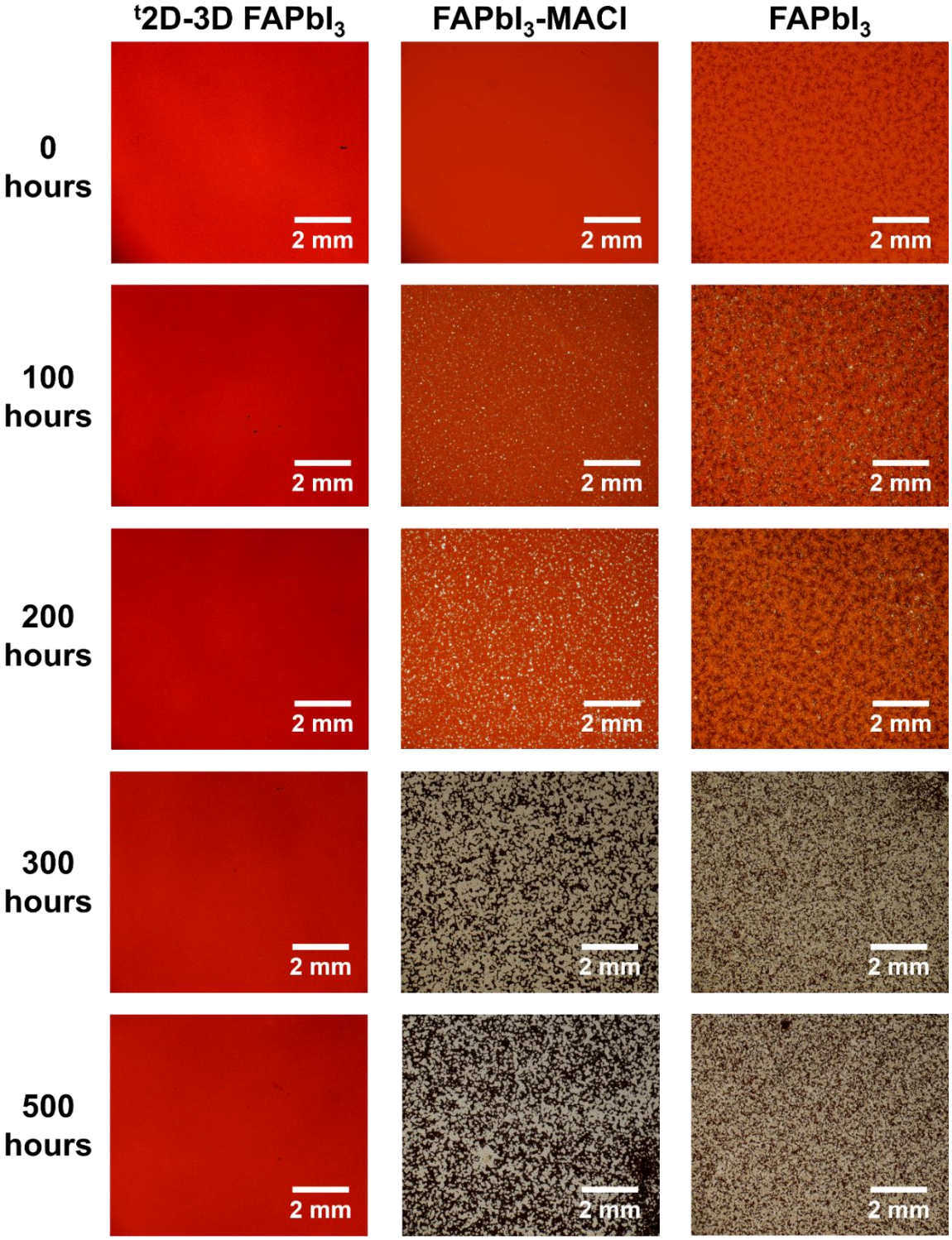


Figure 5.3 | Enhanced ambient stability: Visible light microscopy. Evolution of macrostructure of ^{t}2D-3D $FAPbI_3$ (**a**), $FAPbI_3$-MACl (**b**) and $FAPbI_3$ (**c**) over 500 hours under ambient conditions (18-22 °C, 20-55% relative humidity). Perovskite layers are directly deposited on fluorine-doped tin oxide substrates.

reduction in overall optical density (absorbance). Similarly, this may be a result of the increase in wider-bandgap *2H*-phase formation, but could also correspond to the formation of pinholes in the material. We confirm the formation of regions of high

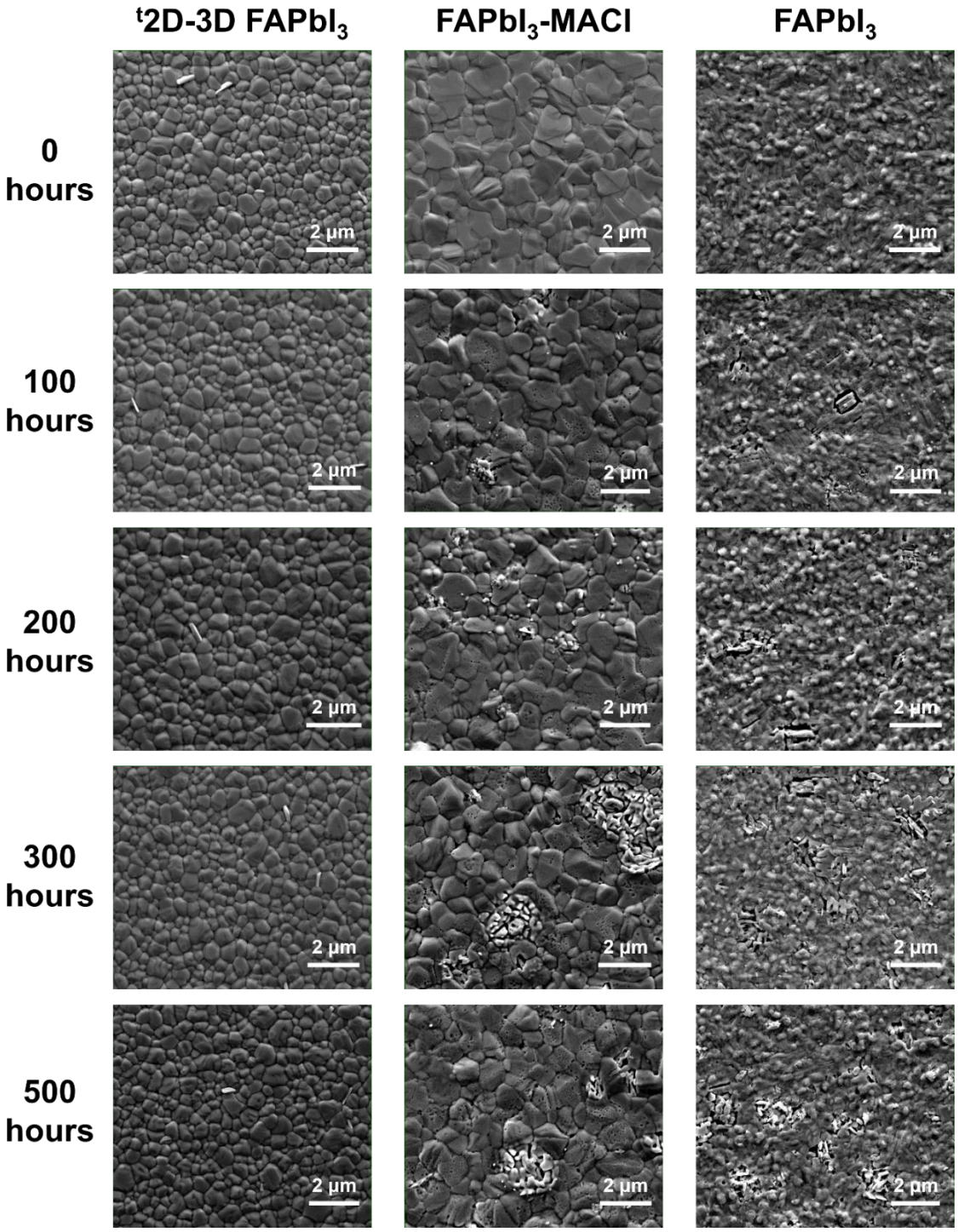


Figure 5.4 | Enhanced ambient stability: Scanning electron microscopy. Evolution of microstructure of ^{t}2D-3D $FAPbI_3$ (**a**), $FAPbI_3$-MACl (**b**) and $FAPbI_3$ (**c**) over 500 hours under ambient conditions (18-22 °C, 20-55% relative humidity). Perovskite layers are directly deposited on fluorine-doped tin oxide substrates.

optical transmission in the $FAPbI_3$-MACl and $FAPbI_3$ materials with transmission visible light microscopy (VLM, **Figure 5.3**). Again, however, it is not readily apparent if these are regions of a phase impurity or simply holes in the thin film. Corresponding scanning electron microscopy (SEM) images (**Figure 5.4**) shed more light on the problem, showing the formation regions with a high density of material degradation. Two degradation modes are apparent: (1) formation of <100 nm cavities, which are especially apparent in $FAPbI_3$-MACl and appear to form selectively in high density on certain grains, and (2) formation of a secondary phase, which is somewhat dendritic, with corresponding void formation. On account of our absorbance spectra (**Figure 5.1**) we interpret this secondary phase as the thermodynamically preferred *2H* polytype. However, while the formation of cavities most likely corresponds to loss of material during degradation, it is unclear if void formation associated with the secondary phase occurs for the same reason or due to a volume contraction/phase transformation effect. Possible mechanisms by which material may be lost post-deposition are discussed below when we explore the thermal degradation of these materials.

In **Figure 5.2** we present X-ray diffraction (XRD) patterns of the materials over this time. In the context of our results in **Figures 5.1, 5.3** and **5.4**, these data are somewhat misleading. The extremely high crystallinity and texturing of $FAPbI_3$-MACl, especially in comparison to neat $FAPbI_3$ leads to a high degree of ordering, and thus reduced peak broadening (smaller FWHM) associated with reduced disorder, and very high counts in the XRD patterns for this material. This effect swamps the evolving peak corresponding to the *2H* phase in $FAPbI_3$-MACl, making it seem that degradation of this material is minimal. As is apparent from our absorbance, VLM and SEM results, this is far from the case, highlighting the need for a multi-disciplinary approach to materials characterisation and a particular caution when interpreting XRD data for

metal halide perovskites. Overall, however, it is apparent from all our ambient aging results that the phase stability of ^{t}2D-3D α-$FAPbI_3$ under these conditions is substantially improved in comparison to α-$FAPbI_3$ processed from DMF:DMSO solvent mixtures, either with or without MACl additive.

5.3 – Enhanced ^{t}2D-3D $FAPbI_3$ thermal stability

Another often reported advantage of $FAPbI_3$-based perovskites is the absence of MA^+, which is thought to be more thermally labile from perovskite materials[5,6]. In order to investigate how the fundamental stability of our ^{t}2D-3D α-$FAPbI_3$ films compares to other archetypal perovskite compositions and processing routes, we subjected a selection of different perovskite films to a range of extreme environmental stressing conditions, and investigated how their material properties changed over time. We first performed in-situ XRD measurements to track the thermal degradation at 130 °C in ambient air (~30% RH) of a selection of lead halide perovskites (**Figure 5.5a-g**). Full details of all perovskite materials investigated are given in **Section 3.2.4**. The primary features identified in the degradation of each of the perovskites shown in **Figure 5.5a-g** are a reduction in the perovskite [100] scattering intensity over time, and a corresponding increase in the PbI_2 scattering intensity, consistent with thermal decomposition of FA^+-rich perovskites into PbI_2. For decomposition of a general acidic organic cation, AH^+, such a process is expected to proceed via[7]:

$$AH^+ + X^- \rightleftharpoons A + HX \tag{5.1}$$

leading to an overall decomposition of:

$$(AH)PbX_3 \rightarrow PbX_2\ (s) + A\ (g) + HX\ (g) \tag{5.2}$$

The most striking results from our measurements are the greatly reduced rate of PbI_2 evolution under thermal aging of both ^{t}2D-3D α-$FAPbI_3$ (*via* MeTHF, **Figure 5.5g**) and $MAPbI_3$ (processed *via* ACN, **Figure 5.5f**), in comparison with the same compositions fabricated *via* DMF:DMSO solvent systems. It is immediately striking that both $FAPbI_3$ and $MAPbI_3$ processed via volatile solvent routes show substantially enhanced thermal stability in comparison to the same materials processed from DMF:DMSO (**Figure 5.5a** and **5.5e**, respectively). Given reports on the thermal instability of MA^+ cations[5,6], besides $MAPbI_3$ (to allow comparison between processing from DMF:DMSO and volatile ACN) we avoid investigating the thermal degradation of MA^+-containing perovskites in our XRD study. For this reason, as the quantity of MA^+ or Cl^- incorporated into the final perovskite material[8] when the $FAPbI_3$-MACl route is employed, we also do not investigate this composition in this study.

To further probe the impact of processing on thermal degradation pathways we employ a complimentary technique on the same materials investigated via XRD, thermal desorption-gas chromatography-mass spectrometry (TD-GCMS). This technique desorbs volatile organic components (VOCs) from the perovskite material (between 400-1,000 nm thick layers) before separating these and characterising each individually (thermal extraction of volatiles carried out at 165 °C for 60 minutes, see **Chapter 3** for full details). These may be volatile species retained during processing, or degradation products of the perovskite material itself formed during the thermal desorption process. TD-GCMS is extremely sensitive. Based on previous reports on the retention of DMSO in gelatine media[9], we calculate that the detection limit of this chemical within a 500 nm thick layer of perovskite material coated on a 25 cm^2 substrate is 0.002 wt.%, assuming 50% desorption. The molecular structures shown in **Figure 5.5a-g** indicate the VOCs detected *via* TD-GCMS for each perovskite composition investigated. To our knowledge, this is the first use of TD-GCMS to

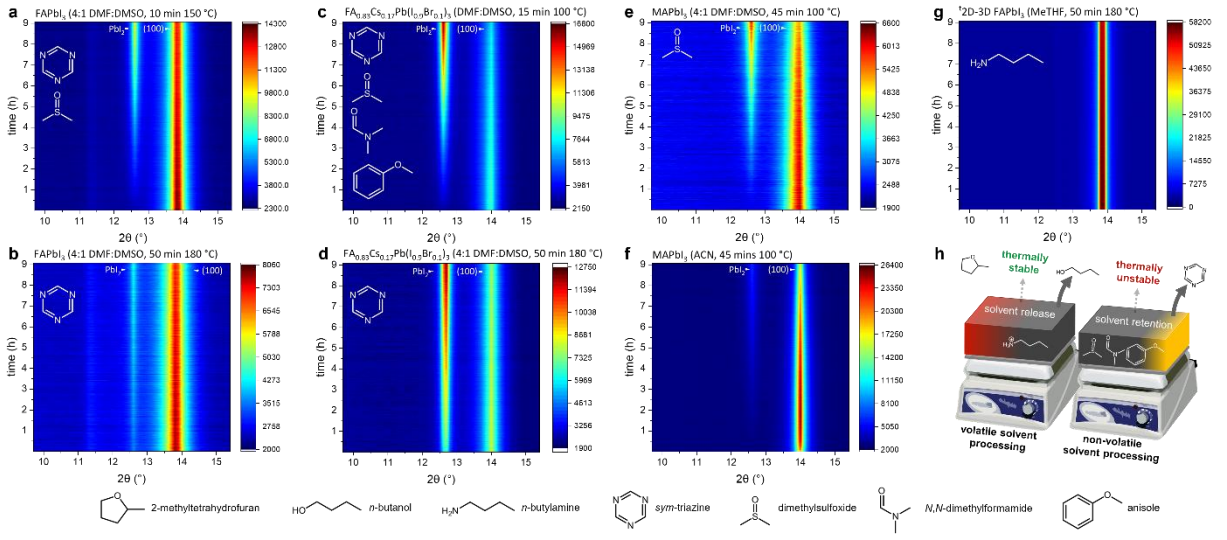


Figure 5.5 | Enhanced thermal stability. a-g, *Measurements and analysis carried out with the assistance of P. Holzhey.* Contour maps depicting in-situ x-ray diffraction (XRD) analysis of perovskite materials thermally degrading whilst held at 130 °C for 9 hours. Labels indicate perovskite composition and fabrication conditions (solvent, thermal curing). Full processing conditions described in Chapter 3. Molecular structures shown correspond to the volatile species detected during TD-GCMS analysis of each perovskite, including antisolvents such as anisole used in the processing of some DMF:DMSO-cast materials. **h**, Schematic highlighting advantages to perovskite material properties of solution processing *via* MeTHF solvent system.

investigate metal halide perovskites, and proves to be pivotal to our understanding of the pathways leading to perovskite instability. By combining our in-situ XRD and TD-GCMS measurements we are able to observe not only the products of degradation remaining in the solid-state, but many of those that are volatilised concurrently.

One manner in which processing may impact material properties is by the incomplete extraction of processing solvents. In the TD-GCMS traces of many of our perovskite materials we detect solvents employed during processing. These results implicate the gradual release of low volatility residual processing solvents (DMSO, DMF) and antisolvents (e.g. anisole) from perovskite materials as an underlying source of thermal instability in many solution-processed perovskite materials. We speculate that slow release of entrapped low volatility solvents may also be a cause of cavity formation, observed in the DMF:DMSO-cast materials investigated in our ambient aging study. The combination of low vapour pressure and strong Pb^{2+}-coordination of DMF and DMSO results in their complete removal from the solid materials being challenging, even with the use of antisolvent engineering and thermal curing. By contrast, high volatility solvents are easily removed by similar or even less severe treatments. As such, harsher thermal curing conditions during fabrication might be expected to more thoroughly remove such residual solvents. To test this hypothesis, we varied the curing temperature employed during fabrication of both pure $FAPbI_3$ and "highly stable", state-of-the-art $FA_{0.83}Cs_{0.17}Pb(I_{0.9}Br_{0.1})_3$ from 100 to 180 °C, over a range of durations, and found by TD-GCMS analysis that only 180 °C curing for 50 minutes was sufficient to fully remove all residual solvents (**Figure A5.1h-n**). As expected, harsher curing also led to improved thermal stability (**Figure 5.5a-d**). Notably, no such VOCs were evolved from perovskites fabricated *via* high volatility -solvents (MeTHF, ACN) (**Figure A5.1a, o**), directly correlating to the improved thermal

stability of these materials (**Figure 5.5f-g**). Notably, $MAPbI_3$ fabricated *via* ACN shows higher thermal stability than pure $FAPbI_3$ *via* DMF:DMSO, despite the absence of thermally unstable MA^+ in the latter. We do, however, find that $MAPbI_3$ thin films fabricated *via* DMF:DMSO contain residual DMSO and display lower thermal stability than both $MAPbI_3$ *via* ACN and $FAPbI_3$ *via* DMF:DMSO (**Figure 5.5e-f**), further corroborating that low volatility solvents adversely impact thermal stability and implying that, when processed by comparable techniques, MA^+-rich perovskites are indeed less stable than FA^+-rich perovskites as expected. Impressively also, ^{t}2D-3D α-$FAPbI_3$ is found to be more thermally stable than $FA_{0.83}Cs_{0.17}Pb(I_{0.9}Br_{0.1})_3$ perovskite regardless of temperature, despite this composition being widely reported as possessing notably higher stability than other perovskites[10].

To our knowledge, a 2021 report from Chen, et al., is the first to link residual solvents with material instability[11]. The authors observed void-formation at the underlying perovskite interface over time and inferred from this the gradual loss of DMSO entrapped during processing. More generally we speculate that strongly Pb^{2+}-coordinating solvents may serve as pseudo-halides substituting Pb^{2+}-coordinated halide ions in the 3D haloplumbate lattice, thus also requiring corresponding A-site vacancies to ensure local charge neutrality. Such non-uniformly distributed defects are undetectable *via* XRD due to their irregular nature[12], but could be revealed as PbI_2 upon subsequent volatilisation of the coordinating solvent followed by thermal ripening to form larger regions of crystalline PbI_2, as observed here.

[12] For constructive interference of scattered X-rays, long-range structural order is required. This would not be expected in the case of dilute, non-uniformly distributed residual solvents entrapped within a perovskite material.

Although harsher curing temperatures go some way to improving long-term thermal stability, this treatment is not without drawbacks. It is clear that more PbI_2 is already present in the as-cured materials cured at a higher temperature (**Figure 5.5a-d**), presumably generated *via* the same pathway. The increased full-width half-maxima (FWHM) of perovskite XRD reflections in materials cured at higher temperature also indicate a reduction in the crystallinity of these materials, in line with the Scherrer equation[13].[12,13] Notably, ^{t}2D-3D α-$FAPbI_3$ is not compromised in either of these ways by high-temperature processing. Indeed, the almost complete absence of PbI_2 evolution observed in ^{t}2D-3D α-$FAPbI_3$ is remarkable and points to a fundamental difference in its degradation pathway under our test conditions.

Again, our TD-GCMS results provide an explanation. ^{t}2D-3D $FAPbI_3$ is unique among all FA^+-containing perovskites investigated (from 15 different perovskites, **Figure A5.1**) in not evolving *sym*-triazine during TD-GCMS analysis (a total of seven individual ^{t}2D-3D $FAPbI_3$ samples were analysed, with no *sym*-triazine detected). *Sym*-triazine has been reported previously as a thermal degradation product of FA^+ [7,14,15], *via* reaction of formamidine (FA) generated by the process described in **Equation 5.2** with FA^+ remaining in the perovskite lattice:

$$FA + 2FA^+ + 2X^- \rightarrow C_3H_3N_3\,(g) + 2HX\,(g) + 3NH_3(g) \quad (5.3)$$

[13] The Scherrer equation relates the FWHM of powder diffraction XRD peaks to the mean crystallite size of a material. The equation takes the form: $\tau = \frac{K\lambda}{\beta \cos\theta}$, where τ is the mean crystallite size, λ is the wavelength of incident X-rays, β is the full-width of a peak at half of its maximum intensity (FWHM) after instrument broadening is accounted for, θ is the corresponding Bragg angle of the centre of the peak, and K is a shape factor related to the shape of the crystallites in question, which are assumed to be all equivalently shaped. Moreover, the original analysis approximates the crystallites to be spherical, with subsequent work[13] showing that deviations of away from this approximation to even ellipsoidal or parallelepipedal shapes lead to substantial changes in K. As such, while the inverse relationship between crystallite size and FWHM is generally taken to hold in the case of polycrystalline domains of varying sizes, direct application of the Scherrer equation to XRD patterns of such materials is erroneous.

α-$FAPbI_3$ perovskites fabricated *via* DMF and DMSO and thermally cured under increasingly harsh conditions (up to 50 minutes at 180 °C) (**Figure A5.1a-e**) all show the production of *sym*-triazine, ruling out perovskite composition or enhanced thermal curing as the cause of this striking difference. Similarly, fabrication *via* a conventional sequential deposition approach and even α-$FAPbI_3$ deposited *via* thermal evaporation (solvent free) fails to obviate *sym*-triazine evolution (**Figure A5.6f-g**). This implies that the 2D-templating process itself is responsible for the suppression of *sym*-triazine production. These results are summarised schematically in **Figure 5.5h**, and correlate with the enhanced thermal stability of ^{t}2D-3D $FAPbI_3$ observed in our XRD measurements (**Figures 5.5**).

To determine if the suppression effect is kinetic (the rate of *sym*-triazine formation is reduced) or thermodynamic (the formation energy of *sym*-triazine is increased such as to become non-spontaneous at lower temperatures), we carry out thermal gravimetric analysis-mass spectrometry (TGA-MS) measurements on a range different FA^{+}-rich perovskite thin films (**Figure 5.6**). In contrast to our XRD or TD-GCMS experiments where samples are thermally degraded at a given temperature for a period of hours the TGA-MS measurement rapidly increases the temperature that the material is exposed to (5 °C min^{-1}) leading to detection of a sharp decrease in mass when volatile species are lost. We find that for iodide-rich perovskites the temperature of *sym*-triazine formation is consistent at around 310 °C. This suggests that the mechanism by which *sym*-triazine production is suppressed in ^{t}2D-3D $FAPbI_3$ is kinetic, and that the rate of formation is so low at the temperature of our thermal aging (130 °C) that insufficient quantities are detected by TD-GCMS. Interestingly, the

temperature at which $FAPbBr_3$ evolves *sym*-triazine is somewhat lower (266 °C) than for the iodide-rich perovskites. As bromide perovskites are not a focus of our study we have not investigated further, but we speculate that this may be related to the ease with which proton abstraction by the halide (**Equation 5.1**) is affected (Br^- > I^-), consistent with the H-I being the weakest of the hydrogen halide bonds. Moreover, we

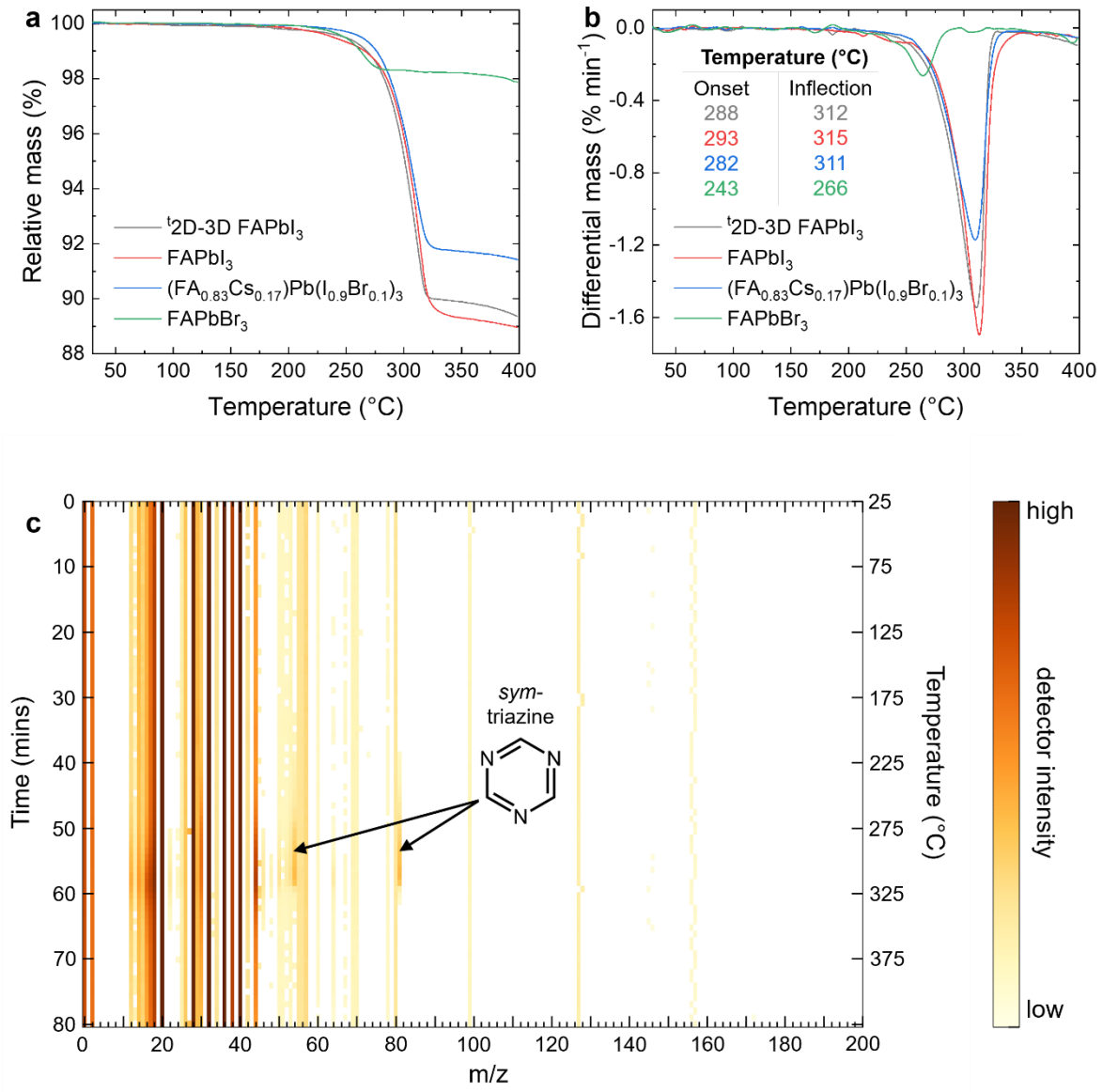


Figure 5.6 | Investigating *sym*-triazine evolution. Thermal profiles (5 °C min^{-1}) of four perovskite materials during thermal gravimetric analysis-mass spectrometry (TGA-MS), with both relative mass (**a**) and differential mass (**b**) shown. Inset in **b** shows extracted onset and inflection temperatures of mass loss event corresponding to *sym*-triazine loss. (**c**) Corresponding time- (left) and temperature-resolved (right) mass spectrum for t2D-3D $FAPbI_3$ highlight onset of *sym*-triazine. Intensity detected at consistency throughout the measurement is attributed to species introduced by the N_2 carrier gas.

note the presence of two peaks in the thermogram of $FAPbBr_3$, the second much smaller peak coinciding with the temperature of mass loss from the iodide-rich perovskites studied and being caused by a second *sym*-triazine loss event. Although surprising, the most obvious explanations for this are iodide contamination in our $FAPbBr_3$ material, or cross-contamination between from the triiodide materials measured in the same chamber.

The exact mechanism by which *sym*-triazine formation is suppressed in ^{t}2D-3D $FAPbI_3$ remains unclear. It is possible that the effect is related to defect density, whereby local vacancies reduce the energetic barrier, perhaps sterically, to *sym*-triazine formation within the $FAPbI_3$ lattice by facilitating the close alignment of FA and FA^+ within the perovskite structure necessary for reaction towards aromatisation, in line with **Equation 5.3**. This would be consistent with the substantially reduced rate of monomolecular recombination calculated for ^{t}2D-3D $FAPbI_3$ (**Chapter 4**, **Figure 4.8**). As discussed, this reduction implies a reduced density of non-radiative recombination sites in this material, from which we infer a reduction in defect density. However, all such hypotheses remain highly speculative. Studies identifying the presence in perovskite materials of particular atomic-level defects[4,16] (for example iodide vacancies, as distinguished from – for example – identifying vacancies of any type, or determining the density of all positively charge defects present) remain relatively uncommon, with theoretical studies dominating existing reports[17,18]. Works that go further and relate the presence of a particular atomic-level defect type directly to a mechanism of long-term material degradation are, to my knowledge, yet to be realised.

Further, such a thermal stabilisation mechanism may also go some way to explaining the phase stabilisation of ^{t}2D-3D $FAPbI_3$. Nanoscale polytype impurities have been shown to be sources of both phase degradation[19,20] and of defect formation, on

account of a reduced defect formation energy[21]. Thus, the presence of a reduced density of polytype impurities may be the source of both phase stabilisation and, by affecting a decrease in the rate of defect formation, thermal stabilisation of ^{t}2D-3D $FAPbI_3$. Such hypotheses remain highly speculative, but could be supported by appropriate theoretical calculations or by direct observation of (i) δ-$FAPbI_3$ (under ambient conditions), and (ii) PbI_2 formation (under *in-situ* thermal degradation) at defect-rich centres, such as nanoscale polytype regions or grain boundaries, by means of nano-XRD or low-dose scanning electron nanodiffraction (SEND). Thus far such approaches have remained beyond the scope of this work, however they certainly warrant future investigation.

We note that in some of our TD-GCMS measurements of ^{t}2D-3D α-$FAPbI_3$, trace quantities of BA^+ were detected (**Figure A5.1a**). Given that BA^+ is not detected in ^{1}H NMR measurements (**Figure 4.3e**), the quantity of BA^+ must be below the detection limit of ^{1}H NMR (<< 1 mol%). However, while it is apparent this retention does not hamper n-i-p configuration PSC performance (**Figure 4.9**), even trace quantities of large A-site cations such as BA^+ within the 3D perovskite may contribute towards the improvement in ambient α-$FAPbI_3$ phase stability observed[3,22]. As such, this may be a contributing mechanism by which ^{t}2D-3D α-$FAPbI_3$ is ambiently phase stabilised in comparison to other $FAPbI_3$ materials.

To compare the stability of ^{t}2D-3D α-$FAPbI_3$ to other highly stable perovskite compositions reported, under more conventional environmental stressing conditions, we encapsulated perovskite films in glass-glass laminates employing an industry standard butyl-rubber edge seal (**Figure A5.7c**), and subjected the perovskite material to the conditions of two of the most demanding stability tests for perovskites; ISOS-D-3 “damp heat” test (85 °C and 85% relative humidity, **Figure 5.7a, 5.8a-c**) and ISOS-

L-2 (85 °C under a 1-sun equivalent light source, **Figure 5.7b, 5.8d-f**). Strikingly, we observe very little change in the UV-vis absorption spectra for our ^{t}2D-3D α-$FAPbI_3$ films when aged for over 3000 hours (3 times the IEC standard) under both stressing conditions. In **Figure 5.7**, we show the optical density (OD) of the films, at wavelengths between 500 to 510 nm, as a function of stressing time. This gives a relatively sensitive indication of the evolution of "pin-holes" in the perovskite films, which have previously been observed to form during degradation[10,23]. A drop in OD from 5, to 4, to 3 corresponds to a pin-hole density increase from 0.001, to 0.01 to 0.1%, respectively. We therefore interpret the maintenance of high absorbance in aged ^{t}2D-3D α-$FAPbI_3$ – in contrast to two perovskite compositions that have previously been reported as amongst the most stable[10,24] - under both test scenarios to correspond to a low rate of pin-hole formation and hence degradation. We confirm this with visible light microscopy, where in **Figure 5.8** we show images of the different perovskite films post stressing. Notably, the survival of the ^{t}2D-3D α-$FAPbI_3$ for over 3,000 hours under damp-heat stressing, suggest that these materials may be capable of lasting for 25 years under real world conditions, when encapsulated similarly in a PV module. For copper indium gallium selenide PV modules, 3,000 hours of damp heat stressing has been shown to be comparable to 20 years deployment in Miami, USA[25]. The remarkable stability of the α-$FAPbI_3$ perovskite films that we have shown suggest that, despite the known delta-phase instability, this simple three-ion perovskite may ultimately prove capable of providing the long-term operational stability required for PSC applications. In particular this simplicity overcomes compositional inhomogeneities, and the instabilities they can induce, in the $FA_yCs_{1-y}Pb(I_xBr_{1-x})_3$ perovskite family, which have to-date delivered the highest stability in complete PSCs.

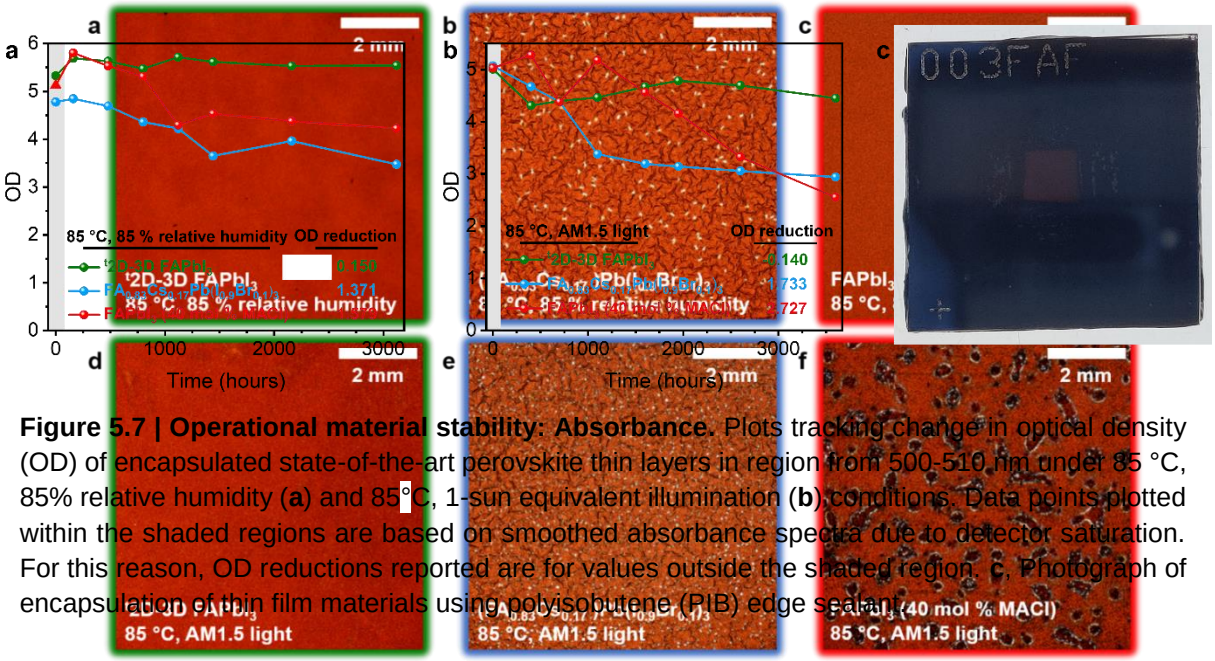


Figure 5.7 | Operational material stability: Absorbance. Plots tracking change in optical density (OD) of encapsulated state-of-the-art perovskite thin layers in region from 500-510 nm under 85 °C, 85% relative humidity (**a**) and 85 °C, 1-sun equivalent illumination (**b**) conditions. Data points plotted within the shaded regions are based on smoothed absorbance spectra due to detector saturation. For this reason, OD reductions reported are for values outside the shaded region. **c**, Photograph of encapsulation of thin film materials using polyisobutene (PIB) edge sealant.

Figure 5.8 | Operational material stability: Visible light microscopy. Visible light microscopy images of perovskite materials after accelerated operational aging at 85 °C and 85% relative humidity (**a-c**) and at 85 °C under AM1.5 illumination (**d-f**).

5.4 – ^{t}2D-3D $FAPbI_3$ perovskite solar cell stability

In order to demonstrate the impressive stability of ^{t}2D-3D α-$FAPbI_3$ in PSCs it is necessary to integrate a thin film of this material into a photovoltaic device. As set out in **Section 5.1**, for such a device to reflect the inherent stability of the perovskite material itself it is important that both that the other components in the devices are themselves stable and that physical and electronic connection between ^{t}2D-3D α-$FAPbI_3$ and these other components does not also lead to new mechanisms of instability.

As described in **Chapter 4**, we are able to integrate ^{t}2D-3D α-$FAPbI_3$ into PSCs in n-i-p configuration and achieve promising PCE (**Figure 4.9**). In **Figure 5.9a**, we show the unencapsulated “shelf stability” (stored in dark in dry air, <10% relative humidity, at room temperature) of such devices, where we observe a gradual improvement in performance over 13,500 hours (~1.5 years). In **Figure 5.9b** we review and summarise the highest reported ambient stability, noting that to our knowledge the performance

of our devices (champion and median) is substantially superior to previous reports. Generally, such estimates of stability are of only limited usefulness in assessing long-term PSC stability[1]. However, in this instance, since the α-$FAPbI_3$ absorber material is known to possess only kinetic metastability[26] – and is typically observed to undergo rapid transition to the non-perovskite hexagonal phase in ambient conditions[3,4], as demonstrated in our ambient aging studies (**Figures 5.1-4**) – such maintenance of performance demonstrates the promising phase-stability offered by the ^{t}2D-3D approach. It is also consistent with our findings on the substantially enhanced α-phase stability of ^{t}2D-3D α-$FAPbI_3$ (**Figure 5.1-4**). However, as many of the degradation pathways of PSCs are known to only be active under operational conditions it is certainly necessary to carry out stability testing under more rigorous conditions.

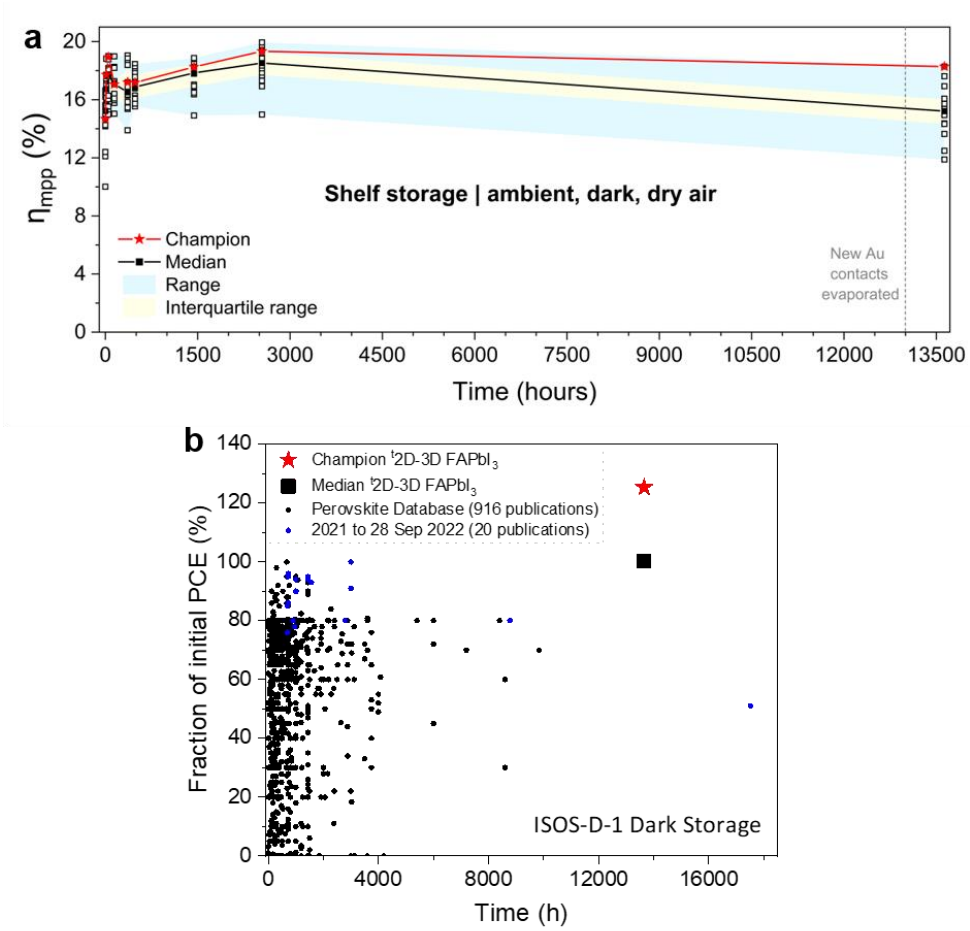


Figure 5.9 | Enhanced ambient PSC stability. Top, Unencapsulated PSCs stored in dark in dry air, <10% relative humidity, at room temperature. **Bottom**, Summary of state-of-the-art 'ambient dark storage' performance.

Unfortunately, the n-i-p PSC architecture suffers from a number of inherent instabilities under both elevated temperature and light. The near-ubiquitous use of doped spiro-OMeTAD (2,2′,7,7′-tetrakis(*N*,*N*-di-*p*-methoxyphenylamine)-9,9′-spirobifluorene) as a hole transport material (HTM) in high-performance n-i-p PSCs is a particularly potent source of instability. Pristine spiro-OMeTAD possesses low hole mobility and conductivity[27]. p-doping with lithium bis(trifluoromethane)sulfonimide (LiTFSI), or a similar dopant, is therefore necessary to oxidise the organic. However, the oxidised spiro-OMeTAD is susceptible to reduction by iodide ions[28], which – under elevated temperature – diffuse rapidly into the material from the adjacent perovskite, facilitating the degradation of the perovskite and rendering the HTM impotent. Moreover, the

LiTFSI salt is hygroscopic[27,29], promoting ingress of moisture that may rapidly degrade the perovskite, and also induces crystallisation of the spiro-OMeTAD under thermal treatment[30]. Finally, mobile Li ions – the oxidation product of spiro-OMeTAD reduction – may diffuse throughout the PSC generating defects and acting as an effective reducing agent[31].

Spiro-OMeTAD is not the only weak link in high-performance n-i-p PSCs, the overwhelming majority of which employ metal oxide electron transport materials (ETMs), most commonly TiO_2 and SnO_2. Both oxides have been shown to interact adversely with the perovskite, with TiO_2 showing photocatalytic behaviour at the ETM-perovskite interface[32–34] and SnO_2 accelerating the degradation of the perovskite A-site cation[34], among other instabilities[35].

Evidently the n-i-p architecture faces significant inherent challenges for PSC stability. By contrast, p-i-n configuration PSCs typically make use of organic transport materials (such as polyTPD[14], PTAA[15] and C_{60}) that are inherently more stable, and crucially interact minimally with the perovskite material. As a result, PSCs based on the p-i-n architecture have tended to show greater operational stability[10,36]. For this reason, in order to most effectively demonstrate the inherent stability of ^{t}2D-3D α-$FAPbI_3$ we attempt to incorporate our material as the photoactive layer in a p-i-n configuration PSC.

We have found this to be a substantial challenge in its own right. In general, reports of pristine $FAPbI_3$ in p-i-n PSCs are few and far between. Interrogation of the “perovskite database” shows that fewer than 30 publications (up to February 2020) have reported

[14] polyTPD: poly[N,N′-bis(4-butylphenyl)-N,N′-bis(phen-yl)benzidine]
[15] PTAA: poly(bis(4-phenyl)(2,4,6-trimethylphenyl)amine)

the use of $FAPbI_3$ in a p-i-n device, from a total of 15,000 publications in the database[37]. Closer inspection shows that the majority of these in fact either use additives (such as MAX salts) in fabrication of the perovskite, thus altering the composition, or report $FAPbI_3$ in poorly performing (typically <10% PCE) devices for comparison in order to highlight the efficacy of *not* using $FAPbI_3$ in p-i-n architectures. The highest performing PSC employing pristine $FAPbI_3$ in a p-i-n architecture reported in the perovskite database is just 16.0% [38,39].

Moreover, we discovered that our selection of underlying HTM is severely limited by a combination of solvent incompatibility (MeTHF is an apolar solvent, while most underlying HTMs in PSCs have been developed to be orthogonal to solvents such as DMSO and DMF, and are often partially soluble in ether-based solvents), high temperature processing of the ^{t}2D-3D α-$FAPbI_3$ (180 °C) and low mechanical adhesion between the as-deposited ^{t}2D-3D α-$FAPbI_3$ layer. After substantial investigation we determined that a new class of carbazole-phosphonic acid-derived self-assembled monolayers (SAMs) function as the most effective HTMs for our devices. With PSCs composed of FTO / MeO-2PACz[16] / Al_2O_3[17] / ^{t}2D-3D α-$FAPbI_3$ / Al_2O_3 / $EDAI_2$[18] / PCBM[19] / BCP[20] / Cr / Au architecture we are able to achieve a champion maximum power point tracked efficiency (η_{mpp}) of 18.8% (**Figure 5.10**).

To investigate the long-term stability of these devices, we subject them to a series of accelerated aging conditions. Perhaps the most challenging condition routinely used

[16] MeO-2PACz = (2-(3,6-dimethoxy-9H-carbazol-9-yl)ethyl)phosphonic acid

[17] Al_2O_3 interlayer fabricated with an alumina nanoparticle solution, anticipated to be non-continuous with island growth of Al_2O_3 regions, designed to assist increase roughness and wettability to assist growth of a continuous, mechanically adhered overlying perovskite layer.

[18] Ethylendiammonium diiodide passivation layer

[19] PCBM = phenyl-C_{61}-butyric acid methyl ester

[20] BCP = bathocuproine

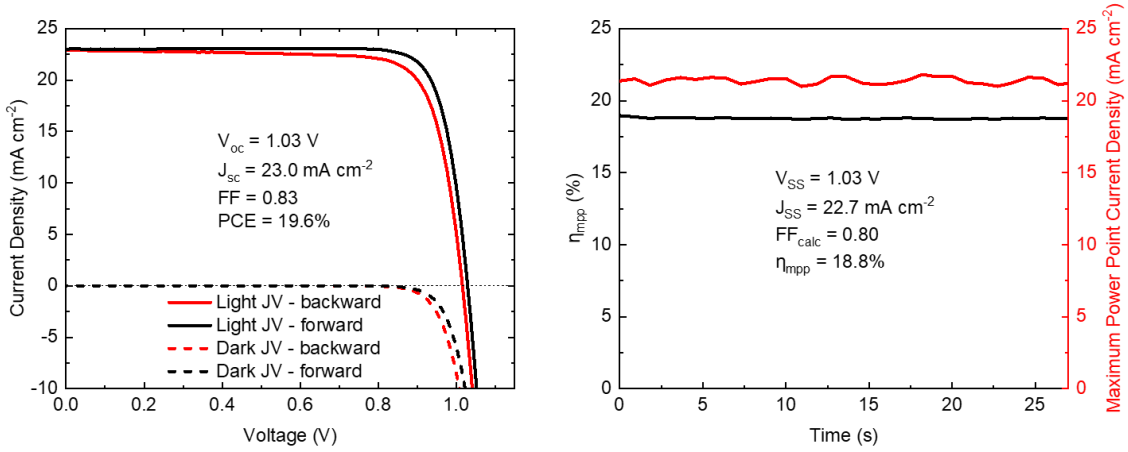


Figure 5.10 | p-i-n PSC champion performance. J-V characteristics (**a**) and corresponding maximum power point tracked efficiency (η_{mpp}) and current density (J_{mpp}) measured at maximum power point (**b**) for champion devices fabricated from ^{t}2D-3D α-$FAPbI_3$ with illuminated area 1.00 cm^2. Light J-V and η_{mpp} measurements were performed under simulated AM1.5 100.7 $mWcm^{-2}$ irradiance. J_{sc} = short-circuit current density, V_{oc} = open-circuit voltage, FF = fill factor, V_{mpp} = maximum power point voltage. V_{SS} = stabilised V_{oc}, J_{SS} = stabilised J_{sc}, FF_{calc} = pseudo-FF calculated from independent stabilised voltage, current density and efficiency measurements.

to age a PSC is at open-circuit, under 1 sun illumination and at 85 °C in air (ISOS-L-2). However, the separate investigation of both thermal and photo-stability of PSCs can often be instructive. To this end, we first show the stability of the unencapsulated p-i-n devices (15 cells) under elevated temperature (85 °C, in the dark in N_2, ISOS-D-2) (**Figure 5.11a**). In line with the results of our thermal stability experiments showing that ^{t}2D-3D $FAPbI_3$ is substantially more thermally stable than other perovskite materials (**Figure 5.5**, **Figure A5.1**), we find that there is minimal change in PSC performance over nearly 2,000 hours of aging. We next isolate the effect of light-induced degradation in the absence of elevated heat. To do this, we actively cool encapsulated perovskite solar cells to between 20-25 °C whilst exposing them to 1 sun equivalent light (ISOS-L-1). In this test, we compare p-i-n cells fabricated with ^{t}2D-3D $FAPbI_3$ as the photoactive layer, and also $FA_{0.83}Cs_{0.17}Pb(I_{0.9}Br_{0.1})_3$. Besides the photoactive layer, the device architectures are identical in both cases. We find that the later cells degrade at a somewhat more accelerated rate. After 850 hours, the cells based on $FA_{0.83}Cs_{0.17}Pb(I_{0.9}Br_{0.1})_3$ have degraded to 80% of their initial median

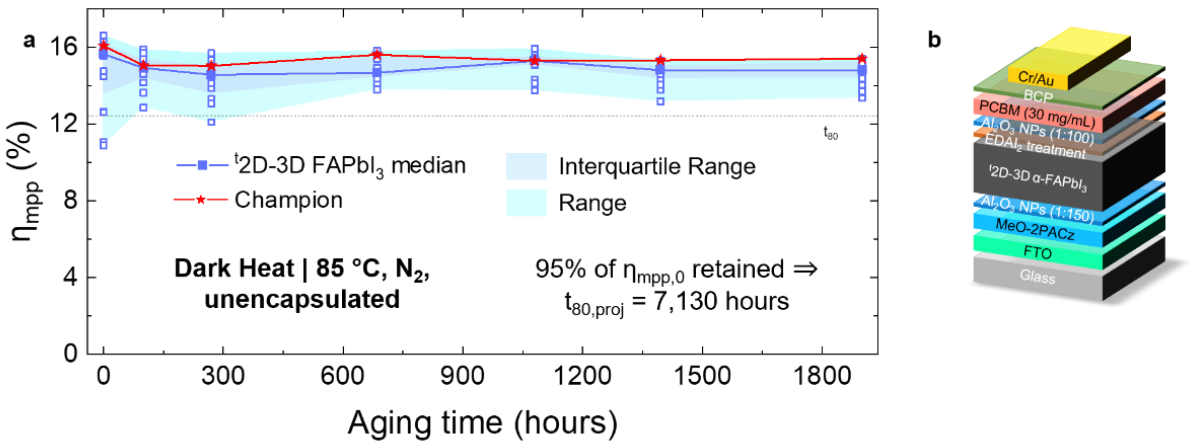


Figure 5.11 | p-i-n PSC dark heat stability. (**a**) Evolution of maximum power tracked efficiency (η_{mpp}) measured periodically on unencapsulated p-i-n PSCs (15 cells) employing ^{t}2D-3D FAPbI$_3$ as the photoactive layer, and thermally aged at 85 °C in the dark in an N_2 atmosphere (ISOS-D-2). Each measurement is taken after removing the device from the aging chamber and allowing it to cool to room temperature. After 1,900 hours, 95% of the initial median η_{mpp} ($\eta_{mpp,0}$) is retained, from which we calculate a projected lifetime to 80% of $\eta_{mpp,0}$ ($t_{80,proj}$) of 7,130 hours (9.8 months) by linear extrapolation. (**b**) Schematic showing p-i-n cell architecture employed in this study (see main text for abbreviations).

efficiency (18.4%, 10 cells), while those based on ^{t}2D-3D FAPbI$_3$ still retain 95% of their initial median efficiency (17.6%, 21 cells) from which we calculate a projected lifetime to 80% initial efficiency ($t_{80,proj}$) of 3,210 hours.

While both photostability (ISOS-L-1) and thermal stability (ISOS-D-2), in isolation, are important measures of solar cell stability, neither is representative of real-world conditions. Both tests isolate and activate a subset of possible degradation processes in the solar cell, and as such only simulate accelerated aging via these processes.

Two tests that more closely represent accelerated real-world aging are the ISOS-D-3 (85 °C at 85% relative humidity) and ISOS-L-2 (85 °C, 1 sun illumination) tests, the same as those we exposed our thin film materials to (**Figures 5.7 and 5.8**). **Figure 5.13a** shows our initial studies on PSCs fabricated utilising ^{t}2D-3D FAPbI$_3$ (9 cells) as the photoactive layer, and also $FA_{0.83}Cs_{0.17}Pb(I_{0.9}Br_{0.1})_3$ (11 cells) exposed to ISOS-D-3 conditions. In order to protect the cells from the harsh humidity conditions, we encapsulate each cell individually using the same industry-standard PIB edge-sealant

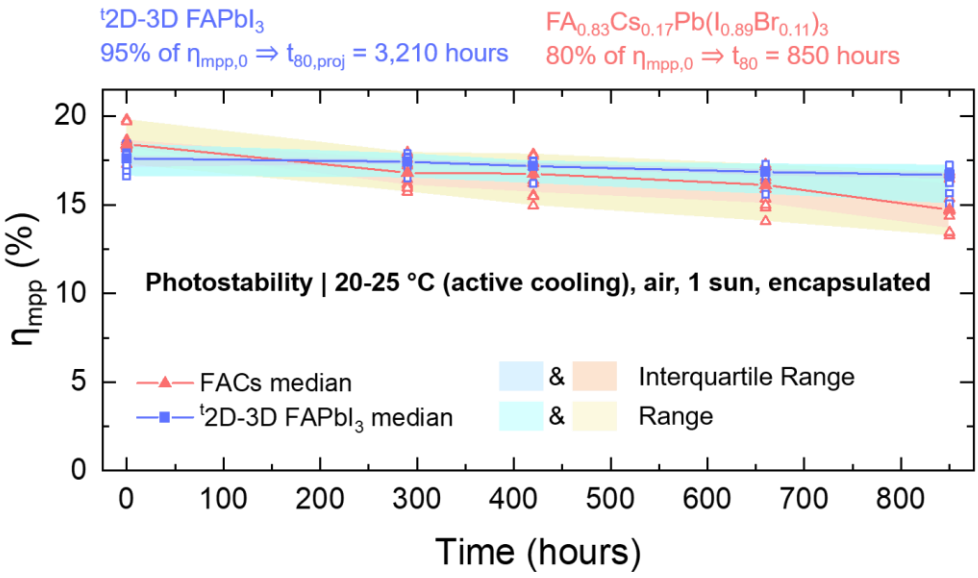


Figure 5.12 | p-i-n PSC photostability. Evolution of maximum power tracked efficiency (η_{mpp}) measured periodically on p-i-n PSCs employing ^{t}2D-3D $FAPbI_3$ (21 cells) or $FA_{0.83}Cs_{0.17}Pb(I_{0.9}Br_{0.1})_3$ (10 cells) as the photoactive layer, and encapsulated with an on-cell epoxy resin and cover slip. Cells actively cooled to between 20-25 °C and exposed to 1 sun equivalent light (LED array) (ISOS-L-1). Projected lifetimes to 80% ($t_{80,proj}$) of initial median efficiency ($\eta_{mpp,0}$) are calculated by linear extrapolation.

used in our thin film study (**Figure 5.13b**). Full details of the method of cell encapsulation are given in **Chapter 3**. Although both compositions appear to be relatively stable over the initial period of aging studied, it appears that again devices

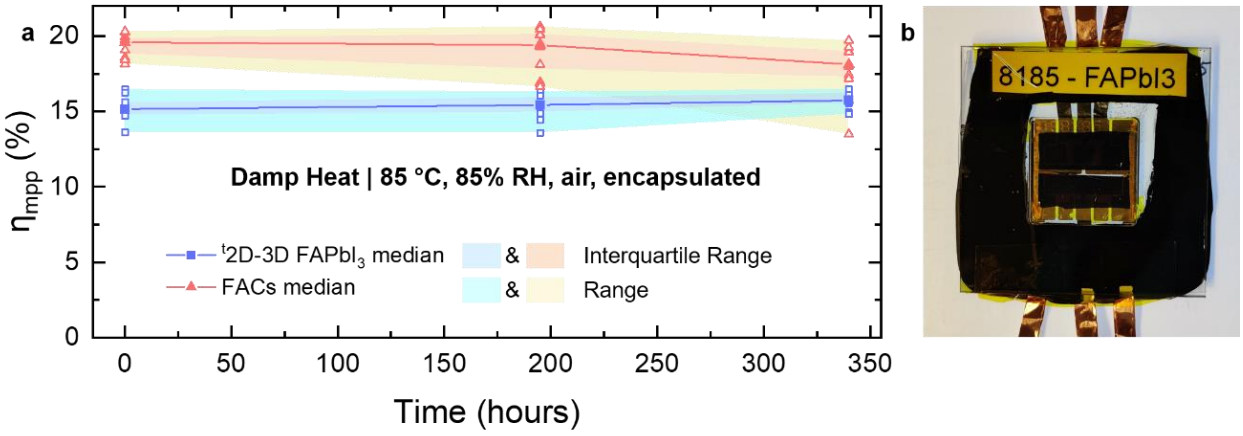


Figure 5.13 | p-i-n PSC damp-heat stability. (**a**) Evolution of maximum power tracked efficiency (η_{mpp}) measured periodically on p-i-n PSCs employing ^{t}2D-3D $FAPbI_3$ (9 cells) or $FA_{0.83}Cs_{0.17}Pb(I_{0.9}Br_{0.1})_3$ (11 cells) as the photoactive layer, and encapsulated with an on-cell epoxy resin and cover slip. Each measurement is taken after removing the device from the aging chamber and allowing it to cool to room temperature. We note that the absolute efficiency values shown are nominal only as, due to our encapsulation, appropriate masking of the PSCs is not possible and so the illuminated area is not known precisely. (**b**) Photograph of encapsulation of PSC. Full processes for encapsulation of thin films and PSCs are described in the **Methods**.

employing the $FA_{0.83}Cs_{0.17}Pb(I_{0.9}Br_{0.1})_3$ perovskite have begun degrading more rapidly that those containing ^{t}2D-3D $FAPbI_3$.

Finally, by introducing a 250 nm thick molybdenum oxide (MoO_3) barrier layer on top of the PSCs (**Figure 5.14c**) before an on-cell epoxy encapsulation, in **Figure 5.14b** we show a substantial increase in t_{80} from 41 hours for $FA_{0.83}Cs_{0.17}Pb(I_{0.9}Br_{0.1})_3$ devices (8 cells) to 575 hours for ^{t}2D-3D $FAPbI_3$ (7 cells) under the harsh conditions of ISOS-L-2 test. As has been previously reported[40], reaction between underlying

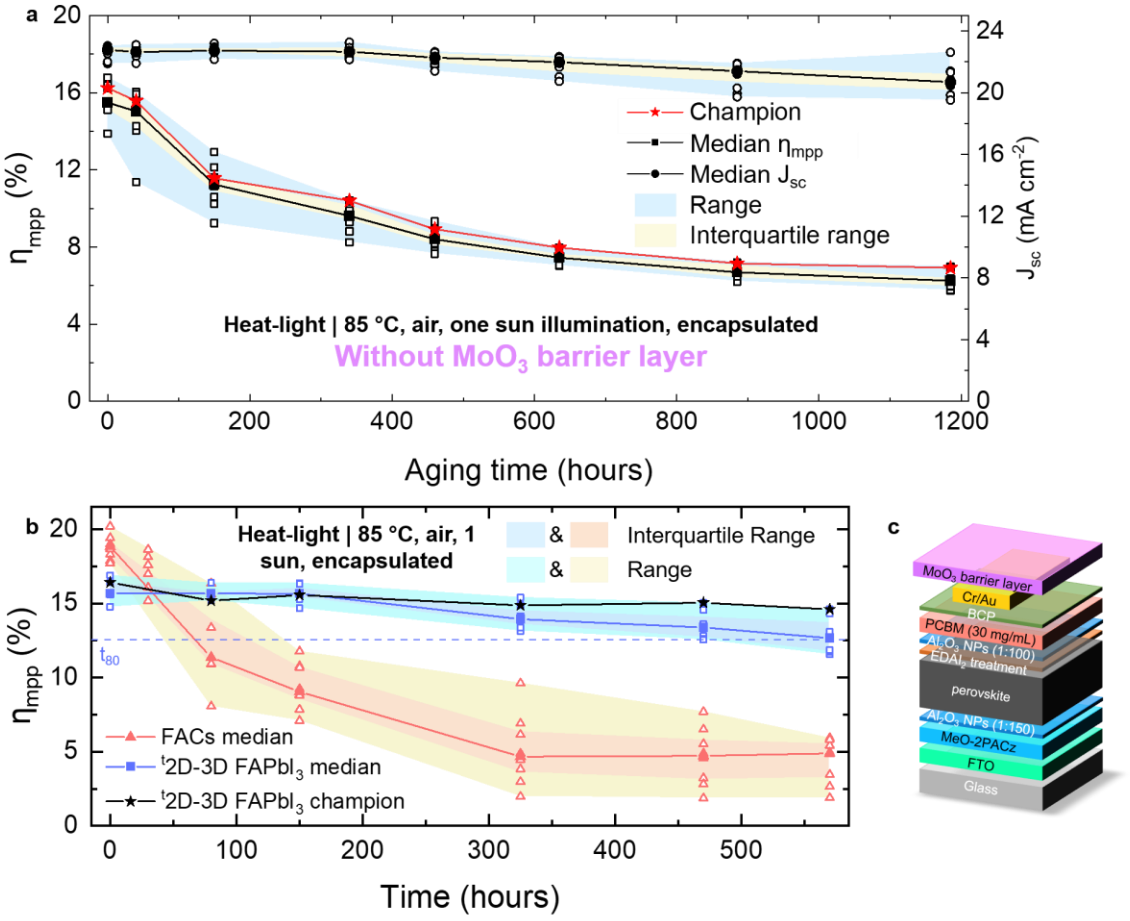


Figure 5.14 | p-i-n PSC heat-light stability. (**a**) Evolution of maximum power tracked efficiency (η_{mpp}) measured periodically on p-i-n PSCs employing ^{t}2D-3D $FAPbI_3$, encapsulated with an on-cell epoxy resin and cover slip (without a MoO_3 barrier layer) and aged at 85 °C under 1 sun illumination (ISOS-L-2). (**b**) Evolution of maximum power tracked efficiency (η_{mpp}) measured periodically on p-i-n PSCs employing ^{t}2D-3D $FAPbI_3$ (7 cells) or $FA_{0.83}Cs_{0.17}Pb(I_{0.9}Br_{0.1})_3$ (8 cells) as the photoactive layer, encapsulated with a 250 nm layer of MoO_3 followed by an on-cell epoxy resin and cover slip, and aged at 85 °C under 1 sun illumination (ISOS-L-2). (**c**) Schematic showing p-i-n cell architecture employed in this study (see main text for abbreviations).

layers and epoxy resins, as well as delamination of weakly adhered organic transport layers from adjacent perovskite or metal electrode layers, is found to be substantially reduced by introducing a MoO_3 barrier layer on top of the metal top electrodes prior to encapsulation with epoxy and cover glass. In **Figure 5.14a** we show the ISOS-L-2 stability of pin devices made using ^{t}2D-3D $FAPbI_3$ and exactly the same architecture as in **Figure 5.14b** except without the MoO_3 barrier layer. Long term retention of stabilised short circuit current density suggests that the rapid drop in efficiency observed in **Figure 5.14a** is not due to degradation of the perovskite material itself, as proves to be the case when the barrier layer is introduced.

5.5 – Conclusion and outlook

With so many processing variables at work, fully isolating and directly identifying the impact of any individual feature of perovskite processing on the properties of the resultant perovskite material is challenging. By developing a novel processing route that shares very little in common with the ubiquitous DMF:DMSO-solvated, anti-solvent engineered one-step approach to perovskite fabrication, here we have begun to disentangle the effect on perovskite stability of a number of processing decisions. These include the choice of precursor solvents, the temperature and duration of annealing, the growth pathway (one-step, sequential, templated sequential, etc.), and the composition of the perovskite itself.

The substantial enhancement in α-$FAPbI_3$ phase stability afforded by our 2D-templated, non-volatile solvent free processing route is exciting, and has permitted fabrication of n-i-p PSCs to retain their initial performance for over 1.5 years when stored in dry conditions. Substantial further study is, however, required in order to precisely identify the underlying mechanism of the enhancement. In a recent study

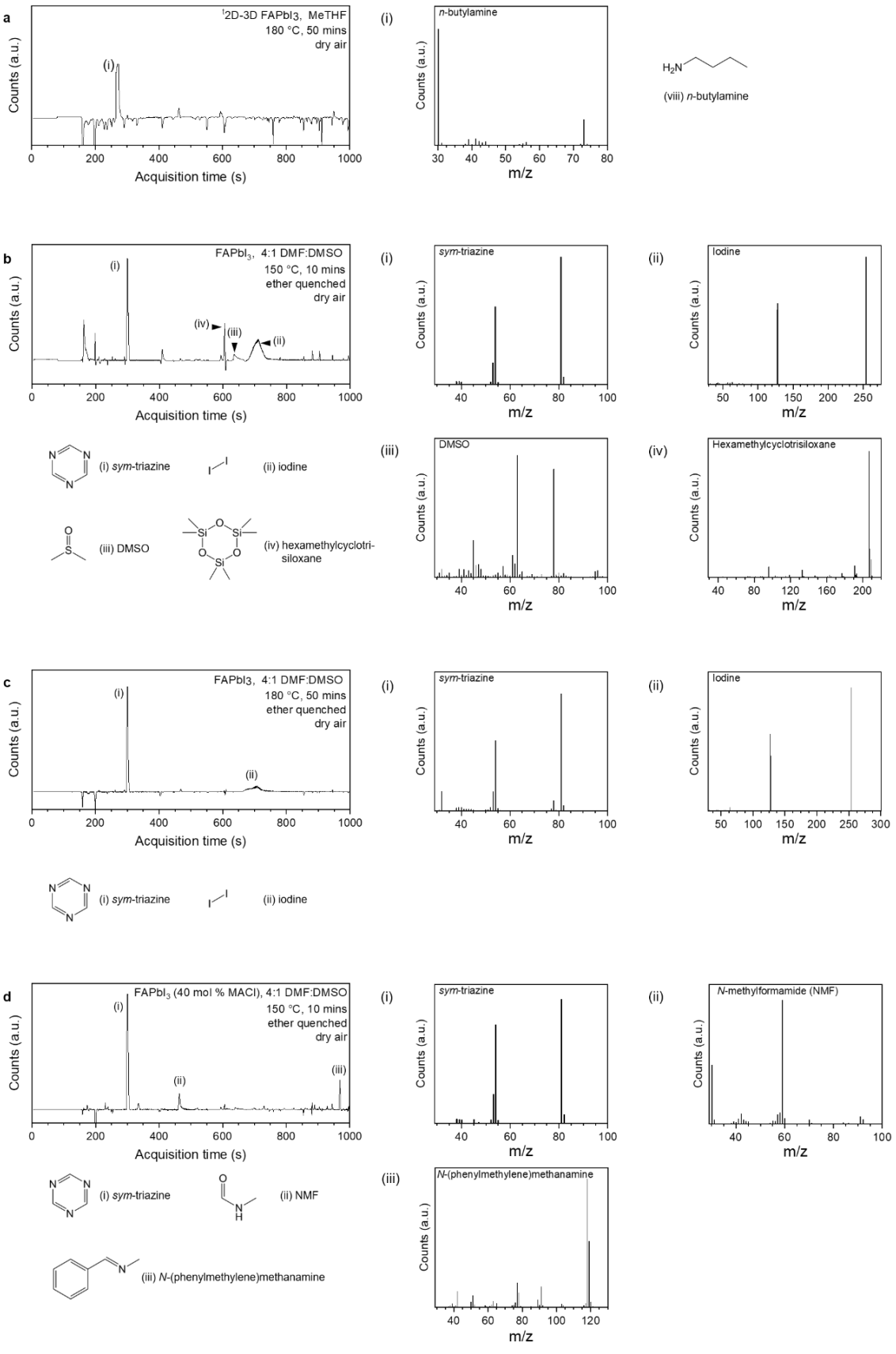
adjacent to this work[41] we have shown that the 2D-templating method leads to an α-$FAPbI_3$ material absent of optical features indicative of quantum confinement. It has been speculated that such quantum confinement may correspond to the presence of nanodomains of *2H*-$FAPbI_3$, which may in turn act to propagate transformation from the α- to the *2H*-phase. Further work to convincingly identify the proposed nanodomains, for example via selected area electron diffraction or nanoXRD, is now required, along with time-resolved methods to determine if such structural features do indeed accelerate the transformation of the bulk α-$FAPbI_3$ phase.

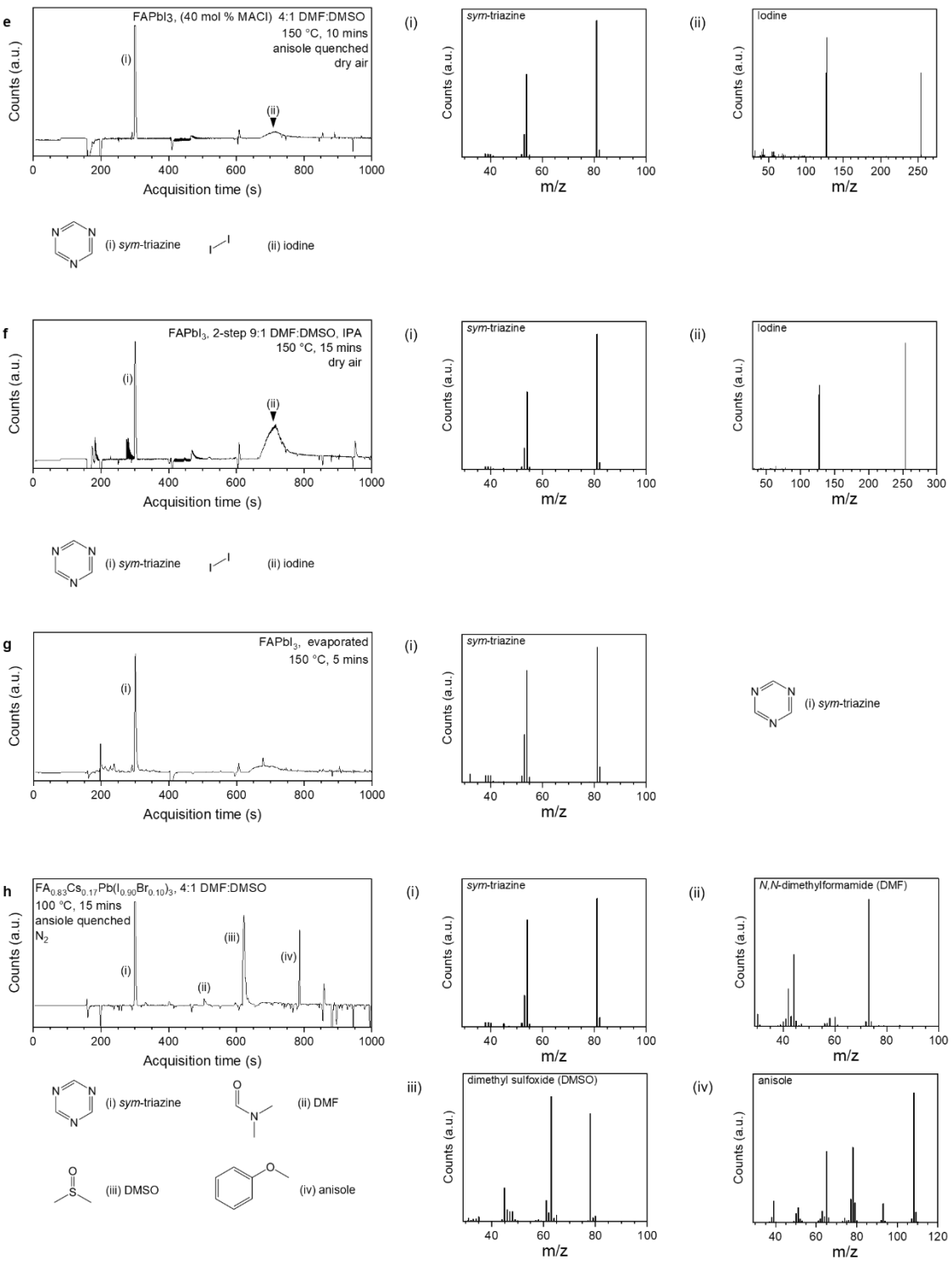
The mode for the retention of low volatility, highly coordinating solvents inside the deposited perovskite material also remains unclear, and is likely a function of the solvents in question and the precursor compounds employed, among other factors. However, the correlation between residual solvent retention and perovskite thermal stability shown in this Chapter across a range of perovskite materials is striking. Simply increasing the curing temperature to volatilise more of these retained solvents enhances resulting thermal stability, but often at the expense of perovskite material quality. We have found that a far superior approach is to employ high volatility processing solvents that are readily extracted during thermal curing. Moreover, we have shown that by templating the growth of the 3D photoactive perovskite by means of a 2D perovskite scaffold leads to even greater enhancements in thermal stability, substantially reducing the rate of a key mechanism for thermal degradation of FA^+; cyclisation to *sym*-triazine. We have speculated that to produce a nominally identical material that shows enhanced thermal stability of the FA^+ ions in its structure, a mechanism that is active at the atomic scale is likely in action. If so, it seems logical that this may be related to the presence of particular defects in the as-deposited perovskite. As discussed above, studies directly linking the presence of atomic-level

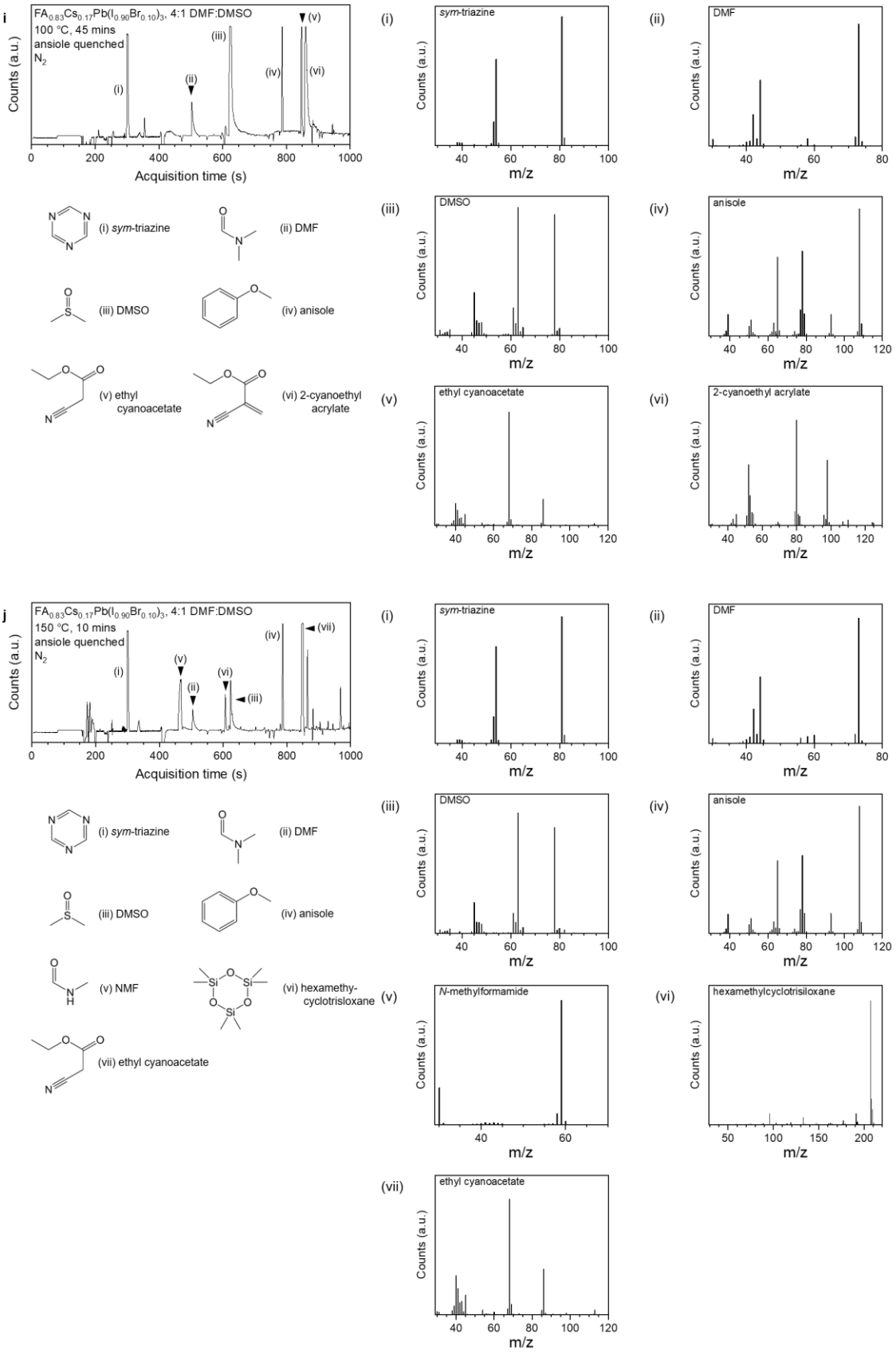
defects and mechanisms of bulk instability are not known to us. However, such work could uncover new approaches to predicting, recognising and – by careful control of defect formation – eliminating mechanisms of long-term degradation in halide perovskites. Techniques such as positron annihilation lifetime spectroscopy might be combined with DFT calculations and bulk measurement techniques such as solid-state nuclear magnetic resonance spectroscopy and nano X-ray diffraction to closely track the evolution of particular atomic-level defects in perovskites over time, and correlate these with simultaneous changes in the bulk material.

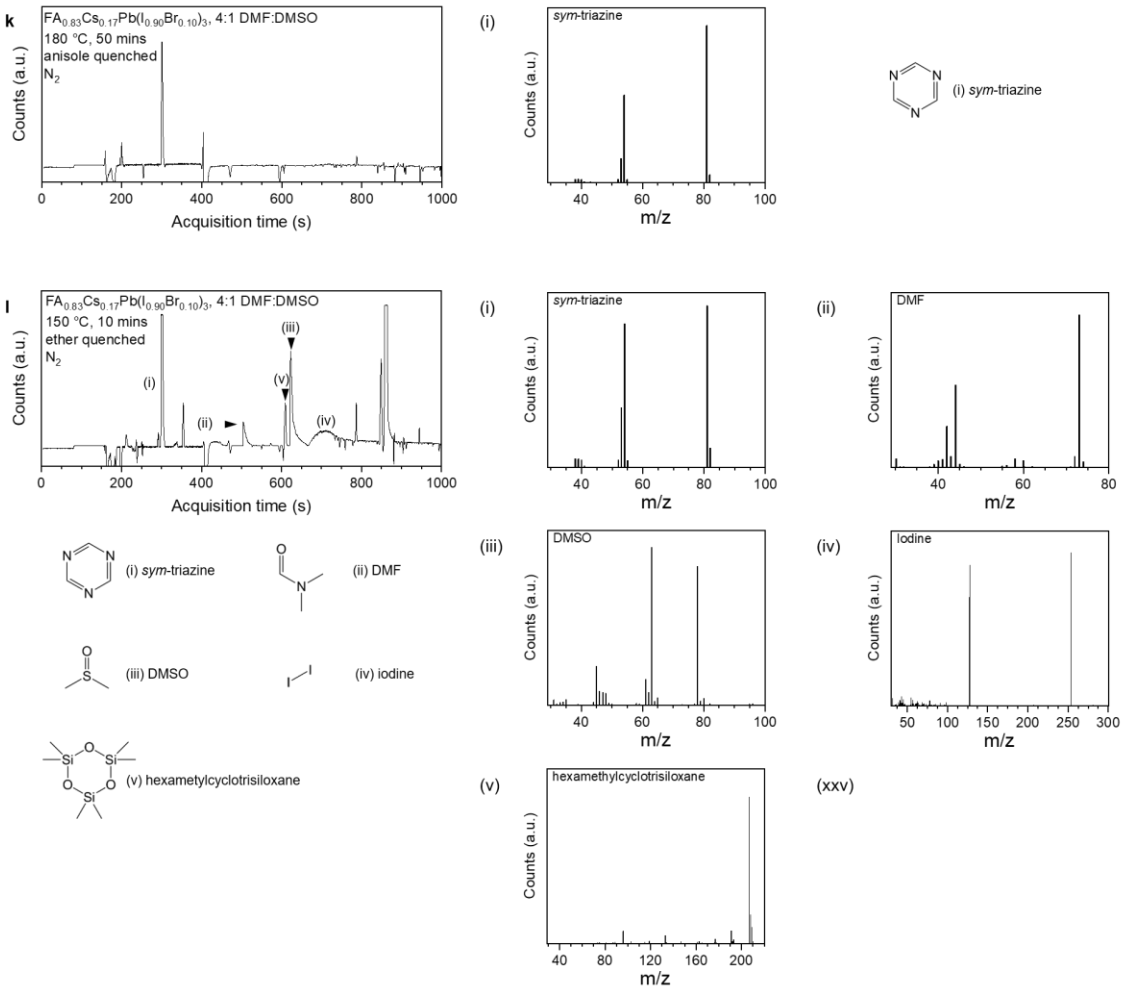
Although further investigation is required to fully understand the underlying mechanisms, we have already been able to demonstrate that these enhancements do impart a measurable improvement in operational stability for our ^{t}2D-3D α-$FAPbI_3$ material of >3,000 hours under both 85 °C, 85% RH and 85 °C, AM1.5 light conditions, as well as promising initial p-i-n PSC stability under same conditions. These results are extremely promising and warrant continued work in order to understand, and thus improve still further, the fundamental link between 2D-templating and enhanced stability.

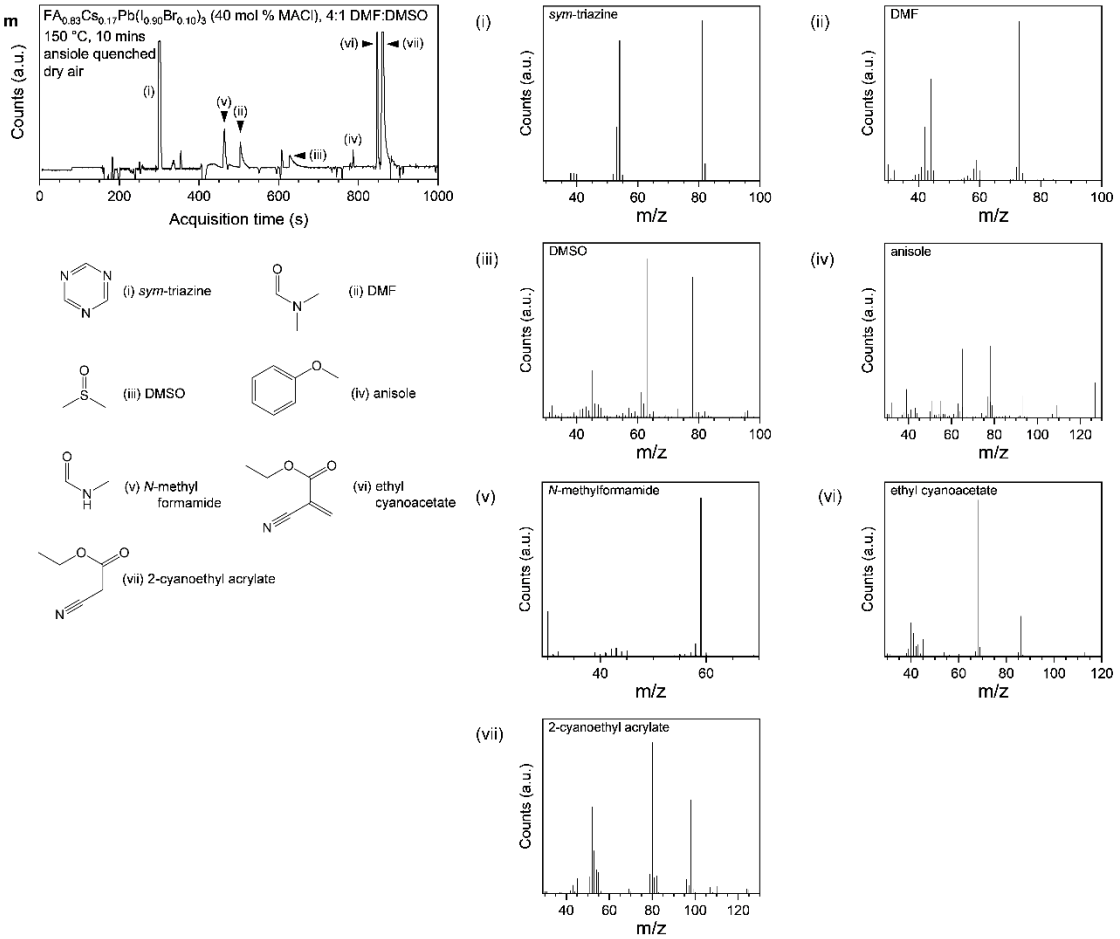
Appendix A5.1: TD-GCMS traces

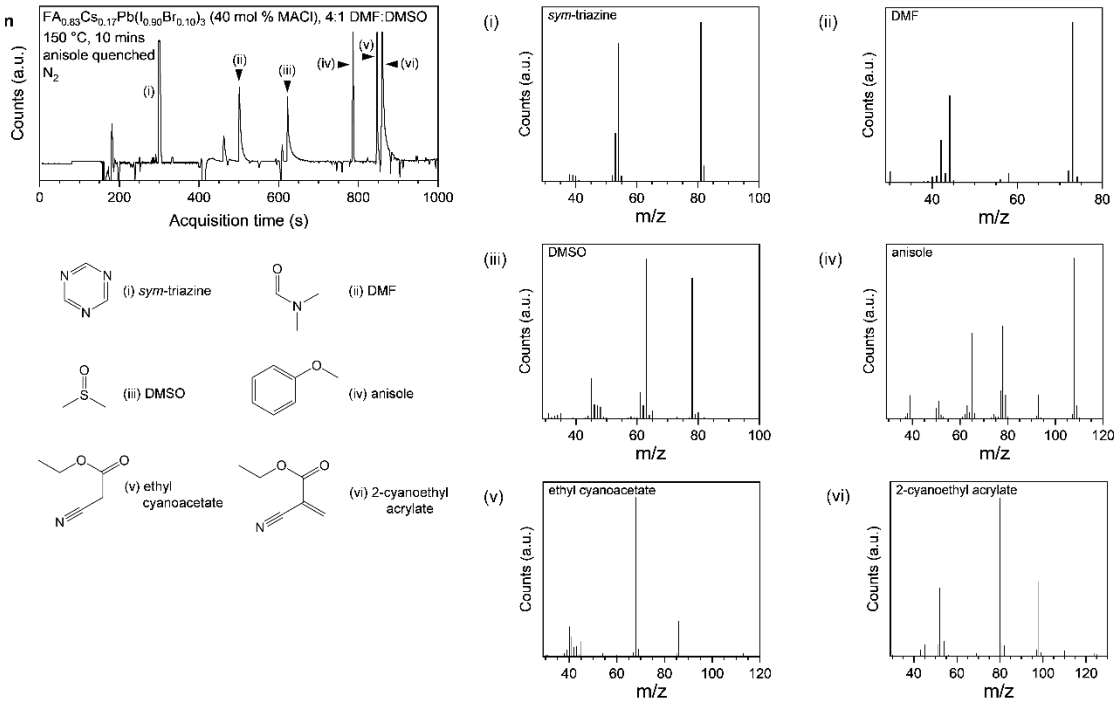



e
FAPbI3, (40 mol % MACl) 4:1 DMF:DMSO
150 °C, 10 mins
anisole quenched
dry air
Counts (a.u.)
Acquisition time (s)
(i)
(ii)
(i) sym-triazine
(ii) iodine
f
FAPbI3, 2-step 9:1 DMF:DMSO, IPA
150 °C, 15 mins
dry air
g
FAPbI3, evaporated
150 °C, 5 mins
h
FA0.83Cs0.17Pb(I0.90Br0.10)3, 4:1 DMF:DMSO
100 °C, 15 mins
ansiole quenched
N2
(iii)
(iv)
m/z
sym-triazine
Iodine
N,N-dimethylformamide (DMF)
dimethyl sulfoxide (DMSO)
anisole
(ii) DMF
(iii) DMSO
(iv) anisole


i
FA0.83Cs0.17Pb(I0.90Br0.10)3, 4:1 DMF:DMSO
100 °C, 45 mins
ansiole quenched
N2
Counts (a.u.)
Acquisition time (s)
(i) sym-triazine
(ii) DMF
(iii) DMSO
(iv) anisole
(v) ethyl cyanoacetate
(vi) 2-cyanoethyl acrylate
m/z
j
FA0.83Cs0.17Pb(I0.90Br0.10)3, 4:1 DMF:DMSO
150 °C, 10 mins
ansiole quenched
N2
(vi) hexamethy-cyclotrisloxane
(v) NMF
(vii) ethyl cyanoacetate
N-methylformamide
hexamethylcyclotrisiloxane


k
FA0.83Cs0.17Pb(I0.90Br0.10)3, 4:1 DMF:DMSO
180 °C, 50 mins
anisole quenched
N2
Counts (a.u.)
Acquisition time (s)
(i)
sym-triazine
m/z
(i) sym-triazine
l
FA0.83Cs0.17Pb(I0.90Br0.10)3, 4:1 DMF:DMSO
150 °C, 10 mins
ether quenched
N2
(i)
(ii)
(iii)
(iv)
(v)
(i) sym-triazine
(ii) DMF
(iii) DMSO
(iv) iodine
(v) hexametylcyclotrisiloxane
DMF
DMSO
Iodine
hexamethylcyclotrisiloxane
(xxv)


m
$FA_{0.83}Cs_{0.17}Pb(I_{0.90}Br_{0.10})_3$ (40 mol % MACl), 4:1 DMF:DMSO
150 °C, 10 mins
ansiole quenched
dry air
Counts (a.u.)
Acquisition time (s)
(i) sym-triazine
(ii) DMF
(iii) DMSO
(iv) anisole
(v) N-methyl formamide
(vi) ethyl cyanoacetate
(vii) 2-cyanoethyl acrylate
m/z


n
$FA_{0.83}Cs_{0.17}Pb(I_{0.90}Br_{0.10})_3$ (40 mol % MACl), 4:1 DMF:DMSO
150 °C, 10 mins
anisole quenched
N_2
Counts (a.u.)
Acquisition time (s)
(i) sym-triazine
(ii) DMF
(iii) DMSO
(iv) anisole
(v) ethyl cyanoacetate
(vi) 2-cyanoethyl acrylate
m/z

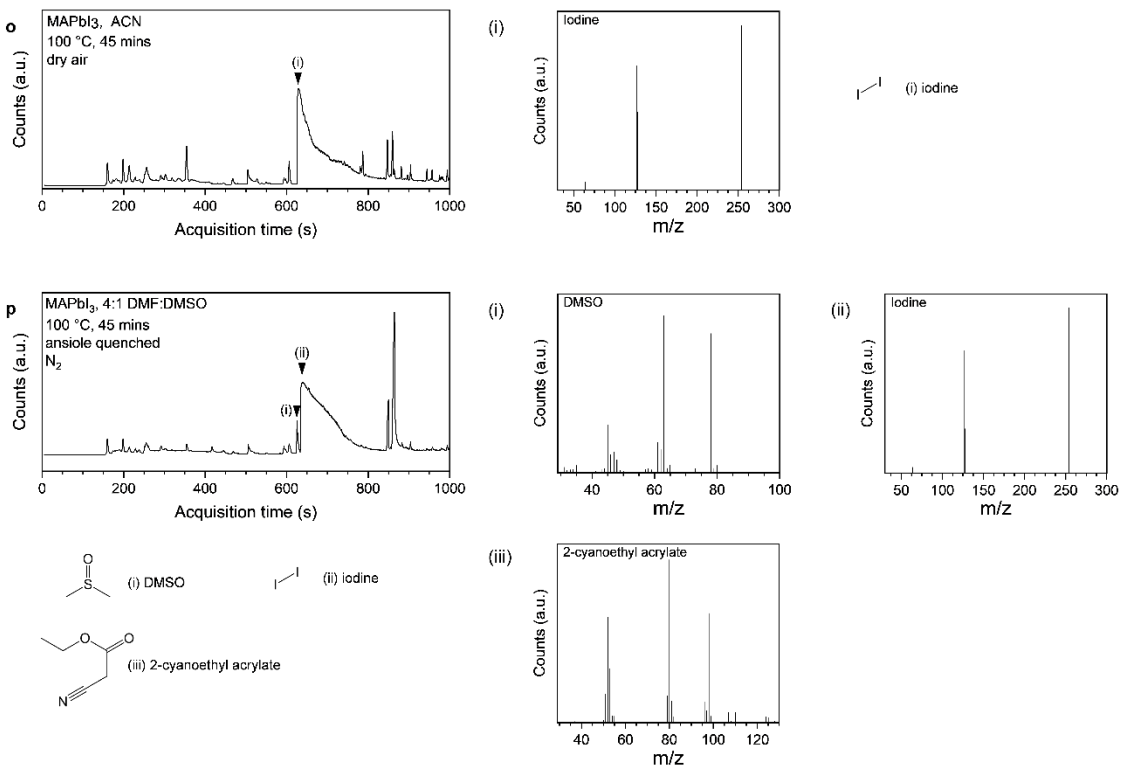


Figure A5.1 | Volatile products of perovskite thermal degradation. *Measurements and analysis carried out with the assistance of S. Reeksting.* Thermal desorption-gas chromatography-mass spectrometry (TD-GCMS) measurements. Chromatograms corresponding to thermal desorption from a wide range of state-of-the-art perovskite materials. Mass spectra of identifiable desorption products. All species are identified using the national institute of standards and technology (NIST) 17 database and show an identification score of at least ≥85%. Unlabelled signals are those for which no satisfactory match was found in the NIST 17 database. In each case a thin layer of material (400-1000 nm thick) is thermally treated (see methods sections for details) and the volatile organics compounds (VOCs) released are collected onto a porous adsorbent. For each experiment, tubes - containing the adsorbent charged with the VOCs released from a particular perovskite - are heated rapidly to desorb the VOCs, which are then directly loaded into a gas chromatography-mass spectrometry separation-detection unit. For each perovskite composition, the experiment was carried out at least in duplicate. Fabrication methods for the perovskite materials employed are reported in **Chapter 3**, where full description of the TD-GCMS technique is also given. A number of common contaminants were detected, notably hexamethylcyclotrisiloxane, *N*-(phenylmethylene)methanamine, ethyl cyanoacetate and 2-cyanoethyl acrylate. These are all associated with plastics and plastic fabrications, and as such we suspect they are introduced in trace quantities by either (i) the contact between the sharp-edged glass substrates and the plastic holding vessels in which samples were transported prior to measurements, or (ii) trace decomposition of the porous absorbent inside the collection tubes used to collect VOCs produced during thermal extraction. Variable decomposition of the porous absorbent during acquisition of reference GC traces (chamber blanks) is likely also responsible for the negative peaks observed in some GC traces. Full details given in the methods (**Chapter 3**).

5.6 – Bibliography

1. Khenkin, M. V. *et al.* Consensus statement for stability assessment and reporting for perovskite photovoltaics based on ISOS procedures. *Nat. Energy* **5**, 35–49 (2020).

2. Domanski, K., Alharbi, E. A., Hagfeldt, A., Grätzel, M. & Tress, W. Systematic investigation of the impact of operation conditions on the degradation behaviour of perovskite solar cells. *Nat. Energy* **3**, 61–67 (2018).

3. Yun, J. S. *et al.* Humidity-Induced Degradation via Grain Boundaries of $HC(NH_2)_2PbI_3$ Planar Perovskite Solar Cells. *Adv. Funct. Mater.* **28**, (2018).

4. Tan, S. *et al.* Shallow Iodine Defects Accelerate the Degradation of α-Phase Formamidinium Perovskite. *Joule* **4**, 2426–2442 (2020).

5. Schwenzer, J. A. *et al.* Thermal Stability and Cation Composition of Hybrid Organic-Inorganic Perovskites. *ACS Appl. Mater. Interfaces* **13**, 15292–15304 (2021).

6. Turren-Cruz, S. H., Hagfeldt, A. & Saliba, M. Methylammonium-free, high-performance, and stable perovskite solar cells on a planar architecture. *Science (6413).* **362**, 449–453 (2018).

7. Juarez-Perez, E. J., Ono, L. K. & Qi, Y. Thermal degradation of formamidinium based lead halide perovskites into: Sym -triazine and hydrogen cyanide observed by coupled thermogravimetry-mass spectrometry analysis. *J. Mater. Chem. A* **7**, 16912–16919 (2019).

8. Kim, M. *et al.* Methylammonium Chloride Induces Intermediate Phase Stabilization for Efficient Perovskite Solar Cells. *Joule* 1–14 (2019).

9. Asfaw, A. A., Wolfs, K., Van Schepdael, A. & Adams, E. Determination of residual dimethylsulphoxide in drug loaded gelatin using thermal desorber – gas chromatography. *J. Pharm. Biomed. Anal.* **153**, 193–198 (2018).

10. Lin, Y. H. *et al.* A piperidinium salt stabilizes efficient metal-halide perovskite solar cells. *Science (6499).* **369**, 96–102 (2020).

11. Chen, S. *et al.* Stabilizing perovskite-substrate interfaces for high-performance perovskite modules. *Science (6557).* **373**, 902–907 (2021).

12. Scherrer, P. *et al.* Nachrichten von der Gesellschaft der Wissenschaften zu Göttingen. *Mathematisch-Physikalische Klasse.* **2**, 98-100 (1918).

13. Patteson, A.L.. *et al.* The Scherrer formula for X-ray particle size determination. *Phys. Rev.* **56** (10), 978-982 (1939).

14. Shi, L. *et al.* Gas chromatography-mass spectrometry analyses of encapsulated stable perovskite solar cells. *Science (6497).* **368**, (2020).

15. Ma, L. *et al.* Temperature-dependent thermal decomposition pathway of organic-inorganic halide perovskite materials. *Chem. Mater.* **31**, 8515–8522 (2019).

16. Keeble, D.J. *et al.* Identification of lead vacancy defects in lead halide perovskites. *Nat Commun* 12, 5566 (2021).

17. Meggiolaro, D. *et al.* Iodine chemistry determines the defect tolerance of lead-halide perovskites. *Energy Environ. Sci.,* 11, 702 (2018).

18. Woo, Y.W. *et al.* Inhomogeneous Defect Distribution in Mixed-Polytype Metal Halide Perovskites. *ACS Energy Lett.*, 8, 1, 356–360 (2023).

19. Doherty, T. A. S. *et al.* Stabilized tilted-octahedra halide perovskites inhibit local formation of performance-limiting phases. *Science (6575).* **374**, 1598–1605 (2021).

20. Rothmann, M. U. *et al.* Direct observation of intrinsic twin domains in tetragonal $CH_3NH_3PbI_3$. *Nat. Commun.* **8**, 6–13 (2017).

21. Woo, Y. W., Li, Z., Jung, Y.-K., Park, J.-S. & Walsh, A. Inhomogeneous Defect Distribution in

Mixed-Polytype Metal Halide Perovskites. *ACS Energy Lett.* **8**, 356–360 (2022).

22. Wang, Z. *et al.* Efficient ambient-air-stable solar cells with 2D-3D heterostructured butylammonium-caesium-formamidinium lead halide perovskites. *Nat. Energy* **2**, 1–10 (2017).

23. Fu, F. *et al.* I_2 vapor-induced degradation of formamidinium lead iodide based perovskite solar cells under heat-light soaking conditions. *Energy Environ. Sci.* **12**, 3074–3088 (2019).

24. Jeong, M. *et al.* Stable perovskite solar cells with efficiency exceeding 24.8% and 0.3-V voltage loss. *Science (6511).* **369**, 1615–1620 (2020).

25. Kempe, M. D., Panchagade, D., Reese, M. O. & Dameron, A. A. Modelling moisture ingress through polyisobutylene-based edge-seals. *Prog. Photovol. Res. App.* **23**, 570–581 (2014).

26. Chen, T. et al. Entropy-driven structural transition and kinetic trapping in formamidinium lead iodide perovskite. Sci. Adv. 2, 1–7 (2016).

27. Ren, G. *et al.* Strategies of modifying spiro-OMeTAD materials for perovskite solar cells: a review. *J. Mater. Chem. A* **9**, 4589–4625 (2021).

28. Kasparavicius, E. *et al.* Oxidized Spiro-OMeTAD: Investigation of Stability in Contact with Various Perovskite Compositions. *ACS Appl. Energy Mater.* **4**, 13696–13705 (2021).

29. Schloemer, T. H., Christians, J. A., Luther, J. M. & Sellinger, A. Doping strategies for small molecule organic hole-transport materials: impacts on perovskite solar cell performance and stability. *Chem. Sci.* **10**, 1904–1935 (2019).

30. Zhao, X., Kim, H. S., Seo, J. Y. & Park, N. G. Effect of Selective Contacts on the Thermal Stability of Perovskite Solar Cells. *ACS Appl. Mater. Interfaces* **9**, 7148–7153 (2017).

31. Li, Z. *et al.* Extrinsic ion migration in perovskite solar cells. *Energy Environ. Sci.* **10**, 1234–1242 (2017).

32. Roose, B. *et al.* Mesoporous SnO_2 electron selective contact enables UV-stable perovskite solar cells. *Nano Energy* **30**, 517–522 (2016).

33. Wang, K. *et al.* Novel inorganic electron transport layers for planar perovskite solar cells: Progress and prospective. *Nano Energy* **68**, 104289 (2020).

34. Thampy, S., Zhang, B., Hong, K. H., Cho, K. & Hsu, J. W. P. Altered Stability and Degradation Pathway of $CH_3NH_3PbI_3$ in Contact with Metal Oxide. *ACS Energy Lett.* **5**, 1147–1152 (2020).

35. Uddin, A. & Yi, H. Progress and Challenges of SnO_2 Electron Transport Layer for Perovskite Solar Cells: A Critical Review. *Sol. RRL* **6**, (2022).

36. Jiang, Q. *et al.* Surface reaction for efficient and stable inverted perovskite solar cells. *Nature* **611**, 278–283 (2022).

37. Jacobsson, T. J. *et al.* An open-access database and analysis tool for perovskite solar cells based on the FAIR data principles. *Nat. Energy* **7**, 107–115 (2022).

38. Wang, H. *et al.* Enhanced crystallization and performance of formamidinium lead triiodide perovskite solar cells through PbI_2-$SrCl_2$ modulation. *Mater. Today Energy* **7**, 239–245 (2018).

39. Xi, J. *et al.* Deciphering perovskite crystal growth in interdiffusion protocol for planar heterojunction photovoltaic devices. *Org. Electron.* **53**, 88–95 (2018).

40. Belich, N.A. *et al.* How to stabilize standard perovskite solar cells to withstand operating conditions under an ambient environment for more than 1000 hours using simple and universal encapsulation. *J. Energy. Chem.* **78**, 246–252 (2023).

41. Elmestekawy, K.A. *et al.* Photovoltaic Performance of $FAPbI_3$ Perovskite Is Hampered by Intrinsic Quantum Confinement. *ACS Energy Lett.,* 8, 6, 2543–2551 (2023).

Chapter 6 – Understanding the degradation of methylenediammonium and its stabilisation of formamidinium lead triiodide single crystals

The work in this chapter is adapted from: “Understanding the degradation of methylenediammonium and its stabilisation of formamidinium lead triiodide single crystals”, Benjamin M. Gallant, Elisabeth A. Duijnstee, Philippe Holzhey, Dominik J. Kubicki, Silvia Collavini, Bernd Sturdza, Harry C. Sansom, Joel Smith, Matthias J. Gutmann, Santanu Saha, Murali Gedda, Mohamad I. Nugraha, Manuel Kober-Czerny, Chelsea Xia, Adam D. Wright, Yen-Hun Lin, Alexandra J. Ramadan, Esther Y.-H. Hung, Seongrok Seo, Suer Zhou, Jongchul Lim, Thomas D. Anthopoulos, Marina R. Filip, Michael B. Johnston, Robin Nicholas, Juan Luis Delgado, Henry J. Snaith (*Accepted, JACS*).

6.1 – Introduction

Hybrid organic-inorganic metal halide perovskites are recognized as one of the most promising emerging semiconducting materials for optoelectronic applications due to their excellent properties including tuneable bandgaps[1], high absorption coefficients[2] and long carrier diffusion lengths[3]. Among the “ABX_3” lead-halide perovskites reported to-date, $FAPbI_3$ (FA^+ is formamidinium, $HC(NH_2)_2^+$)[4] has the narrowest achievable bandgap, allowing for the highest theoretical photovoltaic power conversion efficiency (PCE) in a single-junction architecture[5]. For this reason, the majority of recent world record PCE perovskite photovoltaics have employed $FAPbI_3$-based materials as their

photoabsorbing layer[6–8]. However, under ambient conditions, the cubic α-phase of $FAPbI_3$ is thermodynamically unstable with respect to transformation to the non-perovskite hexagonal δ-phase, which possesses an undesirable wider bandgap. Despite this, the phase transition is kinetically inhibited under ambient conditions permitting metastable α-$FAPbI_3$ to persist for hours, days and even months, with strong dependence on both conditions of processing and the relative humidity in which the processed material is stored[9,10]. The phase stability of $FAPbI_3$ thin films and single crystals is necessary for their practical use, and major efforts are directed at finding approaches to suppress the α-to-δ phase transition. In particular, smaller A-site cations have been used to stabilise the perovskite lattice by alloying with FA^+. Most frequently used are MA^+ (which has been shown to introduce the thermal instability[11,12]) and the alkali-metal Cs^+,[13,14] often in conjugation with I^-, Br^- and Cl^- X-site alloying. Although promising, such approaches can introduce undesirable properties. Bandgap increases induced by structural changes due to inclusion of smaller cations[15] are unideal for single junction photovoltaics. Furthermore, compositional inhomogeneities introduced during growth can render materials susceptible to ion segregation under operation.[11,16] It is therefore crucial to develop strategies to improve the stability of $FAPbI_3$, without diminishing its useful properties.

In 2019, Min et al.,[17] reported highly efficient α-$FAPbI_3$ solar cells based on polycrystalline thin films by incorporating a small amount of methylenediammonium dichloride ($MDACl_2$, 3.8 mol%) into the precursor solution, while maintaining the inherent bandgap of $FAPbI_3$. The authors attribute the high certified PCE of 23.7% to the addition of $MDACl_2$ and report that MDA^{2+} leads to structural stabilization of α-$FAPbI_3$ *via* partial replacement of FA^+ with MDA^{2+} alongside interstitial Cl^- incorporation. In a subsequent work, Kim, et al.,[18] propose that dual substitution of 3

mol% of Cs^+ and MDA^{2+} on FA^+ sites lowers the lattice strain and trap density in perovskite solar cells. In a third work – again from Seok and co-workers – MDA^{2+} was used alongside $FAPbI_3$ with a chemical bath deposited SnO_2 layer to reach the highest yet-reported efficiency of 25.8% (certified 25.5%) for perovskite solar cells.[6,19]

In order to isolate the role of $MDACl_2$ we here study the effect of its addition to the precursor solution during the growth of $FAPbI_3$ single crystals (denoted $FAPbI_3$-M). We find that the highly acidic MDA^{2+} cation is unstable in solution, degrading rapidly into ammonium and hexamethylenetetramine (HMTA). However, this degradation is further complicated by the presence of FA^+ in the precursor solution, reaction with which can interrupt the degradation pathway and instead lead to formation of tetrahydro-1,3,5-triazinium (THTZ-H^+). We find that of all the degradation products formed, it is THTZ-H^+ that is present in $FAPbI_3$-M crystals. We show that $FAPbI_3$-M crystals grown possess vastly improved α-phase stability (>1 year in air) and significantly reduced defect density.

6.2 – Single crystal growth and optoelectronic performance

We grow the single crystals via the inverse temperature crystallization method.[20,21] The control $FAPbI_3$ single crystals are prepared by dissolving equimolar FAI and PbI_2 in γ-butyrolactone (GBL). Crystal growth is directed by addition of an appropriate seed crystal to this precursor solution. Heating to a temperature of 95 °C leads to growth of the seed into an α-$FAPbI_3$ single crystal between 2-4 mm in length. For the $FAPbI_3$-M single crystals, we add 3.8 mol% (with respect to the Pb content) of $MDACl_2$ to the $FAPbI_3$ perovskite precursor solution. We note that in contrast to Min et al.[19] we do not add MACl to any of our precursor solutions, as we aim to isolate and investigate the effect of $MDACl_2$ on $FAPbI_3$ phase stability. Further details on crystal growth are

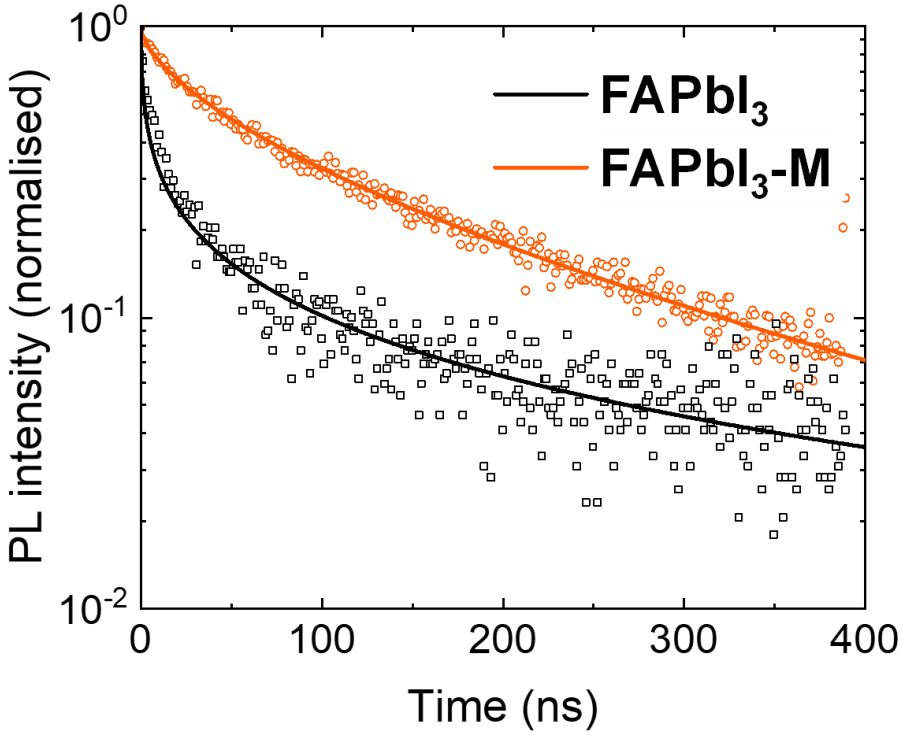


Figure 6.1 | Single crystal optoelectronics. *All measurements and analysis carried out by A. Wright.* (**a**) Time-resolved photoluminescence measurements of $FAPbI_3$ and $FAPbI_3$-M.

discussed in **Chapter 3.2.5**. We heat the single crystals in a vacuum oven at 180 °C for 30 minutes to remove residual solvent on the crystal surface. Single crystal X-ray diffraction (SCXRD) confirms the 3D perovskite phase in each case, with crystal structures solved in the $Pm\bar{3}m$ cubic space group, as previously reported[22]. Crystal data and structure refinement statistics are shown in **Appendix A6.1** (p193), where we also discuss our SCXRD measurements in detail, including our observation of a pronounced difference in the degree of twinning detected in $FAPbI_3$ crystals grown in the presence of different additives.

We first investigate the impact of $MDACl_2$ on the optoelectronic properties of the $FAPbI_3$ single crystals. Fitting of time-resolved photoluminescence (TRPL, **Figure 6.1**) decay traces reveals a significant increase in photoluminescence lifetime from 47 ns for the $FAPbI_3$ single crystal to 121 ns for the $FAPbI_3$-M single crystal at a fluence of

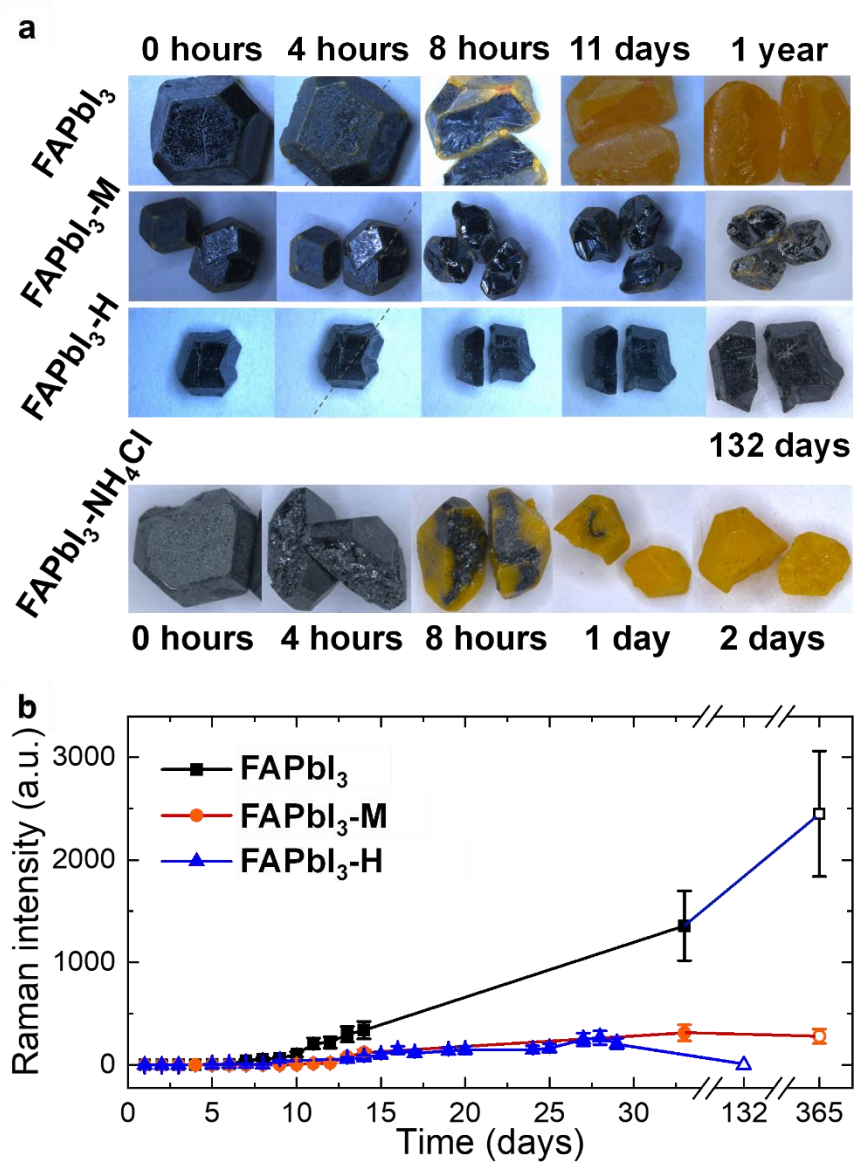


Figure 6.2 | Single crystal stability. *Raman measurements and analysis carried out by B. Sturdza.* **a)** Optical microscope images of $FAPbI_3$, $FAPbI_3$-M, $FAPbI_3$-H and $FAPbI_3$-NH_4Cl crystals (grown in the presence of no additive, $MDACl_2$, HMTA and NH_4Cl, respectively). The crystals are cleaved after 4 hours. The crystals were kept in glass vials under ambient conditions (dark, relative humidity ~30-80%) throughout the measurement period. **b)** Temporal evolution of δ-phase Raman peak intensity for $FAPbI_3$, $FAPbI_3$-M, $FAPbI_3$-H single crystals. The single crystals were kept in air for the first 33 days and stored afterwards in a glass vial under ambient conditions.

18 nJ/cm^2. More details on this measurement and the fitting are given in the **Chapter 3.3.1**.

Significantly, we also find that $FAPbI_3$-M crystals possess substantially greater α-phase (black) stability in ambient air than neat $FAPbI_3$. We observe optically the growth of trace regions of a δ-phase on the crystal surface of both materials after only a few hours of storage in air (**Figure 6.2a**). For $FAPbI_3$-M the degradation does not

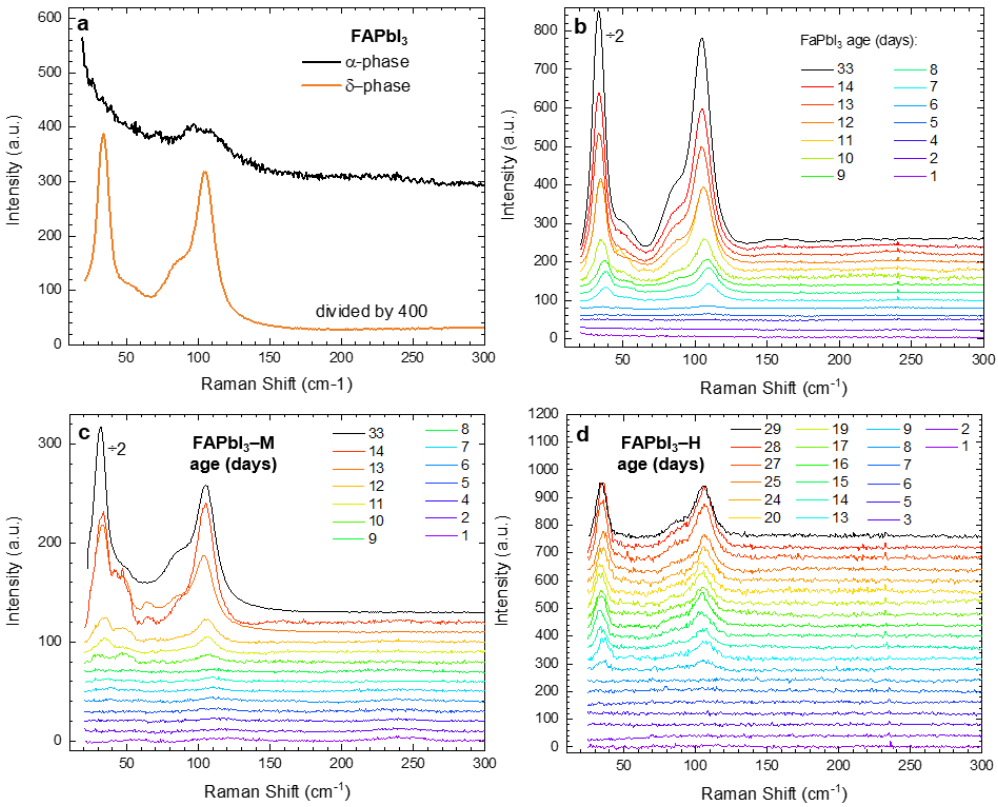


Figure 6.3 | Investigating α-$FAPbI_3$ single crystal with Raman spectroscopy. *Raman measurements and analysis carried out by B. Sturdza.* Raman spectra of different $FAPbI_3$ single crystals. **(a)** Comparison of α-phase and δ-phase $FAPbI_3$. **(b) – (d)** Aging of $FAPbI_3$, $FAPbI_3$-M and $FAPbI_3$-H single crystals in ambient conditions. All crystals were kept at ambient conditions in the Raman setup for the duration of the entire stability experiment and multiple spots on the surface were compared, which resulted in a relative deviation of about 25% between peak intensities measured at different positions on the same day.

propagate significantly upon the surface, nor into the bulk of the material, as seen when we cleave the crystals after several hours. Notably, the $FAPbI_3$-M crystals remain predominantly in their α-phase after a year of storage in ambient air. By contrast, $FAPbI_3$ crystals display complete phase transformation to the photoinactive δ-phase (yellow) in a few days (**Figure 6.2a**).

To quantitatively track the phase stability of the crystals, we monitor the absolute Raman intensity of the best resolved δ-phase peak (at a Raman shift of 108 cm^{-1}) under ambient conditions. As **Figure 6.2b** shows (complete Raman spectra shown in **Figure 6.3**), neat $FAPbI_3$ undergoes detectable δ-phase formation after 7 days. This onset occurs at 11 days for $FAPbI_3$-M. In Raman spectra of the same crystals after 1

year of storage in air-filled vials we detect (2.5 ± 0.5) x 10^3 and (0.25 ± 0.06) x 10^3 δ-phase peak counts for $FAPbI_3$ and $FAPbI_3$-M respectively. Peak intensity is proportional to the fraction of the probed surface layer in the δ-phase. Notably, the thickness of the probed layer for α-phase $FAPbI_3$ is estimated to be ~100 nm via the absorption coefficient (ca. 10^5 cm^{-1} at the Raman laser wavelength of 532 nm)[27]. Thus, onset of the δ-phase peak in **Figure 6.3** corresponds to degradation of only the top surface of the crystals. We obtain complementary bulk degradation data by carrying out the Raman measurement on freshly cleaved crystals. Cleaving a $FAPbI_3$-M crystal after 285 days of aging gives a ratio of $I_{bulk}/I_{surface}$ = 0.10 ± 0.03 for the δ-phase. This confirms that the observed δ-phase formation occurs in only a thin surface layer of $FAPbI_3$-M crystals, while the bulk remains largely unaffected. By contrast, the neat $FAPbI_3$ crystal is entirely converted to the δ-phase.

6.3 – MDA^{2+} solution instability

Having established the substantial advantages to $FAPbI_3$ single crystal properties of $MDACl_2$ addition, we now investigate in detail the activity of this additive in solution. It has been reported that MDA^{2+} is incorporated within the cubic ABX_3 perovskite lattice on the A-site in solution-processed polycrystalline thin films based on $FAPbI_3$, and thus that A-site cation mixing is responsible for the enhanced α-phase stability[17,18]. However, we do not observe the presence of MDA^{2+} in any of the precursor solutions at any time. **Figure 6.4** shows the ^{1}H solution NMR spectra acquired from a solution of $MDACl_2$ dissolved in DMSO-d_6 at 1 minute, 10 minutes and 6 days after initial dissolution. In **Figure 6.5** we show the predicted ^{1}H NMR spectrum of MDA^{2+} in DMSO-d_6 and contrast this to the experimental spectra. At the shortest time after dissolution the ^{1}H NMR spectrum already shows several unexpected species are present in solution. We attribute the distinctive 1:1:1 triplet to NH_4^+, with the splitting

due to a J-coupling of ^{1}H to the quadrupolar (I = 1) ^{14}N nucleus ($^{1}J_{14N\text{-}1H}$ = 50.8 Hz). The signal, initially at 7.30 ppm, rapidly shifts and stabilizes at 7.41 ppm, as is common for ammonium species under varying pH conditions. We note that the coupling observed as a result of ^{1}H interaction with the quadrupolar I = 1 ^{14}N nuclei is typically only observed in the case of a near-zero electric field gradient at the quadrupolar nucleus, otherwise quadrupolar relaxation becomes too rapid to permit coupling[28].

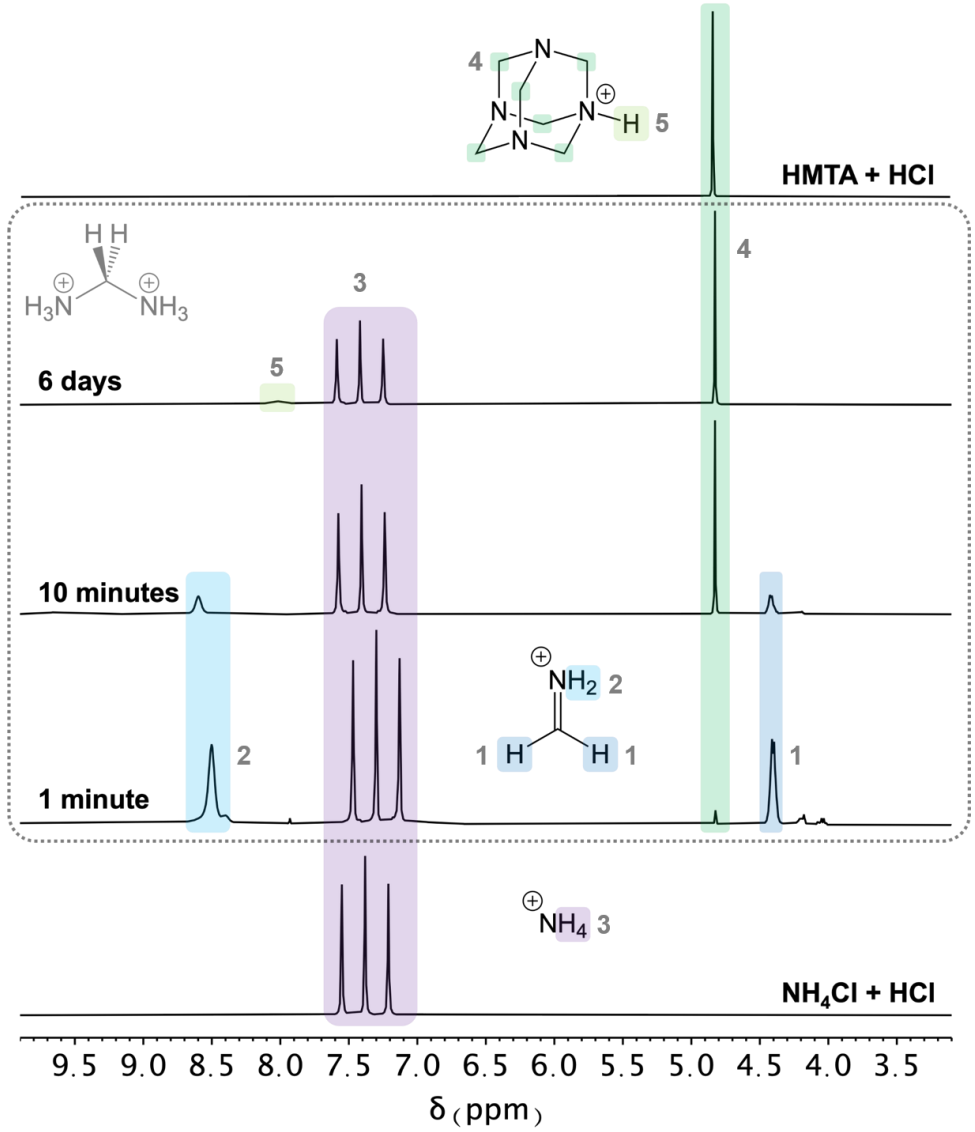


Figure 6.4 | Degradation of MDA^{2+}. ^{1}H solution nuclear magnetic resonance (NMR) spectra tracking the evolution of $MDACl_2$ upon dissolution in DMSO-d_6 . Bottom: Spectra acquired from acidified solution of ammonium chloride, showing diagnostic 1:1:1 triplet due to $^{1}J_{14N\text{-}1H}$ coupling. Variation in chemical shift of ammonium ^{1}H between samples is attributed to slight differences in pH. Top: Spectra acquired from acidified solution of (HMTA). Colour scheme correlates detected signals with ^{1}H chemical environments in detected species

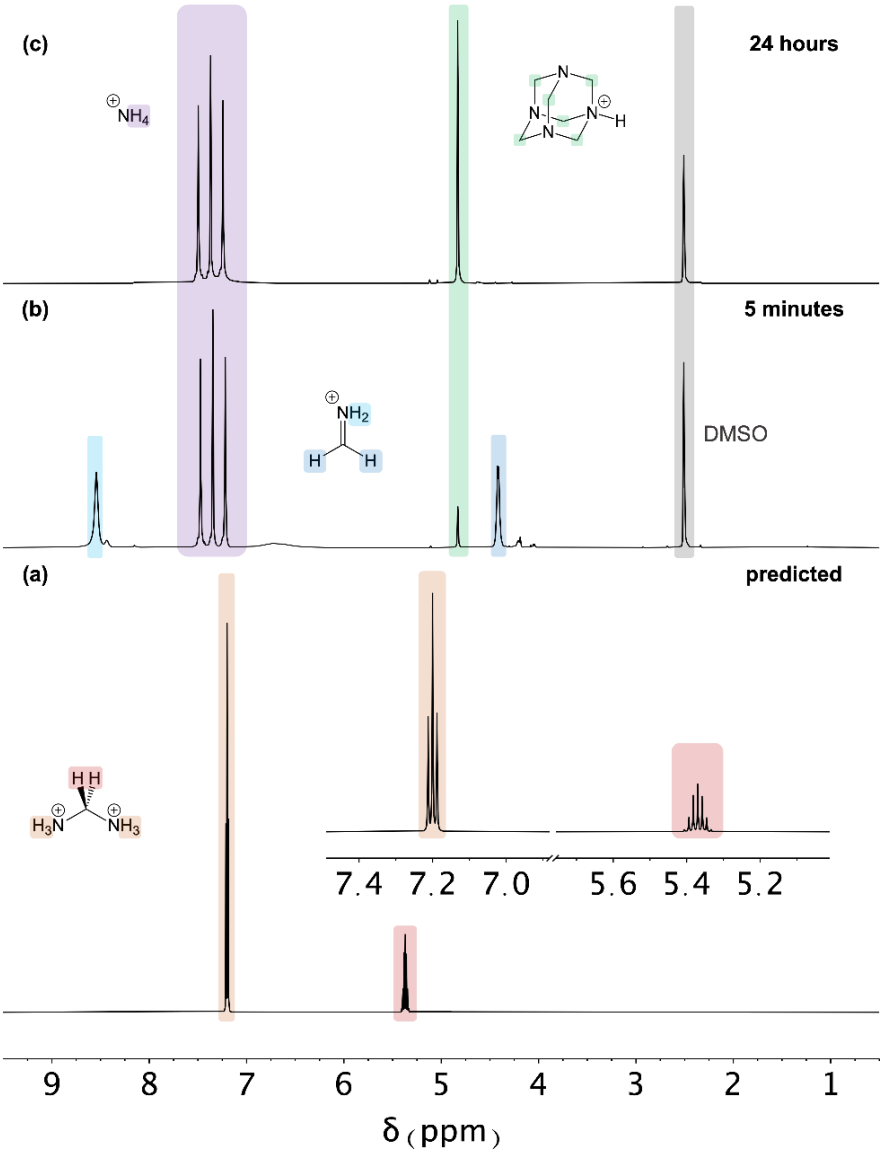


Figure 6.5 | MDA^{2+} predicted NMR spectra. ^{1}H solution nuclear magnetic resonance spectra of $MDACl_2$. **a**, Predicted spectrum of $MDACl_2$ in d^6-DMSO, generated using Mestrenova 14.1.1 software. Inset: expansion of spectral regions of interest. Experimental spectra measured (**b**) 5 minutes and (**c**) 24 hours after dissolution of $MDACl_2$ precursor powder. We note that the spectrum after 5 minutes bears close resemblance to that reported previously by Min et al.[17]

This suggests a species with a high degree of molecular symmetry. Moreover, the substantial coupling constant observed precludes anything but a ^{1}J interaction, implicating direct ^{14}N-^{1}H bonding and leaving NH_4^+ as the only likely candidate species. This assignment is confirmed by comparison with the solution ^{1}H NMR spectra of NH_4Cl in DMSO-d_6 (**Figure 6.6**). ^{1}H-^{1}H Correlation Spectroscopy (COSY), depicted in **Figure 6.7**, reveals that the two other substantial signals in the ^{1}H solution NMR of $MDACl_2$ after 1 minute correspond to nuclei present in the same species.

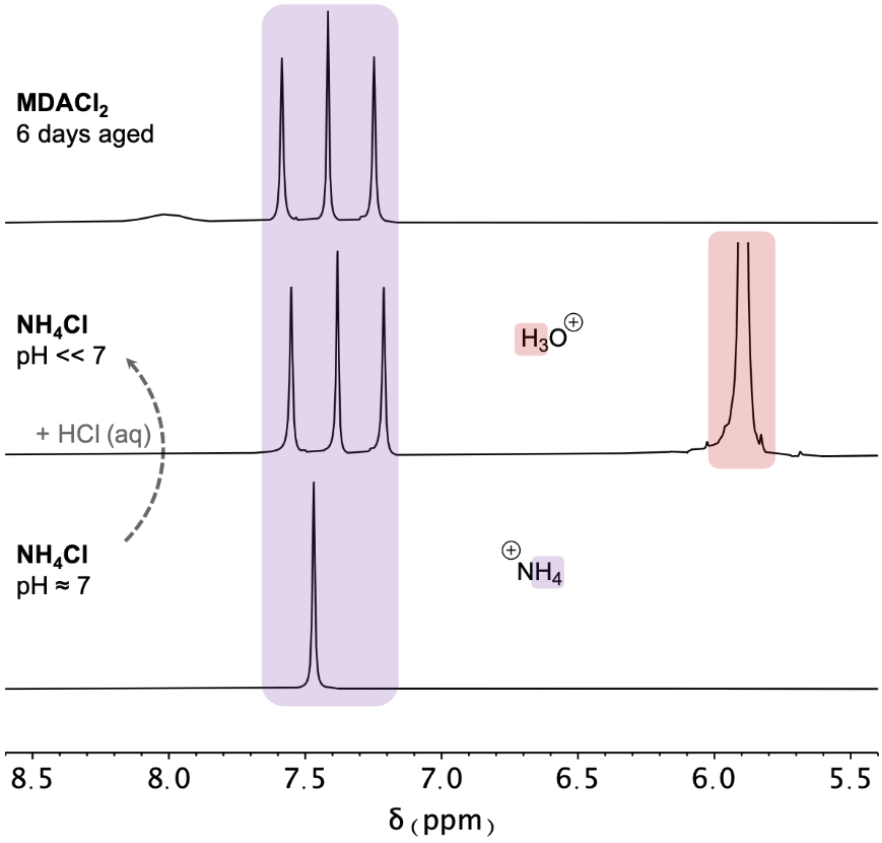


Figure 6.6 | Demonstrating NH_4^+ as a degradation product. ^1H solution nuclear magnetic resonance spectra of NH_4Cl dissolved in d^6-DMSO (bottom) and with HCl (aq) added (middle) to mimic the acidic environment of the solution upon in-situ $MDACl_2$ degradation. A solution of fully degraded (6 days) $MDACl_2$ is shown for comparison (top). We note that the $^1J_{14N\text{-}1H}$ coupling characteristic of ammonium is not initially observed in the spectrum of NH_4Cl (pH unadjusted). This could be due to a breakdown in the tetrahedral symmetry of the cation caused by either the rapid exchange of acidic H^+ in solution, or the close association of the chloride ion with the cation. Addition of hydrochloric acid to the NH_4Cl solution simulates the pH environment of ammonium formed during the degradation of $MDACl_2$ and reveals the expected 1:1:1 triplet, while also shifting the ^1H signal upfield and aligning it with that observed in the degradation of MDA^{2+}.

Integration of these signals shows a near 1:1 correspondence of the signals. These data, along with the concurrent formation of this species with ammonium and the chemical shifts of the signals, implicate methaniminium (mim^+, **A**) formation, as might be expected when MDA^{2+} is dissolved in pH neutral, aprotic polar solvents such as DMF, DMSO and GBL. The charge dense cation acts as a Brønsted acid before eliminating a secondary product, NH_4^+ - consistent with our observations – to yield mim^+. This rapid release of acidic H^+ is the first step in an extended degradation

sequence (**Figure 6.8**), a complete mechanistic description of which we propose in **Appendix A6.2** (p 202).

Once produced mim^+ is itself unstable in solution, also acting as an acidic salt to reversibly release methanimine (**B**). Methanimine, like most unhindered primary imines, rapidly oligomerizes when present in sufficient concentrations[29]. As set out in Step 2 of **Figure 6.8**, cyclisation to 1,3,5-triazinane followed by further additions of methaniminium and subsequent cage-closure, driven entropically by release of additional NH_4^+, is expected to lead rapidly to the formation of HMTA-H^+. Experimentally, between 1 and 10 minutes after initial dissolution of $MDACl_2$ a singlet signal of increasing intensity is observed in the ^1H solution NMR spectra at 4.83 ppm.

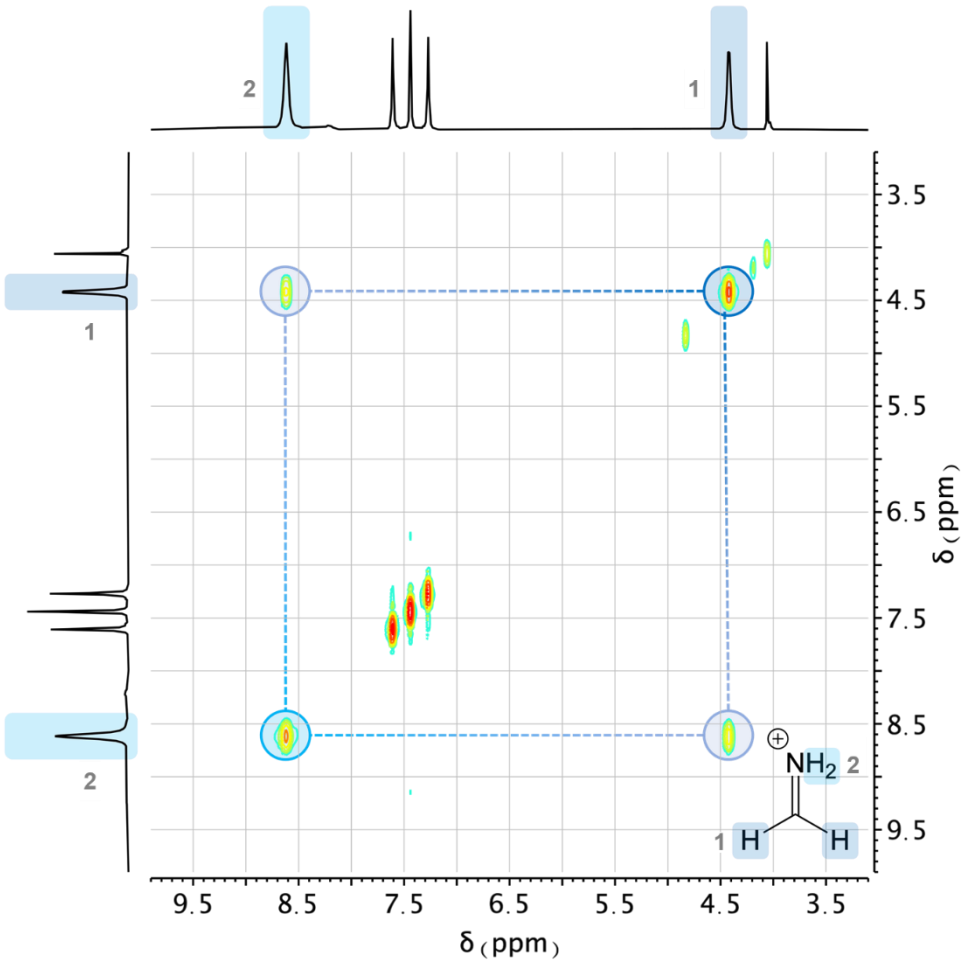


Figure 6.7 | Degradation of MDA^{2+}. ^1H-^1H solution correlation NMR spectrum of $MDACl_2$ degradation in-situ five minutes after initial dissolution in DMSO-d_6.

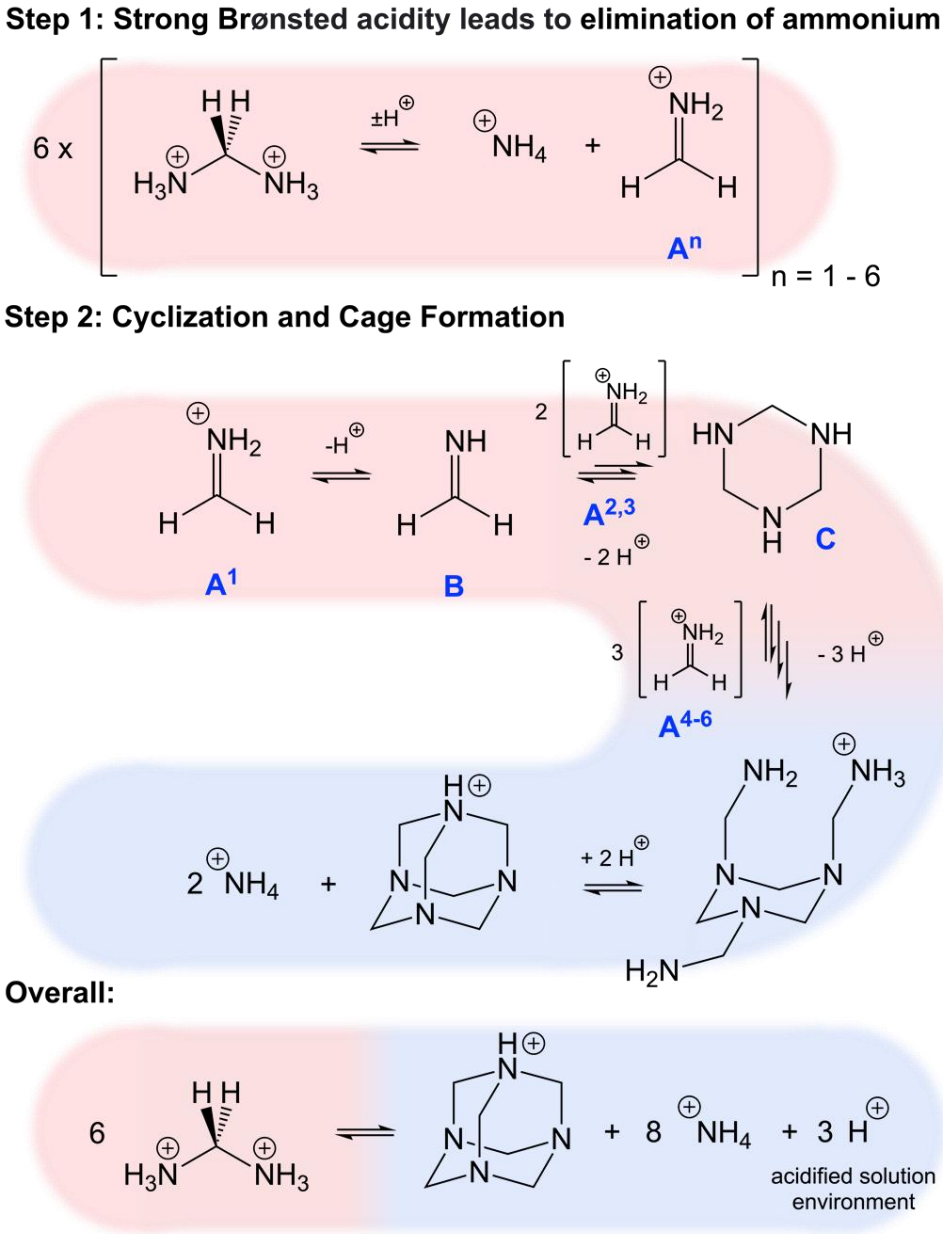


Figure 6.8 | Mechanism of degradation of MDA^{2+}. Degradation pathway of MDA^{2+} upon dissolution in a polar solvent. Hexamethylenetetramine (HMTA) and ammonia are represented in their protonated forms in line with our observations and on account of the acidic environment generated in solution as a result of the degradation.

By 6 days after initial dissolution the spectrum consists only of this singlet, the 1:1:1 triplet corresponding to ammonium and a broad singlet at 8.00 ppm. HMTA dissolved in DMSO-d_6 at neutral pH shows a singlet at 4.56 ppm (**Figure 6.9**). However, incremental addition of hydrochloric acid to this solution produces a downfield shift of this singlet to 4.83 ppm in line with the reported monoprotic pK_{aH} value for HMTA (4.93),[30] confirming the identity of the final product of MDA^{2+} degradation as HMTA-

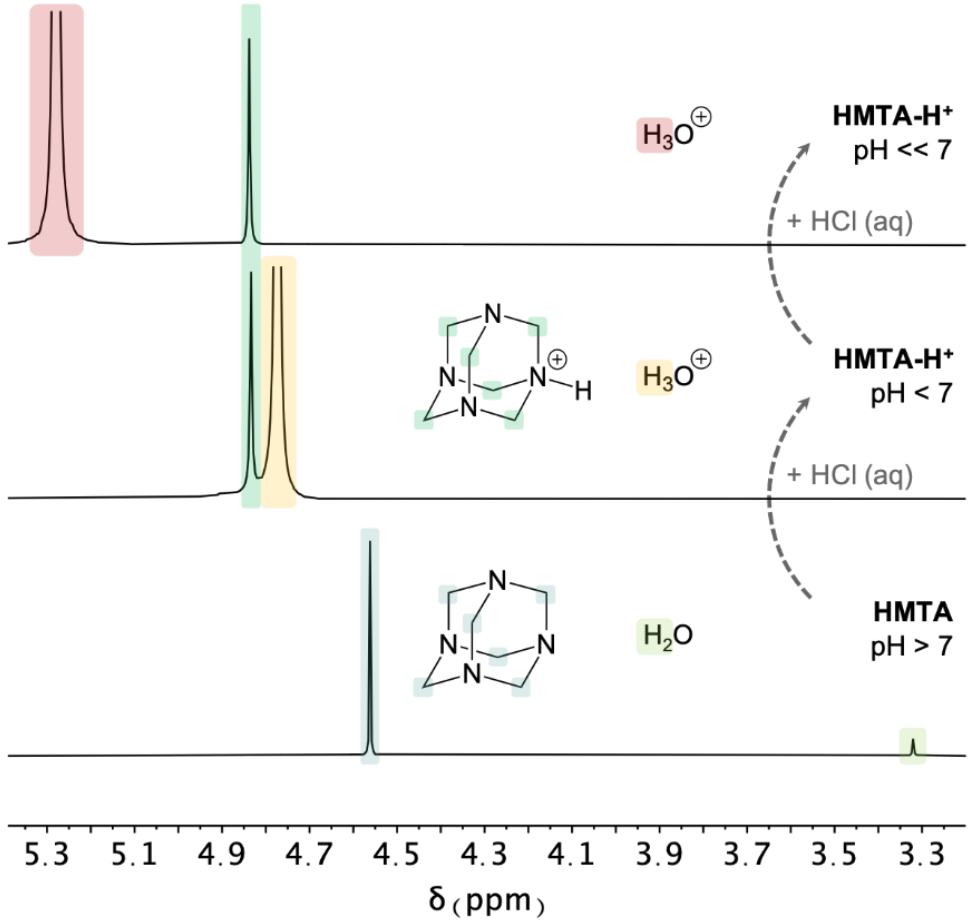


Figure 6.9 | Demonstrating HMTA-H$^+$ as a degradation product. ^{1}H solution nuclear magnetic resonance spectra of HMTA dissolved in d^6-DMSO (bottom) before with stepwise addition of HCl (aq) (middle, top) to mimic the acidic environment of the solution upon in-situ $MDACl_2$ degradation.

H^+. Integration of the relevant ^{1}H NMR signals confirms the stoichiometric 8:1 ratio of NH_4^+:HMTA-H$^+$ expected as a result of the proposed degradation route. We attribute the broad singlet at 8.00 ppm to the acidic ^{1}H of HMTA-H$^+$. We emphasize that despite the bias toward formation of HMTA-H$^+$ and NH_4^+, as all mechanistic steps are reversible, it should be expected that the system at equilibrium will include small quantities of all intermediates.

6.4 – $FAPbI_3$-$MDACl_2$ precursor solution chemistry

Having identified that HMTA and NH_4Cl are the degradation products of $MDACl_2$, we now investigate if either plays an active role in improving $FAPbI_3$ crystal properties. We first perform the crystal growth as described above, but with the addition of HMTA

or NH_4Cl. Each additive is added in the 8:1 stoichiometry expected in the case that 3.8 mol% $MDACl_2$ degrades entirely to NH_4^+ (5.07 mol%) and HMTA-H^+ (0.63 mol%). $FAPbI_3$ crystals grown with NH_4Cl additive alone undergo α-phase degradation at a rate comparable to $FAPbI_3$ single crystals grown in the absence of additives **(Figure 6.2a**). Strikingly, however, $FAPbI_3$ crystals grown in the presence of HMTA ($FAPbI_3$-H) show neither surface degradation, nor bulk degradation to the δ-phase (**Figure 6.2a**). We quantify the stability of $FAPbI_3$-H using Raman spectroscopy, as we report above for $FAPbI_3$ and $FAPbI_3$-M crystals, and find that after 132 days of ambient air aging $FAPbI_3$-H crystals show no evidence (0 counts, background subtracted) of δ-phase formation (**Figure 6.2b**).

Having established that replacing $MDACl_2$ addition with a corresponding quantity of HMTA mimics the α-phase stability enhancement of $FAPbI_3$-M, we conduct liquid-state ^1H and directionless enhancement by polarisation transfer (DEPT-135) NMR spectroscopy (**Figure 6.10a** and **6.10b**, respectively) on solutions of $FAPbI_3$-M crystals dissolved in DMSO-*d*^{6}. Unexpectedly we do not observe the presence of HMTA-H^+. Instead in the ^1H spectrum we observe signals at 9.36 (d, 6.09 Hz), 8.10 (t, 6.02 Hz) and 4.19 (d, 1.96 Hz) ppm in 2:1:4 stoichiometry. Analysis of the fine structure of each of these signals suggests spin-spin coupling between nuclei giving rise to the signals at 8.10 ppm and 9.36 ppm, with a *J*-coupling constant consistent with vicinal ^1H-^1H coupling trans across a sp^2 system ($^3J_{H9\text{-}H10}$ ~ 6 Hz). To confirm this, we carry out ^1H-^1H COSY (**Figure 6.11**). These data not only confirm the atomic proximity of noted above, but an off-diagonal cross-peak between signals at 9.36 and 4.19 ppm suggests a similar proximity in space between these chemical environments. The DEPT-135 ^{13}C spectrum shows a CH/CH_3 signal (151.1 ppm) with chemical shift comparable to the methine of FA^+ (156.6 ppm) and a CH_2 signal at 53.8 ppm, indicating an electron-

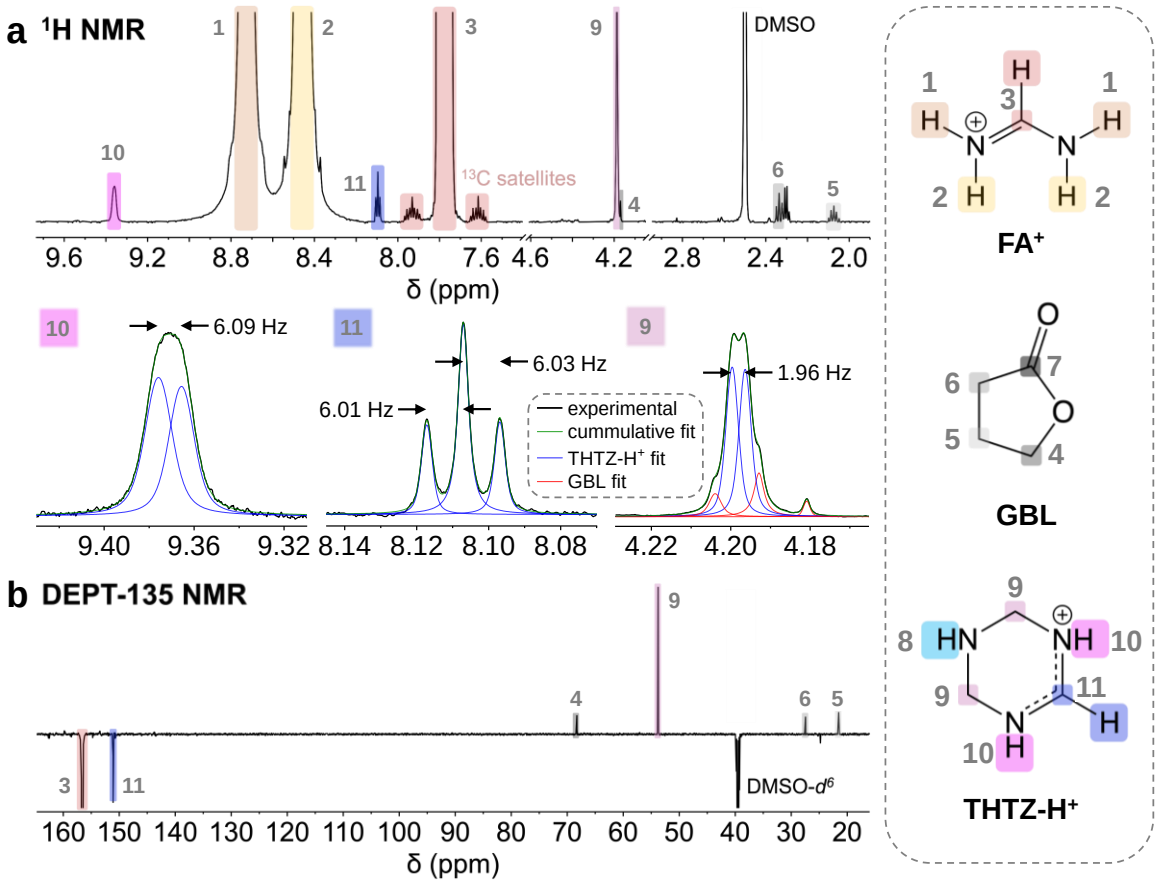


Figure 6.10 | $FAPbI_3$-M single crystal composition. ^1H solution **(a)** and directionless enhancement by polarization transfer (^1H-^{13}C) (DEPT-135) **(b)** NMR spectra (600 MHz) of $FAPbI_3$-M single crystal dissolved in DMSO-d^6. Spectra a referenced to DMSO signal. Insets below ^1H spectra show expansions of signals corresponding to THTZ-H^+ with signal fitting and spin-spin coupling constants displayed in Hz.

depleted sp^3 environment. These data are all consistent with the presence of tetrahydro-1,3,5-triazinium (THTZ-H^+)[31]. Integration of ^1H methine signals in both organic species indicate that THTZ-H^+ is present in solution at ~0.5 mol% with respect to FA^+. From these findings it is evident that the degradation of MDA^{2+} is further complicated by the presence of other organic cations in our precursor solutions, in this instance excess FA^+.

Acquisition of ^1H NMR spectra over time upon addition of 3.8 mol% $MDACl_2$ to a solution of FAI in DMSO-d_6 initially show formation of only HMTA-H^+ and NH_4^+ (**Figure 6.12**). However, upon aging a third product gradually evolves; THTZ-H^+. From this we infer that, while HMTA-H^+ and NH_4^+ are the kinetic products of $MDACl_2$ degradation,

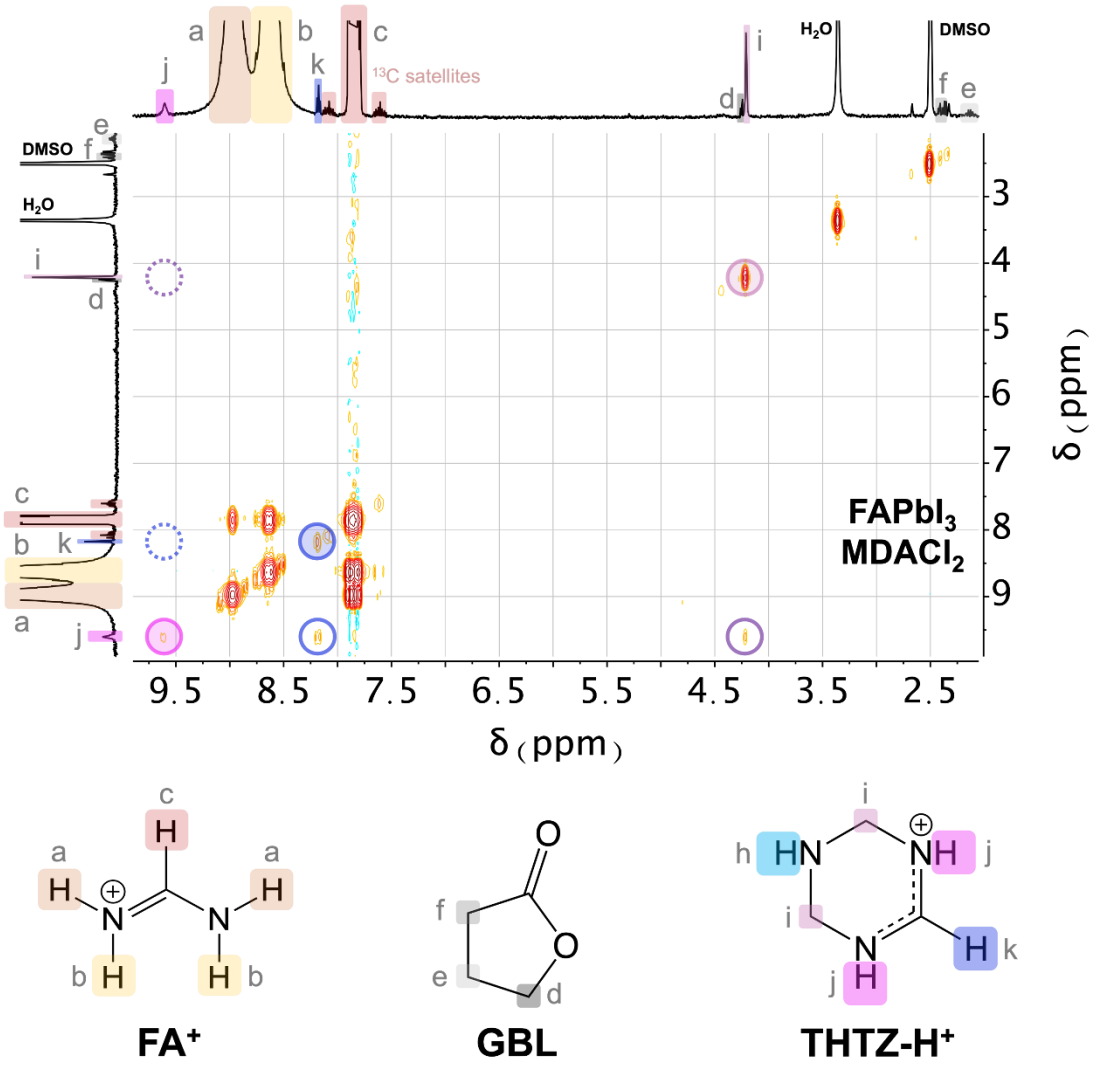


Figure 6.11 | THTZ-H⁺ in $FAPbI_3$-M single crystals. ^{1}H-^{1}H 2D correlation spectrum showing off-diagonal cross-peaks denoting correlation between ^{1}H nuclei in the chemical environments giving rise to signals at 8.18 and 9.60 ppm, and between those at 4.21 and 9.60 ppm. Cross-peaks between signals at 4.21 and 8.18 ppm is not expected as these ^{1}H nuclei are too greatly separated in THTZ-H+. The absence of corresponding off-diagonal intensity in the top left of the spectrum, as would be expected, is notable but not altogether unexpected given the trace quantities of THTZ-H⁺ in solution. Note: this 2D COSY spectrum was obtained from a sample of a $FAPbI_3$-M single crystal dissolved in d^6-DMSO.

in the presence of FA⁺ THTZ-H⁺ is a slower-forming but thermodynamically-favoured product. We account mechanistically for the formation of THTZ-H⁺ from MDA^{2+} in **Figure 6.13** (highlighted red-purple). Methanimine-initiated cage formation (step 2 in **Figure 6.8**) is interrupted by the addition of FA⁺, in place of further mim⁺, during oligomerisation of mim⁺. Cyclisation with a single FA⁺ cation leads to THTZ-H⁺. Although other methanimine-FA⁺ reaction products are mechanistically possible, as

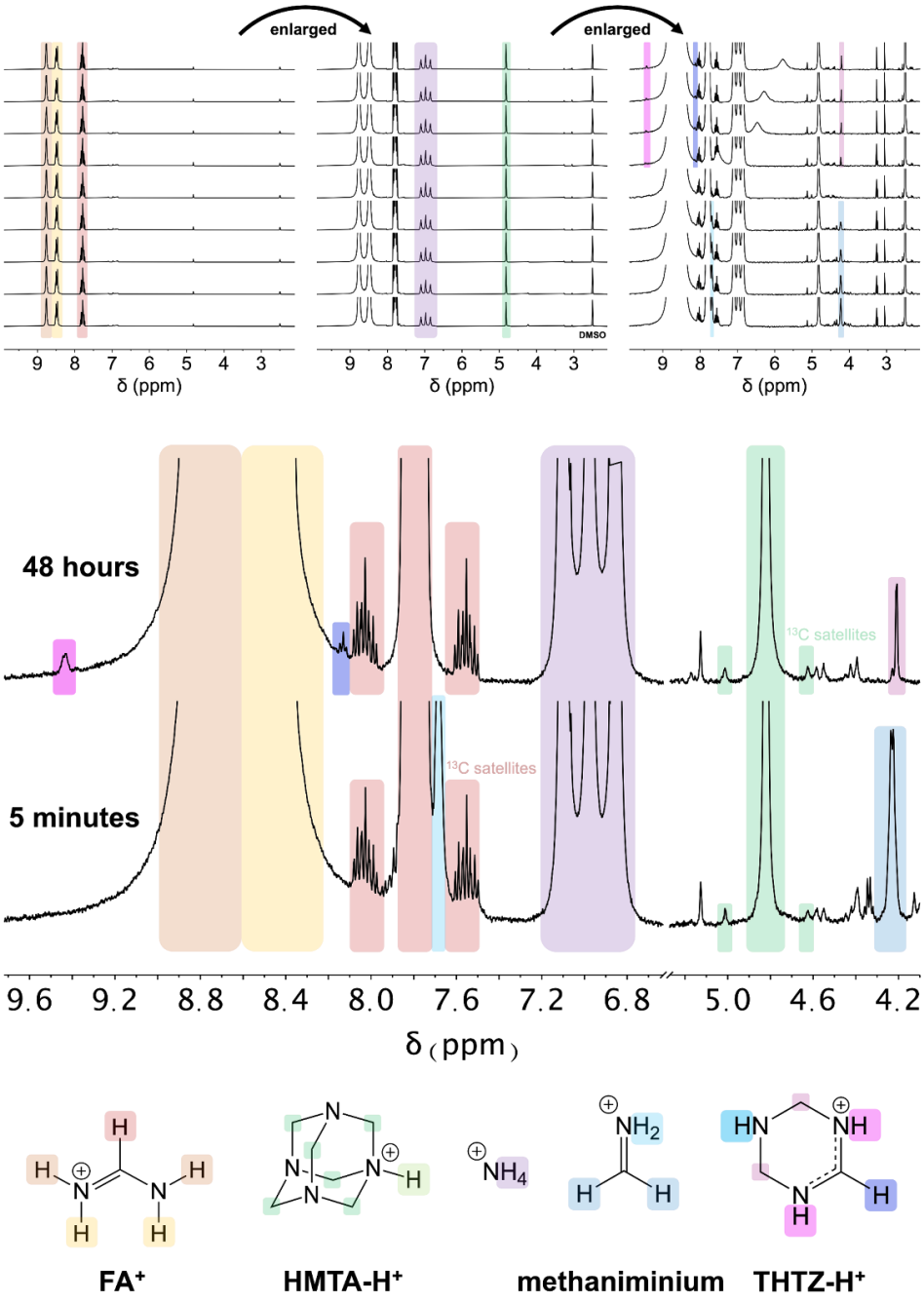


Figure 6.12 | THTZ-H⁺ formation from $MDACl_2$ degradation in presence of FA⁺. ^{1}H solution nuclear magnetic resonance (NMR) spectra of $MDACl_2$ (3.8 mol%) aged in the presence of formamidinium iodide (FAI) and lead (II) iodide (PbI_2). Top row: gradual enlargements of stacks of full spectra taken at (bottom to top): 5 minutes, 10 minutes, 15 minutes, 20 minutes, 1 hour, 2 hours, 12 hours, 36 hours, 48 hours. Signals corresponding to THTZ-H⁺ appear as minority degradation products (beside NH_4^+ and HMTA-H⁺) from around 36 hours after dissolution of the precursors. The NMR tubes in which the experiment was conducted were sealed in a N_2 glovebox and stored at room temperature during aging. The absence of a fourth ^{1}H signal corresponding to the THTZ-H⁺ secondary amine environment is likely due to rapid acidic H⁺ exchange in solution, as commonly observed in amines.

described in **Appendix A6.2** (p 202), THTZ-H⁺ is expected to dominate against other minor products.

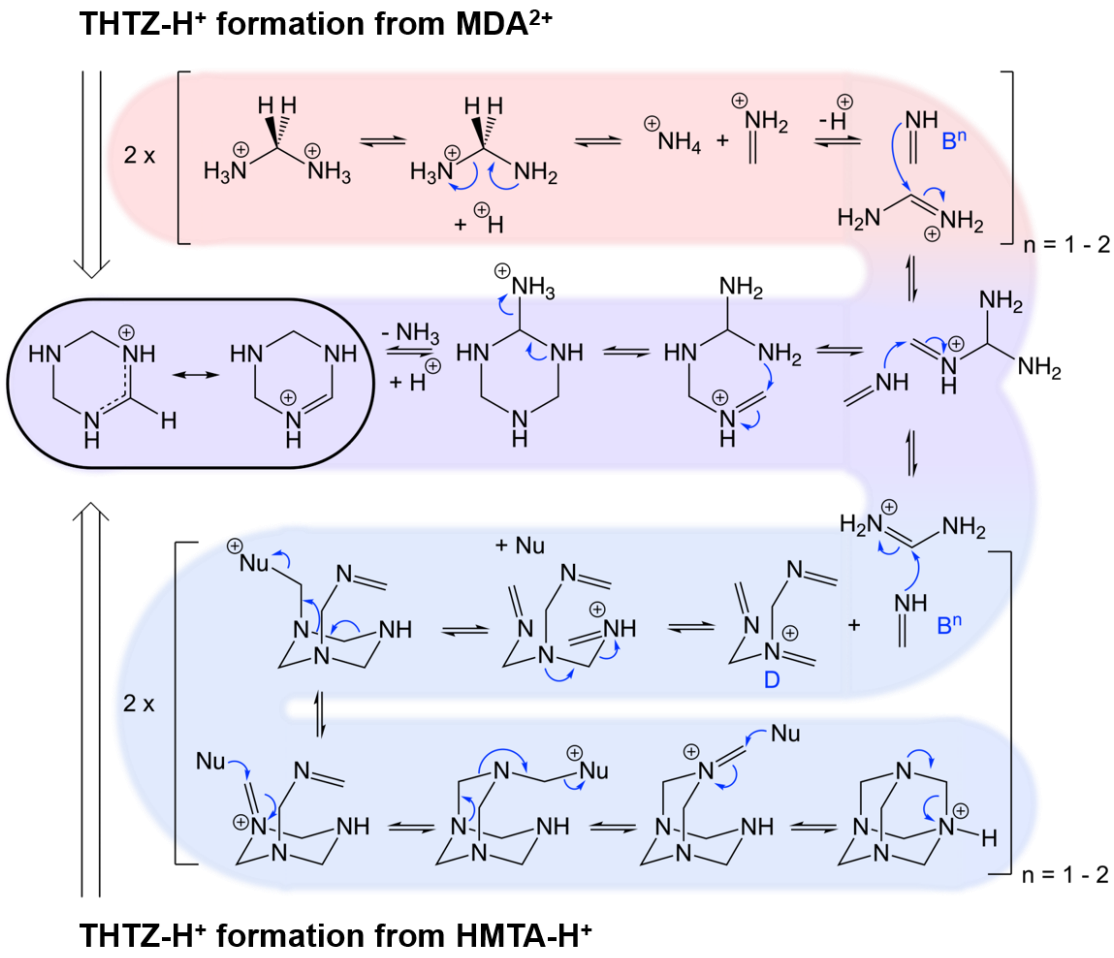


Figure 6.13 | THTZ-H⁺ formation from MDA²⁺ or HMTA-H⁺. Proposed mechanism for formation of THTZ-H⁺ from MDA²⁺ (top left) or HMTA-H⁺ (bottom right) via generation of two equivalents of methanimine, and reaction with FA⁺. Nu corresponds to any available nucleophile in solution, most likely HMTA additive. Further discussion is presented in **Appendix A6.4**.

That all steps in the reactions of **Figure 6.13** are either additions or eliminations, and thus mechanistically reversible, is critical to the activity of MDA^{2+} in $FAPbI_3$ crystal growth, for two reasons. Firstly, reversibility ensures that the whole reaction pathway is in dynamic equilibrium in solution. Thus, although HMTA-H⁺ formation occurs most rapidly, gradual evolution of a more favourable product by subsequent consumption of HMTA-H⁺ is possible, as emphasised in **Figure 6.13** (highlighted blue-purple). This explains the gradual formation of THTZ-H⁺ in solution over time from a solution of $MDACl_2$ and FAI (**Figure 6.12**). Secondly, selective removal of any species from such a dynamic system disturbs it from equilibrium, resulting in production of more of the species removed in line with Chatelier's principle. Repeated incorporation of THTZ-H⁺

into the solid state of a growing single crystal depletes its concentration remaining in solution, resulting in production of further THTZ-H^+. By this mechanism, ultimately all MDA^{2+} added can be converted to THTZ-H^+ via HMTA-H^+ and incorporated into a growing single crystal, despite THTZ-H^+ only ever being present in solution at very low concentration. As with all mechanistic details presented in this work, however, we emphasize that this scheme should be interpreted as a mechanistic justification only. We have not conducted extensive mechanistic studies and have only identified a relatively small number of the species displayed in the mechanistic schemes. This represents a chemically feasible route between the species we have clearly identified.

Significantly, the analysis above depends on the formation of THTZ-H^+ from decomposition of HMTA (via protonation by weakly acidic FA^+), as proposed in **Figure 6.13** (highlighted blue). To confirm this is indeed the case, we obtain ^{1}H NMR spectra when single crystals grown in the presence of HMTA ($FAPbI_3$-H) or NH_4Cl are dissolved in DMSO-d_6 (**Figure 6.14**). In line with our proposed mechanism, we find that signals corresponding to THTZ-H^+ are observed in the spectra of all crystals grown with either HMTA or $MDACl_2$ present in their precursor solution but not when NH_4Cl alone is added. In all cases the absence of any signals in these spectra corresponding to either ammonium or HMTA confirm that these additives are not included in the materials. We have therefore correlated the enhanced α-phase stability of $FAPbI_3$-M and $FAPbI_3$-H crystals with the presence of THTZ-H^+ in solutions of dissolved single crystals.

6.5 – Solid-state compositional analysis of $FAPbI_3$ single crystals

When $FAPbI_3$-M or $FAPbI_3$-H single crystals are dissolved, a solution rich in FA^+ and with only trace quantities of THTZ-H^+ is produced. However, as we have shown,

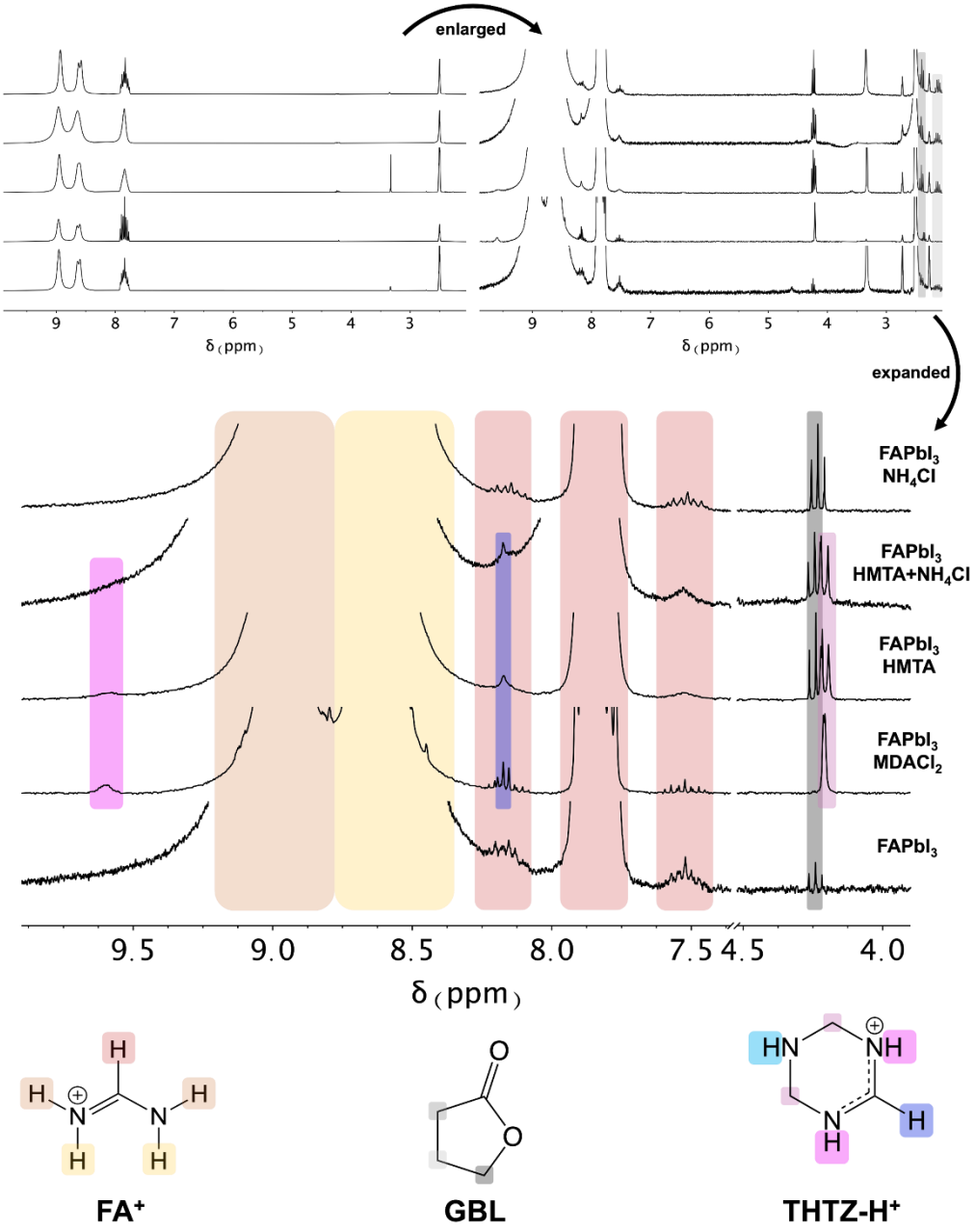


Figure 6.14 | $FAPbI_3$-additive single crystal composition. ^1H solution nuclear magnetic resonance spectra of $FAPbI_3$ single crystals that have been grown in the presence of a range of additives (3.8 mol% $MDACl_2$, 0.63 mol% HMTA, 5.07 mol% NH_4Cl, and both 0.63 mol% HMTA and 5.07 mol% NH_4Cl) showing that $THTZ\text{-}H^+$ is observed in any crystal in which HMTA or $MDACl_2$ are employed.

$THTZ\text{-}H^+$ formation occurs spontaneously in solutions containing excess FA^+ alongside MDA^{2+}, HMTA, mim^+ or many intermediates in the decomposition of these. Therefore, the observation of $THTZ\text{-}H^+$ in solutions of dissolved crystals does not confirm that this species is present in the crystals in the solid state. Kinetic entrapment of another intermediate species during crystal growth, for example mim^+, might be

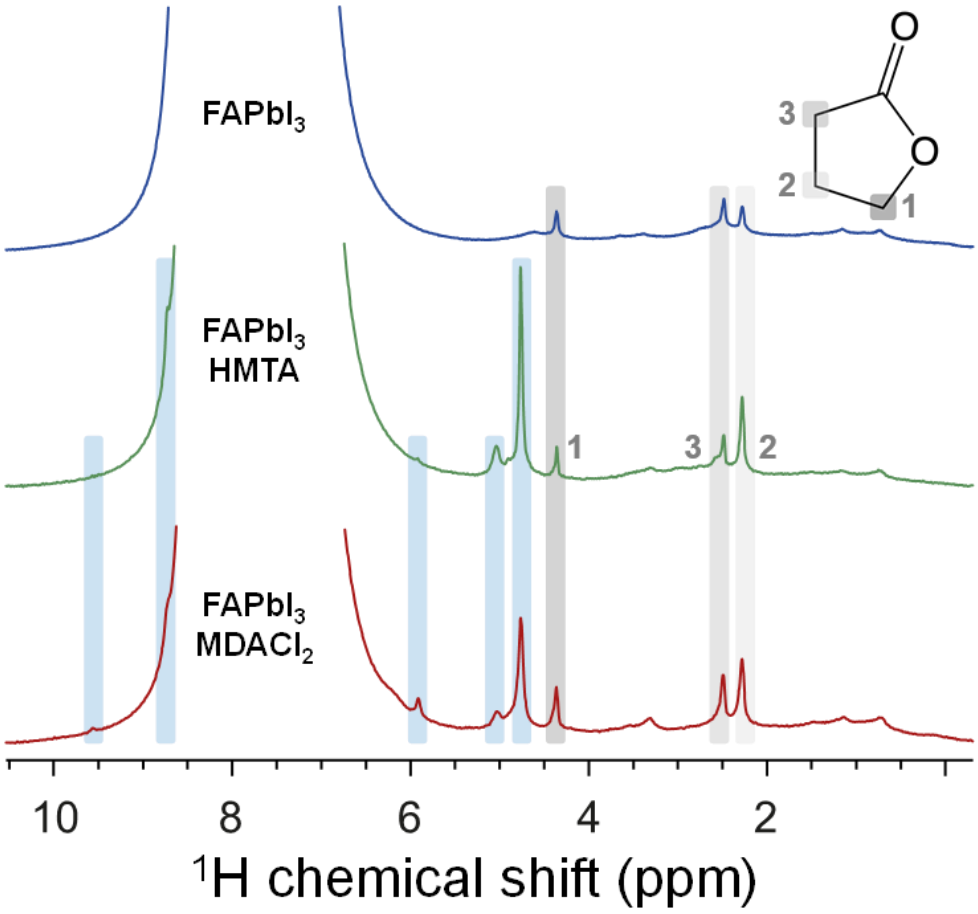


Figure 6.15 | ^{1}H solid-state NMR of $FAPbI_3$ single crystals. *Measurements and analysis carried out with assistance of D. Kubicki.* **a)** ^{1}H MAS (50 kHz) NMR spectra of neat $FAPbI_3$, $FAPbI_3$-H and $FAPbI_3$-M crystals. Signals highlighted in blue cannot be unambiguously assigned.

expected to give the same result. Nor do our liquid-state experiments provide any evidence of how a new organic species might be incorporated into the perovskite material. Therefore, to better investigate the composition of the crystals we conduct a range of solid-state NMR (ssNMR) and nuclear quadrupole resonance (NQR) spectroscopy measurements.

In **Figure 6.15** we show ^{1}H magic angle spinning (MAS) NMR spectra of $FAPbI_3$, $FAPbI_3$-M and $FAPbI_3$-H crystals. While the spectra are dominated by intense FA^+ signals (6-9 ppm), several additional, well-resolved signals (highlighted in blue) are present in both $FAPbI_3$-M and $FAPbI_3$-H spectra that are not present in neat $FAPbI_3$

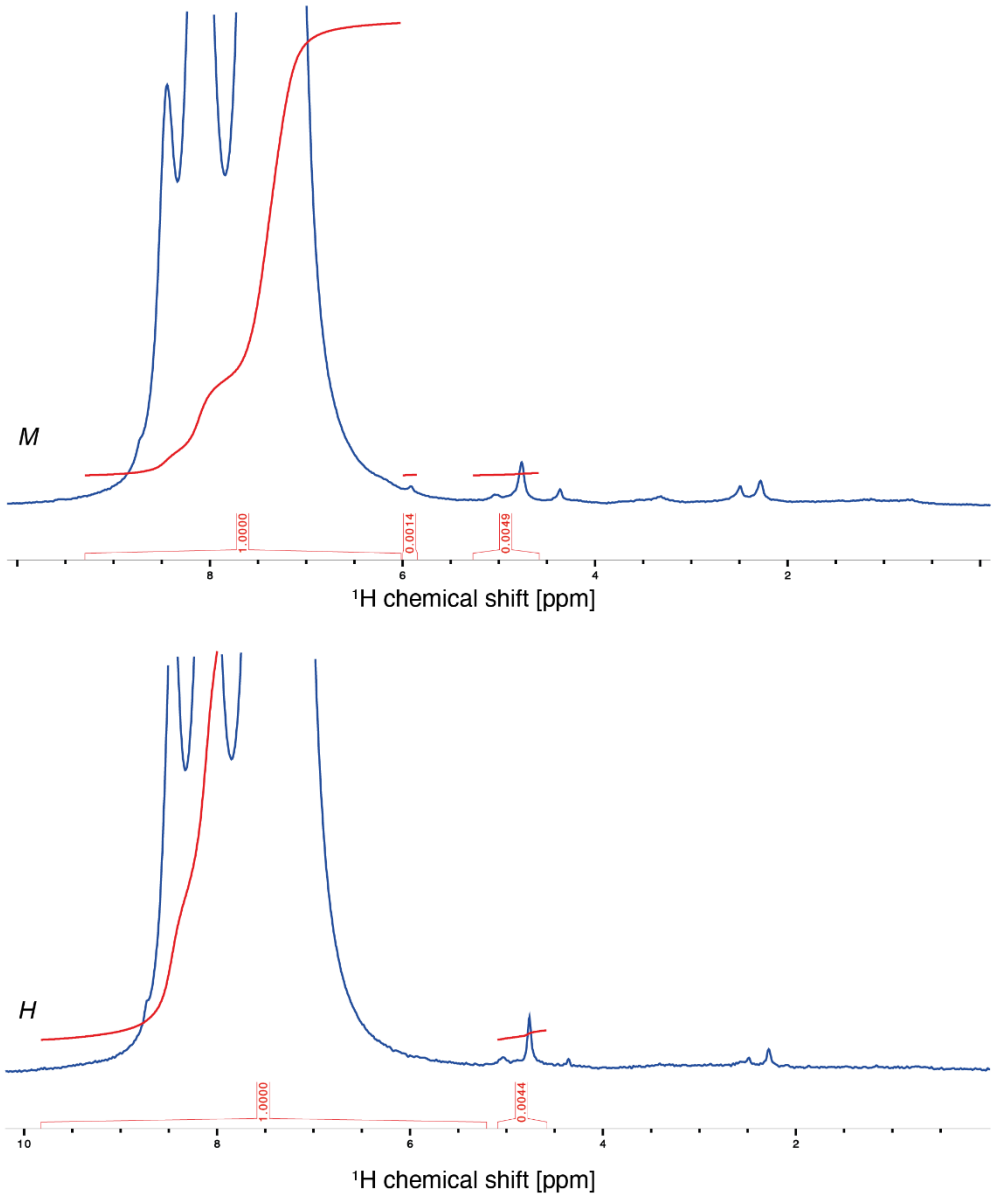


Figure 6.16 | Quantitative ^{1}H MAS (50 kHz) NMR spectra of FAPbI$_3$-H and FAPbI$_3$-M crystals. *Measurements and analysis carried out with the assistance of D. Kubicki.* Integration of the selected regions indicates that the new species is present at ~0.5 mol% relative to FA in both materials, assuming that the number of protons in FA and in the new species is the same.

crystals. These signals correspond to ^{1}H environments in organic species other than FA^{+}. Although it is not possible to assign these signals based on the ^{1}H spectra alone, we note their close correspondence to those observed in liquid ^{1}H NMR of the same crystals (**Figure 6.10a**). Further, we observe clear evidence of GBL in all three crystals, suggesting that small quantities of the processing solvent are entrapped within the crystals, despite prolonged vacuum drying (110 °C, overnight)[10,32]. By

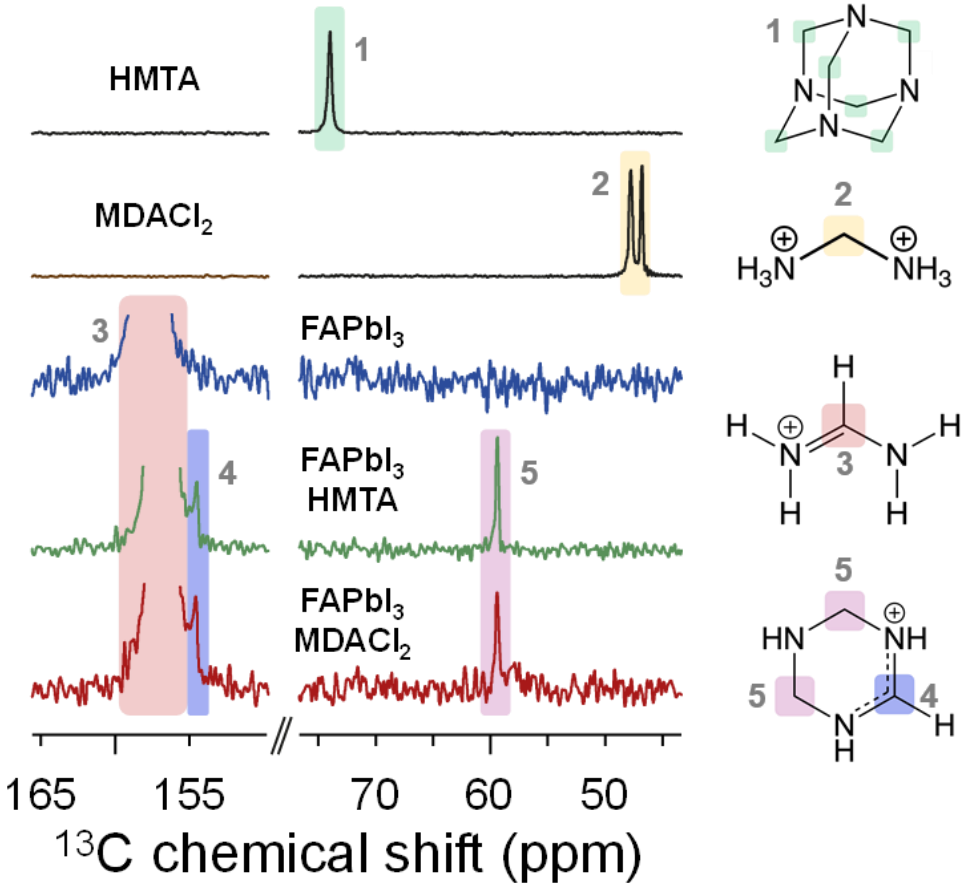


Figure 6.17 | ^{13}C solid-state NMR of $FAPbI_3$ single crystals. *Measurements and analysis carried out with assistance of D. Kubicki.* ^{13}C echo-detected (12 kHz MAS) NMR spectra comparing different $FAPbI_3$ crystals with additives employed in their growth.

recording quantitative ^{1}H solid-state NMR spectra, and assuming a 1:1 stoichiometry of FA^+:additive hydrogen nuclei, we approximate that the new species is present at ~0.5 mol% in both $FAPbI_3$-M and $FAPbI_3$-H crystals (**Figure 6.16** shows the integrated regions).

To confirm that the additive detected in the solid state is indeed THTZ-H^+, we perform ^{13}C MAS NMR (**Figure 6.17**). As in the case of ^{1}H, we observe new signals (154.5, 59.4 ppm) in $FAPbI_3$-M and $FAPbI_3$-H, which are identical in both materials but are absent in reference $FAPbI_3$. This result corroborates that the same species is present in $FAPbI_3$-M and $FAPbI_3$-H despite their differing growth environments. The new signals do not correspond to $MDACl_2$ (46.8, 47.7 ppm), HMTA (74.0 ppm), or δ-$FAPbI_3$

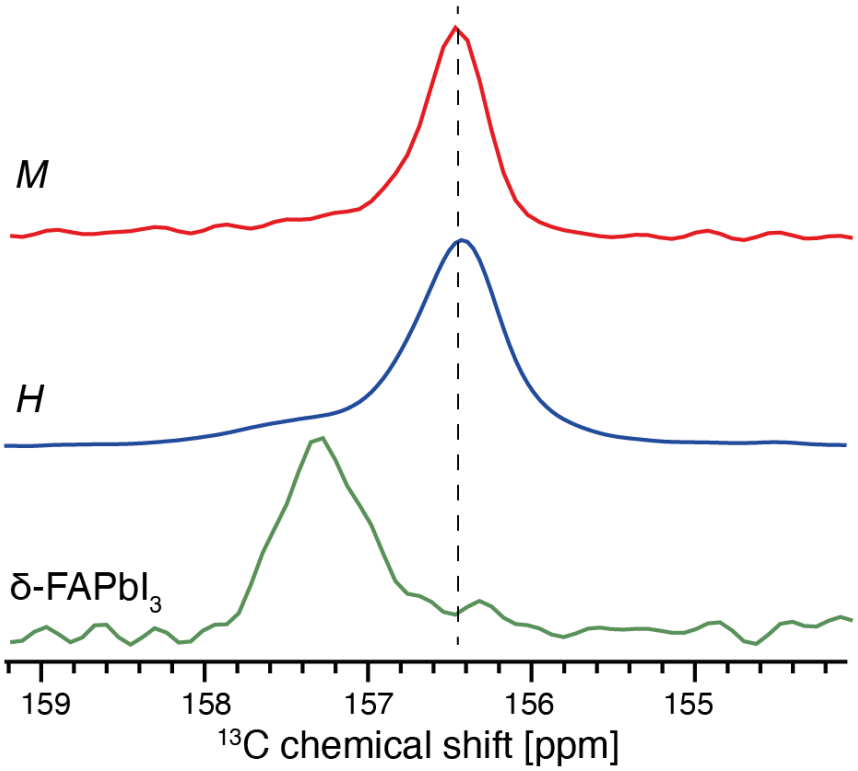


Figure A6.18 | Comparison of the ^{13}C signatures of FA in the δ (yellow) and black phases. *Measurements and analysis carried out with the assistance of D. Kubicki.* ^{13}C echo-detected NMR spectra (12 kHz MAS, 14 T) of yellow δ-$FAPbI_3$ (obtained from reference α-$FAPbI_3$ crystals that transformed in air) and the black $FAPbI_3$-H and $FAPbI_3$-M crystals.

(157.3 ppm, **Figure 6.18**). Instead, they closely match those expected for THTZ-H^+ as observed via DEPT-135 in solution (151.1, 53.8 ppm) (**Figure 6.10b**).

Having detected the presence of THTZ-H^+ in the single crystals, we next seek to elucidate its mode of incorporation within the 3D perovskite material. This question is important as THTZ-H^+ is too large to replace FA^+ on the A-site and therefore how it might interact with the ABX_3 material is unclear. We first perform a ^{1}H-^{1}H spin diffusion (SD) experiment, which relies on the exchange of magnetization between dipolar-coupled nuclei and therefore in atomic level contact on the order of tens of Å. SD therefore indicates whether the different local ^{1}H environments are present within the same phase, which is the prerequisite for their being dipolar coupled[33]. **Figure 6.19** shows the ^{1}H-^{1}H SD spectrum of $FAPbI_3$-H. We observe intense cross-peaks between

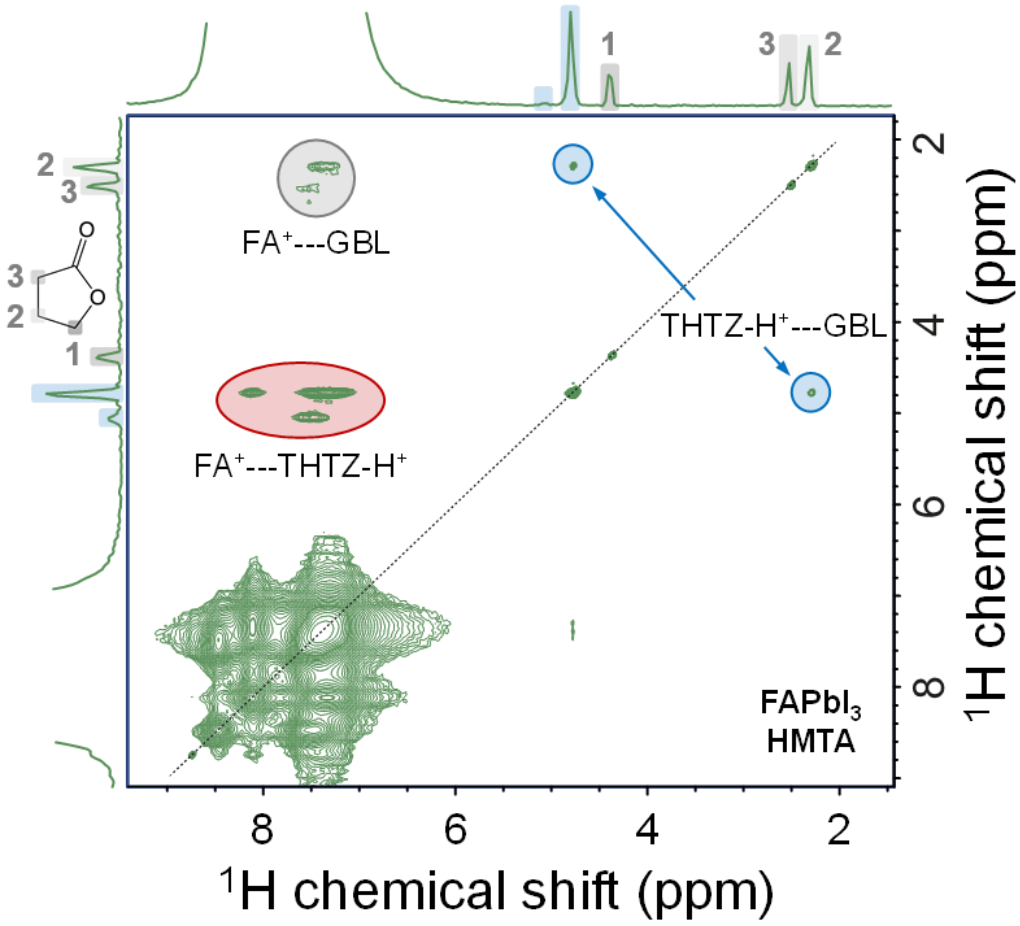


Figure 6.19 | ^{1}H-^{1}H spin diffusion spectroscopy. *Measurements and analysis carried out with assistance of D. Kubicki.* ^{1}H-^{1}H (50 kHz MAS) spin diffusion spectrum of $FAPbI_3$-H.

FA^+ and THTZ-H^+, as well as between GBL and both cations. Thus, we infer that a mixed phase containing THTZ-H^+ and FA^+ exists in $FAPbI_3$-H and $FAPbI_3$-M, rather than an isolated THTZ-H^+ secondary phase. Further discussion of the SD experiments regarding structural models of THTZ-H^+ incorporation is given in **Appendix A6.3** (p 207).

We next use ^{14}N MAS NMR to establish if the stabilization protocol leads to any detectable change to the local structure of the FA^+ cations. It has previously been shown that ^{14}N MAS NMR can be employed as a sensitive technique to probe perovskite lattice distortions from the perspective of A-site cation dynamics[34–36]. ^{14}N is a quadrupolar (I = 1) nucleus and its NMR lineshape is determined by the symmetry

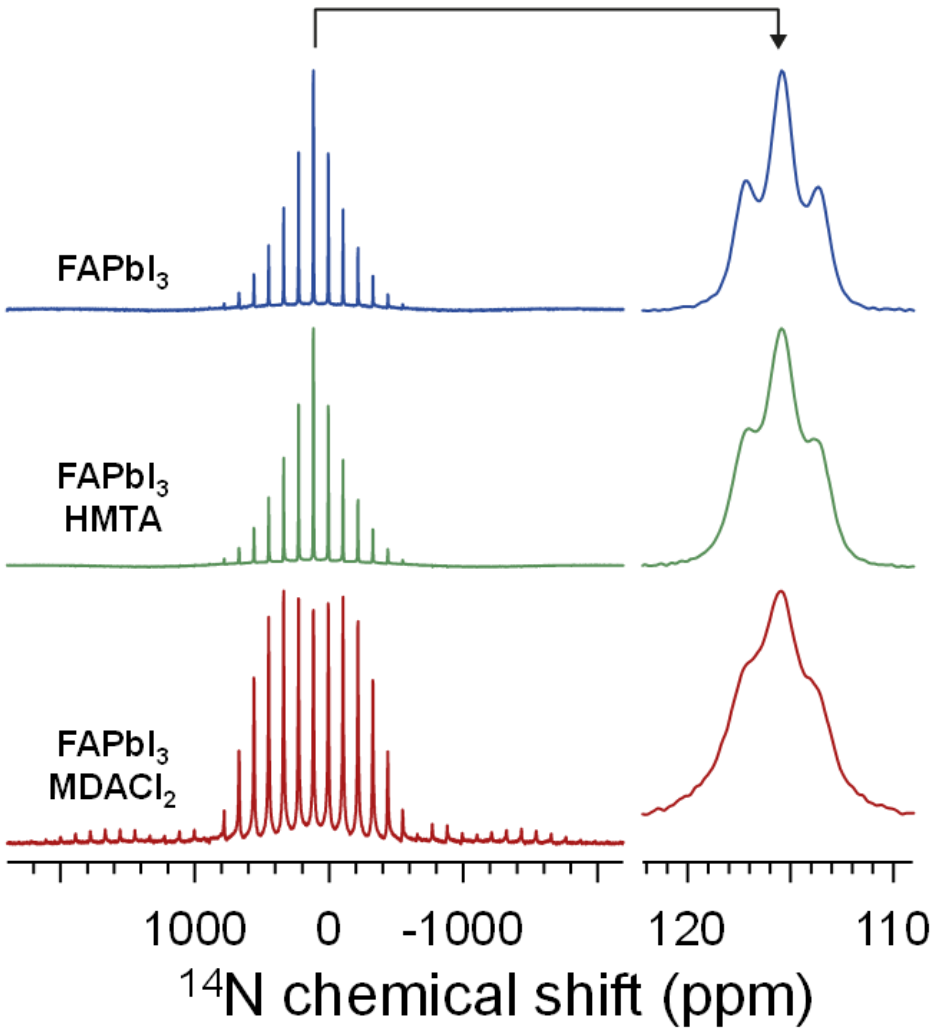


Figure 6.20 | ^{14}N solid-state NMR of $FAPbI_3$ single crystals. *Measurements and analysis carried out with assistance of D. Kubicki.* ^{14}N NMR spectra of $FAPbI_3$, $FAPbI_3$-H and $FAPbI_3$-M crystals (left). Central signal of spectral envelope shown in inset to right.

of the local environment. In cubic α-$FAPbI_3$, FA^+ rapidly reorients on a ps timescale, giving a near-isotropic electric field around the ^{14}N nuclei. The interaction between the small residual electric field gradient (EFG) at the ^{14}N nucleus and the electric quadrupole moment (eQ) of the ^{14}N nuclear spin leads to a relatively narrow FA^+ signal linewidth and a narrow envelope of spinning sidebands[37]. Incorporation of additive ions in the ABX_3 lattice or distortions in the cubooctahedral haloplumbate structure de-symmetrise the A-site, leading to increased anisotropy in FA^+ dynamics, an increased EFG at the FA^+ ^{14}N nuclei and a broadening of the spectral envelope[34–36]. ^{14}N MAS

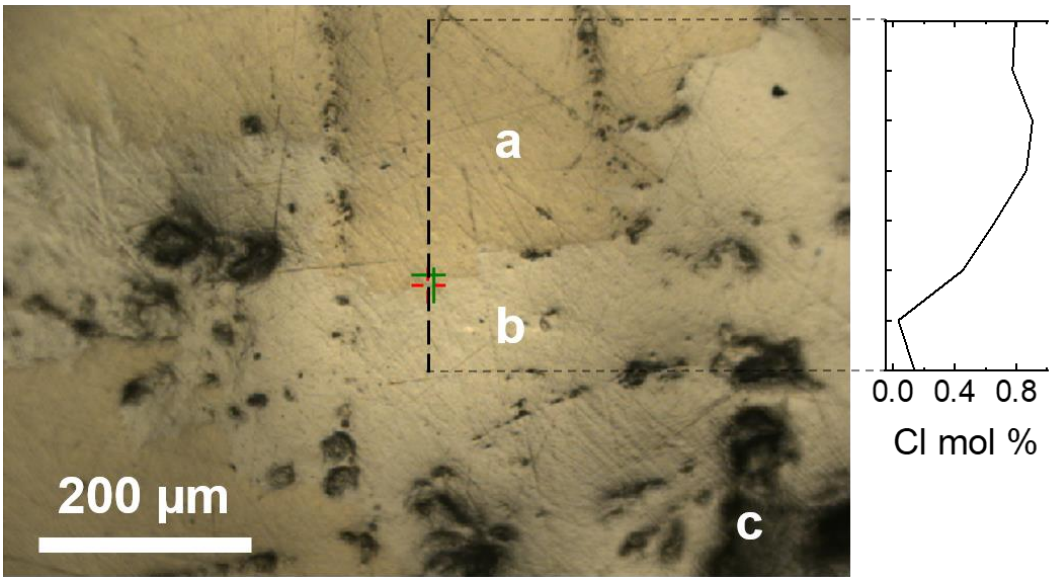


Figure 6.21 | Quantifying chloride content. *Measurements and analysis carried out with assistance of A. Matzen.* Reflected light microscope image of cleaved, polished $FAPbI_3$-M crystal showing regions of Cl-rich (a, light brown) and Cl-depleted (b, golden) perovskite material. Lineplot tracks Cl mol% (as proportion of total halide content) as EPMA measurement is carried out along a series of points traversing from a region Cl-depleted to Cl-rich material. Also highlighted is a region where material has been incidentally removed during the polishing process (c). We note that this damage occurs far more readily in the chloride-depleted region, suggesting that the material may be softer here. Also visible in the image are scratch marks, introduced during polishing. The concentration of Cl in the $FAPbI_3$-M crystals is ~1300 ppm (average of 62-point measurements), compared to a detection limit of approximately 130 ppm. The neat crystals have little to no detectable Cl; an average of 42-point measurements gives a concentration of only 50 ppm, below the sensitivity of this technique.

NMR reveals a pronounced broadening of the spectral envelope of $FAPbI_3$–M, which is not observed in the spectra of either $FAPbI_3$-H or neat $FAPbI_3$ (**Figure 6.20**). This implies the incorporation of a new species into $FAPbI_3$–M crystals that is not present under the growth conditions of $FAPbI_3$-H or neat $FAPbI_3$. Considering the consistency between the ^{13}C and ^{1}H ssNMR spectra and the comparable quantities of THTZ-H^+ detected in $FAPbI_3$-M and $FAPbI_3$-H crystals, we attribute this broadening to the presence of chloride in $FAPbI_3$-M crystals. To confirm and quantify the presence of chloride we perform electron probe microanalysis (EPMA) on $FAPbI_3$-M and $FAPbI_3$ crystals. These measurements show that chloride makes up ~0.8 at% of total halide content inside the bulk of $FAPbI_3$-M crystals (**Figure 6.21**).

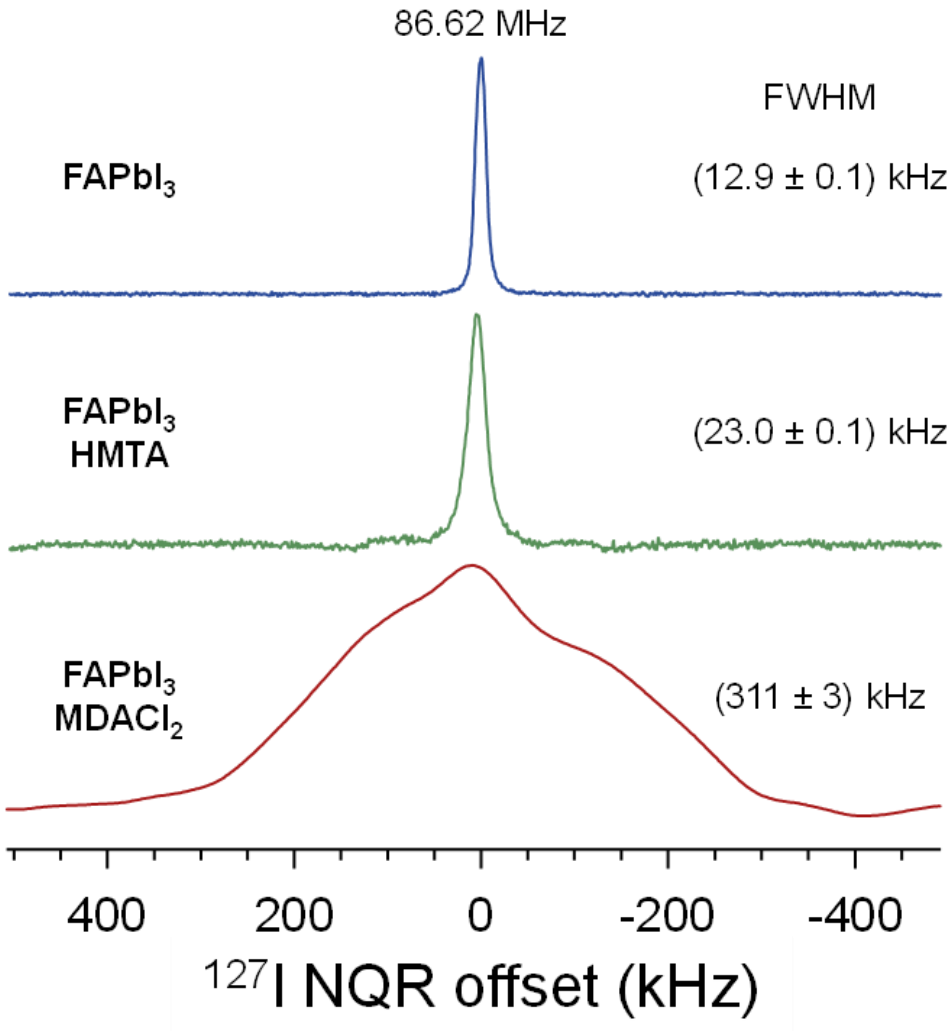


Figure 6.22 | ^{127}I NQR of $FAPbI_3$ single crystals. *Measurements and analysis carried out with assistance of D. Kubicki.* ^{127}I NQR spectra of $FAPbI_3$, $FAPbI_3$-H and $FAPbI_3$-M crystals.

Incorporation of THTZ-H^+ into the $FAPbI_3$ lattice might be expected to also result in changes in ^{14}N MAS NMR. However, we detect no significant difference between $FAPbI_3$-H and reference $FAPbI_3$, where spectral broadening due to chloride incorporation is absent. The absence in the spectra of signals corresponding to ^{14}N in incorporated THTZ-H^+ suggests that these signals are substantially broadened with intensity spread across a large number of spinning sidebands resulting in their not being detectable. This result suggests that the EFGs at the ^{14}N nuclei of THTZ-H^+ are relatively large, most likely due to incorporated THTZ-H^+ being static, consistent with its strong coordination to the ABX_3 structure.

To better isolate the independent effects of THTZ-H^+ and chloride incorporation, we conduct ^{127}I NQR spectroscopy on the three materials (**Figure 6.22**). NQR measurements are carried out without an external magnetic field and are a direct measure of the strength of the local EFG. Because the electric quadrupole moment of ^{127}I is remarkably large (-71 Q fm^{-2}, compared to the value for ^{14}N: 2 Q fm^{-2}), small structural changes lead to large changes to the NQR frequency. Interrogation of the full-width half-maxima (FWHM) of the NQR transition at 86.62 MHz shows resolvable differences between all three $FAPbI_3$ materials. We attribute the doubling of the FWHM in $FAPbI_3$-H relative to $FAPbI_3$ to the incorporation of THTZ-H^+ into the perovskite structure, which leads to the emergence of a distribution of ^{127}I local environments (static disorder) throughout the bulk (discussed further in **Appendix A6.3**, p207). The same ^{127}I NQR transition in $FAPbI_3$-M is broadened by approximately an order of magnitude more than $FAPbI_3$-H, in line with additional disordering induced by the incorporation of chloride in addition to THTZ-H^+. Previous work assessing the impact of bromide substitution in α-$FAPbI_3$ on ^{127}I NQR broadening suggests approximately a 1% halide substitution, consistent with our EPMA results[38].

6.6 – Conclusion and outlook

Precisely determining the composition and structure of complex materials is rarely trivial. Consequently, the advantage of considered and in-depth characterization to inform the rational design of new materials is not always apparent. Here we have demonstrated that growth of α-$FAPbI_3$ single crystals in the presence of $MDACl_2$, a high-performance additive, leads to significantly reduced trap density and improved ambient α-phase stability. However, by systematically studying the solution growth conditions, we find that MDA^{2+} degrades rapidly in solution and thus cannot be

incorporated into the α-$FAPbI_3$ material. Instead, we show that HMTA-H^+ and NH_4^+ are rapidly generated in solution as majority degradation products. From this informed position we propose and demonstrate an evolved form of this highly phase-stable material, $FAPbI_3$-H. However, utilizing a multi-disciplinary suite of characterization techniques, we find that neither $FAPbI_3$-M nor $FAPbI_3$-H crystals show evidence of incorporation of MDA^{2+}, HMTA-H^+, NH_4^+ or any other intermediates in the degradation of MDA^{2+}. Instead, THTZ-H^+ is detected in these crystals. We also discover that chloride is present in $FAPbI_3$-M crystals. However, the comparable α-phase stability of our $FAPbI_3$-H material allows us to isolate that it is THTZ-H^+, not chloride, that leads to the improved performance. We rationalize the formation of THTZ-H^+ mechanistically and perform experiments confirming that this new cation is distributed throughout the single crystals. Using a combination of ^{1}H-^{1}H SD ssNMR and ^{127}I NQR we determine that the THTZ-H^+ cations are incorporated into the perovskite lattice in atomic level contact with FA^+ and leading to an appreciable distortion of the cuboctahedral symmetry.

Appendix A6.1: Single crystal X-ray diffraction (SCXRD)

SCXRD confirms the 3D perovskite phase in each of the $FAPbI_3$, $FAPbI_3$-M and $FAPbI_3$-H crystals. The crystal structures were solved in the $Pm\bar{3}m$ cubic space group as previously reported[22], with crystal data and structure refinement statistics shown in **Table A6.1**. The solved crystal structure of the $FAPbI_3$ crystal is shown in **Figure A6.1**, which is representative of all three crystals, with a near-spherical distribution for the organic cation on the A-site, as expected from its rotational disorder. $FAPbI_3$-M and $FAPbI_3$-H show slightly longer average Pb-I bond lengths (and larger unit cells) and slightly lower atomic displacement parameters for Pb compared to $FAPbI_3$, shown in **Tables A6.2 and A6.3**. It is difficult to assess whether these differences are significant, with the average bulk structures attained from the SCXRD less sensitive to such small compositional substitutions or local distortions than, for example, our solid-state nuclear magnetic resonance (ssNMR) and electron probe microanalysis (EPMA) measurements, highlighting the need for advanced characterisation techniques which can enrich the halide perovskite literature.

What is more apparent from our SCXRD measurements, however, is the difference in the amount of twinning in the crystals (**Figure A6.2**). Without background subtraction, we can see the presence of weakly diffracting powder rings in the diffraction pattern for $FAPbI_3$ which show the presence of many randomly orientated crystallographic domains. The polycrystalline-like diffraction spots are readily removed by the background removal, making the resulting diffraction pattern of $FAPbI_3$ crystals falsely appear to be a perfectly single crystal domain. We observe a greatly reduced presence of the polycrystalline-like diffraction spots in $FAPbI_3$-M and $FAPbI_3$-H crystals, particularly for the $FAPbI_3$-M crystal.

After background subtraction, 100% of the diffraction spots obtained for the $FAPbI_3$ crystal could be indexed to a single cubic unit cell. For $FAPbI_3$-M, 77% of diffraction spots could be fitted to a single cubic unit cell, increasing to 87% and 96% by the addition of two more twin components. The main component was detwinned and used to solve the structure. In the case of $FAPbI_3$-H, only 47% of diffraction spots could be fitted with a single cubic unit cell. This could increase to 57% and then 66% by adding two more twin components. Fitting a fourth twin component only indexed 2% more of the diffraction spots, and so we stopped at three twin components. The remaining diffraction spots are likely to be due to the presence of some randomly orientated grains. The main component attributed to 47% of the diffraction spots was detwinned and used to solve the crystal structure. The twin laws and overlap statistics for $FAPbI_3$-M and $FAPbI_3$-H are shown below. In all cases. there is little overlap between twins. The twinning in FAPI-M and FAPI-H may be similar; both crystals have a twin component rotated ~174° from the main component, and in both FAPI-M and FAPI-H the second and third twin components are related by a ~120° rotation.

In general, many of the crystals grown and measured in this work appear to be single crystals. However, for metal halide perovskites there have been several reports showing that both thin film grains and “single” crystals can contain several distinct crystallographic domains[39–41]. It is unclear if there is a link between the density of twinning in our crystals and the enhanced α-phase stability we observe. It has been suggested that point-defects can be the origin of domain boundaries due to memory effects seen when heating and cooling domain boundaries through phase transitions[40,41]. Comparing the diffraction spots observed for each crystal shows that our more stable crystals ($FAPbI_3$-M and $FAPbI_3$-H) also show a significantly greater density of well-defined twins, rather than the randomly orientated crystallites seen in

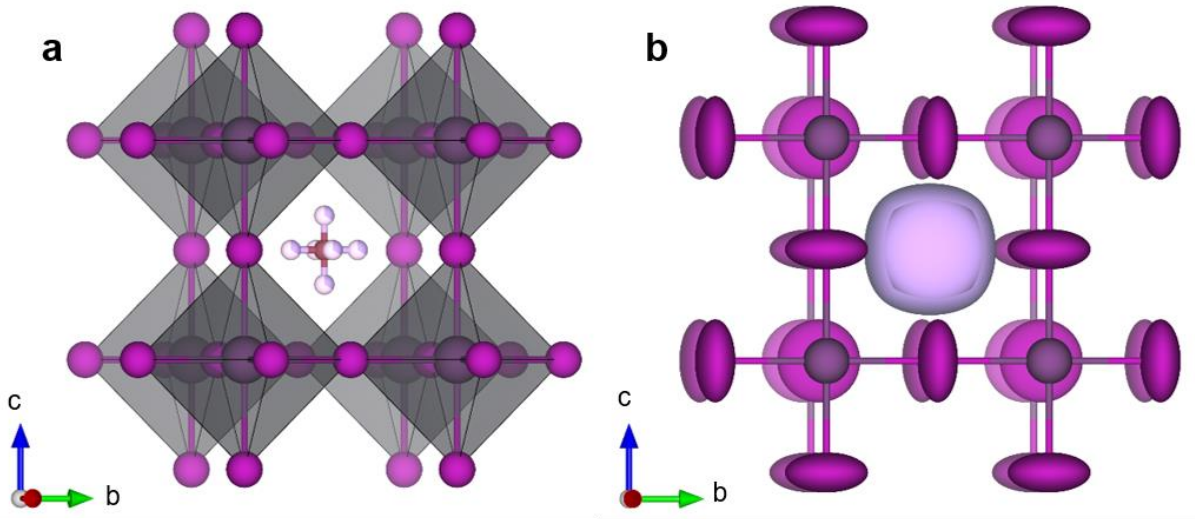


Figure A6.1 | Single crystal X-ray diffraction of $FAPbI_3$. *Measurements and analysis carried out by M. Guttman and H. Sansom.* **a**, The crystal structure solved for $FAPbI_3$ crystals in the cubic $Pm\bar{3}m$ space group, as reported. **b**, The crystal structure of $FAPbI_3$ crystals, shown with 100% displacement parameters showing the near-spherical electron distribution of the organic cation. The plane of I^- ions have been removed to show the displacement parameters of the Pb^{2+}. These images are also representative of the $FAPbI_3$-M and $FAPbI_3$-H crystals.

$FAPbI_3$. It is possible that the inclusion mode of THTZ-H^+ is such to have caused this effect, perhaps by inducing point defects that in turn induce distinct twin domains that are less likely to lead to propagation of the photoinactive δ-phase. Equally, however, this may be a confusion of cause and effect; the observation of many more randomly ordered domains in the $FAPbI_3$ crystals may instead be early evidence of the onset of phase degradation, especially as it is not straightforward to assess if the majority of these disordered domains correspond to crystallites in the α- or δ-phase. We emphasise that all our SCXRD measurements were performed on crystals that were freshly grown (<1 day old, in the case of $FAPbI_3$) and had been stored in a static N_2 environment from time of fabrication to time of measurement. As above, the measurements themselves were performed under a flow of temperature-controlled N_2. All these precautions were taken in order to minimise degradation of the as-fabricated crystals to the δ-phase prior to measurement, nonetheless we cannot eliminate this possibility.

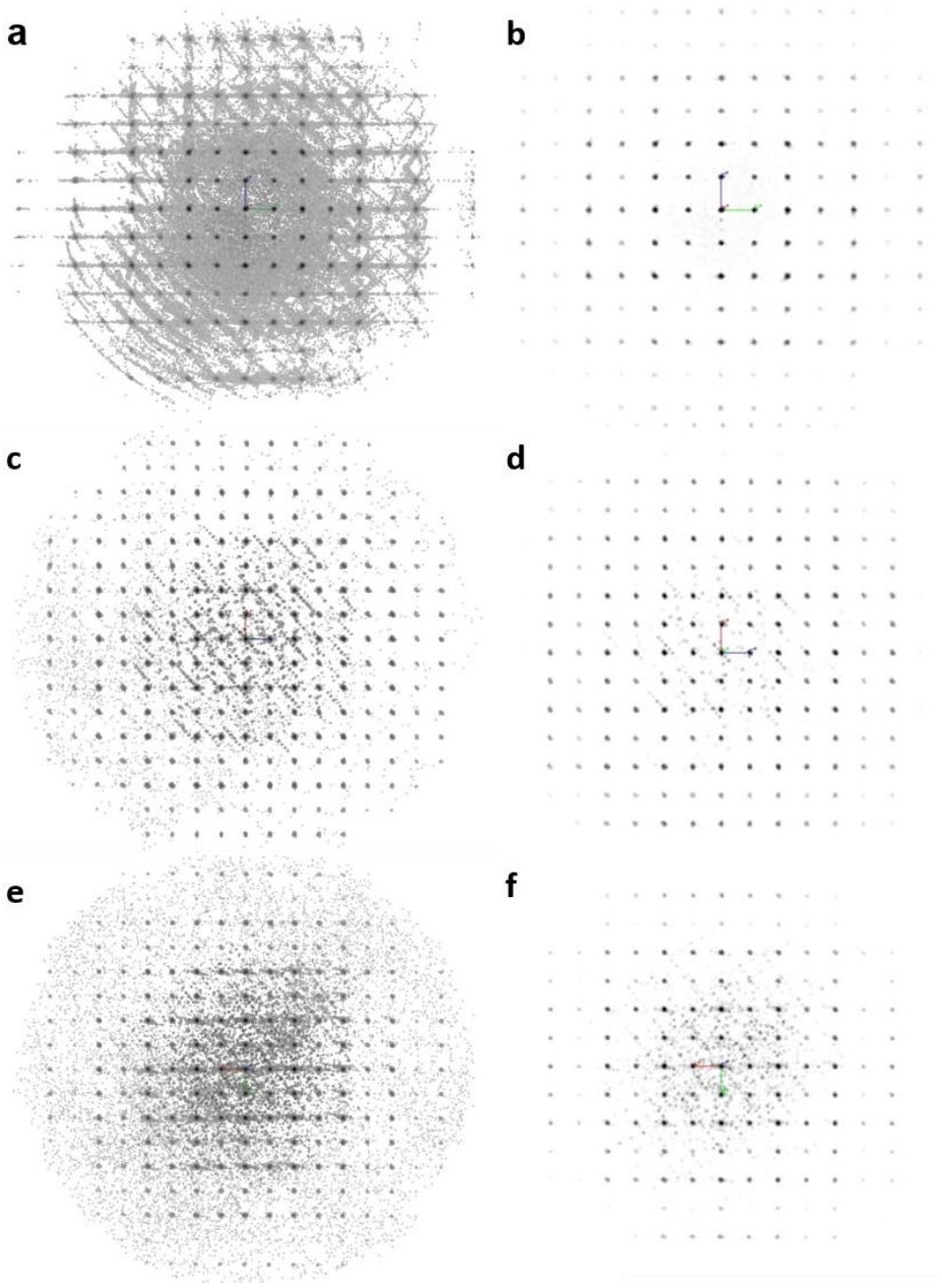


Figure A6.2 | Diffraction patterns for $FAPbI_3$ crystals. *Measurements and analysis carried out by M. Guttman and H. Sansom.* The sphere of diffraction spots collected for $FAPbI_3$ (**a**), $FAPbI_3$-M (**c**) and $FAPbI_3$-H (**e**) crystals without background subtraction. The sphere of diffraction spots collected for $FAPbI_3$ (**b**), $FAPbI_3$-M (**d**) and $FAPbI_3$-H (**f**) crystals with background subtraction. Views are projected in the (0kl) plane. projected in the (0kl) plane.

Table A6.1 | Crystal data and structure refinement for the $FAPbI_3$, $FAPbI_3$-M and $FAPbI_3$-H crystals.

Identification code	$FAPbI_3$	$FAPbI_3$-M	$FAPbI_3$-H
Empirical formula	$(C_2H_5N_2)PbI_3$	$(C_2H_5N_2)PbI_3$	$(C_2H_5N_2)PbI_3$
Formula weight	627.92	627.92	627.92
Temperature/K	289.99(10)	289.99(10)	290.0(4)
Crystal system	cubic	cubic	cubic
Space group	$Pm\bar{3}m$	$Pm\bar{3}m$	$Pm\bar{3}m$
a/Å	6.35253(12)	6.35469(4)	6.35530(19)
b/Å	6.35253(12)	6.35469(4)	6.35530(19)
c/Å	6.35253(12)	6.35469(4)	6.35530(19)
α/°	90	90	90
β/°	90	90	90
γ/°	90	90	90
Volume/Å^3	256.354(15)	256.616(5)	256.690(12)
Z	1	1	1
ρ_{calc}g/cm^3	4.067	4.063	4.062
μ/mm^{-1}	25.41	25.384	25.377
F(000)	261	261	261
Crystal size/mm^3	0.023 × 0.039 × 0.061	0.035 × 0.065 × 0.107	0.025 × 0.066 × 0.079
Radiation	Mo Kα (λ = 0.71073)	Mo Kα (λ = 0.71073)	Mo Kα (λ = 0.71073)
2Θ range for data collection/°	6.414 to 64.504	6.412 to 64.478	6.41 to 64.4728
Index ranges	-9 ≤ h ≤ 9, -9 ≤ k ≤ 9, -9 ≤ l ≤ 9	-9 ≤ h ≤ 9, -9 ≤ k ≤ 9, -9 ≤ l ≤ 9	-9 ≤ h ≤ 9, -9 ≤ k ≤ 9, -9 ≤ l ≤ 9
Reflections collected	6054	6500	6568
Independent reflections	128 [R_{int} = 0.0653, R_{sigma} = 0.0131]	127 [R_{int} = 0.0345, R_{sigma} = 0.0060]	128 [R_{int} = 0.0587, R_{sigma} = 0.0131]
Data/restraints/parameters	128/0/9	127/0/9	128/0/9
Goodness-of-fit on F^2	1.099	1.113	1.291
Final R indexes [I>=2σ (I)]	R_1 = 0.0146, wR_2 = 0.0333	R_1 = 0.0100, wR_2 = 0.0285	R_1 = 0.0207, wR_2 = 0.0503
Final R indexes [all data]	R_1 = 0.0177, wR_2 = 0.0335	R_1 = 0.0100, wR_2 = 0.0285	R_1 = 0.0207, wR_2 = 0.0503
Largest diff. peak/hole / e Å^{-3}	0.58/-0.41	0.50/-0.40	1.17/-0.36

Table A6.2 | Anisotropic displacement parameters ($Å^2 \times 10^3$) of the solved crystal structures for the $FAPbI_3$, $FAPbI_3$-M and $FAPbI_3$-H crystals. The anisotropic displacement factor exponent takes the form: $-2\pi^2[h^2a^{*2}U_{11}+2hka^*b^*U_{12}+\ldots]$.

Atom	U_{11}	U_{22}	U_{33}	U_{23}	U_{13}	U_{12}
			$FAPbI_3$			
Pb1	38.36(18)	38.36(18)	38.36(18)	0	0	0
I1	28.8(3)	123.5(5)	123.5(5)	0	0	0
C1	151(16)	151(16)	151(16)	0	0	0
N1	220(20)	68(19)	220(20)	0	0	0
			$FAPbI_3$-M			
Pb1	35.73(14)	35.73(14)	35.73(14)	0	0	0
I1	121.7(4)(2)	27.3(2)	121.7(4)	0	0	0
C1	141(14)	141(14)	141(14)	0	0	0
N1	210(20)	74(17)	210(20)	0	0	0
			$FAPbI_3$-H			
Pb1	36.5(2)	36.5(2)	36.5(2)	0	0	0
I1	122.2(7)	122.2(7)	28.7(4)	0	0	0
C1	140(20)	140(20)	140(20)	0	0	0
N1	190(30)	70(20)	190(30)	0	0	0

Table A6.3 | Bond lengths of the solved crystal structures for the FAPI, FAPI-M and FAPI-H crystals.

Atom	Atom	Length/Å
	$FAPbI_3$	
Pb1	I1	3.17627(6)
C1	N1	1.00(3)
N1	N1	1.41(4)
	$FAPbI_3$-M	
Pb1	I1	3.17735(2)
C1	N1	1.01(3)
N1	N1	1.42(4)
	$FAPbI_3$-H	
Pb1	I1	3.17765(5)
C1	N1	0.99(4)
N1	N1	1.40(6)

Twin laws and overlap statistics for detwinning in $FAPbI_3$-M crystals.

Twin law for component 1 with component 2, where UB[n] is the orientation matrix for component n:

$$\text{UB[1]-1*UB[2]} = \begin{pmatrix} 0.1315 & 0.9802 & 0.1479 \\ 0.1503 & 0.1278 & -0.9791 \\ -0.9795 & 0.1506 & -0.1297 \end{pmatrix},$$

a 115.8348˚ rotation around reciprocal space vector (h,k,l): (0.6288, 0.6263, -0.4608)

Twin law for component 1 with component 3:

$$\text{UB[1]-1*UB[3]} = \begin{pmatrix} 0.6011 & -0.3840 & -0.6977 \\ -0.3043 & -0.9208 & 0.2410 \\ -0.7395 & 0.2429 & -0.6724 \end{pmatrix},$$

a -174.4062 ˚ rotation around reciprocal space vector (h,k,l): (0.8944, -0.1925, -0.4037)

Twin law for component 2 with component 3:

$$\text{UB[2]-1*UB[3]} = \begin{pmatrix} 0.7582 & -0.2556 & 0.6038 \\ 0.4385 & -0.4839 & -0.7547 \\ 0.4844 & 0.8381 & -0.2520 \end{pmatrix},$$

a -119.2953 ˚ rotation around reciprocal space vector (h,k,l): (0.9149, 0.0669, 0.3981)

Overlap statistics of components 1 and 2:

Overlap factor	Number in range	Percentage of all observations
0.0-0.2	81	0.4
0.2-0.4	50	0.3
0.4-0.6	17	0.1
0.6-0.8	2	0.0
0.8-1.0	16	0.1
Total:	**166**	**0.9**

Overlap statistics of components 1 and 3:

Overlap factor	Number in range	Percentage of all observations
0.0-0.2	67	0.4
0.2-0.4	23	0.1
0.4-0.6	7	0.0
0.6-0.8	3	0.0
0.8-1.0	0	0.0
Total:	**100**	**0.5**

Overlap statistics of components 2 and 3:

Overlap factor	Number in range	Percentage of all observations
0.0-0.2	71	0.4
0.2-0.4	17	0.1
0.4-0.6	13	0.1
0.6-0.8	10	0.1
0.8-1.0	22	0.1
Total:	**133**	**0.7**

Twin laws and overlap statistics for detwinning in $FAPbI_3$-H crystals.

Twin law for component 1 with component 2, where UB[n] is the orientation matrix for component n:

$$\text{UB[1]-1*UB[2]} = \begin{pmatrix} -0.9865 & -0.1590 & -0.0172 \\ -0.0210 & 0.0306 & 1.0002 \\ -0.1580 & 0.9870 & -0.0333 \end{pmatrix},$$

a 174.3107˚ rotation around reciprocal space vector (h,k,l): (-0.0633, 0.7169, 0.6943)

Twin law for component 1 with component 3:

$$\text{UB[1]-1*UB[3]} = \begin{pmatrix} 0.6093 & -0.6799 & -0.4098 \\ -0.7870 & -0.5863 & -0.1968 \\ -0.1066 & 0.4427 & -0.8914 \end{pmatrix},$$

a 159.0332˚ rotation around reciprocal space vector (h,k,l): (0.8931, -0.4243, -0.1496)

Twin law for component 2 with component 3:

$$\text{UB[2]-1*UB[3]} = \begin{pmatrix} 0.5675 & 0.6145 & 0.5504 \\ -0.2256 & 0.5271 & -0.8204 \\ -0.7919 & 0.5894 & -0.1601 \end{pmatrix},$$

a -126.9241 ˚ rotation around reciprocal space vector (h,k,l): (0.1451, 0.8393, -0.5239)

Overlap statistics of components 1 and 2:

Overlap factor	Number in range	Percentage of all observations

0.0-0.2	239	1.2
0.2-0.4	52	0.3
0.4-0.6	14	0.1
0.6-0.8	5	0.0
0.8-1.0	5	0.0
Total:	**315**	**1.6**

Overlap statistics of components 1 and 3:

Overlap factor	Number in range	Percentage of all observations
0.0-0.2	27	0.1
0.2-0.4	8	0.0
0.4-0.6	6	0.0
0.6-0.8	3	0.0
0.8-1.0	1	0.0
Total:	**45**	**0.2**

Overlap statistics of components 2 and 3:

Overlap factor	Number in range	Percentage of all observations
0.0-0.2	46	0.2
0.2-0.4	10	0.1
0.4-0.6	12	0.1
0.6-0.8	7	0.0
0.8-1.0	7	0.0
Total:	**82**	**0.4**

Appendix A6.2: Mechanistic discussion

Proposed full mechanism of MDA^{2+} degradation

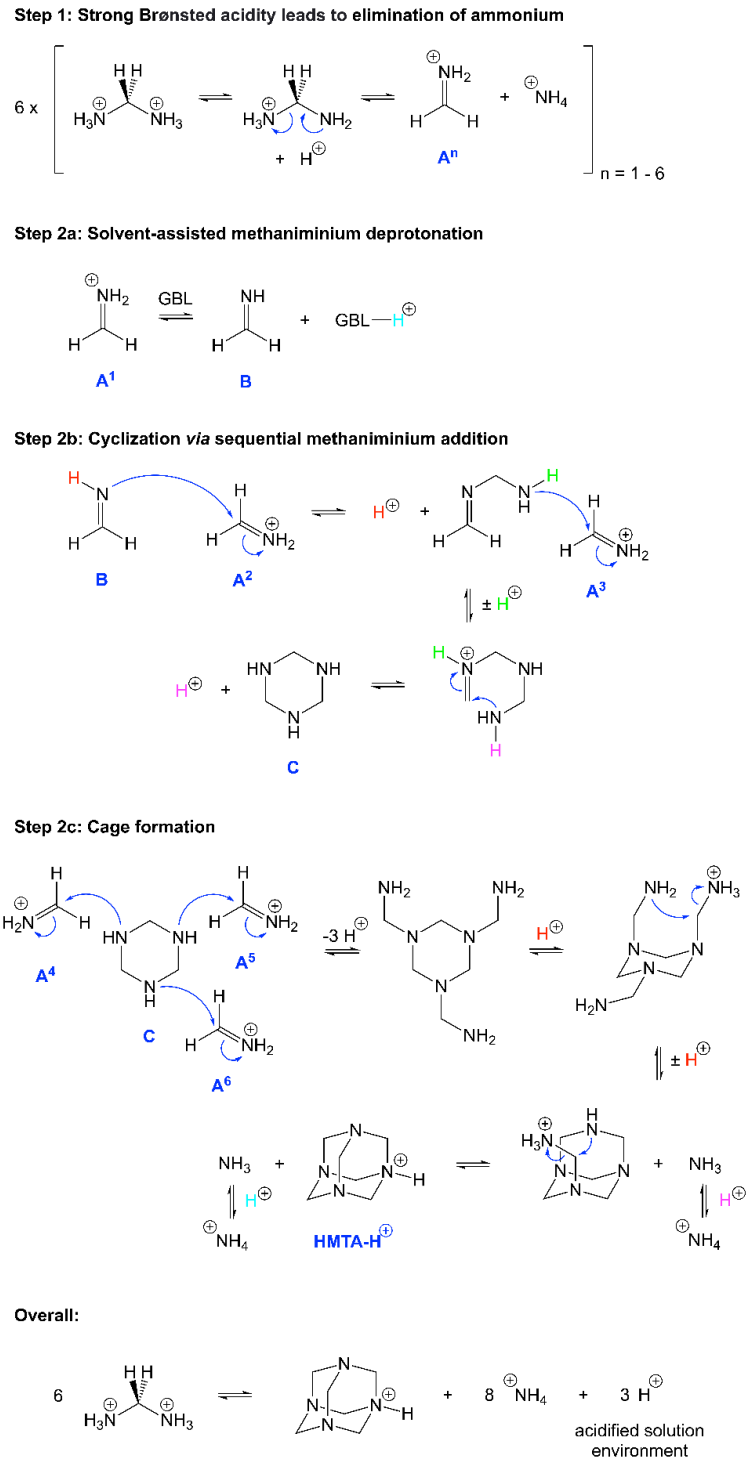


Figure A6.3 | MDA^{2+} degradation mechanism. Full mechanistic description of MDA^{2+} into ammonium and hexamethylenetetrammonium ($HMTA\text{-}H^{+}$), resulting in an acidified growth environment containing these products for our $FAPbI_3$-M single crystals.

THTZ-H^+ from HMTA

For simplicity, the mechanism shown in the main text only produces a single mim^+ cation from each HMTA consumed. This is sufficient to demonstrate mechanistically that THTZ-H^+ can form in-situ in solution containing multiple HMTA molecules and FA^+.

However, in a protic environment, species **D** (*N*-methylene-1-(methyleneamino)-*N*-((methyleneamino)methyl)methanaminium) can itself degrade further by addition – and subsequent consumption of – HMTA acting as a nucleophile, as shown. Overall, and disentangling the requirement for multiple HMTA molecules playing a role, each single HMTA molecule is expected to give rise to four methanimine molecules. This is highlighted in **Figure A6.4**.

By contrast, each MDA^{2+} cation added produces only a single methanimine. Thus, addition of 3.8 mol% $MDACl_2$ produces a maximum 3.8 mol% mim^+, while 0.63 mol% HMTA produces a maximum of 2.53 mol% mim^+ in solution.

We emphasise that, as with all mechanistic details presented in this work, the schemes set out should be interpreted as mechanistic justifications only, demonstrating that – by established chemical mechanisms – it is possible for the observed species to have been produced from one another. We have not conducted extensive mechanistic studies, and have only identified a relatively small number of the species displayed in the mechanistic schemes.

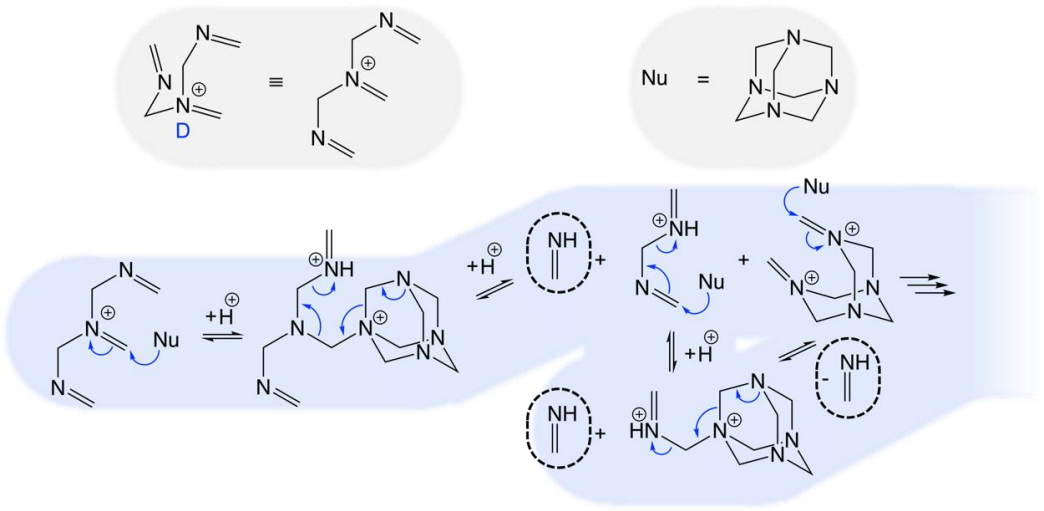


Figure A6.4 | Mechanistic justification for methaniminium formation from HMTA.

On the selective formation of THTZ-H$^+$ (against other mim$^+$-FA$^+$ reaction products)

Considering the wide range of intermediates expected to form transiently during the degradation of $MDACl_2$, it is not straightforward to predict at what stage FA^+ present in solution might interact, nor which from a variety of possible reactions products might be favoured or observable. However, a consideration of both the kinetics (expected rate) of postulated reactions and the thermodynamic stability of proposed products (driven by entropic loss of by-products or energetic stabilisation of products/by-products) is instructive.

As has been highlighted, methanimine is highly reactive as both a nucleophile and an electrophile. mim^+ is an extremely reactive electrophile. Formation of methanimine in solution from MDA^{2+} requires the deprotonation of mim^+ (acting as a weak acid), which likely occurs rapidly. However, that none of the proposed intermediates between mim^+ and HMTA-H$^+$ have been convincingly detected in our NMR studies suggests that methanimine generation from mim^+ is actually the rate determining step in cage

formation. This could be due to the acidity of the environment in which methanimine is generated (weakly acidic), which ensures that most methanimine formed is reprotonated. From HMTA, methanimine is generated directly, although it may be reprotonated and deprotonated before further reaction. However, it is clear that in any of these cases methanimine formed in solution reacts extremely rapidly. We might therefore expect that its reactivity is under kinetic control; methanimine will react with the molecules in its immediate vicinity, regardless of whether this leads directly to the thermodynamic product.

Given the stability of FA^+ in perovskite precursor solutions (typically on the order of at least days, in contrast to mim^+ which reacts via methanimine with either itself or FA^+ within seconds-to-minutes), despite FA^+ also functioning as a weak acid in solution, suggests that either formamidine is a poor nucleophile compared to methanimine, or FA^+ is a poor electrophile compared to mim^+, or – most likely – both. Thus, in a stoichiometric mixture of FA^+ and mim^+ we might expect methanimine reaction with mim^+ to dominate. However, in all the cases presented, methanimine generated in-situ is in an environment in which FA^+ is in a vast excess (>100:1). Thus, in such an environment, reaction with the most available electrophile (FA^+) – not simply the most reactive electrophile (mim^+) – will dominate. As shown in **Figure 6.13** this leads to the formation of 1,1-diamino-*N*-methylenemethanaminium. This cation is itself susceptible to further nucleophilic attack. It could itself instead eliminate ammonia and go on to act as a nucleophile, reacting with either reactive mim^+ (also leading to THTZ-H^+) or with FA^+ (in excess) to give alternative MDA^{2+}-FA^+ degradation products, however kinetics are again expected to take precedence over this relatively slow process. Thus, we expect that nucleophilic attack by further reactive methanimine will dominate. Once this addition is complete, rapid intramolecular ring closure is expected, kinetically.

Finally, THTZ-H^+ formation is achieved by elimination of ammonia. Although all steps are reversible, formation of the resonant amidinium system in THTZ-H^+ is thermodynamically favoured, while NH_3 formation is also entropically favourable and likely leads to loss of NH_3 into the gas phase thus effectively preventing the backward reaction and ensuring that the majority of methanimine generated ends up producing THTZ-H^+ by reaction with FA^+, rather than any other product.

Appendix A6.3: Appendix A6.3: Structural model of $FAPbI_3$ with additive THTZ-H^+

^1H-^1H spin diffusion spectra enable establishing atomic-level contact between species in solid materials. This is because for the cross-peaks to appear, there needs to be a pathway for the ^1H magnetization to travel between the two species. This can only be the case when the two species are present within the same phase, within a network of dipolar coupled ^1H spins. In our experiment, we observe cross-peaks between GBL and THTZ-H^+, THTZ-H^+ and FA, and GBL and FA. This result indicates that all three components are present within the same phase, and not as separate phases.

Conceptually, there are a number of structural scenarios in which impurities can be incorporated into crystalline materials: surface absorption, solid solution, co-crystal (for molecular solids), agglomeration or inclusion[42]. In each of these cases, the impurities are in atomic-level contact with the perovskite lattice and would lead to the appearance of cross-peaks in spin-diffusion spectra. We identify the incorporation mechanism based on the other NMR results, as follows. The ^{127}I NQR spectrum of $FAPbI_3$-H is qualitatively different (broader) compared to that of reference $FAPbI_3$, which indicates that all iodide sites within the crystal are affected by the presence of THTZ -H^+. This would not be the case if THTZ-H^+ was merely adsorbed on the surface of the crystal or kinetically trapped in a pocket of mother liquor during crystallization (as is the case during agglomeration and formation of crystal inclusions). The formation of a solid solution is therefore the only mechanism that agrees with the experimental ^1H-^1H spin-diffusion and ^{127}I NQR data. On the other hand, the presence of GBL within all three types of crystals (reference $FAPbI_3$, $FAPbI_3$-H and $FAPbI_3$-M) indicates that the solvent is kinetically trapped during crystallization as inclusions

which exist independently of the THTZ -H^+ (note that those inclusions are present also in the reference $FAPbI_3$ which has no THTZ -H^+).

For completeness, we also consider the hypothesis that THTZ-H^+ could template the growth of $FAPbI_3$ such that the resulting perovskite lattice is more disordered relative to undoped $FAPbI_3$ (octahedral tilting induced by surface templating, as reported by Doherty et al.[43]). In this scenario, the dopant would only be present on the crystal surface but still lead to a qualitative change in the local iodide environments, as probed by ^{127}I NQR, throughout the crystal volume. While our results could be consistent with this hypothesis, we present a series of arguments – with supporting experimentation – from which we eliminate this possibility.

First, we note the relatively large THTZ-H^+ content in the crystals (ca. 0.5 mol% relative to FA). Considering the low surface area of the crystals (on the order of 0.001 m^2/g), the amount of incorporated THTZ-H^+ is several orders of magnitude larger relative to what would be expected for a surface monolayer. For example, considering a cubic $FAPbI_3$ crystal with an edge length of 1 mm and a density of 4.16 g cm^{-3}, a uniform layer of THTZ-H^+ (assuming density 1.5 g cm^{-3} and a FA:THTZ-H^+ molar ratio of 1:0.005) on the cube surface would have a thickness of about 100 µm. Such a thick surface layer of THTZ-H^+ (or THTZ iodoplumbate) would be expected to diffract X-rays, but in none of our XRD experiments did we detect any additional phases. Further, it might be expected that such a capping layer could be removed by an appropriate solvent. We washed away the exterior layers of $FAPbI_3$-M and $FAPbI_3$-H crystals by repeated submersion in GBL (three washes) and conducted ^1H NMR solution NMR measurements on the resultant crystals. As shown in **Figure A6.5** the washing process did not remove signals corresponding to THTZ-H^+. Quantitative analysis of a reduction in THTZ-H^+ content by this treatment is impossible due to crystal-to-crystal

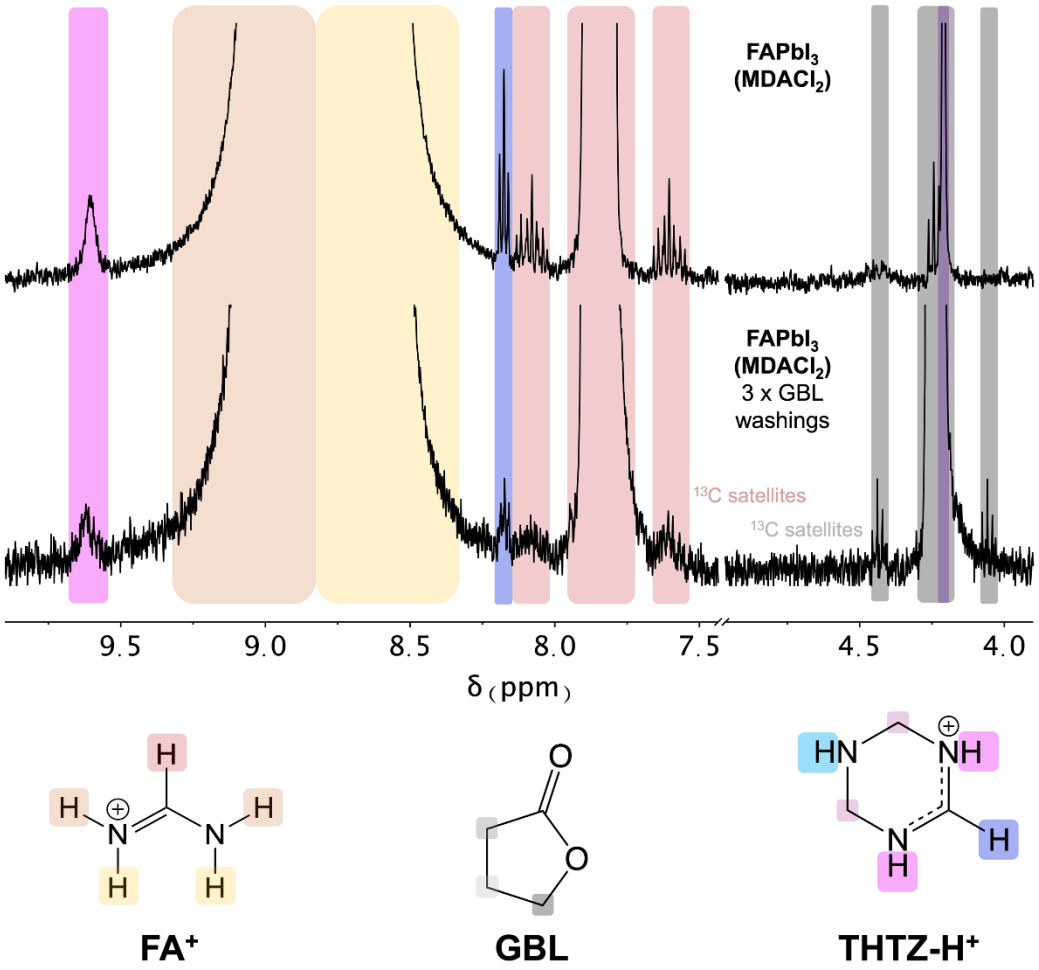


Figure A6.5 | GBL washing to investigate THTZ-H$^+$ in bulk or on surface of FAPbI$_3$-M/FAPbI$_3$-H crystals. ^{1}H solution nuclear magnetic resonance spectra of an untreated FAPbI$_3$-M crystal dissolved in d^6-DMSO (bottom), and of a FAPbI$_3$-M crystal grown in the same batch but after vacuum drying is washed three times with 1 mL of GBL to remove the outer layers of the crystal, before addition of DMSO-*d*^{6}.

variation (in this experiment a crystal is irreversibly dissolved in DMSO-*d*^{6} to acquire each spectrum, and so the two spectra shown are from the dissolution of two different crystals, which – on account of the surface area:volume ratio of each crystal being different, and important to the FA$^+$:THTZ-H$^+$ ratio under the surface capping model – complicates the analysis possible). It is possible that our washing process failed to remove all surface features or that THTZ-H$^+$ remaining in the washing solvent is retained on the surface during drying. However, we further note from our Raman spectroscopy that we do not observe that the use of either HMTA or MDACl$_2$ additives has any effect on the position and width of the Raman modes of FAPbI$_3$, as might be

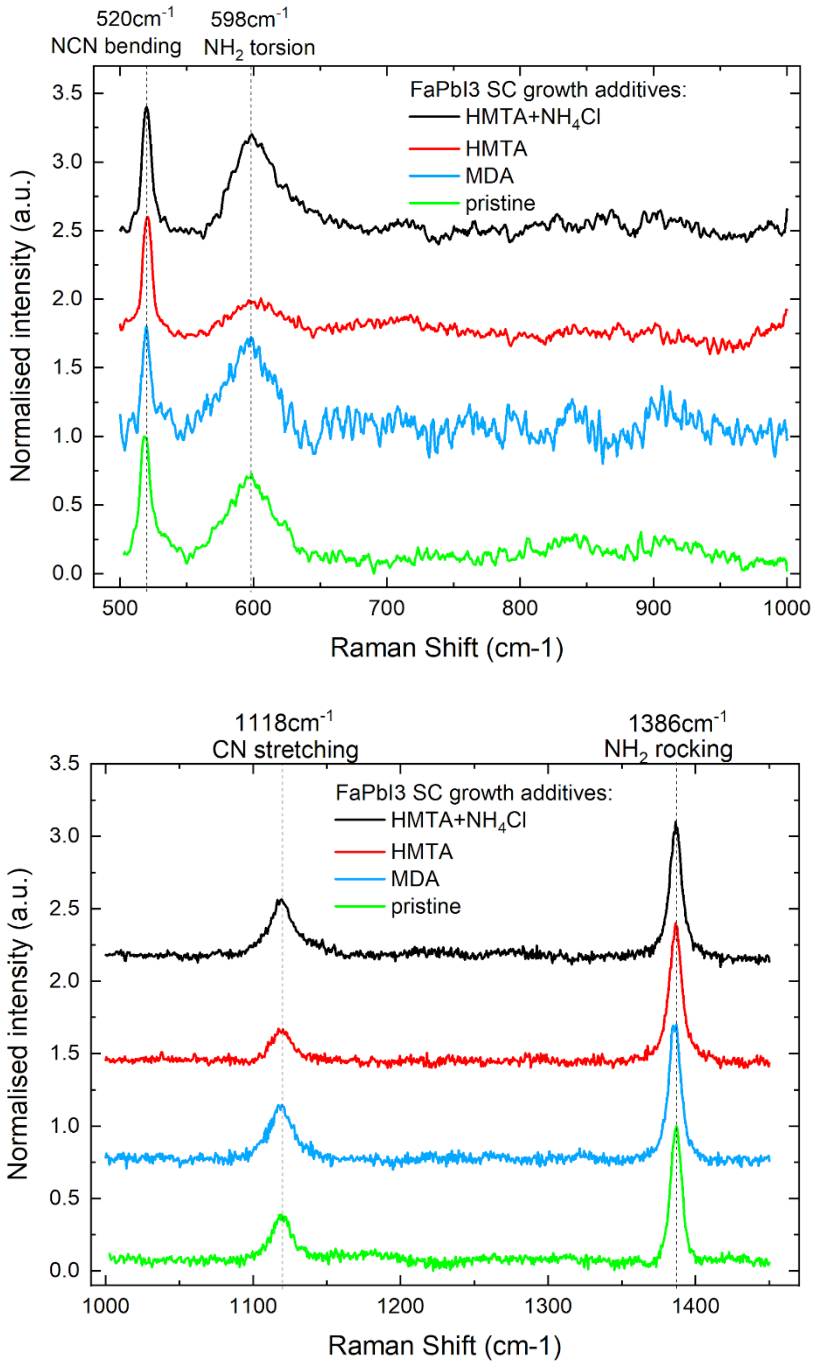


Figure A6.6 | Non-FA⁺ organics in $FAPbI_3$ single crystals by Raman spectroscopy. *Measurements and analysis carried out by B. Sturdza.* Raman spectra of $FAPbI_3$ (pristine), $FAPbI_3$-M ($MDACl_2$), $FAPbI_3$-H (HMTA) and $FAPbI_3$-H-NH_4Cl (HMTA+NH_4Cl) in the region in which vibrational modes corresponding to the organic components in the perovskite material are observed. There is no evidence of the inclusion of species besides FA^+ visible on the resolution of this measurement. We note that the frequency of C=N stretching vibrational modes corresponding to mim^+ are expected to be very similar to those of FA^+.

expected in the presence of substantial non-FA^+ organic components at the surface[44] (**Figure A6.6**). Perhaps most conclusively, however, is the observation that crystals cleaved to reveal the bulk α-$FAPbI_3$-M and α-$FAPbI_3$-H material do not degrade at an

enhanced rate (**Figure 6.2**) as would be expected as these surfaces don't benefit from the hypothesised capping layer.

6.7 – Bibliography

1. Saliba, M., Correa-Baena, J. P., Grätzel, M., Hagfeldt, A. & Abate, A. Perovskite Solar Cells: From the Atomic Level to Film Quality and Device Performance. *Angew. Chem., Int. Ed.* **57**, 2554–2569 (2018).

2. De Wolf, S. *et al.* Organometallic halide perovskites: Sharp optical absorption edge and its relation to photovoltaic performance. *J. Phys. Chem. Lett.* **5**, 1035–1039 (2014).

3. Lim, J. *et al.* Elucidating the long-range charge carrier mobility in metal halide perovskite thin films. *Energy Environ. Sci.* **12**, 169–176 (2019).

4. Eperon, G. E. *et al.* Formamidinium lead trihalide: A broadly tunable perovskite for efficient planar heterojunction solar cells. *Energy Environ. Sci.* **7**, 982–988 (2014).

5. Shockley, W. & Queisser, H. J. H. J. Detailed Balance Limit of Efficiency of p-n Junction Solar Cells. *J. Appl. Phys.* **32**, 510–519 (1961).

6. Min, H. *et al.* Perovskite solar cells with atomically coherent interlayers on SnO_2 electrodes. *Nature* **598**, 444–450 (2021).

7. Jeong, J. *et al.* Pseudo-halide anion engineering for α-$FAPbI_3$ perovskite solar cells. *Nature* **592**, (2021).

8. Yoo, J. J. *et al.* Efficient perovskite solar cells via improved carrier management. *Nature* **590**, 587–593 (2021).

9. Chen, T. *et al.* Entropy-driven structural transition and kinetic trapping in formamidinium lead iodide perovskite. *Sci. Adv.* **2**, 1–7 (2016).

10. Chen, L., Yoo, J. W., Hu, M., Lee, S. & Seok, S. Il. Intrinsic Phase Stability and Inherent Bandgap of Formamidinium Lead Triiodide Perovskite Single Crystals. *Angew. Chemie* **44919**, 1–7 (2022).

11. Conings, B. *et al.* Intrinsic Thermal Instability of Methylammonium Lead Trihalide Perovskite. *Adv. Energy Mater.* **5**, 0–6 (2015).

12. Schwenzer, J. A. *et al.* Thermal Stability and Cation Composition of Hybrid Organic-Inorganic Perovskites. *ACS Appl. Mater. Interfaces* **13**, 15292–15304 (2021).

13. Yi, C. *et al.* Entropic Stabilization of Mixed A-Cation ABX_3 Metal Halide Perovskites for High Performance Perovskite Solar Cells. *Energy Environ. Sci.* **9**, 656–662 (2015).

14. Jeon, N. J. *et al.* Compositional engineering of perovskite materials for high-performance solar cells. *Nature* **517**, 476–480 (2015).

15. Filip, M. R., Eperon, G. E., Snaith, H. J. & Giustino, F. Steric engineering of metal-halide perovskites with tunable optical band gaps. *Nat. Commun.* **5**, (2014).

16. Ho, K., Wei, M., Sargent, E. H. & Walker, G. C. Grain Transformation and Degradation Mechanism of Formamidinium and Cesium Lead Iodide Perovskite under Humidity and Light. *ACS Energy Lett.* 934–940 (2021).

17. Min, H. *et al.* Efficient, stable solar cells by using inherent bandgap of a-phase formamidinium lead iodide. *Science (6466).* **366**, 749–753 (2019).

18. Kim, G. *et al.* Impact of strain relaxation on performance of a-formamidinium lead iodide perovskite solar cells. *Science (6512).* **370**, 108–112 (2020).

19. Jin-Wook, L., Shaun, T., Il, S. S., Yang, Y. & Nam-Gyu, P. Rethinking the A cation in halide perovskites. *Science (6583).* **375**, eabj1186 (2022).

20. Nayak, P. K. *et al.* Mechanism for rapid growth of organic–inorganic halide perovskite crystals. *Nat. Commun.* **7**, 13303 (2016).

21. Wenger, B. *et al.* Consolidation of the optoelectronic properties of $CH_3NH_3PbBr_3$ perovskite single crystals. *Nat. Commun.* **8**, 590 (2017).

22. Weller, M. T., Weber, O. J., Frost, J. M. & Walsh, A. Cubic Perovskite Structure of Black Formamidinium Lead Iodide, α-$[HC(NH_2)_2]PbI_3$, at 298 K. *J. Phys. Chem. Lett.* **6**, 3209–3212 (2015).

23. Duijnstee, E. A. *et al.* Toward Understanding Space-Charge Limited Current Measurements on Metal Halide Perovskites. *ACS Energy Lett.* **5**, 376–384 (2020).

24. Le Corre, V. M. *et al.* Revealing Charge Carrier Mobility and Defect Densities in Metal Halide Perovskites via Space-Charge-Limited Current Measurements. *ACS Energy Lett.* **6**, 1087–1094 (2021).

25. Duijnstee, E. A. *et al.* Understanding Dark Current-Voltage Characteristics in Metal-Halide Perovskite Single Crystals. *Phys. Rev. Appl.* **15**, 14006 (2021).

26. Han, Q. *et al.* Single Crystal Formamidinium Lead Iodide ($FAPbI_3$): Insight into the Structural, Optical, and Electrical Properties. *Adv. Mater.* **28**, 2253–2258 (2016).

27. Chang, J., Jiang, L., Wang, G., Huang, Y. & Chen, H. Theoretical insight into the CdS/$FAPbI_3$ heterostructure: a promising visible-light absorber. *New J. Chem.* **45**, 4393–4400 (2021).

28. Lehn, J. M. & Seher, R. Nuclear spin–spin interactions. ^{14}N–^{1}H spin–spin coupling in quaternary enammonium salts. *Chem. Commun.* 847–849 (1966).

29. Grigoras, M. & Catanescu, C. O. Imine oligomers and polymers. *J. Macromol. Sci. - Polym. Rev.* **44**, 131–173 (2004).

30. Takayanagi, T., Shimakami, N., Kurashina, M., Mizuguchi, H. & Yabutani, T. Determination of the Acid-Base Dissociation Constant of Acid-Degradable Hexamethylenetetramine by Capillary Zone Electrophoresis. *Anal. Sci.* **32**, 1327–1332 (2016).

31. Mohrle, H. & Scharf, U. Tetrahydro-s-triaziniumsalz: 1. Mitt. uber Hydro-s-triazine. *Arch. Pharm. (Weinheim)* **307**, 51–57 (1974).

32. Fateev, S. A. *et al.* Solution Processing of Methylammonium Lead Iodide Perovskite from γ-Butyrolactone: Crystallization Mediated by Solvation Equilibrium. *Chem. Mater.* **30**, 5237–5244 (2018).

33. Kubicki, D. J., Stranks, S. D., Grey, C. P. & Emsley, L. NMR spectroscopy probes microstructure, dynamics and doping of metal halide perovskites. *Nat. Rev. Chem.* **5**, 624–645 (2021).

34. Kubicki, D. J. *et al.* Cation Dynamics in Mixed-Cation (MA)x(FA)1-xPbI3 Hybrid Perovskites from Solid-State NMR. *J. Am. Chem. Soc.* **139**, 10055–10061 (2017).

35. Kubicki, D. J. *et al.* Formation of Stable Mixed Guanidinium-Methylammonium Phases with Exceptionally Long Carrier Lifetimes for High-Efficiency Lead Iodide-Based Perovskite Photovoltaics. *J. Am. Chem. Soc.* **140**, 3345–3351 (2018).

36. Alanazi, A. Q. *et al.* Atomic-Level Microstructure of Efficient Formamidinium-Based Perovskite Solar Cells Stabilized by 5-Ammonium Valeric Acid Iodide Revealed by Multinuclear and Two-Dimensional Solid-State NMR. *J. Am. Chem. Soc.* **141**, 17659–17669 (2019).

37. Piveteau, L., Morad, V. & Kovalenko, M. V. Solid-State NMR and NQR Spectroscopy of Lead-Halide Perovskite Materials. *J. Am. Chem. Soc.* **142**, 19413–19437 (2020).

38. Aebli, M., Porenta, N., Aregger, N. & Kovalenko, M. V. Local Structure of Multinary Hybrid Lead Halide Perovskites Investigated by Nuclear Quadrupole Resonance Spectroscopy. *Chem. Mater.* **33**, 6965–6973 (2021).

39. Uller Rothmann, M. *et al.* Atomic-scale microstructure of metal halide perovskite. *Science (6516).* **370**, (2020).

40. Zhang, X., Wang, F., Zhang, B. Bin, Zha, G. & Jie, W. Ferroelastic Domains in a $CsPbBr_3$ Single Crystal and Their Phase Transition Characteristics: An in Situ TEM Study. *Cryst. Growth Des.* **20**, 4585–4592 (2020).

41. Rothmann, M. U. *et al.* Direct observation of intrinsic twin domains in tetragonal $CH_3NH_3PbI_3$. *Nat. Commun.* **8**, 6–13 (2017).

42. Urwin, S. J. *et al.* A Structured Approach to Cope with Impurities during Industrial Crystallization Development. *Org. Process Res. Dev.* **24**, 1443–1456 (2020).

43. Doherty, T. A. S. *et al.* Stabilized tilted-octahedra halide perovskites inhibit local formation of performance-limiting phases. *Science (6575).* **374**, 1598–1605 (2021).

44. Pérez-Osorio, M. A. *et al.* Raman Spectrum of the Organic-Inorganic Halide Perovskite $CH_3NH_3PbI_3$ from First Principles and High-Resolution Low-Temperature Raman Measurements. *J. Phys. Chem. C* **122**, 21703–21717 (2018).

Chapter 7 – Conclusion and Outlook

α-$FAPbI_3$ is a remarkable semiconductor material. Facile and inexpensive both to synthesise and to process into high-quality thin layers suitable for use in PSCs, and with the optimal bandgap of any lead halide perovskite for single junction PV, α-$FAPbI_3$ has remained overlooked principally on account of its apparent phase instability. This thesis has sought to encourage the research community to consider if this concern has been overblown.

7.1 – Key findings of the thesis

In pursuit of this aim, we confirmed that α-$FAPbI_3$ is capable of performing in PSCs (**Section 4.5**) with efficiency comparable to more complex perovskite alloys fabricated in our laboratories[1–4]. Importantly, we also establish that – when fabricated by our new 2D-templated processing route – PSCs based on α-$FAPbI_3$ retain their initial PCE for >1.5 years unencapsulated under dry air storage conditions (**Section 5.2**), suggesting that it is certainly possible to fabricate α-$FAPbI_3$ in a fashion that renders it long term ambient phase metastability, without compromising the impressive optoelectronic properties displayed by halide perovskites.

It is well understood that how perovskite materials are processed – especially when processing from solution – strongly impacts the efficiency of the resulting PSC. It is therefore no surprise that the same is true for the stability of perovskite materials and solar cells. However, for the most part, the implications of this observation have been overlooked. In part this is due to the ubiquity of the so-called “one-step” processing of perovskite materials from mixed DMF and DMSO solvent systems. The absence of variety in processing has narrowed the field of view such that the obvious can remain

underappreciated. By developing a novel solution processing route (**Section 4.2-4**) that enables strongly directed crystallisation of the α-$FAPbI_3$ material and is based on solvents with very different properties to DMF and DMSO, we have been able to cast the substantial advantages of strategic tailoring perovskite processing towards enhanced stability into stark relief (**Section 5.2-3**). By highlighting improvements in both α-$FAPbI_3$ thermal and ambient phase stability we make clear that how perovskites are processed directly impacts their stability, and moreover that what constitutes ideal processing for the stability of one perovskite composition may not translate to another. α-$FAPbI_3$ may be substantially less forgiving than other lead halide perovskites when it comes to stability optimisation, but the potential advantages of successfully harnessing this material certainly justify our own – and future – efforts to do so. We compliment, and re-emphasise, the significance of our materials stability studies by effectively translating our new processing route for α-$FAPbI_3$ to a compatible p-i-n PSC architecture and demonstrating substantial enhanced PSC stability with α-$FAPbI_3$ in comparison with an established 'highly stable' perovskite material, $FA_{0.83}Cs_{0.17}Pb(I_{0.9}Br_{0.1})_3$ (**Section 5.4**)[1,3,5].

The work presented in **Chapter 6** is something of a double-edged sword when weighing the arguments above. We show clearly that there is plenty more than meets the eye when it comes to additive engineering with α-$FAPbI_3$, and perovskites more widely (**Section 6.3-4**). Further, we re-emphasise the need for rigorous application of advanced materials characterisation techniques, in tandem with research efforts to enhance efficiency and stability in PSCs, in order to understand the action of even seemingly simple additives. This is especially important as a means to inform the rational design of new perovskite additives and alloys, which is too often based on trial and error. However, in this final Chapter we also show that it is possible to alloy α-

$FAPbI_3$, without altering either its basic processing route or any of its fundamental optoelectronic properties, and yet substantially enhance its stability (**Section 6.2** and **6.5**). In this regard, we have once again shown that precise control of the synthesis conditions of halide perovskites is crucial for their long-term material stability.

Ultimately it is clear that a combined approach to improving α-$FAPbI_3$ stability will be required, with minority additives alloyed into α-$FAPbI_3$ by strategically designed processes that imbue the material with the stability it is capable of possessing, without compromising its remarkable qualities.

7.2 – Outlook, and future investigation

Throughout the thesis, where current understanding has proven limited or restrictive we have noted a number of areas where further investigation would be particularly valuable. Here, in light of the summary presented in **Section 7.1**, we revisit a number of these, cast them in a broader context and discuss more wide-reaching future directions for the field in light of this thesis.

Although not a key focus of this thesis, use of 2-methyltetrahydrofuan (MeTHF) as a processing solvent for perovskites has wide-reaching advantages. It's high volatility and low-toxicity make it ideal for at-scale, roll-to-roll (R2R) solution processing and – as we have demonstrated in **Section 5.3** – imbue perovskite materials fabricated from it with higher thermal stability than those fabricated from low volatility solvents, which are liable to be retained post-processing and act to degrade the perovskite slowly over time. However, as noted in the conclusion to **Chapter 4**, MeTHF alone cannot dissolve perovskite precursors and so a co-solvent is required. Use of butylamine (BA), or indeed most amines (the majority of which are substantially more toxic than MeTHF), substantially limits the attractiveness of this system. Firstly by increasing the effective

toxicity of the solvent mixture, and secondly by leading directly to 2D perovskite materials, rather than their optoelectonically more inviting cousins the 3D perovskites. Thus, discovery of a new, highly Pb^{2+}-coordinating and highly volatile solvent or solvent blend, for use alongside MeTHF, would be of great advantage if this system is to be utilised in at-scale solution processing. Moreover, if such a solvent mixture can be fully removed from the final perovskite material, without the need for a solid state lower dimensionality intermediate, this may be advantageous from the point of view of simplifying perovskite layer processing significantly.

However, use of an amine as a co-solvent leading to formation of a 2D perovskite template has led us to discover how effective such 2D materials can be in templating the growth of highly stable 3D perovskites. Use of solid-state layered intermediates already possessing the corner-sharing haloplumbate scaffold common to all 3D lead halide perovskites is an extremely exciting new avenue for perovskite processing. First, it should be established that the 2D templating effect and the use of the MeTHF/BA co-solvent system are orthogonal. Based on our understanding herein, it should be possible to process a 2D perovskite from conventional solvents (e.g. DMF/DMSO) and use this material as the template for a 3D perovskite. Further, here we have concentrated all our effort on just one perovskite composition; α-$FAPbI_3$. Again, based on the understanding presented, it should be trivial to translate the same 2D-templating approach to mixed-bromide perovskite, which will allow straightforward manipulation of the photoabsorber bandgap towards applications in, for example, multi-junction solar cells. Use of halide blends involving bromide, which possesses a substantially smaller ionic radius than iodide, will open up a range of interesting questions regarding how 2D-templating is affected. We have shown (**Section 4.3**) that the precise phase mixture of the 2D template is essential to affecting complete

conversion to the 3D perovskite without either introducing undesirable amounts of lead halide (PbI_2, in the case of the triiodide system) or rupturing the thin layer by necessitating too great a degree of volume contraction during conversion. Presumably, use of a smaller anion (bromide) in either the 2D template or conversion solution will – at least – alter the optimal 2D template phase composition. Of perhaps even greater interest, both in the context of halide mixing or 2D-templating in general, investigation into the relative merits of different 2D organic spacer cations should be affected. Here we have universally concentrated on butylammonium (BA^+), but could cations (other alkylammoniums, or arylammoniums, for example) with different properties prove more effective still, or at least more suitable in the case of mixed halide compositions? This could be done either in conjunction with the search for co-solvents with lower toxicity than BA, or perhaps by using DMF/DMSO solvent systems to process a range of different 2D perovskite by more conventional means.

Equally, no effort has yet been expended in utilising the 2D perovskites deposited directly from the MeTHF/BA system as the photoactive layer in PSCs. If this could be effectively accomplished several advantages might be had. Firstly, again, simplifying processing of the perovskite layer. In addition, avoidance of the high temperature annealing step required to complete conversion in the ^{t}2D-3D method would allow for compatibility of the processing method with flexible, plastic substrates used in R2R fabrication. Moreover, 2D perovskites possess a wider bandgap than 3D perovskites and so might be used towards applications such as multijunction PV, and have also been shown to possess enhanced moisture stability in comparison to 3D perovskites[6]. In a similar vein, my judicious choice of the amine co-solvent, it may be possible to directly fabricate lower dimensionality perovskites, including so-called 0D materials suitable for use in LED applications[7].

In general, an obvious next step for the MeTHF/BA system presented is to confirm and demonstrate its compatibility with at-scale processing. Deposition methods such as slot-die or bar coating would be especially suitable. The high volatility of the MeTHF/BA system allows for direct crystallisation of the 2D perovskite phase without the need for external stimuli, while the conversion process could be achieved by a R2R-compatible dip coating method, followed by an air knife to remove excess solution before drying and conversion either by conventional thermal annealing or, for example, photonic curing[8] to avoid the need for a lengthy high temperature curing step.

The discovery that the phase stability boosting effect of employing $MDACl_2$ as an additive to α-$FAPbI_3$ is actually due to incorporation of trace quantities of THTZ-H^+ is an exciting finding in its own right. However, further work to demonstrate that use of this additive can be translated into the production of α-$FAPbI_3$ thin films is urgently needed. This might be achieved either by synthesis of THTZ-HCl (or a similar THTZ-H^+ salt) and direct addition to the precursor solution, or by using $FAPbI_3$-M crystals as the precursor material for perovskite inks. Although more synthetically challenging, the former route seems advantageous in that it avoids the need to pre-synthesise $FAPbI_3$-M crystals, which is rather cumbersome and inefficient in raw materials. Further, synthesis of THTZ-HCl might be done alongside other FA^+ moiety-containing additives, which have been much overlooked by the field, principally due to their commercial unavailability, in favour of alkylammonium additives. Alkyl-, aryl- or other cyclic amidinium salts are a class of perovskite A-site compatible materials that require substantial further study, as our discovery of THTZ-H^+ demonstrates[2,9].

In summary, while the relentless focus in this thesis on α-$FAPbI_3$ has allowed for significant development of this underutilised perovskite semiconductor towards use in

PSCs, it is clear that there are now a substantial growth number of areas where application of the processes put forward herein to a more diverse range of perovskite compositions could lead to substantial further material enhancement, in particular for perovskite stability, and further fundamental understanding of how perovskite synthesis and processing directs the performance of the resulting material.

7.3 – Bibliography

1. Lin, Y. H. *et al.* A piperidinium salt stabilizes efficient metal-halide perovskite solar cells. *Science (6499).* **369**, 96–102 (2020).

2. Taddei, M. et al. Ethylenediamine Addition Improves Performance and Suppresses Phase Instabilities in Mixed-Halide Perovskites. *ACS Energy Lett.*, **7**, 4265–4273 (2022).

3. McMeekin, D. P. et al. Intermediate-phase engineering via dimethylammonium cation additive for stable perovskite solar cells. *Nat. Mater.* **22**, 73–83 (2023).

4. Caprioglio, P. et al. Open-circuit and short-circuit loss management in wide-gap perovskite p-i-n solar cells. *Nat. Commun.* **14**, 1–13 (2023).

5. Turren-Cruz, S. H., Hagfeldt, A. & Saliba, M. Methylammonium-free, high-performance, and stable perovskite solar cells on a planar architecture. *Science (6413).* **362**, 449–453 (2018).

6. Kore, B. P., Zhang, W., Hoogendoorn, B. W., Safdari, M. & Gardner, J. M. Moisture tolerant solar cells by encapsulating 3D perovskite with long-chain alkylammonium cation-based 2D perovskite. *Commun. Mater.* **2**, 1–10 (2021).

7. Sun, S. et al. 0D Perovskites: Unique Properties, Synthesis, and Their Applications. *Adv. Sci.* **8**, 1–23 (2021).

8. Xu, W., Daunis, T. B., Piper, R. T. & Hsu, J. W. P. Effects of Photonic Curing Processing Conditions on $MAPbI_3$ Film Properties and Solar Cell Performance. *ACS Appl. Energy Mater.* **3**, 8636–8645 (2020).

9. Duijnstee, E. A. et al. Understanding the Degradation of Methylenediammonium and Its Role in Phase-Stabilizing Formamidinium Lead Triiodide. J. Am. Chem. Soc. **2023**, 145 (18), 10275-10284